Effect of spin-orbit scattering on transport properties of low-dimensional dilute alloys

von

Dipl.-Phys. Swantje Heers

aus

Hamburg, Deutschland

Table of Contents

Introduction

The control and manipulation of electron spin currents in metals is one of the grand challenges in the field of spintronics. Being a truly multidisciplinary field it combines key insights from magnetism research, semiconductor and mesoscopic physics, and optics with technological advances such as the structure miniaturization of nanodevices. Even though it is a relatively recent field, it relies closely on a long tradition of investigations. One of the pioneering work was provided by Mott already in 1936 [1, 2], who explained the unusual behavior of the resistance in ferromagnetic metals with the concept of spin-polarized currents. Furthermore, the discovery of the giant magnetoresistance effect (GMR) by Albert Fert [3] and Peter Grünberg [4] in 1988 mark a breakthrough in spintronics, which was rewarded with the Nobel price in 2007 and led to a very successful application: already eight years after its discovery, the effect was exploited in hard disk drives common to most PCs; its spectacular innovation was the transformation of spin information into charge current. Almost at the same time, Johnson and Silsbee [5, 6] for the first time succeeded to electrically inject and measure a non-equilibrium spin accumulation in metals, establishing a new method to detect spin relaxation.

All these findings rely on three fundamental characteristics of electrons, making them highly attractive for the transfer of information [7]: First, they can be polarized and store information in their spin state (up or down). Secondly, their mobility allows to transfer the information to another place, where, third, the information can be read out. Of course, this works only if the information is not lost, i.e. the spin state has not changed during the transport process.

The decay of a non-equilibrium spin state towards an equilibrium is generally called spin relaxation. The strength of spin relaxation is quantitatively specified by a spin-relaxation time T_1, after which the system has come close to equilibrium, or the related spin-relaxation length λ, characterizing the length after which the spin current has decayed. In order to ensure the successful transfer of information, long spin relaxation times are desired[1]. Furthermore, the active manipulation of the spin states must be able to benefit fully from these properties; otherwise, the sheer existence of two spin states is of limited use. These two closely related issues are the major subject of most of theoretical and experimental investigations in the field of spintronics.

---

[1]An exception are devices, for which short switching times are required.

Spin relaxation is a very complex phenomenon. It strongly depends on the investigated material, and can be modulated by a great variety of parameters. Changing the dimensionality, doping or alloying can reduce or enhance the spin relaxation by several orders of magnitude [8]. There are several mechanisms of spin relaxation, but most of them are induced by spin-orbit coupling, providing a spin-dependent potential, which together with momentum scattering processes can be considered as a randomizing force. The two most important mechanisms of spin relaxation are the Elliott-Yafet mechanism [9] and the D'yakonov-Perel' mechanism [10]. Whereas the first one leads to a decrease of spin-relaxation times for large momentum scattering rates, the latter mechanism yields the inverse behavior: large momentum scattering rates entail long spin-relaxation times.

The Elliott-Yafet mechanism is dominating in inversion-symmetric metals, in small-gap semiconductors as well as in those with a large spin-orbit coupling. In contrast, the D'yakonov-Perel' mechanism is uniquely present in systems without inversion symmetry and based on the splitting of the energy levels caused by the interplay of asymmetry and spin orbit-coupling together with momentum scattering.

Although spin relaxation in semiconductors has been studied intensively, there are not so many studies on this subject in metals. Theoretical investigations of spin relaxation due to electron-electron scattering was recently published by [11], while first results for *ab initio* spin-relaxation times in metals caused by impurity-scattering have been published in [12, 13]. Furthermore, an investigation of conduction electrons in polyvalent metals (Al) was provided by [14].

Experimentally, spin relaxation in metals has been first studied in Na, Be and Li with the conduction-electron spin resonance technique (CESR) [15], allowing for an indirect measurement of spin-relaxation times. Already these early investigations have shown that spin-relaxation times strongly depend on the impurity concentration. Furthermore, a linear scaling with temperature has been observed [16, 17]. With the development of the spin-injection technique in [5], the detection of spin-relaxation times became experimentally feasible. Compared to the spin resonance technique, it has the advantage of not requiring magnetic fields and enabling the measurement of spin-relaxation times in films [6, 18, 19], superconductors, spin-glasses, and Kondo systems. Just recently, the measurement of spin-relaxation times via the inverse spin Hall effect was realized in two different setups [20, 21] and spin relaxation in e.g. Pt, Pd, Au and Mo has been studied.

As already mentioned, the experimental investigations of spin-relaxation times in metals have revealed, that spin-relaxation processes are dominated by scattering at impurities and phonons. Whereas phonons can be frozen out, in preparing samples a small concentration of impurities and defects cannot be avoided. A first goal of this thesis is to contribute to this field of exciting physics, providing a systematic *ab initio* study of impurity scattering in the bulk of noble metals. The calculations of spin-relaxation times together with momentum relaxation allow to draw conclusions about the dominating spin-relaxation mechanisms.

Coming back to the aspect of downscaling of nanoelectronic devices, not only the characteristic of materials on an atomic scales gains importance, but also two-dimensional systems get into the focus of research. Often, at surfaces or thin films, physics completely change. In some materials such as at the (111) surfaces of the noble metals copper, silver and gold surface states form and dominate the electron dynamics. To understand these electronic

excitations at surfaces even without spin-orbit coupling is of great interest, because their temporal evolution determines the effectiveness of many important applications [22]. In this extensive field of research, in the last years a lot of theoretical and experimental research was done, which is not only due to the widespread of the subject; apart from the great variety of systems which could be investigated, several very powerful methods for its investigation have been developed [23]. While in (angle-resolved) photoemission experiments an indirect measurement of surface-state lifetimes via the linewidth is possible [24], two photon photoemission (2PPE) [25, 26] enables a direct measurement of lifetimes. In addition, lifetime measurements using scanning tunneling microscopy and spectroscopy [22] allows for a local investigation of surfaces, enabling the exclusion of defects and grain boundaries. Similar as in photoemission spectroscopy, surface-state lifetimes can then be extracted from the spectral linewidth. Just as spin-relaxation times, surface state lifetimes are reduced by different scattering mechanisms [23], namely scattering at crystal defects, phonons and by electron-electron scattering [27]. Therefore, a second goal of this thesis is to focus on the lifetime reduction of the (111) surface states of copper, silver and gold caused by scattering at impurities and defects; these are dominant at low temperatures, and in contrast to electron-electron scattering [27] and scattering at phonons they are not so well studied so far. Filling this gap is the second aim of this thesis.

The third goal of this thesis is to combine the first two aspects, i.e. to gain inside into spin-relaxation mechanisms at surfaces and in ultrathin films. As we find, the reduction of dimensionality affects the spin relaxation in non-trivial ways, due to effects of quantum confinement or by the onset of structural asymmetry in deposited films.

The thesis is structured as follows. The first two chapters give a short introduction to the theories providing the basis of our calculations, namely density functional theory (DFT) [28, 29] in chapter 1 and the Korringa-Kohn-Rostoker method (KKR) [30, 31] for electronic-structure calculations in chapter 2. The latter is based on Green functions and follows a multiple scattering ansatz. Therefore, it is very well suited for the numerical treatment of scattering processes; the scattering ansatz is exploited in chapter 3, where a scheme to calculate the band structure, the Fermi surface and the momentum-dependent wavefunction on the Fermi surface is derived. Furthermore, the formalism used to describe impurity scattering is introduced. The resulting scattering matrix yields the scattering rate from one momentum state to a second one due to scattering at impurities in momentum space. It is a central quantity from which a number of physical quantities can be obtained. In this work, we use it for the calculation of momentum-relaxation times and residual resistivities.

In chapter 4 spin-orbit coupling is discussed which is of central importance to this work. After giving a short introduction into the underlying theory, we will outline how it is included in the multiple scattering formalism of the KKR method. The derivation of this scheme and its implementation within the KKR code was an important part of this thesis. It allows for the calculation of the (momentum-dependent) spin expectation values and the Elliott-Yafet spin-flip parameters. We demonstrate that the degeneracy of wavefunctions for inversion-symmetric systems due to spin-orbit coupling leads to unexpected phenomena concerning the spin expectation values. Using a simple analytic model we show that these are not due to a numerical mistake but of fundamental nature.

Furthermore, the Lippmann-Schwinger equation applied to impurity scattering is extended to spin-flip scattering processes. A general expression including the spin degrees of freedom for the scattering matrix is given. Finally, we demonstrate how spin-conserving momentum-relaxation times as well as spin-flip relaxation times are obtained from the scattering matrix. Chapter 5 provides some numerical tests of the implementation of spin-orbit coupling in the code and discusses solutions of some of the problems we have encountered.

In the remaining three chapters 6 to 8, we finally present our calculated results. The main topic of chapter 6 are spin-conserving and spin-relaxation processes due to impurity scattering in the fcc bulk metals copper and gold. In these systems, the Elliott-Yafet mechanism for spin-flip scattering prevails. Therefore, this chapter starts with a theoretical outline of this mechanism. Afterwards, we discuss unexpected results from test calculations of spin-conserving and spin-flip scattering rates. These results are substantiated by similar findings obtained for a simple tight-binding program, documented in Appendix C. Furthermore, we compare the calculated momentum-relaxation and spin-relaxation times to numerical and experimental data.

A systematic study of momentum-relaxation and spin-relaxation times for $3d$, $4sp$, $4d$, $5sp$, $5d$ and $6sp$ impurities in gold and copper hosts is presented. The role of the spin-orbit coupling in the host is investigated and the trends for spin-conserving and spin-flip scattering rates are compared. In order to understand the differences between these two trends, Wigner delay times as well as residual resistivities are calculated.

At the end of this chapter we investigate correlated scattering processes, i.e. multiple scattering at neighboring impurities, which have not been investigated so far.

Chapter 7 focuses on spin-conserving scattering processes occurring at the (111) surfaces of copper, silver and gold. Surface-state lifetimes due to impurity scattering are calculated for impurities in the surface, one layer below the surface as well as for adatoms. Significant qualitative differences in the trends are obtained. At the end of this chapter, we present surface-states lifetimes as well as residual resistivities in thin films for different film thicknesses.

For many applications such as the spin Hall effect [32] as well as for spin relaxation, spin-orbit induced effects occurring on surfaces and thin films are of crucial importance. Therefore, in chapter 8 of this thesis we consider quasi two-dimensional copper and gold systems as in the chapter before, but under the influence of spin-orbit coupling. Furthermore, thin films with broken symmetry are investigated, where the spin-transport processes are fundamentally different compared to symmetric systems due to the appearance of spin-orbit fields, leading to the D'yakonov-Perel' mechanism. In the presented results we show that quantum confinement leads to hot spots for spin-flip scattering that are absent in the bulk, and we investigate the shape and strength of spin-orbit fields.

The results of this thesis are summarized in chapter 9.

CHAPTER 1

Density functional theory

In order to describe the chemical and physical properties of materials correctly, a quantum-mechanical treatment of the many-particle system of electrons and nuclei with their basic electrostatic Coulomb interactions is indispensable. Such systems are characterized by the many-body Hamiltonian

$$\hat{H}(\mathbf{r}_1, \ldots, \mathbf{r}_N) = \left[\hat{T} + \hat{U} + \hat{V}_{\text{ext}} \right] \tag{1.1}$$

$$= \left[-\sum_{i=1}^{N} \nabla_i^2 + \sum_{i,j} \frac{1}{|\mathbf{r}_i - \mathbf{r}_j|^2} + \sum_{i=1}^{N} V_{\text{ext}}(\mathbf{r}_i) \right],$$

where V_{ext} denotes an external potential and $\mathbf{r}_i$ are the positions of the particles. In the above formula, atomic units $\hbar = 1$, $m_e = 1/2$ and $e = \sqrt{2}$ have been used. The solution of the corresponding Schrödinger equation

$$\hat{H}\Psi = E\Psi, \tag{1.2}$$

the many-body wavefunction $\Psi(\mathbf{r}_1, \cdots, \mathbf{r}_N)$, is a very complicated object since it is a function of $3N$ spatial variables and N spin variables. It is obvious that it cannot be obtained without an approximation and even if this was the case, it would have been a too complicated object to understand and predict properties of real materials.

The first idea how to deal with this problem came by Thomas [33] and Fermi [34] in 1927, who obtained a heuristic description of the many-electron system totally in terms of the electronic density. With this ansatz they provided the conceptual root of modern density functional theory (DFT) which formally reduces the many-body problem to a single-electron problem. The basic statement of DFT is that all ground state properties of the system are uniquely determined by the ground state electron density $n_0(\mathbf{r})$. It goes back to the original works of Hohenberg and Kohn in 1964 [28]. In this publication, Hohenberg and Kohn showed that any property of a system of interacting electrons can be viewed as

a functional of the ground state density $n_0(\mathbf{r})$. However, since the exact functional is not known, the statement is rather abstract and just by itself of no practical use. The key to its application was provided only shortly after that in 1965 by Kohn and Sham [29] by introducing a fictitious, auxiliary electron system of non-interacting particles with an effective potential $V_{\text{eff}}(\mathbf{r})$ constructed such that the density of the auxiliary non-interacting electron system equals the density of the original system.

With this formulation Kohn and Sham paved the way to modern density functional theory which since then has had many applications. It is nowadays the basis of most present-day methods for treating electrons in atoms, molecules and solids.

1.1 Hohenberg-Kohn theorems

In their publication of 1964 [28], Hohenberg and Kohn formulated density-functional theory as an exact theory of many-body systems. This fundamental work consists of two basic theorems.

Theorem I   For any system of interacting fermions in an external potential $V_{\text{ext}}(\mathbf{r})$, the potential $V_{\text{ext}}(\mathbf{r})$ is determined uniquely, up to a constant, by the ground state particle density $n_0(\mathbf{r})$.

Corollary I   Since both the kinetic energy and the Coulomb interaction are known, according to the first theorem the Hamiltonian is fully determined, except for a constant shift in the energy. Therefore, the many-body wavefunctions for all states including the ground state and all excited states are fully determined, too. Consequently, it follows that all properties of the system are completely determined by the ground state density only.

According to Levy [35], the unique energy functional $E[n]$ can be defined as the minimum over all wavefunctions which yield the density $n(\mathbf{r})$,

$$
\begin{aligned}
E[n] \;&=\; \min_{\Psi \to n} \left\langle \Psi | \hat{T} + \hat{U} + \hat{V}_{\text{ext}} | \Psi \right\rangle \\
&=\; F[n] + \int d^3r \; n(\mathbf{r}) V_{\text{ext}}(\mathbf{r}) \,.
\end{aligned}
\tag{1.3}
$$

In the latter equation, the universal functional $F[n]$ with

$$
F[n] = \left\langle \Psi | \hat{T} + \hat{U} | \Psi \right\rangle
\tag{1.4}
$$

was introduced being universal in the sense that it does not depend on the external potential $V_{\text{ext}}(\mathbf{r})$.

Theorem II   For any particular $V_{\text{ext}}(\mathbf{r})$, the energy obtains its minimum for the ground state density n_0 and yields the ground state energy $E_0 = E[n_0]$.

Corollary II The functional $E[n]$ alone is sufficient to determine the exact ground state energy E_0 and ground state density $n_0(\mathbf{r})$. In general, excited states of the electrons must be determined by other means. Nevertheless, the work of Mermin [36] shows that thermal equilibrium properties such as specific heat are determined directly by the free-energy functional of the density.

The proof of the Hohenberg-Kohn theorem is simple and based on the Rayleigh-Ritz principle for the ground state energy, given by $E_0 = \langle \Psi_0 | \hat{H} | \Psi_0 \rangle$. It enables the ground state electron density to be calculated variational. For further information, see [37].

Originally, Hohenberg and Kohn formulated the two theorems for non-degenerate ground states. However, at later times, the theorems were extended to the case of degenerate systems.

1.2 Kohn-Sham equations

Hohenberg and Kohn have transformed the formidable problem of finding the minimum of $\langle \Psi | \hat{H} | \Psi \rangle$ with respect to the $3N$-dimensional trial wave function Ψ into the problem of finding the minimum of $E[n]$. However, since the explicit form of the functional $E[n]$ (see eq. (1.4)) is not known, the theorems themselves are of no practical use. The key for their application was given by Kohn and Sham [29] who used the variational principle implied by the minimal properties of the energy functional to derive single-electron Schrödinger equations. Their basic idea was to to introduce a fictitious auxiliary system of non-interacting particles with an effective external potential $V_{\text{eff}}(\mathbf{r})$ constructed such that the density of the auxiliary non-interacting system equals the density of the interacting system of interest. The one-to-one correspondence between the densities and the effective potentials is guaranteed by the Hohenberg-Kohn-theorems applied for $U = 0$. In this case, the universal functional $F[n]$ reduces to the single-particle kinetic energy functional $T_{\text{s}}[n]$, and the total-energy functional results in

$$E_{\text{s}}[n] = T_{\text{s}}[n] + \int d^3r \; V_{\text{eff}}(\mathbf{r})n(\mathbf{r}) \quad . \tag{1.5}$$

Application of the Hohenberg-Kohn variational principle as formulated in Theorem II in section 1.1 then leads to

$$\frac{\delta}{\delta n(\mathbf{r})}\left[E_{\text{s}}[n] + \mu\left[N - \int d^3r \; n(\mathbf{r}) \right] \right] = \frac{\delta T_{\text{s}}[n]}{\delta n(\mathbf{r})} + V_{\text{eff}}(\mathbf{r}) - \mu = 0 \tag{1.6}$$

where we have introduced the Lagrange parameter μ so that conservation of particles $\int n(\mathbf{r}) = N$ is guaranteed.

Using single-particle wavefunctions $\Phi_i(\mathbf{r})$ allows to construct the density $n(\mathbf{r})$ as well as the kinetic energy functional $T_{\text{s}}[n]$ in the form

$$n(\mathbf{r}) = \sum_{i=1}^{N} |\Phi_i(\mathbf{r})|^2 \tag{1.7}$$

and

$$T_s[n] = \sum_{i=1}^{N} \int d^3r \, \nabla \Phi_i^\star(\mathbf{r}) \nabla \Phi_i(\mathbf{r}), \tag{1.8}$$

respectively. The index i denotes both the spatial as well as the spin quantum numbers, and N is the highest occupied state. Variation of $E[n]$ with respect to the single-particle wavefunctions $\psi_i(\mathbf{r})$ then yields the N equations

$$\left[-\nabla^2 + V_{\mathrm{eff}}(\mathbf{r}) - \mu\right]\Phi_i(\mathbf{r}) = \epsilon_i\Phi_i(\mathbf{r}) \,, \tag{1.9}$$

which are the so-called Kohn-Sham equations. The parameter ϵ_i was introduced to guarantee for the normalization of the orbitals $\Phi_i(\mathbf{r})$, thus $\langle\Phi_i|\Phi_i\rangle = 1$.
For solving the Kohn-Sham equations, it is necessary to find a useful expression for the effective potential $V_{\mathrm{eff}}(\mathbf{r})$, which is still unknown. Therefore, Kohn and Sham suggested the following splitting of the functional $E[n]$ (see eq. (1.5))

$$E[n] = T_s[n] + \int d^3r \, V_{\mathrm{ext}}(\mathbf{r})n(\mathbf{r}) + \frac{1}{2}\iint d^3r \, d^3r' \, \frac{n(\mathbf{r})n(\mathbf{r}')}{|\mathbf{r}-\mathbf{r}'|} + E_{\mathrm{xc}}[n], \tag{1.10}$$

where the third term represents the well-established Hartree-functional; the fourth term is the so-called exchange-correlation energy functional defined as

$$E_{\mathrm{xc}}[n] = F[n] - T_{\mathrm{s}}[n] - \frac{1}{2}\iint d^3r \, d^3r' \, \frac{n(\mathbf{r})n(\mathbf{r}')}{|\mathbf{r}-\mathbf{r}'|}. \tag{1.11}$$

Application of the Hohenberg-Kohn variational principle (1.4) to eq. (1.10) results in

$$\frac{\delta T_{\mathrm{s}}[n]}{\delta n(\mathbf{r})} + V_{\mathrm{ext}}(\mathbf{r}) + \int d^3r' \, \frac{n(\mathbf{r}')}{|\mathbf{r}-\mathbf{r}'|} + \frac{\delta E_{\mathrm{xc}}[n]}{\delta n(\mathbf{r})} - \mu = 0. \tag{1.12}$$

Comparison of the latter equation with eq. (1.6) allows to find an expression of the effective potential $V_{\mathrm{eff}}(\mathbf{r})$

$$V_{\mathrm{eff}}(\mathbf{r}) = V_{\mathrm{ext}}(\mathbf{r}) + \int d^3r' \, \frac{n(\mathbf{r}')}{|\mathbf{r}-\mathbf{r}'|} + V_{\mathrm{xc}}(\mathbf{r}) \tag{1.13}$$

with the exchange-correlation functional

$$V_{\mathrm{xc}}(\mathbf{r}) = \frac{\delta E_{\mathrm{xc}}[n]}{\delta n(\mathbf{r})}. \tag{1.14}$$

The Kohn-Sham equations (1.9) together with (1.7) and (1.8) are probably the most important equations in Density-Functional Theory. Although they are principally exact, their practical solution requires approximations, since the exchange-correlation potential is not known explicitly. The whole problem constitutes a self-consistent field problem, since the effective potential depends on the density which, obviously, is directly connected to the wave functions (see eq. (1.7)).
The Kohn-Sham equations can be solved iteratively, starting from a trial density which is inserted into eq. (1.13) to obtain a first effective potential. This is used to calculate the wave

functions via eq. (1.9) and, finally, using eq. (1.7), a new density. The procedure is repeated, until the difference between the starting density and the resulting one becomes sufficiently small. A proof that the iteration process can always be made convergent to a stable solution can be found in [38].

After having solved the Kohn-Sham equations, the ground state density can be used to calculate the energy of the ground state. Considering that

$$T_{\mathrm{s}}[n] = \sum_{i=1}^{N} \epsilon_i - \int d^3r \, V_{\mathrm{eff}}(\mathbf{r})n(\mathbf{r}) \,, \tag{1.15}$$

the energy functional (see eq. (1.10)) becomes

$$E[n] = \sum_{i=1}^{N} \epsilon_i - \int d^3r \, V_{\mathrm{eff}}(\mathbf{r})n(\mathbf{r}) + \frac{1}{2} \iint d^3r \, d^3r' \, \frac{n(\mathbf{r})n(\mathbf{r}')}{|\mathbf{r} - \mathbf{r}'|}$$
$$+ \int d^3r \, V_{\mathrm{ext}}(\mathbf{r})n(\mathbf{r}) + E_{\mathrm{xc}}[n] \,. \tag{1.16}$$

The total energy thus equals the sum over the eigenvalues ϵ_i minus the so-called double counting terms. Expression (1.16) gives the ground state energy for the exact exchange-correlation functional, provided that the inserted values for the density and the effective potential are the results of the self-consistent solution.

Note that the eigenvalues ϵ_i do not equal the true single-particle excitation energies, since they are introduced as Lagrange parameters without having a physical meaning. However, in reality they are often and quite successfully taken even as excitation energies.

1.3 The local spin-density approximation

Although density-functional theory as presented in the last sections, i.e. the Hohenberg-Kohn theorems as well as the Kohn-Sham equations, is formally exact, its practical application requires to approximate the exchange-correlation potential $V_{\mathrm{xc}}(\mathbf{r})$, which is not known explicitly. The most simple approximation is to assume the effects of exchange and correlation to be local in character. For the noble metals considered in this thesis this approximation leads to sufficiently good results, while it fails for other materials with more complicated band structures. Following the above assumption leads to the so-called local density approximation, or more general, the local spin-density approximation (LSDA), which was already proposed by Kohn and Sham. It replaces the exact functional $E_{\mathrm{xc}}[n]$, i.e. $E_{\mathrm{xc}}[n^{\uparrow}, n^{\downarrow}]$ by

$$E_{\mathrm{xc}}^{\mathrm{LSDA}}[n^{\uparrow}, n^{\downarrow}] = \int d^3r \, n(\mathbf{r})\epsilon_{\mathrm{xc}}^{\mathrm{LSDA}}(n^{\uparrow}(\mathbf{r}), n^{\downarrow}(\mathbf{r})) \,, \tag{1.17}$$

where $n^{\uparrow} = n^{\uparrow}(\mathbf{r})$ and $n^{\downarrow} = n^{\downarrow}(\mathbf{r})$ are the (spin-dependent) densities of electrons and $n(\mathbf{r}) = n^{\downarrow}(\mathbf{r}) + n^{\uparrow}(\mathbf{r})$. Furthermore, $\epsilon_{\mathrm{xc}}^{\mathrm{LSDA}}(n(\mathbf{r}))$ is not a functional but a function evaluated at each point $\mathbf{r}$ with the values of the up and down densities $n^{\uparrow}(\mathbf{r})$ and $n^{\downarrow}(\mathbf{r})$.

Then, the exchange-correlation potential $V_{\mathrm{xc}}(\mathbf{r})$ appearing in the Kohn-Sham equations eq. (1.9) is easily calculated, because it is just the functional derivative of the exchange-correlation energy. Variation of the exchange-correlation energy functional (1.17) results in

$$\delta E_{\mathrm{xc}}[n] = \sum_s \int d^3r \left[\epsilon_{\mathrm{xc}}^{\mathrm{hom}} + n \frac{\delta \epsilon_{\mathrm{xc}}^{\mathrm{hom}}}{\delta n_s} \right]_{\mathbf{r},s} \delta n(\mathbf{r}, s) \qquad (1.18)$$

where the spin index s was introduced.
Thus, the exchange correlation potential becomes

$$V_{\mathrm{xc}}^s(n) = \left[\epsilon_{\mathrm{xc}}^{\mathrm{hom}} + n \frac{\delta \epsilon_{\mathrm{xc}}^{\mathrm{hom}}}{\delta n_s} \right]_{\mathbf{r},s} . \qquad (1.19)$$

It is convenient to split the correlation part from the exchange part $\epsilon_{\mathrm{xc}}^{\mathrm{LSDA}}(n) = \epsilon_{\mathrm{c}}^{\mathrm{LSDA}}(n) + \epsilon_{\mathrm{x}}^{\mathrm{LSDA}}(n)$ since the latter one can be obtained by the Hartree-Fock method, neglecting correlation but taking exchange effects into account. It is given by

$$\epsilon_{\mathrm{x}}^{\mathrm{LSDA}}(n) = -\frac{3}{2} \left(\frac{3}{\pi} \right)^{\frac{1}{3}} n^{\frac{1}{3}} \qquad (1.20)$$

and hence

$$V_{\mathrm{x}}^{\mathrm{LSDA}}(n) = -2 \left(\frac{3}{\pi} \right)^{\frac{1}{3}} n^{\frac{1}{3}}. \qquad (1.21)$$

The correlation part $\epsilon_{\mathrm{c}}^{\mathrm{LSDA}}(n)$ is more difficult to calculate, but can be accurately determined by a quantum Monte Carlo method [39]. Interpolation of the results allows to extract a parametrization for $\epsilon_{\mathrm{c}}^{\mathrm{LSDA}}(n)$ (see [40] and [41]).
For some systems with more inhomogeneous densities, however, the local density approximation fails and a more accurate description is necessary. An improvement can be reached by taking not only the local density into account but also the gradient of the density

$$E_{\mathrm{xc}}^{\mathrm{GGA}}[n] = \int d^3r \, f(n(\mathbf{r}), \nabla n(\mathbf{r})) . \qquad (1.22)$$

However, the function $f(n(\mathbf{r}), \nabla n(\mathbf{r}))$ is not unique and many different forms have been suggested. The most common one is the generalized gradient approximation (GGA) [42],[43], which is very well tested and leads to good numerical results. For instance, an improvement for the cohesive energies and lattice constants for the $3d$ transition metals is achieved. Nevertheless, in the present work all results are obtained within the local spin density approximation which leads to good results for the applied materials.

The KKR Green function method

The multiple-scattering method for electronic structure calculations was introduced in 1947 by Korringa [30] and in 1954 by Kohn and Rostoker [31] (KKR). At its heart is the multiple-scattering ansatz which proved to be an especially powerful tool for the solution of the Schrödinger equation, electronic structure and band structure calculations. The first step in KKR is to determine the scattering properties of each scattering site, resulting in a single-site scattering matrix. Then, in a second step, multiple scattering by all atoms in the lattice is taken into account by demanding that the incoming wave at one lattice site equals the sum over the outgoing waves from all other scattering centers. In this way, geometric properties are separated from the potential properties of each atomic site which allows an efficient calculation scheme.

Further improvement of the method was obtained when it was reformulated as a Green function method [44, 45, 46]. While the separation between the single-site scattering and the multiple scattering effects was retained, the Dyson equation provided an efficient way to calculate the Green function of the considered system from the Green function of free space. Furthermore, impurity scattering could be easily taken into account by considering the Green function of the crystal as a reference and relating it to the Green function of the crystal including the impurity via the Dyson equation [47]. The efficiency of this procedure lies on the fact that no large supercells have to be constructed, which would have been the case in a wavefunction method.

A further significant step into the development of the KKR scheme was the introduction of the screened or tight-binding method [48, 49]. Via a transformation of the reference system a decoupling of remote lattice sites was achieved and the numerical efficiency of the method was enhanced enormously. The principal layer technique enables the computation time to scale linearly with the number of atoms in systems with two-dimensional translational symmetry. This is especially efficient for layered systems such as surfaces, interfaces and multilayers and cleared the way for the study of e.g. interlayer exchange coupling or ballis-

tic transport through junctions. Successful applications of the KKR method for calculations of the electronic structure of solids within the frame of density functional theory include bulk materials [50], surfaces [51], interfaces and tunnel junctions [52], and impurities in bulk and on surfaces [53]. Spectroscopic properties and transport properties [54, 55, 56], have also been studied using this method.

Furthermore, the KKR scheme can incorporate the Dirac equation, enabling fully relativistic calculations [57].

The current chapter provides a brief introduction to the KKR method and follows the introduction given in [58]. It starts by giving an overview about the basic aspects of Green functions needed for understanding the following sections. Before illuminating the Green function approach of the method, the single-site scattering problem is treated. Then, the full-potential treatment is explained and a sketch of the screened KKR method is given. We close the chapter with the presentation of the self-consistency cycle of the KKR method.

2.1 The Green function approach

2.1.1 Obtaining physical quantities from Green functions

The central problem of density functional calculations as presented in the first chapter, section 1.2, is the solution of the Kohn-Sham-equations in order to obtain the single-particle wavefunctions Φ_i and the corresponding eigenvalues ϵ_i. However, all information about the ground state is also contained in the single-particle Green function $G(\mathbf{r}, \mathbf{r}'; E)$. In particular, the local density of states and the charge density can be directly calculated from the single-particle Green function $G(\mathbf{r}, \mathbf{r}'; E)$. Therefore, it is not mandatory to calculate the Kohn-Sham orbitals Φ_i and the corresponding eigenvalues ϵ_i, if the single-particle Green function is known.

The Green function solves the Schrödinger equation at an energy E with a source at position $\mathbf{r}'$

$$\left[-\nabla_r^2 + V(\mathbf{r}) - E \right] G(\mathbf{r}, \mathbf{r}'; E) = -\delta(\mathbf{r} - \mathbf{r}') . \qquad (2.1)$$

In terms of a complete set of eigenfunctions $\varphi_i(\mathbf{r})$ and eigenenergies E_i of the Hamilton operator $H = -\nabla_r^2 + V(\mathbf{r})$ the Green function can be written in its spectral representation

$$G(\mathbf{r}, \mathbf{r}'; E + i\varepsilon) = \sum_i \frac{\varphi_i(\mathbf{r}) \varphi_i^\star(\mathbf{r}')}{E + i\varepsilon - E_i}. \qquad (2.2)$$

Using the Dirac identity it can be shown that the imaginary part of $G(\mathbf{r}, \mathbf{r}'; E)$ is directly related to the spectral- and space-resolved local density of states $n(\mathbf{r}, E)$

$$n(\mathbf{r}; E) = -\frac{1}{\pi} \operatorname{Im} G(\mathbf{r}, \mathbf{r}; E). \qquad (2.3)$$

Integration over the energy yields the expression for the charge density $\rho(\mathbf{r})$

$$\rho(\mathbf{r}) = 2 \sum_{i, E_i < E_F} |\varphi_i(\mathbf{r})|^2 \quad = \quad -\frac{2}{\pi} \int_{-\infty}^{E_F} dE \, \mathrm{Im} \, G(\mathbf{r}, \mathbf{r}; E) \tag{2.4}$$

$$= \quad -\frac{2}{\pi} \mathrm{Im} \int_{-\infty}^{E_F} dE \, \mathrm{Tr} \left[\hat{r} G(E) \right],$$

where $\hat{r} = |\mathbf{r}\rangle \, \delta(\mathbf{r} - \mathbf{r}') \, \langle \mathbf{r}'|$ is the position operator and the factor two accounts for the two spin directions.

Thus, as claimed at the beginning of this section, the charge density can be directly calculated from the imaginary part of the diagonal elements of the Green function. It can be interpreted as the local density of states $n(\mathbf{r}; E)$ at the position $\mathbf{r}$.

On the other hand, the local density of states of a particular atom in a defined volume V can be determined by integration over the atomic volume

$$n_V(E) = -\frac{2}{\pi} \int_V d^3 r \, \mathrm{Im} \, G(\mathbf{r}, \mathbf{r}; E). \tag{2.5}$$

In general, from the spectral representation follows that the expectation value of any single-particle physical quantity, represented by an operator $\hat{A}$, can be obtained via the relation

$$\langle A \rangle = -\frac{1}{\pi} \mathrm{Im} \int_{-\infty}^{E_F} dE \, \mathrm{Tr} \left[\hat{A} G(E) \right]. \tag{2.6}$$

Hence, there is no need to evaluate the wavefunctions $\varphi_i(\mathbf{r})$.

In eq. (2.2) a small imaginary part $i\varepsilon$ was added to the energy in order to guarantee the convergence of the integrals, and, after performing the integration, the limit $\varepsilon \to 0^+$ is taken. The reason for that procedure can be found in the analytical properties of the Green function: $G(\mathbf{r}, \mathbf{r}'; E)$ has poles for real energies, but is analytic for $\mathrm{Im}\, E > 0$. Therefore it is allowed and convenient for its computation to transform the energy integrals to contour integrals closed in the upper complex energy plane

$$\rho(\mathbf{r}) = -\frac{2}{\pi} \mathrm{Im} \int_{E_B}^{E_F} dz \, G(\mathbf{r}, \mathbf{r}; z) \tag{2.7}$$

with $z = E + i\varepsilon$, but the imaginary part ε is not small anymore. The contour starts at E_B, an energy below the bottom of the valence bands, but higher than the core states, goes into the complex energy plane and comes back to the real frequency axis close to the Fermi energy. The core states are treated differently, their wavefunctions are calculated via an integration of the Schrödigner equation. Then, their contribution to the density $\rho(\mathbf{r})$ is simply obtained by calculating their norm. For complex energies with an imaginary part ε, the structure of the Green function is broadened and thus typically only 20 to 30 energy points are required for a sufficiently accurate numerical evaluation of the integral. However, special care is necessary for the points close to the Fermi level, since here the full structure of $G(E)$ reappears as the real axis is approached.

Whereas the order of approximately 10^3 integration points are usually needed on the real

axis, about 20 to 40 points suffice when the contour described above is chosen. Obviously, in this way a large amount of computation time can be saved.

Additionally, for systems with two- or three-dimensional translational symmetry, computation time can be further reduced, since the smooth behavior of the Green function at large $\mathrm{Im}E$ allows for a coarse $\mathbf{k}$-mesh in the Brillouin zone integration.

2.1.2 Relation between the Green function of perturbed and unperturbed system

We focus now on another important issue concerning Green functions and show how to obtain them by relating Green functions of different systems with each other.

The formal solution of the Schrödinger equation (2.1) at a given energy, characterized by the Hamiltonian $H = H_0 + V$, with H_0, V being the Hamiltonian of the original system and the perturbing potential, respectively, reads

$$G(E) = \frac{1}{E + i\varepsilon - H} = \frac{1}{E + i\varepsilon - H_0 - V} \quad . \tag{2.8}$$

The same holds for the Green function G_0 solving the Schrödinger equation corresponding to H_0. Thus, we can write

$$G(E)^{-1} = G_0(E)^{-1} - V \tag{2.9}$$

being equivalent to

$$G(E) = G_0(E) + G_0(E)VG(E) = G_0(E)\frac{1}{1 - VG_0(E)} \; . \tag{2.10}$$

The latter equation, known as Dyson equation, can be expanded as

$$G(E) = G_0(E) + G_0(E)VG_0(E) + G_0(E)VG_0(E)VG_0(E) + \ldots \tag{2.11}$$

and hence allows an interpretation in terms of scattering events, representing an analogue of a Born series for Green functions.

In analogy to Green functions, the Schrödinger equation for wavefunctions of a perturbed system can be written as

$$(E - H_0)\ket{\psi} = V\ket{\psi} \; . \tag{2.12}$$

Furthermore, the solution $\ket{\psi}$ can be expressed in terms of the unperturbed eigenstates $\ket{\psi_0}$, the perturbing potential $V(\mathbf{r})$ and the Green function of the unperturbed system G_0

$$\ket{\psi} = \ket{\psi_0} + G_0(E)V\ket{\psi} \; . \tag{2.13}$$

The above equation is the famous Lippmann-Schwinger equation[1]. Substitution of the solution $|\psi\rangle$ on the right hand side of eq. (2.13) leads to the Born series

$$|\psi\rangle = |\psi_0\rangle + G_0(E)V|\psi_0\rangle + G_0(E)VG_0(E)V|\psi_0\rangle\ldots. \tag{2.15}$$

If E does not belong to the spectrum of the unperturbed Hamiltonian H_0, $|\psi_0\rangle$ vanishes and the Lippmann-Schwinger equation reduces to the homogeneous equation

$$|\psi\rangle = G_0(E)V|\psi\rangle \tag{2.16}$$

from which the bound states follow.

Now, we introduce the transition matrix T, defined by

$$V|\psi\rangle = T(E)|\psi_0\rangle, \tag{2.17}$$

relating the wavefunction $|\psi\rangle$ of the perturbed system to the wavefunction $|\psi_0\rangle$ of the unperturbed system.

Using this definition, both the Lippmann-Schwinger equation and the Dyson equation can be formulated in terms of the T-Matrix instead of the potential V, hence

$$|\psi\rangle = |\psi_0\rangle + G_0(E)T(E)|\psi_0\rangle \qquad \text{and} \tag{2.18}$$
$$G(E) = G_0(E) + G_0(E)T(E)G_0(E). \tag{2.19}$$

Furthermore, in some cases it is very practical to deal with the scattering matrix denoted as S, which transforms an incoming into an outgoing wave. Because of norm conservation during an elastic scattering process, S must be a unitary operator

$$S^\dagger S = 1. \tag{2.20}$$

It can be shown that S is related to the transition matrix T by

$$S = 1 - 2i\sqrt{E}T. \tag{2.21}$$

Inserting the above expression in eq. (2.20) leads to the optical theorem for the T-matrix

$$\frac{1}{2}(T^\dagger - T) = i\sqrt{E}T^\dagger T. \tag{2.22}$$

Details concerning the operator S can be found in [59].

We will now come back to the solution of the Dyson equation (2.10). In order to solve it in practice, the Hamiltonian H_0 is chosen such that $G_0(E)$ can be easily calculated. For example, in order to obtain the Green function G_{bulk} of a bulk crystal, the free space is taken

---

[1]In space, both the Dyson equation and the Lippmann-Schwinger equation are integral equations; in chapter 3, we will need the Lippmann-Schwinger equation (2.13) in direct space, thus

$$\psi(\mathbf{r}) = \psi_0(\mathbf{r}) + \int d^3r'\, G_0(\mathbf{r}, \mathbf{r}'; E)V(\mathbf{r}')\psi(\mathbf{r}'). \tag{2.14}$$

as reference system. In this case, G_0 is known analytically and V is just the sum over all atomic potentials. When calculating the Green function of a surface geometry G_{surface}, an adequate choice of the reference system is the corresponding bulk crystal, i.e. G_{bulk}. The potential difference V entering in the Dyson equation is then simply the difference of the potential at the surface and in the bulk.

Going one step further, this scheme also provides an easy way for calculating the Green function of an impurity embedded in a bulk crystal or localized at the surface. In the first case, G_0 is identified with the bulk Green function and V is the change caused by the impurity potential with respect to the bulk potential at the impurity site as well as the change at the neighboring potentials. In the latter case, first the Green function of the surface is needed: an essential condition to obtain an accurate solution of the Dyson equation is that the perturbing potential V has to be well localized. The locality of the perturbed wavefunctions is not required – and usually not realized – but this behavior does not affect the accuracy of the Dyson equation and favors the use of Green functions instead of wavefunctions.

Naturally, the presented Green function method can be also applied to small clusters of impurities in bulk or at surfaces, provided that the change in potential is restricted to a well-defined volume. These facts make the Impurity-KKR Green function method applicable to a great variety of interesting problems.

2.2 Single-site scattering

As already mentioned in the introduction of this chapter, the KKR Green function method allows a decoupling of the potential and the structural properties of the system of scattering atoms. Therefore, in a first step the scattering of a single impurity with spherical potential V embedded in free space is dealt with. In this case, the potential of the reference system is zero, and the Green function g of free space which obeys the Hamiltonian $H_0 = -\nabla_{\mathbf{r}}^2$ is

$$g(\mathbf{r}, \mathbf{r}'; E) = -\frac{1}{4\pi} \frac{e^{ik|\mathbf{r}-\mathbf{r}'|}}{|\mathbf{r} - \mathbf{r}'|} \tag{2.23}$$

with $k = \sqrt{E}$ [60, 61]. The corresponding eigenfunctions are plane waves with $\varphi_{\mathbf{k}}(\mathbf{r}) = e^{i\mathbf{k}\cdot\mathbf{r}}$. Considering the scattering by a central potential, it is useful to work in angular-momentum representation, in which an incoming wavefunction $\varphi_{\mathbf{k}}^{\text{inc}}(\mathbf{r})$ is expanded in

$$\varphi_{\mathbf{k}}^{\text{inc}}(\mathbf{r}) = e^{i\mathbf{k}\cdot\mathbf{r}} = \sum_L 4\pi i^l j_l(\sqrt{E}r) Y_L(\mathbf{k}) Y_L(\mathbf{r}) . \tag{2.24}$$

Here, the combined index $L := (l, m)$ is used, j_l is the spherical Bessel function, and Y_L denotes the real spherical harmonics. Expanding the Green function g in spherical harmonics results in

$$g(\mathbf{r}, \mathbf{r}'; E) = \sum_L Y_L(\mathbf{r}) g_l(r, r'; E) Y_L(\mathbf{r}') \tag{2.25}$$

with

$$g_l(r, r'; E) = -i\sqrt{E} j_l(\sqrt{E}r_<) h_l(\sqrt{E}r_>), \tag{2.26}$$

where $h_l = j_l + in_l$ are spherical Hankel functions, n_l are spherical Neumann functions [62], while $r_<(r_>)$ is the smaller (larger) of the radii r and r'. The Bessel functions $j_l(r)$ are finite in the limit $r \to 0$, behaving asymptotically as r^l, whereas $h_l(r)$ and $n_l(r)$ diverge as $r \to 0$, behaving as r^{-l-1}.

In the following, a spherical scattering potential of finite range

$$V(\mathbf{r}) = \begin{cases} V(r) & \text{for } r \le r_{\max} \\ 0 & \text{for } r > r_{\max} \end{cases} \tag{2.27}$$

is assumed. Then, a separation of coordinates $\phi(\mathbf{r}) = \sum_L Y_L(\hat{r}) R_l(r; E)$ is possible, the radial scattering wavefunctions $R_l(r; E)$ satisfy the radial Schrödinger equation

$$\left[-\frac{1}{r} \frac{\partial}{\partial r^2} r + \frac{l(l+1)}{r^2} + V(r) - E \right] R_l(r; E) = 0. \tag{2.28}$$

The asymptotic form of the wavefunctions $R_l(r; E)$ for $r \to \infty$, where $V = 0$, following from the above equation, is

$$R_l(r; E) \to \frac{A_l}{\sqrt{E}r} \sin\left[\sqrt{E}r - \frac{l\pi}{2} + \delta_l(E) \right], \tag{2.29}$$

where A_l is a constant and δ_l is the phase shift with respect to the incoming wavefunction. Outside the range of the potential, thus for $r > r_{\max}$, the radial wavefunction $R_l(r; E)$ is just a linear combination of two independent solutions

$$R_l(r; E) = B_l j_l(\sqrt{E}r) + C_l n_l(\sqrt{E}r) \tag{2.30}$$

with the constants B_l and C_l. They can be determined with the help of the asymptotic forms of $j_l(r)$ and $n_l(r)$ for $r \to \infty$

$$j_l(r) \quad \sim \quad \frac{1}{r} \sin\left(r - \frac{l\pi}{2} \right) \tag{2.31}$$

$$n_l(r) \quad \sim \quad -\frac{1}{r} \cos\left(r - \frac{l\pi}{2} \right) \tag{2.32}$$

and equations (2.29) and (2.30), leading to

$$R_l(r; E) = A_l \left[j_l(\sqrt{E}r) \cos\delta_l - n_l(\sqrt{E}r) \sin\delta_l \right] \text{ for } r > r_{\max}. \tag{2.33}$$

On the other hand, using the Lippmann-Schwinger equation (2.14) the expression

$$R_l(r; E) = j_l(\sqrt{E}r) + \int_0^{r_{\max}} r'^2 dr' \, g_l(r, r'; E) V(r') R_l(r'; E). \tag{2.34}$$

can be obtained. Combining the latter equation with eq. (2.26), for $r > r_{\max}$ follows

$$R_l(r; E) = j_l(\sqrt{E}r) - i\sqrt{E}h_l(\sqrt{E}r) \int_0^{r_{\max}} r'^2 dr' \, j_l(\sqrt{E}r') V(r') R_l(r'; E). \tag{2.35}$$

The integral is just the atomic scattering (t-)matrix in angular-momentum representation

$$t_l(E) = \int_0^{r_{\max}} r'^2 dr' \, j_l(\sqrt{E}r')V(r')R_l(r';E).$$

(2.36)

With the above definition the regular radial wavefunction results in

$$R_l(r;E) = j_l(\sqrt{E}r) - i\sqrt{E}t_l(E)h_l(\sqrt{E}r) \quad r > r_{\max},$$

(2.37)

or, using eq. (2.33), in terms of the phase shift $\delta_l(E)$

$$t_l(E) = -\frac{1}{\sqrt{E}}\sin\delta_l(E)e^{i\delta_l(E)}.$$

(2.38)

Before closing the section we give the Green function for scattering at a central potential without proof. It can be written as the product of two linearly independent solutions R_l (regular, i.e. finite as $r \to 0$) and H_l (irregular, i.e. diverging as $r \to 0$) of the radial Schrödinger equation, hence

$$\begin{aligned}
G(\mathbf{r},\mathbf{r}';E) &= -i\sqrt{E}\sum_L R_l(r_<;E)H_l(r_>;E)Y_L(\mathbf{r})Y_L(\mathbf{r}') \\
&= -i\sqrt{E}\sum_L G_l(r,r';E)Y_L(\mathbf{r})Y_L(\mathbf{r}').
\end{aligned}$$

(2.39)

The boundary conditions for the regular solutions R_l are determined by eq. (2.37).
In analogy to eq. (2.34), the Lippmann-Schwinger equation for the irregular wavefunction H_l writes as

$$H_l(r;E) = h_l(\sqrt{E}r) + \int_0^{r_{\max}} r'^2 dr' \, g_l(r,r';E)V(r')H_l(r';E) .$$

(2.40)

The boundary conditions for H_l can be found using the identity $G_l = g_l + g_l t_l g_l$ with g_l given by eq. (2.26)

$$H_l(r;E) = h_l(\sqrt{E}r) \quad \text{for } r > r_{\max} .$$

(2.41)

In practice, the general procedure to obtain the wavefuntions is the following: First, the radial Schrödinger equation (2.28) is integrated outwards up to $r = r_{\max}$ to obtain R_l. The continuity of the logarithmic derivative at $r = r_{\max}$ yields the t-matrix t_l. Then, in a second step the irregular wavefunction H_l is calculated by an integration inwards starting at $r = r_{\max}$. Here, only one boundary condition (at $r = r_{\max}$) has to be satisfied. Finally, the Green function of a single scatterer can be constructed according to (2.39) just by multiplying the regular with the irregular wavefunctions.

2.3 KKR as a Green function method

In this section, we proceed to derive the full Green function taking multiple scattering events into account.

A periodic crystal with spherical potentials[2] given by

$$V(\mathbf{r} + \mathbf{R}^n) = V^n(r) \tag{2.42}$$

is assumed and the Green function is the solution of the Schrödinger equation

$$\left(-\nabla_{\mathbf{r}}^2 + V^n(r) - E\right) G(\mathbf{r} + \mathbf{R}^n, \mathbf{r}' + \mathbf{R}^{n'}; E) = -\delta_{nn'}\delta(\mathbf{r} - \mathbf{r}'). \tag{2.43}$$

Here, cell-centered coordinates $\mathbf{r} + \mathbf{R}^n, \mathbf{r}' + \mathbf{R}^{n'}$ have been introduced, where $\mathbf{r}$ and $\mathbf{r}'$ are restricted to the cells n and n' and $\mathbf{R}^n$ and $\mathbf{R}^{n'}$ are the vectors pointing to the center of the cells n and n', respectively. For simplicity, we stay in the formalism of the atomic sphere approximation (ASA), where the scattering potential is assumed to be spherically symmetric around each scattering center (atomic site) within a sphere of radius r_{max} (which is also called Wigner-Seitz radius R_{WS}) and constant otherwise; the spheres are overlapping such that the sum over the volumes of all spheres equals the total volume of the crystal.

In the case of $n \neq n'$, the Green function satisfies the homogeneous Schrödinger equation and thus can be expanded in regular solutions $R_L^n(\mathbf{r}; E)$, which in the atomic sphere approximation have the form $R_L^n(\mathbf{r}; E) = R_l^n(r; E)Y_L(\hat{r})$. Close to the origin, they are proportional to r^l and represent the solutions for an incoming spherical Bessel function $j_l(\sqrt{E}r)Y_L(\hat{r})$. An $\mathbf{r}$-dependent potential demands more cumbersome calculations (see section 2.4).

For $n = n'$, the Schrödinger equation becomes inhomogeneous, and the solution is the Green function for a central potential eq. (2.39), but with a boundary condition of back-scattering by all other potentials in the crystal. In contrast to the case of $n \neq n'$, additionally to the regular solution R_L^n, the corresponding irregular solutions H_L^n enter, behaving as $H_l^n \propto r^{-l-1}$ at the origin and being identical with the spherical Hankel function $h_l(\sqrt{E}r)$ outside the range of the potential.

Finally, the Green function for the whole crystal is a sum of the general solution of the homogeneous equation plus a special solution of the inhomogeneous one

$$\begin{aligned}
G(\mathbf{r} + \mathbf{R}^n, \mathbf{r}' + \mathbf{R}^{n'}; E) = \\
-i\sqrt{E} \sum_L R_L^n(\mathbf{r}_<; E)H_L^n(\mathbf{r}_>; E)\delta_{nn'} + \sum_{LL'} R_L^n(\mathbf{r}; E)G_{LL'}^{nn'}(E)R_{L'}^{n'}(\mathbf{r}'; E).
\end{aligned} \tag{2.44}$$

In the second summand, the homogeneous part, the so-called structural Green function $G_{LL'}^{nn'}(E)$ enters, which has not been defined yet and which shall be calculated in the following. We will use the Dyson equation in the form

$$\begin{aligned}
G(\mathbf{r} + \mathbf{R}^n, \mathbf{r}' + \mathbf{R}^{n'}; E) = g(\mathbf{r} + \mathbf{R}^n, \mathbf{r}' + \mathbf{R}^{n'}; E) \\
+ \sum_{n''} \int d^3r'' \, g(\mathbf{r} + \mathbf{R}^n, \mathbf{r}'' + \mathbf{R}^{n''}; E)V^{n''}(\mathbf{r}'')G(\mathbf{r}'' + \mathbf{R}^{n''}, \mathbf{r}' + \mathbf{R}^{n'}; E),
\end{aligned} \tag{2.45}$$

---

[2] The procedure presented in the following is also valid when taking the full potential $V(\mathbf{r})$ into account, the special case of spherical symmetric is chosen just for reasons of brevity.

taking free space as reference system. Substitution of expansion (2.44) and the corresponding expression for the free Green function

$$
\begin{aligned}
g(\mathbf{r} + \mathbf{R}^n, \mathbf{r}' + \mathbf{R}^{n'}; E) = \\
-i\sqrt{E} \sum_L j_L(\mathbf{r}_<; E) h_L(\mathbf{r}_>; E) \delta_{nn'} + \sum_{LL'} j_L(\mathbf{r}; E) g_{LL'}^{nn'}(E) j_L(\mathbf{r}'; E) \quad (2.46)
\end{aligned}
$$

in equation (2.45) results in the algebraic Dyson equation

$$
G_{LL'}^{nn'}(E) = g_{LL'}^{nn'}(E) + \sum_{n''L''} g_{LL''}^{nn''}(E) t_{l''}^{n''}(E) G_{L''L'}^{n''n'}(E) \,. \quad (2.47)
$$

Here, we have introduced the structural Green functions for free space $g_{LL'}^{nn'}(E)$, which are also denoted as free space structure constants. They are given analytically by

$$
g_{LL'}^{nn'}(E) = -(1 - \delta_{nn'}) 4\pi i \sqrt{E} \sum_{L''} i^{l-l'+l''} C_{LL'L''} h_{L''}(\mathbf{R}^n - \mathbf{R}^{n'}; E) \,, \quad (2.48)
$$

where $C_{LL'L''}$ are the Gaunt coefficients defined as

$$
C_{LL'L''} = \int d\Omega \, Y_L(\hat{r}) Y_{L'}(\hat{r}) Y_{L''}(\hat{r}) \,. \quad (2.49)
$$

While the potential $V^n(r)$ enters in the usual Dyson equation (2.45), here it is the atomic t-matrix $t_l^n(E)$ eq. (2.36) that enters the algebraic Dyson equation. The derivation of eq. (2.47) is lengthy and can be found in [63].

In practice, the structural Green functions $G_{LL'}^{nn'}(E)$ are first calculated in $\mathbf{k}$-space. Therefore, in a first step, the free space structure constants $g_{LL'}^{nn'}(E)$ are Fourier transformed, yielding

$$
g_{LL'}(\mathbf{k}; E) = \sum_{n'} g_{LL'}^{nn'}(E) e^{-i\mathbf{k}\cdot\left(\mathbf{R}^n - \mathbf{R}^{n'}\right)} \,. \quad (2.50)
$$

The choice of n is arbitrary, because only the difference $e^{i\mathbf{k}\cdot\left(\mathbf{R}^n - \mathbf{R}^{n'}\right)}$ enters and the sum has to be performed over all n'. In analogy, the $G(\mathbf{k}; E)$ are defined as

$$
G_{LL'}(\mathbf{k}; E) = \sum_{n'} G_{LL'}^{nn'}(E) e^{-i\mathbf{k}\cdot\left(\mathbf{R}^n - \mathbf{R}^{n'}\right)} \,. \quad (2.51)
$$

Then, the algebraic Dyson equation 2.47 in reciprocal space becomes

$$
G_{LL'}(\mathbf{k}; E) = g_{LL'}(\mathbf{k}; E) + \sum_{L''} g_{LL''}(\mathbf{k}; E) t_{l''}(E) G_{L''L'}(\mathbf{k}; E) \,. \quad (2.52)
$$

It is solved by matrix inversion, making a cutoff at some $l = l_{\max}$ for which the t-matrix becomes negligible. Usually, the choice of $l_{\max} = 3$ or 4 is sufficient. Then, the resulting Green function $G_{LL'}(\mathbf{k}; E)$ has to be Fourier transformed to the real space matrix $G_{LL'}^{nn'}(E)$. The last two steps can be subsumed to the formula

$$
G_{LL'}^{nn'}(E) = \frac{1}{V_{\mathrm{BZ}}} \int_{\mathrm{BZ}} d^3 k \, e^{i\mathbf{k}\cdot(\mathbf{R}^n - \mathbf{R}^{n'})} \left[(1 - g(\mathbf{k}; E) t(E))^{-1} g(\mathbf{k}; E) \right]_{LL'} \,, \quad (2.53)
$$

where $g(\mathbf{k}; E)$ and $t(E)$ are matrices in L and L' and the integral has to be taken over the Brillouin zone volume V_{BZ}.

Once the structural Green function $\mathring{G}_{LL'}^{nn'}(E)$ of the ideal crystal is known, the Green function $G_{LL'}^{nn'}(E)$ of the crystal with impurity can be evaluated by a modified Dyson equation

$$G_{LL'}^{nn'}(E) = \mathring{G}_{LL'}^{nn'}(E) + \sum_{n''L''} \mathring{G}_{LL''}^{nn''}(E)\Delta t_{l''}^{n''}(E)G_{L''L'}^{n''n'}(E), \qquad (2.54)$$

where $\Delta t_l^n(E) = t_l^n(E) - \mathring{t}_l^n(E)$ is the difference between the t-matrices of the perturbed and the ideal lattice[3]. Since this difference, caused by the perturbation of the potential, is restricted to the vicinity of the impurity, the Green function in this subspace can be determined in real space by matrix inversion. The rank of the matrices to be inverted is given by $N \cdot (l_{\max} + 1)^2$, i.e. the number N of perturbed sites times the number $(l_{\max} + 1)^2$ of angular momenta (l and m_l) used in the expansion of the potential, the Green function and the wavefunctions. In this thesis, the maximum angular momentum generally is set to $l_{\max} = 3$, which leads to a satisfying accuracy for the treated materials and problems.

For a single impurity it is often sufficient to consider only the perturbation at the impurity site and thus neglect the perturbation at neighboring sites. For a more accurate description, the perturbations of the neighboring atoms have to be included. The difference between the two results depends on several criteria, e.g. the strength of the scatterer, the geometry and the scattering properties of the host system the impurity is embedded and above all the range of displaced charge by the impurity.

A different possibility to increase the accuracy[4], which is more general and not only valid for impurity calculations, is to take the non-spherical contributions of the potential into account. A summary of the full-potential treatment within the KKR method is the subject of the next section.

2.4 Full-potential treatment within the KKR method

The atomic sphere approximation which was presented so far, describes the physics of many systems quite reasonably and efficiently. Nevertheless, systems with lower symmetry such as non-cubic crystals, surfaces or interfaces require a more accurate treatment beyond the spherical approximation. If forces and lattice relaxations have to be calculated, the atomic sphere approximation even fails and the correct description of the full anisotropic potential becomes necessary.

The multiple scattering expansion eq. (2.44) of the KKR-Green function is still valid in the case of a full potential treatment, so that the important separation between the single-potential problem and the multiple-scattering problem remains the same. In this section, we will introduce the basics of the full potential treatment, further details can be found in

---

[3]The difference $\Delta t_l^n(E) = t_l^n(E) - \mathring{t}_l^n(E)$ can be calculated equivalently using $\Delta t_l^n(E) = \int r^2 dr R_l^{0,n}(r; E)\Delta V^n(r)R_l^n(r; E)$. The proof (for full potential, thus the t-matrix $\Delta t_{LL'}$) is given in the Appendix, section A.4.

[4]apart from increasing the number of sites in the impurity calculation, i.e. in eq. (2.54)

[63, 46, 64] and [65].

In contrast to the previous sections, the potential $V(\mathbf{r})$ depends not only on the norm of $\mathbf{r}$ but on the full vector, and scattering from an incoming wave with angular momentum L to another wave characterized by L' is no longer forbidden. Hence, the Lippmann-Schwinger equation for the regular wavefunction (see eq. (2.34)) has to be written as

$$R_L(\mathbf{r}; E) = j_l(\sqrt{E}r)Y_L(\hat{r}) + \int d^3r' \, g(\mathbf{r}, \mathbf{r}'; E)V(\mathbf{r}')R_L(\mathbf{r}'; E), \qquad (2.55)$$

and requires a three-dimensional instead of a one-dimensional integral.

However, expansion of the regular wavefunctions $R_L(\mathbf{r}; E)$ and the potential $V(\mathbf{r})$ in spherical harmonics

$$R_L(\mathbf{r}; E) = \sum_{L'} R_{L'L}(r; E)Y_{L'}(\hat{r}) \qquad (2.56)$$

and

$$V(\mathbf{r}) = \sum_{L} V_L(r)Y_L(\hat{r}) = \sum_{LL'} V_{LL'}(r)Y_L(\hat{r})Y_{L'}(\hat{r}) \qquad (2.57)$$

allows to reformulate the corresponding Lippmann-Schwinger-equation for the components $R_{L'L}(r; E)$ (see also the Appendix, section A.3)

$$R_{L'L}(r; E) = j_{l'}(\sqrt{E}r)\delta_{LL'} + \int_0^{r_{\max}} r'^2 dr' \, g_{l'}(r, r'; E) \sum_{L''} V_{L'L''}(r')R_{L''L}(r'; E). \quad (2.58)$$

The component of the potential $V_{LL'}(r)$ is defined as

$$V_{LL'}(r) = \sum_{L''} C_{LL'L''}V_{L''}(r), \qquad (2.59)$$

with the Gaunt coefficients $C_{LL'L''}$ defined in eq. (2.49). Although the integral in the Lippmann-Schwinger-equation (2.58) is now one-dimensional, its solution is not as trivial as it might seem at first glance, since a system of coupled equations has to be solved

$$\sum_{L''} \left[\left(-\frac{1}{r}\frac{\partial}{\partial r^2}r + \frac{l(l+1)}{r^2} - E \right)\delta_{LL''} + V_{LL''}(r) \right] R_{L''L'}(r; E) = 0. \qquad (2.60)$$

Substitution of $g_{l'}(r, r'; E)$ in terms of the regular and irregular solutions as expanded in eq. (2.39) leads to a system of coupled equations

$$R_{LL'}(r; E) = a_{LL'}(r; E)j_l(r; E) + b_{LL'}(r; E)h_l(r; E) \qquad (2.61)$$

with

$$a_{LL'}(r; E) \;=\; \delta_{LL'} - i\sqrt{E} \int_r^{r_{\max}} r'^2 dr' \, h_l(r'; E) \sum_{L''} V_{LL''}(r')R_{L''L'}(r'; E) \quad (2.62)$$

$$b_{LL'}(r; E) \;=\; -i\sqrt{E} \int_0^r r'^2 dr' \, j_l(r'; E) \sum_{L''} V_{LL''}(r')R_{L''L'}(r'; E). \qquad (2.63)$$

In the limit $r \to 0$, the second term of eq. (2.61) approaches 0 and the characteristics of $R_{LL'}(r; E)$ is determined by $a_{LL'}(r; E)$

$$R_{LL'}(r; E) \sim a_{LL'}(r; E)j_l(r; E) \qquad \text{for} \quad r \to 0. \qquad (2.64)$$

$a_{LL'}(0; E)$ is denoted as α-matrix

$$\alpha_{LL'}(E) = \delta_{LL'} - i\sqrt{E} \int_0^{r_{\max}} r'^2 dr'\, h_l(\sqrt{E}r') \sum_{L''} V_{LL''}(r') R_{L''L'}(r'; E), \qquad (2.65)$$

describing the enhancement of the solution $R_{LL'}(r; E)$ compared to the free solution $\delta_{LL'} j_l(\sqrt{E}r)$. The inverse of $\alpha_{LL'}(E)$ transforms the complex wavefunctions $R_L(\mathbf{r})$ to real wavefunctions $U_L(\mathbf{r})$ following [66]

$$U_L(\mathbf{r}) = \sum_{L'} R_{L'}(\mathbf{r}) \alpha_{L'L}^{-1} \qquad (2.66)$$

and

$$R_L(\mathbf{r}) = \sum_{L'} U_{L'}(\mathbf{r}) \alpha_{L'L}. \qquad (2.67)$$

This property of the α-matrix will be used when calculating the scattering matrix $T_{\mathbf{kk'}}$ in section 3.3.

The atomic transition matrix (t-matrix) can be obtained similarly as in the case of a spherical potential, thus by matching $R_{LL'}(r; E)$ to an outgoing free wave at the boundary S

$$t_{LL'}(E) = \int_0^{r_{\max}} r^2 dr\, j_l(\sqrt{E}r) \sum_{L''} V_{LL''}(r) R_{L''L'}(r; E), \qquad (2.68)$$

being equivalent to its definition

$$t_{LL'}(E) = \int d^3r\, J_L(\mathbf{r}; E) V(\mathbf{r}) R_{L'}(\mathbf{r}; E). \qquad (2.69)$$

In contrast to the t-matrix $t_l(E)$ for spherical potential, $t_{LL'(E)}$ is not diagonal any more while it still holds

$$t_{LL'}(E) = t_{L'L}(E) \qquad (2.70)$$

if the potential is local; this condition is not fulfilled, if spin-orbit coupling is included. However, for local potential the property (2.70) follows from the symmetry of the Green function $G(\mathbf{r}, \mathbf{r}'; E) = G(\mathbf{r}', \mathbf{r}; E)$, a proof can be found in [60]. Furthermore, the t-matrix fulfills the optical theorem (2.22), which in the special case of the atomic scattering matrix can be reformulated as

$$\frac{1}{2}(t_{L'L}^\star - t_{LL'}) = -i\sqrt{E} \sum_{L''} t_{L''L}^\star t_{L''L'}, \qquad (2.71)$$

or, for $L = L'$,

$$\mathrm{Im}\, t_{LL} = \sqrt{E} \sum_{L''} |t_{LL''}|^2. \qquad (2.72)$$

Outside the range of the potential, equivalently to eq. (2.37),

$$R_{LL'}(r; E) = \delta_{LL'} j_l(\sqrt{E}r) - i\sqrt{E} t_{LL'}(E) h_l(\sqrt{E}r) \quad \text{for} \quad r \geq r_{\max} \qquad (2.73)$$

is valid.

Similar to the regular wavefunction $R_L(\mathbf{r}; E)$, the irregular one, $H_L(\mathbf{r}; E)$, which diverges at the origin is expanded in spherical harmonics as

$$H_L(\mathbf{r}; E) = \sum_{L'} H_{L'L}(r; E) Y_{L'}(\hat{r}) \,. \tag{2.74}$$

Of course, it would be possible to solve the full-potential problem starting from scratch by solving the systems of linear equations (2.60) but another, much simpler way can be chosen, too. This ansatz is based on perturbation theory exploiting the fact that the non-spherical part of the potential is usually weak compared to the spherical one. It occurs to be much more favorable to first solve the problem for the spherical part of the potential (thus taking $V_{l=0}(r)$ instead of the full one), and obtain spherical wavefunctions $R_l^{\mathrm{sph}}(r; E)$ and $H_l^{\mathrm{sph}}(r; E)$. The Green function corresponding to this problem is then

$$G_l^{\mathrm{sph}}(r, r'; E) = -i\sqrt{E} R_l^{\mathrm{sph}}(r_<; E) H_l^{\mathrm{sph}}(r_>; E) \,. \tag{2.75}$$

Afterwards, in a second step, the results of the spherical problem are used to solve the Lippmann-Schwinger equation

$$R_{LL'}(r; E) = R_l^{\mathrm{sph}}(r; E)\delta_{LL'} + \int_0^{r_{\max}} r'^2 dr' \, G_l^{\mathrm{sph}}(r, r'; E) \sum_{L''} \Delta V_{LL''}(r') R_{L''L'}(r; E) \,, \tag{2.76}$$

where only the non-spherical part of the potential enters

$$\Delta V_{LL'}(r) = \sum_{L'' \neq 0} C_{LL'L''} V_{L''}(r) = V_{LL'}(r) - V_{00}(r) \,. \tag{2.77}$$

Additionally, since the potential inside and close to the core is almost spherical, the non-spherical contribution can be safely neglected within a radius denoted by $r_{\min}$. Then, the coupled equations (2.61) to (2.63) can be rewritten as

$$R_{LL'}(r; E) = A_{LL'}(r; E) R_l^{\mathrm{sph}}(r; E) + B_{LL'}(r; E) H_l^{\mathrm{sph}}(r; E) \tag{2.78}$$

with

$$A_{LL'}(r; E) = \delta_{LL'} - i\sqrt{E} \int_r^{r_{\max}} r'^2 dr' \, H_l^{\mathrm{sph}}(r'; E) \sum_{L''} \Delta V_{LL''}(r') R_{L''L'}(r'; E) \tag{2.79}$$

$$B_{LL'}(r; E) = -i\sqrt{E} \int_0^r r'^2 dr' \, R_l^{\mathrm{sph}}(r'; E) \sum_{L''} \Delta V_{LL''}(r') R_{L''L'}(r'; E) \,. \tag{2.80}$$

For $r < r_{\min}$, $B_{LL'}(r; E)$ in eq. (2.78) vanishes (see eq. (2.80)) and $R_{LL'}(r; E)$ simplifies to

$$\begin{aligned} R_{LL'}(r; E) &= A_{LL'}(r_{\min}; E) R_l^{\mathrm{sph}}(r; E) \quad \text{for} \quad r < r_{\min} \\ &\sim \Delta\alpha_{LL'} R_l^{\mathrm{sph}}(r; E) \\ &\sim \alpha_{LL'} j_l(r; E) \quad \text{for} \quad r \to 0 \,. \end{aligned} \tag{2.81}$$

In the last equation we have used $\alpha_{LL'}(E) = \Delta\alpha_{LL'}(E)\alpha_l^{\mathrm{sph}}(E)$, where $\alpha_l^{\mathrm{sph}}(E)$ is the α-matrix corresponding to the spherical part of the potential $V_{00}(r)$.

Equivalently to the difference in potential $\Delta V_{LL'}(r)$ we obtain a difference in the t-matrix $\Delta t_{LL'} = t_{LL'} - t_l \delta_{LL'}$, which can be calculated via

$$\Delta t_{LL'}(E) = \int_{r_{\min}}^{r_{\max}} r^2 dr\, R_l^{\text{sph}}(r; E) \sum_{L''} \Delta V_{LL''}(r) R_{L''L'}(r; E), \qquad (2.82)$$

or, more general,

$$\Delta t_{LL'}(E) = \int d^3r\, R_L^{\text{sph}}(\mathbf{r}; E) \Delta V(\mathbf{r}) R_{L'}(\mathbf{r}; E). \qquad (2.83)$$

The proof of the above equation can be found in the Appendix, section A.4.

Equation (2.76) is solved iteratively via the system of the coupled equations (2.78) to (2.80), while it is sufficient to start the integration in equation (2.80) at $r_{\min}$. The successive solutions obtained for the regular $R_{LL'}(r; E)$ and the non-regular wavefunctions $H_{LL'}(r; E)$ represent a Born series. Usually, convergence is reached within 3 or 4 iterations.

In contrast to the atomic sphere approximation where the spheres are allowed to overlap, in the full-potential treatment the whole crystal is divided into space-filling Wigner-Seitz polyhedra. Outside these cells, the potential is cut off by the introduction of shape functions $\Theta^n(\mathbf{r})$ defined as

$$\Theta^n(\mathbf{r}) = \begin{cases} 1 & \text{if } \mathbf{r} \text{ is inside the Wigner-Seitz cell of site } n \\ 0 & \text{otherwise.} \end{cases} \qquad (2.84)$$

The radius $r_{\max}$, which in the ASA is the Wigner-Seitz radius, i.e. the radius of the ASA-spheres, in the full-potential description it is meant to be the maximal radius of the non-spherical Wigner-Seitz polyhedra.

Then, the crystal potential in the n-th Wigner-Seitz cell can be rewritten as

$$V^n(\mathbf{r}) = \Theta^n(\mathbf{r}) V(\mathbf{r}). \qquad (2.85)$$

As all other quantities the shape functions are expanded in spherical harmonics as

$$\Theta^n(\mathbf{r}) = \sum_L \Theta_L^n(r) Y_L(\hat{r}). \qquad (2.86)$$

The coefficients $\Theta_L^n(r)$ enter the expansions for the charge density and the potential, in order to ensure the correct cutoff at the Wigner-Seitz cell boundary. More details about the calculations of the shape truncation functions for Wigner-Seitz atomic polyhedra can be found in [67, 68].

2.5 Screened KKR

The development of the so-called screened or tight-binding KKR formalism [48, 49] constitutes a substantial improvement of the KKR method. It helps to reduce the calculation time significantly and is in particular favorable for large systems, since it allows the solution of the Dyson equation to scale (in the ideal case) with $O(N)$ instead of $O(N^3)$; here,

N denotes the number of different atoms in one unit cell. The optimal scaling is reached for layered systems.

This achievement became possible by a clever choice of a reference system: It can be chosen such that the reference Green function falls off exponentially with distance, resulting in the inversion of sparse, or even tridiagonal, matrices, which is much faster than a full matrix inversion if only the diagonal elements of the inverse matrix are needed (as it is the case in charge-density calculations). Due to the decoupling between distant atomic sites, the corresponding transformation is called screening transformation and the method screened KKR; because of its formal resemblance to tight-binding theory, the method is also called tight-binding KKR.

Basically, there are three reasons why the screened KKR formalism works so efficiently. First of all, it is based on the Dyson equation which allows the choice of an arbitrary reference system of the same periodic structure, and not the free space only (see Appendix, section A.1). Naturally, taking a constant potential as reference is the most evident choice, since the Green function and structure constants are given by analytical expressions. However, further analysis shows that in practice this choice is not the best. An adequate reference system can be constructed in which there are no states in the energy region of interest (up to 1-2 Ry higher than E_F) and in which the structural Green functions fall off exponentially with distance. Such a system is defined by a collection of repulsive muffin-tin potentials (one around each site n) as

$$V^{\mathrm{ref},n}(\mathbf{r}) = \begin{cases} V_C & \text{for} \quad r \leq R_{\mathrm{rep}} \\ 0 & \text{otherwise} \end{cases} . \tag{2.87}$$

R_{rep} is the radius of the repulsive potential at site n, and V_C a positive constant, usually chosen to be a few Rydbergs, e.g. $V_C = 4\,\mathrm{Ry}$ or $8\,\mathrm{Ry}$. For such a potential, the eigenvalue spectrum starts from an energy $E_{\mathrm{bot}}^{\mathrm{ref}}$ somewhat smaller than V_C but much higher than E_F. Then, because of the absence of eigenvalues, for $E < E_{\mathrm{bot}}^{\mathrm{ref}}$, the Green function of the reference system drops rapidly and in practice exponentially with distance; the same holds for the true structural Green functions.

A further advantage of this choice of reference system is that one avoids a cumbersome calculation of the free-space structure constants $g_{LL'}(\mathbf{k}; E)$ by an Ewald summation. Because of the rapid decay of the screened structural Green functions $G_{LL'}^{\mathrm{ref}\,nn'}$, the matrices $\mathbf{G}^{\mathrm{ref}}(E)$ can be cut off in real space at a finite value of $\left|\mathbf{R}^{n'} - \mathbf{R}^{n}\right|$, for fcc lattices typically after two lattice constants. Then, the Dyson equation is solved by a direct matrix inversion, yielding $G_{LL'}^{\mathrm{ref}\,nn'}$.

2.6 Self-consistency Cycle in the KKR method

At the end of this chapter, we shortly present the algorithm for calculating the potential self-consistently. As the KKR scheme is based on density-functional theory, the basic and central quantity is the electronic density. We start with

    1. an initial guess of input potential $V_{\mathrm{in}}(\mathbf{r})$, which is used

2. to calculate the wavefunctions $R_L(\mathbf{r})$ and $H_L(\mathbf{r})$ and the t-matrix $t_{LL'}(E)$.

3. Determine the t-matrix of the reference system $t_{LL'}^{\mathrm{ref}}(E)$ and
   $\Delta t_{LL'}(E) = t_{LL'}(E) - t_{LL'}^{\mathrm{ref}}(E)$.

4. Then, the structural Green function $G_{LL'}^{\mathrm{ref},nn'}(E)$ of the reference system can be cal-culated.

5. The algebraic Dyson equation is solved to evaluate the structural Green function of the real system $G_{LL'}^{nn'}(E)$.

6. Calculate the Green function using the structural Green function and $R_L(\mathbf{r})$ and $H_L(\mathbf{r})$. Integrate the Green function over complex energies Z from the bottom of the valence band E_{bot} up to E_{F} by using a complex-energy contour (see below) and take the imaginary part to find the valence electron density
   $\rho(\mathbf{r}) = -\frac{1}{\pi} \operatorname{Im} \int_{E_{\mathrm{bot}}}^{E_{\mathrm{F}}} dZ \, G(\mathbf{r}, \mathbf{r}; Z)$.

7. Calculate the core-electron wavefunctions and core-electron density ρ^c;
   here, the multiple-scattering formalism is not needed, because the core wavefunctions are assumed to be highly localized at the atomic sites. Obtain the total density $\rho(\mathbf{r}) = \rho^c(\mathbf{r}) + \rho^v(\mathbf{r})$.

8. Find the output potential $V_{\mathrm{out}}(\mathbf{r})$ by solving the Poisson equation and adding the exchange-correlation potential. If $V_{\mathrm{out}}(\mathbf{r}) = V_{\mathrm{in}}(\mathbf{r})$ to a reasonable accuracy, exit the cycle, otherwise

9. Properly mix $V_{\mathrm{out}}(\mathbf{r})$ with $V_{\mathrm{in}}(\mathbf{r})$ to obtain a new input potential, and return to step 1

In figure 2.1 we present a diagram showing the scheme used for self-consistent calculations of the potential. This might be a bulk potential (in this case the term reference system is more suitable than 'host', which can be found in the scheme) or an impurity potential. The essential quantity to know is the reference or host Green function.

$$V_{\text{in}}(\mathbf{r})$$

$$V^{\text{ref}}(\mathbf{r})$$

$$R_L^n(\mathbf{r}; E), \; H_L^n(\mathbf{r}; E)$$

$$R_L^{\text{ref},n}(\mathbf{r}; E), \; H_L^{\text{ref},n}(\mathbf{r}; E)$$

$$t_{LL'}^n(E)$$

$$t_{LL'}^{\text{ref},n}(E)$$

$$G_{LL'}^{\text{ref},nn'}(E)$$

$$\Delta t_{LL'}^n(E) = t_{LL'}^n(E) - t_{LL'}^{\text{ref},n}(E)$$

structural Dyson equation
$$G_{LL'}^{nn'}(E) = G_{LL'}^{\text{ref},nn'}(E) + \sum_{n''} \sum_{L'',L'''} G_{LL''}^{\text{ref},nn''}(E) \Delta t_{L''L'''}^{n''}(E) G_{L'''L'}^{n''n'}(E)$$

$$G(\mathbf{r} + \mathbf{R}^n, \mathbf{r}' + \mathbf{R}^{n'}; E) = \sum_L R_L^n(\mathbf{r}_<; E) H_L^n(\mathbf{r}_>; E) \delta_{nn'} + \sum_{L,L'} R_L^n(\mathbf{r}; E) G_{LL'}^{nn'}(E) R_{L'}^{n'}(\mathbf{r}'; E)$$

$$\rho^n(\mathbf{r}) = -\frac{1}{\pi} \text{Im} \, G(\mathbf{r} + \mathbf{R}^n, \mathbf{r} + \mathbf{R}^n)$$

Poisson equation $V_{\text{out}}(\mathbf{r})$

if $V_{\text{in}}(\mathbf{r}) = V_{\text{out}}(\mathbf{r})$ stop
otherwise mix $V_{\text{in}}(\mathbf{r})$ and $V_{\text{out}}(\mathbf{r})$
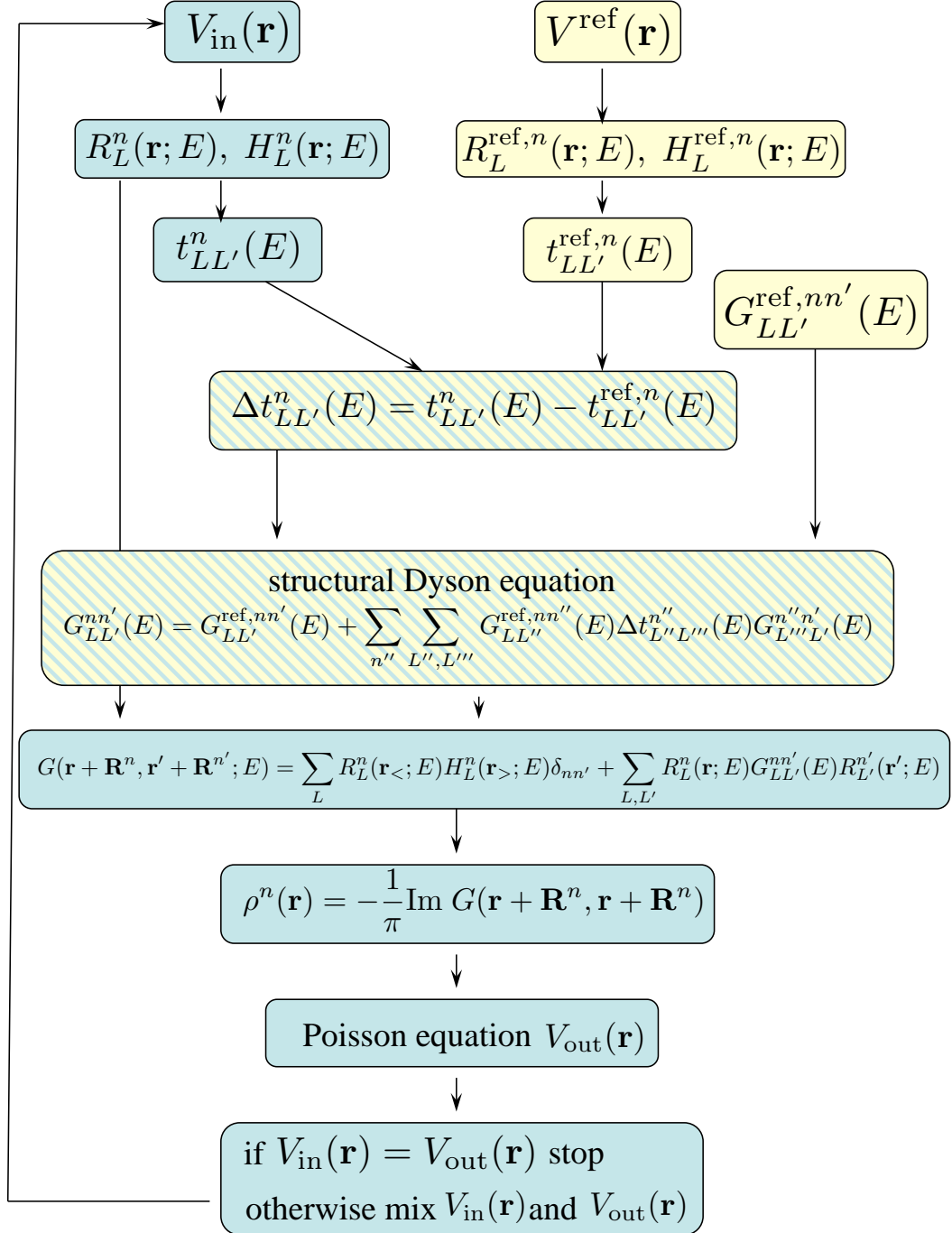
Figure 2.1.: The self-consistency cycle used in the KKR method

Multiple Scattering Theory

The multiple scattering ansatz is one essential characteristic of the KKR method and gives access to the scattered wavefunctions at defects. Through these, many physical properties can be calculated, such as momentum-scattering times, residual resistivities, or surface state lifetimes. The central quantity required for their calculation is the scattering matrix $T_{\mathbf{kk}'}$, describing the elastic scattering process from one state characterized by the reciprocal space vector $\mathbf{k}'$ to another characterized by $\mathbf{k}$. In this chapter, $T_{\mathbf{kk}'}$ is derived for scattering processes where the coupling between the two spin channels is neglected. The formalism for scattering processes including spin-flip scattering by spin-orbit coupling will be presented in chapter 4.

We start with a derivation of the KKR wavefunctions, then explain how band structures are obtained in the KKR method. Since elastic scattering processes at impurities at low temperatures are to be considered, it is assumed that scattering takes place at the Fermi energy E_{F} and therefore the Fermi surface is required; its calculation is analogous to that of the band structure. After having calculated and normalized the wavefunctions on the Fermi surface, scattering processes provoked by impurities will be treated. Both the expressions obtained for the wavefunction of the host as well as of the impurity are used to derive a formula for the scattering matrix $T_{\mathbf{kk}'}$. Finally, starting from $T_{\mathbf{kk}'}$, we will deduce expressions for the residual resistivity, the momentum-relaxation time, the lifetime of surface states and the Wigner delay time. The formalism presented in this chapter will be the foundation of the treatment of spin-flip scattering processes as developed in chapter 4.

A general description of wavefunctions in KKR can be found in [69], while [70] focuses to wavefunctions using screened KKR. For more information about impurity wavefunctions we refer to [71].

3.1 KKR expansion of the wavefunctions $\psi_{\mathbf{k}}(\mathbf{r})$ and band structure calculations

3.1.1 The KKR expansion of the wavefunctions $\psi_{\mathbf{k}}(\mathbf{r})$

In the previous chapter, the problem of multiple scattering events was solved on a level of Green functions, because the full wavefunctions are not needed for the self-consistent calculation of the potential. Nevertheless, we will require the wavefunctions for further purposes such as the calculation of the scattering matrix $T_{\mathbf{k}\mathbf{k}'}$ in section 3.3. Therefore, an expression for the full wavefunction will be derived in this section, taking into account the multiple scattering events which occur in a periodic crystal with many scattering sites. In addition to the wavefunction, the band structure of a periodic crystal is obtained.

The procedure is based on a bookkeeping of incoming and outgoing waves: the amplitude of the incoming wave at scattering site n must be the superposition of the sum of scattered waves from all other scattering sites $n' \neq n$ plus a possible external incident wave. We start by considering a periodic array of scatterers, and focusing on two scattering centers at $\mathbf{R}^n$ and $\mathbf{R}^{n'}$. A wave scattered at site $\mathbf{R}^n$ for $r \geq r_{\max}$ can be expanded in outgoing waves $h_L(\mathbf{r}; E) = h_l(\sqrt{E}r)Y_L(\hat{r})$ around $\mathbf{R}^n$:

$$\psi^{\mathrm{sc}(n)}(\mathbf{r}) = \sum_L \tilde{c}_{\mathbf{k}L}^{\mathrm{sc}(n)} h_L(\mathbf{r}; E) \, . \tag{3.1}$$

Around the site $\mathbf{R}^{n'}$, the same wave can be resolved in incoming waves $j_L(\mathbf{r}'; E)$

$$\psi^{\mathrm{inc}(n')}(\mathbf{r}') = \sum_L \tilde{c}_{\mathbf{k}L}^{(n')} j_L(\mathbf{r}'; E) \tag{3.2}$$

where $j_L(\mathbf{r}; E) = j_l(\sqrt{E}r)Y_L(\hat{r})$.
Using site-centered coordinates and setting $\mathbf{R}^n + \mathbf{r} = \mathbf{R}^{n'} + \mathbf{r}'$ we obtain

$$\sum_L \tilde{c}_{\mathbf{k}L}^{\mathrm{sc}(n)} h_L(\mathbf{r}' + \mathbf{R}^{n'} - \mathbf{R}^n; E) = \sum_L \tilde{c}_{\mathbf{k}L}^{(n')} j_L(\mathbf{r}'; E) \, . \tag{3.3}$$

In order to simplify the above expression and derive a formula for the effective amplitude $\tilde{c}_{\mathbf{k}L}^{(n)}$, we use the theorem of transformation of the Hankel functions

$$h_L(\mathbf{r}' + \mathbf{R}^{n'} - \mathbf{R}^n; E) = \frac{i}{\sqrt{E}} \sum_{L'} g_{LL'}^{nn'}(E) j_{L'}(\mathbf{r}'; E). \tag{3.4}$$

The expansion coefficients $g_{LL'}^{nn'}(E)$ are the free space structure constants defined in eq. (2.48). Using the expansion of Hankel functions (3.4) in terms of Bessel functions, eq. (3.3) can be transformed to

$$
\begin{aligned}
\sum_L \tilde{c}_{\mathbf{k}L}^{(n')} j_L(\mathbf{r}; E) &= \frac{i}{\sqrt{E}} \sum_{L,L'} \tilde{c}_{\mathbf{k}L}^{\mathrm{sc}(n)} g_{LL'}^{nn'}(E) j_{L'}(\mathbf{r}; E) \\
&= \sum_L \frac{i}{\sqrt{E}} \sum_{L'} \tilde{c}_{\mathbf{k}L'}^{\mathrm{sc}(n)} g_{L'L}^{nn'}(E) j_L(\mathbf{r}; E).
\end{aligned}
\tag{3.5}
$$

Comparison of the coefficients links the incoming and scattered amplitudes

$$
\begin{aligned}
\tilde{c}_{\mathbf{k}L}^{(n')} &= \frac{i}{\sqrt{E}} \sum_{L'} g_{L'L}^{nn'}(E) \tilde{c}_{\mathbf{k}L'}^{\mathrm{sc}(n)} \\
&= \frac{i}{\sqrt{E}} \sum_{L'} g_{LL'}^{n'n}(E) e^{i\mathbf{k}\cdot(\mathbf{R}^n - \mathbf{R}^{n'})} \tilde{c}_{\mathbf{k}L'}^{\mathrm{sc}(n')} \ .
\end{aligned}
\tag{3.6}
$$

Besides the equality $g_{L'L}^{nn'}(E) = g_{LL'}^{n'n}(E)$ which follows from the property of the Green function $g(\mathbf{r}, \mathbf{r}'; E) = g(\mathbf{r}', \mathbf{r}; E)$ as defined in eq. (2.23), the Bloch condition for a periodic lattice was used in the last step. It allows to establish a relation between the amplitude $\tilde{c}_{\mathbf{k}L}^{(n')}$ at a position $\mathbf{R}^{n'}$ and the amplitude $\tilde{c}_{\mathbf{k}L}^{(n)}$ of the wave at $\mathbf{R}^n$

$$
\tilde{c}_{\mathbf{k}L}^{(n)} = \exp\left[i\mathbf{k}\cdot\mathbf{R}^n\right] \tilde{c}_{\mathbf{k}L}^{(0)} = \exp\left[i\mathbf{k}\cdot\left(\mathbf{R}^n - \mathbf{R}^{n'}\right)\right] \tilde{c}_{\mathbf{k}L}^{(n')}.
\tag{3.7}
$$

In order to obtain the amplitude of the total incoming wave at the scattering center $\mathbf{R}^{n'}$, we have to sum over all waves originating from all other identical scattering sites n

$$
\begin{aligned}
c_{\mathbf{k}L}^{(n')} &:= \sum_{n \neq n'} \tilde{c}_{\mathbf{k}L}^{(n)} \\
&= \frac{i}{\sqrt{E}} \sum_{n \neq n'} \sum_{L'} g_{LL'}^{nn'}(E) e^{-i\mathbf{k}\cdot(\mathbf{R}^n - \mathbf{R}^{n'})} c_{\mathbf{k}L'}^{\mathrm{sc}(n')} \\
&= \frac{i}{\sqrt{E}} \sum_{L'} g_{LL'}(\mathbf{k}; E) c_{\mathbf{k}L'}^{\mathrm{sc}(n')} \ .
\end{aligned}
\tag{3.8}
$$

The coefficients $c_{\mathbf{k}L}^{(n)}$ and $c_{\mathbf{k}L}^{\mathrm{sc}(n)}$ as introduced in the above equation are the coefficients for the total incoming and scattered wave, respectively. I.e., they are summed over incoming waves from all centers, while $\tilde{c}_{\mathbf{k}L}^{(n')}$ and $\tilde{c}_{\mathbf{k}L}^{\mathrm{sc}(n')}$ were the contributions coming only from the incoming wave due to site $\mathbf{R}^n$. Additionally, the KKR structure constants

$$
g_{LL'}(\mathbf{k}; E) = \sum_{n} g_{LL'}^{nn'}(E) e^{-i\mathbf{k}\cdot(\mathbf{R}^n - \mathbf{R}^{n'})}
\tag{3.9}
$$

have been introduced. They do not depend on the potential, but on the geometry of the lattice only.

The total scattered wave of a scatterer at lattice site n is connected to the total incoming wave at the same site via the t-matrix $t_{LL'}^n(E)$ according to

$$
c_{\mathbf{k}L}^{\mathrm{sc}(n)} = -i\sqrt{E} \sum_{L'} t_{LL'}^n(E)\left(c_{\mathbf{k}L'}^{\mathrm{ext}(n)} + c_{\mathbf{k}L'}^{(n)}\right),
\tag{3.10}
$$

where $c_{\mathbf{k}L'}^{\mathrm{ext}(n)}$ is the amplitude of a possible external wave incoming to the crystal. Combining eqs. (3.10) and (3.8) allows to establish the following system of equations

$$
c_{\mathbf{k}L}^{\mathrm{ext}(n)} = \sum_{L'L'''} \left[\delta_{LL'} - \sum_{L''} g_{LL''}(\mathbf{k}; E) t_{L''L'}^n(E) \right] \frac{i}{\sqrt{E}} \left(t_{L'L'''}^n(E)\right)^{-1} c_{\mathbf{k}L'''}^{\mathrm{sc}(n)} \ .
\tag{3.11}
$$

In the absence of an external incoming wave $c_{\mathbf{k}L}^{\text{ext}(n)} = 0$, they can be rewritten as

$$\sum_{L'} \left[\delta_{LL'} - \sum_{L''} g_{LL''}(\mathbf{k}; E) t_{L''L'}^n(E) \right] c_{\mathbf{k}L'}^{(n)} = 0 \, . \tag{3.12}$$

From their solutions, the electronic eigenvalues in a periodic crystal without incoming wave are derived. Non-trivial solutions of the system of equations (3.12) exist, if the necessary and sufficient condition

$$\det \left[\delta_{LL'} - \sum_{L''} g_{LL''}(\mathbf{k}; E) t_{L''L'}^n(E) \right] = 0 \tag{3.13}$$

is fulfilled. Eq. (3.13) is called the KKR secular equation and allows to determine the band structure $E(\mathbf{k})$ of periodic crystals in KKR theory. Furthermore, it shows the separation between potential and structural properties, which is typical for the KKR method: Whereas the t-matrix $t_{LL'}^n(E)$ solely depends on the single scattering event of the wave at the potential $V^n(\mathbf{r})$, the KKR structure constants $g_{LL'}(\mathbf{k}; E)$ are determined by the given geometrical arrangement of atoms in the crystal only. As we will see in the next section, the KKR secular equation (3.13) can be analogously formulated in terms of the structure constants $G_{LL'}^{\text{ref}}(\mathbf{k}; E)$ of an arbitrary system instead of free space. In this case, the t-matrix must be replaced by the difference $\Delta t_{LL'}^n(E) = t_{LL'}^n(E) - t_{LL'}^{\text{ref}n}(E)$ of the corresponding t-matrices. We have now all necessary ingredients to express the full wavefunction $\psi_{\mathbf{k}}(\mathbf{r} + \mathbf{R}^n)$. In each cell n, the incoming wave scatters at the corresponding potential $V^n(\mathbf{r})$. According to eqs. (2.73) and (2.56), the regular wavefunction $R_L(\mathbf{r}; E)$ for $r > r_{\max}$ is given by

$$R_L(\mathbf{r}; E) = \sum_{L'} \left(\delta_{LL'} j_l(\sqrt{E}r) - i\sqrt{E} t_{LL'}(E) h_l(\sqrt{E}r) \right) Y_{L'}(\hat{r}) \, . \tag{3.14}$$

Therefore, the total wavefunction becomes

$$\psi_{\mathbf{k}}(\mathbf{r} + \mathbf{R}^n) = \sum_L c_{\mathbf{k}L}^{(n)} R_L^n(\mathbf{r}; E) \quad \text{for} \ \ r > r_{\max}. \tag{3.15}$$

On the other hand, for $r < r_{\max}$, the regular wavefunctions are solutions of the Schrödinger equation (2.60) and together with the expansion (2.56), the full wavefunctions write as

$$\psi_{\mathbf{k}}(\mathbf{r} + \mathbf{R}^n) = \sum_L c_{\mathbf{k}L}^{(n)} R_L^n(\mathbf{r}; E) \quad \text{for} \ \ r < r_{\max}. \tag{3.16}$$

Because of the continuity of the regular wavefunctions at $r = r_{\max}$ and the requirement of the total wavefunction to be continuous, the coefficients $c_{\mathbf{k}L}^n$ are the same for all $\mathbf{r}$ and

$$\psi_{\mathbf{k}}(\mathbf{r} + \mathbf{R}^n) = \sum_L c_{\mathbf{k}L}^{(n)} R_L^n(\mathbf{r}; E) \tag{3.17}$$

holds for all $\mathbf{r}$.

It is straightforward to generalize the method to the case of more than one atom per unit cell, say N_{at}. Introducing an index $\mu = 1, \cdots, N_{\text{at}}$ to account for the different atom types and

reserving the index n for the periodic lattice positions, an atomic position in the crystal is defined by the lattice vector $\mathbf{R}^n$ plus the site vector $\boldsymbol{\chi}^\mu$ connecting the lattice point to the basis atom

$$\mathbf{R}^{n\mu} = \mathbf{R}^n + \boldsymbol{\chi}^\mu. \tag{3.18}$$

Then, the Fourier transforms are carried out with respect to n only such that we obtain an expression analogous to eq. (3.9)

$$g_{LL'}^{\mu\mu'}(\mathbf{k}; E) = \sum_{n'} g_{LL'}^{n\mu n'\mu'}(E) e^{-i\mathbf{k}\cdot(\mathbf{R}^n - \mathbf{R}^{n'})} . \tag{3.19}$$

The t-matrix $t(E)$ as well as the coefficients $\mathbf{c_k}$ depend on the atom-type μ and eq. (3.12) must be modified according to

$$c_{\mathbf{k}L}^\mu = \sum_{\mu'L'L''} g_{LL''}^{\mathrm{r}\mu\mu'}(\mathbf{k}; E) \Delta t_{L''L'}^{\mu'}(E) c_{\mathbf{k}L'}^{\mu'} , \tag{3.20}$$

where the index $n = 0$ was dropped to simplify the notation.
Finally, the KKR secular equation becomes

$$\sum_{\mu'L'} \left(\delta_{\mu\mu'}\delta_{LL'} - \sum_{L''} g_{LL''}^{\mu\mu'}(\mathbf{k}; E) t_{L''L'}^{\mu'}(E) \right) c_{\mathbf{k}L'}^{\mu'} = 0 . \tag{3.21}$$

3.1.2 Normalization of the wavefunctions

The regular wavefunctions $R_L^n(\mathbf{r}; E)$ as defined in section 2.2, eq. (2.34) in the ASA and section 2.4, eq. (2.56) for full potential calculations are normalized as scattering solutions of a potential in free space. They are fully determined due the requirement that the $R_L^n(\mathbf{r}; E)$ and their derivatives have to be continuous at $r = r_{\max}$, which is the Wigner-Seitz radius r_{WS} in the case of ASA and the maximal radius of the Wigner-Seitz polyhedra in full potential calculations, respectively. However, for the normalization of the total wavefunctions $\psi_{\mathbf{k}}(\mathbf{r} + \mathbf{R}^n) = \sum_L c_{\mathbf{k}L}^n R_L^n(\mathbf{r}; E)$ we need another normalization; the wavefunctions $\psi_{\mathbf{k}}(\mathbf{r}; E)$ must fulfill the normalization condition

$$\sum_{\mu=1}^{N_{\mathrm{at}}} \int_{V_\mu} d^3r \, \left| \psi_{\mathbf{k}}^\mu(\mathbf{r}) \right|^2 = 1 , \tag{3.22}$$

which is achieved by choosing a prefactor of the coefficients $c_{\mathbf{k}L}^\mu$ accordingly. Since the regular solutions $R_L(\mathbf{r}; E)$ do not comprise a basis set, this is not an algebraic problem, but requires integration. The periodicity of the system makes the choice of the lattice site n arbitrary; however, we must account for all basis atoms in the cell, i.e. take the sum up to N_{at}.
We will first develop the normalization condition for spherical potentials before discussing the condition for non-spherical potentials.

Normalization of $\psi_k(r)$ in the atomic sphere approximation

In the atomic sphere approximation, the radial wavefunctions expand as
$R_L^\mu(\mathbf{r}; E) = R_l^\mu(r; E)Y_L(\hat{r})$ and thus the normalization condition (3.22) becomes

$$
\begin{aligned}
1 &= \sum_{\mu=1}^{N_{\text{at}}} \int_{V_\mu} d^3r \left| \sum_L c_{\mathbf{k}L}^\mu R_l^\mu(r; E)Y_L(\mathbf{r}) \right|^2 \\
&= \sum_{\mu=1}^{N_{\text{at}}} \sum_L \int_0^{r_{\max}} r^2 dr \left| c_{\mathbf{k}L}^\mu R_l^\mu(r; E) \right|^2 ,
\end{aligned}
\tag{3.23}
$$

where the orthogonality of the spherical harmonics is exploited.

Normalization of the wavefunctions for full potential

In the case of full potential calculations, the non-spherical contributions to the potentials have to be taken into account. Furthermore, the volume to be integrated over is that of the non-spherical Wigner-Seitz cells. Therefore, the shapefunction $\Theta(\mathbf{r})$ (see eq. (2.84)) has to be included in the normalization condition, which is one inside the cell and 0 outside

$$
\sum_\mu \int_{V_\mu} d^3r\, \Theta^\mu(\mathbf{r}) |\psi_{\mathbf{k}}(\mathbf{r} + \boldsymbol{\chi}^\mu)|^2 = 1 .
\tag{3.24}
$$

Expanding the wavefunctions according to eq. (3.61) and the shapefunction $\Theta^\mu(\mathbf{r})$ in spherical harmonics

$$
\Theta^\mu(\mathbf{r}) = \sum_L \Theta_L^\mu(r)Y_L(\hat{r})
\tag{3.25}
$$

leads to

$$
\begin{aligned}
1 &= \sum_\mu \int_{V_\mu} d^3r\, \Theta^\mu(\mathbf{r}) |\psi_{\mathbf{k}}(\mathbf{r} + \boldsymbol{\chi}^\mu)|^2 \\
&= \sum_\mu \int_{V_\mu} d^3r \sum_{L_3} \Theta_{L_3}^\mu(r)Y_{L_3}(\hat{r}) \sum_{L_1'L_1} c_{\mathbf{k}L_1}^{\mu\star} R_{L_1'L_1}^{\mu\star}(r; E)Y_{L_1'}(\hat{r}) \\
&\qquad\qquad\qquad\qquad\qquad\qquad \sum_{L_2'L_2} c_{\mathbf{k}L_2}^\mu R_{L_2'L_2}^\mu(r; E)Y_{L_2'}(\hat{r}) .
\end{aligned}
\tag{3.26}
$$

Since only the spherical harmonics depend on the direction of $\mathbf{r}$, the integral over the spherical coordinates can be performed and yields the Gaunt coefficients $C_{L_1 L_2 L_3}$. The above equation hence results in

$$
\begin{aligned}
1 &= \sum_\mu \int_{V_\mu} d^3r\, \Theta^\mu(\mathbf{r}) |\psi_{\mathbf{k}}(\mathbf{r} + \boldsymbol{\chi}^\mu)|^2 \\
&= \sum_\mu \sum_{L_1 L_2} c_{\mathbf{k}L_1}^{\mu\star} c_{\mathbf{k}L_2}^\mu \int_0^{r_{\max}} r^2 dr \sum_{L_1'L_2'L_3} \Theta_{L_3}^\mu(r) C_{L_1'L_2'L_3} R_{L_1'L_1}^{\mu\star}(r; E) R_{L_2'L_2}^\mu(r; E) \\
&= \sum_\mu \sum_{L_1 L_2} c_{\mathbf{k}L_1}^{\mu\star} c_{\mathbf{k}L_2}^\mu \rho_{L_1 L_2}^\mu(E) ,
\end{aligned}
\tag{3.27}
$$

where we have introduced

$$\rho_{L_1 L_2}^\mu(E) = \int_0^{r_{\max}} r^2 dr \sum_{L_1' L_2' L_3} \Theta_{L_3}^\mu(r) C_{L_1' L_2' L_3} R_{L_1' L_1}^{\mu\star}(r;E) R_{L_2' L_2}^\mu(r;E) . \qquad (3.28)$$

The quantity $\rho_{L_1 L_2}^\mu(E)$ containing the integral over r and the summation over L_1', L_2' and L_3 does not depend on $\mathbf{k}$. Therefore, it has to be calculated only once for all $\mathbf{k}$. In practice, the spherically symmetric contribution ($L_3 = 0$) is calculated independently from the non-spherically symmetric one, since in this case the Gaunt coefficients $C_{L_1 L_2 L_3 = 0}$ reduce to $C_{L_1 L_2 0} = 1/\sqrt{4\pi}\,\delta_{L_1 L_2}$ and the shape function $\Theta_{L_3}^\mu(r)$ to $\Theta_0^\mu(r) = \sqrt{4\pi}$.
Once $\rho_{L_1 L_2}^\mu(E)$ is known, the normalized coefficients $c_{\mathbf{k}L}^\mu$ are finally determined by

$$c_{\mathbf{k}L}^\mu \to \left[\sum_{\mu'} \sum_{L_1 L_2} c_{\mathbf{k}L_1}^{\mu'\star} c_{\mathbf{k}L_2}^{\mu'} \rho_{L_1 L_2}^{\mu'}(E) \right]^{-\frac{1}{2}} c_{\mathbf{k}L}^\mu . \qquad (3.29)$$

3.1.3 The KKR secular equation in terms of the reference system

Although we have already presented a method to obtain the KKR energy eigenvalues in the last section, a second, slightly different method should be introduced [71]. It avoids the cumbersome evaluation of the free-space structure constants and uses the structural Green function of a reference system instead, making it more efficient for practical use. Its derivation starts with the Lippmann-Schwinger-equation (2.13) in its integral form

$$\psi_\mathbf{k}(\mathbf{r}+\mathbf{R}^n; E) = \psi_\mathbf{k}^r(\mathbf{r}+\mathbf{R}^n; E) + \sum_{n'} \int d^3 r' \, G^r(\mathbf{r}+\mathbf{R}^n, \mathbf{r}'+\mathbf{R}^{n'}; E) \Delta V^{n'}(\mathbf{r}')\psi_\mathbf{k}(\mathbf{r}'+\mathbf{R}^{n'}),$$
$$(3.30)$$

which relates the wave function $\psi_\mathbf{k}(\mathbf{r} + \mathbf{R}^n; E)$ of the considered system with the wave function $\psi_\mathbf{k}^r(\mathbf{r} + \mathbf{R}^n; E)$ of a reference system, which has the crystal periodicity but is otherwise arbitrary. It is described by the Green function $G^r(\mathbf{r} + \mathbf{R}^n, \mathbf{r}' + \mathbf{R}^{n'}; E)$. $\Delta V^n(\mathbf{r}) = V^n(\mathbf{r}) - V^{r,n}(\mathbf{r})$ denotes the difference of the potential at site n.
If the energy E is not part of the energy spectrum of the reference system, as it is the case for the system of repulsive potentials described in section 2.5, the first term $\psi_\mathbf{k}^r(\mathbf{r} + \mathbf{R}^n; E)$ of the Lippmann-Schwinger equation (3.30) vanishes. Then, the above equation simplifies to the homogeneous integral equation

$$\psi_\mathbf{k}(\mathbf{r} + \mathbf{R}^n; E) = \sum_{n'} \int d^3 r' \, G^r(\mathbf{r} + \mathbf{R}^n, \mathbf{r}' + \mathbf{R}^{n'}; E) \Delta V^{n'}(\mathbf{r}')\psi_\mathbf{k}(\mathbf{r}' + \mathbf{R}^{n'}) . \qquad (3.31)$$

In the following, we will insert the expansions of the wavefunctions as well as the Green function in the above equation; furthermore, we assume that the potential of the reference system is spherical, hence $V^{r,n}(\mathbf{r}) = V^{r,n}(r)$. Again, the system of repulsive potentials from section 2.5 fulfills this condition.
As derived in the previous section, the wavefunctions expand as (see eq. (3.17))

$$\psi_\mathbf{k}(\mathbf{r} + \mathbf{R}^n) = \sum_L c_{\mathbf{k}L}^n R_L^n(\mathbf{r}; E) . \qquad (3.32)$$

The same holds for the true reference system

$$\psi_{\mathbf{k}}^{\mathrm{r}}(\mathbf{r} + \mathbf{R}^n) = \sum_L c_{\mathbf{k}L}^{\mathrm{r},n} R_L^{\mathrm{r},n}(\mathbf{r}; E) \,. \tag{3.33}$$

As shown in chapter 2, eq. (2.44), the Green function $G^{\mathrm{r}}(\mathbf{r} + \mathbf{R}^n, \mathbf{r}' + \mathbf{R}^{n'}; E)$ can be expanded in its spherical components according to

$$G^{\mathrm{r}}(\mathbf{r} + \mathbf{R}^n, \mathbf{r}' + \mathbf{R}^{n'}; E) =$$
$$\sum_{L_1} G_{l_1}^{\mathrm{r},\mathrm{s},nn}(r, r'; E) Y_{L_1}(\hat{r}) Y_{L_1}(\hat{r}') \delta_{nn'} + \sum_{L_1,L_2} R_{L_1}^{\mathrm{r},n}(\mathbf{r}; E) G_{L_1 L_2}^{\mathrm{r},nn'}(E) R_{L_2}^{\mathrm{r},n'}(\mathbf{r}'; E), \tag{3.34}$$

where the first term is the single-site scattering term, resulting from the scattering within cell n, whereas the second one contains the backscattering of all other atoms.
The single-site Green function can be expanded in regular and irregular solutions of the Schrödinger equation $R_L^{\mathrm{r},n}(\mathbf{r}; E)$ and $H_L^{\mathrm{r},n}(\mathbf{r}; E)$ as

$$G_l^{\mathrm{r},\mathrm{s},nn}(r, r'; E) = -i\sqrt{E} R_l^{\mathrm{r},n}(r_<; E) H_l^{\mathrm{r},n}(r_>; E) \,, \tag{3.35}$$

where we have exploited that the reference potential is spherical at each site n.
In order to calculate the coefficients $c_{\mathbf{k}L}^n$, we insert the expansions (3.32), (3.33) and (3.34) in the homogeneous Lippmann-Schwinger equation (3.31) and obtain

$$\sum_{L_1 L_2} c_{\mathbf{k}L_2}^n R_{L_1 L_2}^n(r; E) Y_{L_1}(\hat{r}) =$$
$$\sum_{n'} \int d^3 r' \cdot \Bigg[\sum_{L_1} G_{l_1}^{\mathrm{r},\mathrm{s},nn}(r, r'; E) Y_{L_1}(\hat{r}) Y_{L_1}(\hat{r}') \delta_{nn'}$$
$$\sum_{L_3} \Delta V_{L_3}^{n'}(r') Y_{L_3}(\hat{r}') \sum_{L_2 L_4} c_{\mathbf{k}L_2}^{n'} R_{L_4 L_2}^{n'}(r'; E) Y_{L_4}(\hat{r}')$$
$$+ \sum_{L_1 L_2} R_{l_1}^{\mathrm{r},n}(r; E) Y_{L_1}(\hat{r}) G_{L_1 L_2}^{\mathrm{r},nn'}(E) R_{l_2}^{\mathrm{r},n'}(r'; E) Y_{L_2}(\hat{r}')$$
$$\sum_{L_3} \Delta V_{L_3}^{n'}(r') Y_{L_3}(\hat{r}') \sum_{L_4 L_5} c_{\mathbf{k}L_4}^{n'} R_{L_5 L_4}^{n'}(r'; E) Y_{L_5}(\hat{r}') \Bigg].$$
$$\tag{3.36}$$

The spherical contribution to the integral is

$$\int d\Omega' \, Y_{L_1}(\hat{r}') Y_{L_2}(\hat{r}') Y_{L_3}(\hat{r}') = C_{L_1 L_2 L_3} \,. \tag{3.37}$$

Using the definition of $V_{L_1 L_2(r')}$, see eq. (2.59),

$$V_{L_1 L_2}(r) = \sum_{L_3} C_{L_1 L_2 L_3} V_{L_3} \,, \tag{3.38}$$

eq. (3.36) simplifies to

$$\sum_{L_1 L_2} c^n_{\mathbf{k}L_2} R^n_{L_1 L_2}(r; E) Y_{L_1}(\hat{r}) =$$

$$\sum_{L_1 L_2} c^n_{\mathbf{k}L_2} \int r'^2 dr' \, G^{\mathrm{r,s},nn}_{l_1}(r, r'; E) \sum_{L_4} \Delta V^n_{L_1 L_4}(r') R^n_{L_4 L_2}(r'; E) Y_{L_1}(\hat{r})$$

$$+ \sum_{n'} \sum_{L_1 L_2 L_4} c^{n'}_{\mathbf{k}L_4} \int r'^2 dr' \, R^{\mathrm{r},n}_{l_1}(r; E) Y_{L_1}(\hat{r}) G^{\mathrm{r},nn'}_{L_1 L_2}(E) R^{\mathrm{r},n'}_{l_2}(r'; E)$$

$$\sum_{L_5} \Delta V^{n'}_{L_2 L_5}(r') R^{n'}_{L_5 L_4}(r'; E). \tag{3.39}$$

As the radial solutions $R^n_{L_1 L_2}(r; E)$ obey the radial Lippmann-Schwinger equation (A.31)

$$R^n_{L_1 L_2}(r; E) = R^{\mathrm{r},n}_{l_1}(r; E) + \int r'^2 dr' \, G^{\mathrm{r,s},nn}_{l_1}(r, r'; E) \sum_{L_3} \Delta V^n_{L_1 L_3}(r') R^n_{L_3 L_2}(r'; E) \,, \tag{3.40}$$

the first term on the right-hand side can be merged with the left-hand side, hence

$$\sum_{L_1 L_2} c^n_{\mathbf{k}L_2} R^{\mathrm{r},n}_{L_1}(r; E) \delta_{L_1 L_2} Y_{L_1}(\hat{r}) =$$

$$\sum_{n'} \sum_{L_1 L_2} \sum_{L_4} c^{n'}_{\mathbf{k}L_4} \int r'^2 dr' \, R^{\mathrm{r},n}_{l_1}(r; E) Y_{L_1}(\hat{r}) G^{\mathrm{r},nn'}_{L_1 L_2}(E) R^{\mathrm{r},n'}_{l_2}(r'; E)$$

$$\sum_{L_5} \Delta V^{n'}_{L_2 L_5}(r') R^{n'}_{L_5 L_4}(r'; E). \tag{3.41}$$

Exploiting the linear independence of the spherical harmonics yields

$$c^n_{\mathbf{k}L_1} = \sum_{n'} \sum_{L_2} \sum_{L_4} c^{n'}_{\mathbf{k}L_4} \int r'^2 dr' \, G^{\mathrm{r},nn'}_{L_1 L_2}(E) R^{\mathrm{r},n'}_{l_2}(r'; E) \sum_{L_3} \Delta V^{n'}_{L_2 L_3}(r') R^{n'}_{L_3 L_4}(r'; E). \tag{3.42}$$

The integral on the right side can be evaluated using the definition of the Δt-matrix (see Appendix A.4, eq. (A.34))

$$\Delta t^n_{L_1 L_2}(E) = \int r^2 dr \, R^{\mathrm{r},n}_{l_1}(r; E) \sum_{L_3} \Delta V^n_{L_1 L_3}(r) R^n_{L_3 L_2}(r; E) \tag{3.43}$$

with $\Delta t^n_{L_1 L_2}(E) = t^n_{L_1 L_2}(E) - t^{\mathrm{r},n}_{L_1 L_2}(E)$. Because of the periodicity of the potential, the t-matrix is identical for all lattice sites. Thus, $\Delta t^n_{L_1 L_2}(E) = \Delta t^0_{L_1 L_2}(E)$ for all n and eq. (3.42) becomes

$$\begin{aligned} c^n_{\mathbf{k}L_1} &= \sum_{n'} \sum_{L_2 L_3} G^{\mathrm{r},nn'}_{L_1 L_2}(E) \Delta t^0_{L_2 L_3}(E) c^{n'}_{\mathbf{k}L_3} \\ &= \sum_{n'} \sum_{L_2 L_3} G^{\mathrm{r},nn'}_{L_1 L_2}(E) \Delta t^0_{L_2 L_3}(E) e^{-i\mathbf{k}\cdot(\mathbf{R}^n - \mathbf{R}^{n'})} c^n_{\mathbf{k}L_3} \\ &= \sum_{L_2 L_3} G^{\mathrm{r}}_{L_1 L_2}(\mathbf{k}; E) \Delta t^0_{L_2 L_3}(E) c^n_{\mathbf{k}L_3} \,. \end{aligned} \tag{3.44}$$

This can be written as

$$\sum_{L_2} \left(\delta_{L_1 L_2} - \sum_{L_3} G^{\mathrm{r}}_{L_1 L_3}(\mathbf{k}; E) \Delta t^0_{L_3 L_2}(E) \right) c^0_{\mathbf{k} L_2} = 0 \,, \tag{3.45}$$

which is the sought-after secular equation for the band structure calculation.

Taking the free space as reference system, the t-matrix $t^{\mathrm{r},n}_l(E)$ becomes zero, the structural Green functions $G^{\mathrm{r}}_{LL'}(\mathbf{k}; E)$ are simply the free structure constants $g_{LL'}(\mathbf{k}; E)$ and eq. (3.45) reduces to

$$\sum_{L'} \left(\delta_{LL'} - \sum_{L''} g_{LL''}(\mathbf{k}; E) t^0_{L''L'}(E) \right) c^0_{\mathbf{k} L'} = 0 \,, \tag{3.46}$$

which is equivalent to the secular eq. (3.12) derived in the previous section.

In analogy to the previous section, the above equation can be extended to the case of several atoms being in a unit cell. Then, the structural Green function of the reference system writes as

$$G^{\mathrm{r},\mu\mu'}_{LL'}(\mathbf{k}; E) = \sum_{n'} G^{n\mu n'\mu'}_{LL'}(E) e^{-i\mathbf{k}(\mathbf{R}^n - \mathbf{R}^{n'})} \,, \tag{3.47}$$

and eq. (3.44) must be modified according to

$$c^{\mu}_{\mathbf{k} L} = \sum_{\mu' L' L''} G^{\mathrm{r}\mu\mu'}_{LL''}(\mathbf{k}; E) \Delta t^{\mu'}_{L''L'}(E) c^{\mu'}_{\mathbf{k} L'} \,, \tag{3.48}$$

where the index $n = 0$ was dropped to simplify the notation.

Finally, the KKR secular equation becomes

$$\sum_{\mu' L'} \left(\delta_{\mu\mu'} \delta_{LL'} - \sum_{L''} G^{\mathrm{r}\mu\mu'}_{LL'}(\mathbf{k}; E) \Delta t^{\mu'}_{L''L'}(E) \right) c^{\mu'}_{\mathbf{k} L'} = 0 \,, \tag{3.49}$$

which formally is an eigenvalue problem with eigenvectors

$$c^{\mu}_{\mathbf{k} L}; \mu = 1, \dots, N_{\mathrm{at}}, \ L = 1, \dots, L_{\max} \tag{3.50}$$

and eigenvalues $\lambda = 0$. The scheme used in the band structure calculation employing eq. (3.49) is explained in appendix A.2.

3.1.4 The Fermi surface

At $T = 0$, all energy levels are up to the Fermi energy E_{F} are occupied. In momentum space, this energy corresponds to an energy isosurface $E(\mathbf{k}) = E_{\mathrm{F}}$, which is determined by the band structure and denoted as Fermi surface. For the free electron gas, it is simply a sphere, since the energy E is proportional to $\mathbf{k}^2$. However, even for simple metals like Cu, Ag or Au the shape of the Fermi surface exhibits significant deviations from that of the free electron gas. For example, the Fermi surfaces of Cu and Au are shown in chapter 6. For complex materials it might be a very complicated object.

The Fermi surface allows to gain inside into many characteristics of materials such as scattering and transport processes. Due to the Fermi Dirac distribution (especially at low temperatures) mainly electrons close to the Fermi energy contribute and determine the transport properties of a material. In the current work, elastic scattering processes without energy dissipation will be treated, i.e. scattering processes, in which the electrons keep their energy and only the $\mathbf{k}$-vector changes. Hence, scattering processes are only allowed from one $\mathbf{k}$-vector on the Fermi surface to another reciprocal space vector $\mathbf{k}'$ also being on the Fermi surface.

The calculation of the Fermi surface is very similar to the band structure calculation as explained in the previous section and in appendix A.2; the energy is pinned to $E = E_F$ while the $\mathbf{k}$ vector is varied such that eq. (3.49) is fulfilled.

Once the $\mathbf{k}$-vectors $\mathbf{k}_F$ obeying eq. (3.49) are found, the corresponding coefficients $c_{\mathbf{k}L}^{n,\mu}$ can be determined by calculating the eigenvectors $c_{\mathbf{k}L}^{\mu}$ in eq. (3.49). In order to identify the full wavefunctions $\psi_{\mathbf{k}}(\mathbf{r})$ at the Fermi surface, the regular solutions $R_L(\mathbf{r}; E)$ of the Schrödinger equation have to be calculated by solving the Schrödinger equation as described in chapter 2, section 2.2 or 2.4, respectively. Besides, the coefficients $c_{\mathbf{k}L}^{n,\mu}$ are needed for the calculation of the scattering matrix $T_{\mathbf{k}\mathbf{k}'}$, describing the scattering amplitude for scattering from one state with crystal momentum $\mathbf{k}'$ to another state characterized by $\mathbf{k}$. The scattering matrix $T_{\mathbf{k}\mathbf{k}'}$ will be derived in section 3.3.

3.2 Impurity scattering

Whenever an impurity or a defect exists in a crystal, the periodicity is broken, and the wavefunctions are not Bloch functions any more. Hence, they cannot be determined as described in the previous sections. However, the wavefunctions $\psi_{\mathbf{k}}^{\mathrm{imp}}(\mathbf{r}+\mathbf{R}^n; E)$ of the impurity problem with the boundary condition of an incoming wave $\psi_{\mathbf{k}}(\mathbf{r} + \mathbf{R}^n; E)$ are given by the full Lippmann-Schwinger equation (3.30)

$$\psi_{\mathbf{k}}^{\mathrm{imp}}(\mathbf{r} + \mathbf{R}^n; E) = \psi_{\mathbf{k}}(\mathbf{r} + \mathbf{R}^n; E)$$
$$+ \sum_{n'} \int d^3r' G(\mathbf{r} + \mathbf{R}^n, \mathbf{r}' + \mathbf{R}^{n'}; E)\Delta V^{n'}(\mathbf{r}')\psi_{\mathbf{k}}^{\mathrm{imp}}(\mathbf{r}' + \mathbf{R}^{n'}). \quad (3.51)$$

Here, $\Delta V^{n'}(\mathbf{r}') = V^{\mathrm{imp},n'}(\mathbf{r}') - V^{n'}(\mathbf{r}')$ denotes the difference of the impurity potential and that of the periodic host system, whereas $G(\mathbf{r}+\mathbf{R}^n, \mathbf{r}'+\mathbf{R}^{n'}; E)$ is the corresponding Green function of the homogeneous (host) system. Since the perturbation is localized, the difference between the potentials $\Delta V^{n'}(\mathbf{r}')$ is non-zero for a finite number of sites only. Hence, the sum over n' has no longer to be performed over the whole crystal but can be restricted to the finite number of perturbed lattice sites, in contrast to the case of the homogeneous system in section 3.1.

In analogy to the expansion (3.17) of the wavefunction of the homogeneous system, the wavefunction $\psi_{\mathbf{k}}^{\mathrm{imp}}(\mathbf{r} + \mathbf{R}^n; E)$ in the presence of an impurity expands as

$$\psi_{\mathbf{k}}^{\mathrm{imp}}(\mathbf{r} + \mathbf{R}^n; E) = \sum_L c_{\mathbf{k}L}^{\mathrm{imp},n} R_L^{\mathrm{imp},n}(\mathbf{r}; E), \quad (3.52)$$

where $R_L^{\text{imp},n}(\mathbf{r}; E)$ is the regular solution of the Schrödinger equation at the lattice site n of the impurity problem. Because of the locality of the perturbation, for atoms far away from the impurity where $\Delta V(\mathbf{r}) \approx 0$, it simplifies to the regular solution of the homogeneous system, i.e. $R_L^{\text{imp},n}(\mathbf{r}; E) \approx R_L^n(\mathbf{r}; E)$.

In a first step, we will consider the case of a spherical potential, thus $\Delta V^{n'}(\mathbf{r}') = \Delta V^{n'}(r')$, while in a second step, the full potential $\Delta V^{n'}(\mathbf{r}')$ will be treated. As the exact derivations are lengthy, they are just outlined in the following sections and discussed in detail in appendix A.5.1 and A.5.2.

3.2.1 Impurity scattering in the atomic sphere approximation

The procedure pursued to obtain the impurity coefficients $c_{\mathbf{k}L}^{\text{imp}}$ is the following: We insert the expansion for the wavefunctions calculated within the ASA

$$\psi_{\mathbf{k}}^{\text{imp}}(\mathbf{r} + \mathbf{R}^n; E) = \sum_L c_{\mathbf{k}L}^{\text{imp},n} R_l^{\text{imp},n}(r; E) Y_L(\hat{r}) \,, \tag{3.53}$$

the Green function eq. (2.44) and the difference of the potentials

$$\Delta V^n(r) = V^{\text{imp},n}(r) - V^n(r) \tag{3.54}$$

into the Lippmann-Schwinger equation (3.51). Integration over the spherical part, replacing the radial integral by the t-matrix $\Delta t_l^n(E) = t_l^{\text{imp},n}(E) - t_l^n(E)$ and comparison of the coefficients yields the relation

$$c_{\mathbf{k}L}^{\text{imp},n} = c_{\mathbf{k}L}^n + \sum_{n'} \sum_{L_1} G_{LL_1}^{nn'}(E) \Delta t_{l_1}^{n'}(E) c_{\mathbf{k}L_1}^{\text{imp},n'}. \tag{3.55}$$

Viewed as a matrix multiplication, the above expression is equivalent to

$$\left(\mathbf{c}_{\mathbf{k}}^{\text{imp}}\right) = \left[\sum_{n',L_1} \left(\delta_{LL_1} \delta_{nn'} - G_{LL_1}^{nn'}(E) \Delta t_{l_1}^{n'}(E) \right) \right]^{-1} \left(\mathbf{c}_{\mathbf{k}}\right) , \tag{3.56}$$

where $\left(\mathbf{c}_{\mathbf{k}}^{\text{imp}}\right)$ and $\left(\mathbf{c}_{\mathbf{k}}\right)$ are column matrices with elements $c_{\mathbf{k}L}^{\text{imp},n}$ and $c_{\mathbf{k}L}^n$, respectively. In terms of the structural Green function of the impurity instead of the host Green function the above relation can be formulated as

$$c_{\mathbf{k}L_1}^{\text{imp},n} = \sum_{n',L_2} \left(\delta_{L_1 L_2} \delta_{nn'} + G_{L_1 L_2}^{\text{imp},nn'}(E) \Delta t_{l_2}^{n'}(E) \right) c_{\mathbf{k}L_2}^{n'}. \tag{3.57}$$

The equality of $[1 + G^{\text{imp}}(E)\Delta t(E)]$ and $[1 - G(E)\Delta t(E)]^{-1}$ can be proven easily by tracing it back to the Dyson equation (2.10)

$$G^{\text{imp}}(E) = G(E) + G(E)\Delta t(E) G^{\text{imp}}(E) \,. \tag{3.58}$$

We start with the assumption

$$\left[1 - G^{\text{imp}}(E)\Delta t(E)\right] = \left[1 - G(E)\Delta t(E)\right]^{-1} \,. \tag{3.59}$$

This can be rewritten as

$$
\begin{aligned}
1 &= \left[1 - G(E)\Delta t(E)\right]\left[1 + G^{\mathrm{imp}}(E)\Delta t(E)\right] \tag{3.60} \\
&= 1 - G(E)\Delta t(E) + G^{\mathrm{imp}}(E)\Delta t(E) - G(E)\Delta t(E)G^{\mathrm{imp}}(E)\Delta t(E).
\end{aligned}
$$

Subtraction of 1 on both sides and factoring out $\Delta t(E)$ yields the Dyson equation (3.58), q.e.d..

The form (3.57) is more convenient in practice than (3.56), and is used in the calculations of this thesis.

3.2.2 Impurity scattering in the case of a full potential

If the full potential of the host or the impurity is taken into account, the relation as well as the derivation of the impurity coefficients $c_{\mathbf{k}L}^{\mathrm{imp},n}$ in terms of the homogeneous ones $c_{\mathbf{k}L}^{n}$ is very similar to that described for ASA in the last section. Then, the potential $V(\mathbf{r})$ depends not only on the norm of $\mathbf{r}$ but the full vector, scattering from one orbital with angular momentum L_1 to another orbital characterized by L_2 is no longer forbidden and the expansion of the wave function (3.32) has to be modified

$$
\begin{aligned}
\psi_{\mathbf{k}}(\mathbf{r} + \mathbf{R}^n) &= \sum_{L_1} c_{\mathbf{k}L_1}^{n} R_{L_1}^{n}(\mathbf{r}; E) \\
&= \sum_{L_1 L_2} c_{\mathbf{k}L_1}^{n} R_{L_2 L_1}^{n}(r; E) Y_{L_2}(\mathbf{r}) . \tag{3.61}
\end{aligned}
$$

Here, the wave function $R_{L_2 L_1}(r)$ represents the scattering solution for an incoming wave with angular momentum L_1 to a wave with angular momentum L_2.

Similar to the wavefunction, the Green function $G(\mathbf{r} + \mathbf{R}^n, \mathbf{r}' + \mathbf{R}^{n'}; E)$ has to be expanded as (see eq. (2.44) in section 2.3)

$$
\begin{aligned}
G(\mathbf{r}&+\mathbf{R}^n, \mathbf{r}' + \mathbf{R}^{n'}; E) \\
&= -i\sqrt{E} \sum_{L_1} R_{L_1}^{n}(\mathbf{r}_<; E) H_L^{n}(\mathbf{r}_>; E)\delta_{nn'} + \sum_{n'}\sum_{L_1 L_2} R_{L_1}^{n}(\mathbf{r}; E) G_{L_1 L_2}^{nn'}(E) R_{L_2}^{n'}(\mathbf{r}'; E) \\
&= -i\sqrt{E} \sum_{L_1}\sum_{L_2 L_3} R_{L_2 L_1}^{n}(r_<; E) Y_{L_2}(\hat{r}_>) H_{L_3 L_1}^{n}(r_>; E) Y_{L_3}(\hat{r}_>)\delta_{nn'} \\
&\qquad + \sum_{n'}\sum_{L_1 L_2}\sum_{L_3 L_4} Y_{L_3}(\hat{r}) R_{L_3 L_1}^{n}(r; E) G_{L_1 L_2}^{nn'}(E) R_{L_4 L_2}^{n'}(r'; E) Y_{L_4}(\hat{r}') ,
\end{aligned}
$$

$$\tag{3.62}$$

while the difference of the potentials $\Delta V^{n'}(\mathbf{r}')$ is expanded in terms of spherical harmonics as

$$
\Delta V^{n'}(\mathbf{r}') = \sum_L \Delta V_L^{n'}(r') Y_L(\hat{r}) . \tag{3.63}
$$

As in the case of the spherical potential, the Lippmann-Schwinger equation (3.51) provides the basis for establishing the relation between the perturbed and the unperturbed coefficients. Replacing the Green function, the wavefunctions as well as the potential difference

by the right-hand sides of eqs. (3.61), (3.62) and (3.63), integration over the solid angles, identification of the atomic scattering matrix $\Delta t_{L_1 L_2}(E)$ and comparison of the coefficients while exploiting the linear independence of the spherical harmonics and the radial wavefunctions $R^n_{L_2 L_1}(r; E)$ results in

$$c^{\mathrm{imp},n}_{\mathbf{k}L_1} = c^n_{\mathbf{k}L_1} + \sum_{n'} \sum_{L_2 L_3} G^{nn'}_{L_1 L_2}(E) \Delta t_{L_2 L_3} c^{\mathrm{imp},n'}_{\mathbf{k}L_3} \ . \tag{3.64}$$

Finally, we arrive at the general expression

$$c^{\mathrm{imp},n}_{\mathbf{k}L_1} = \sum_{n',L_2} \left(\delta_{L_1 L_2} \delta_{nn'} + \sum_{L_3} G^{\mathrm{imp},nn'}_{L_1 L_3}(E) \Delta t^{n'}_{L_3 L_2}(E) \right) c^{n'}_{\mathbf{k}L_2} \ . \tag{3.65}$$

Naturally, the above equation can be generalized to the case of N_{at} atoms per unit cell as introduced in section 3.1.3. Then, eq. (3.65) transforms to

$$c^{\mathrm{imp},n\mu}_{\mathbf{k}L_1} = \sum_{n'\mu',L_2} \left(\delta_{L_1 L_2} \delta_{nn'} \delta_{\mu\mu'} + \sum_{L_3} G^{\mathrm{imp},nn'\mu\mu'}_{L_1 L_3}(E) \Delta t^{n'\mu'}_{L_3 L_2}(E) \right) c^{n'\mu'}_{\mathbf{k}L_2} \ . \tag{3.66}$$

These expressions reduce to the ones for spherical potentials (eqs. (3.55) and (3.57)) when replacing the full potential Δt-matrix by the spherical one $\Delta t_{L_1 L_2} = \delta_{L_1 L_2} \Delta t_{L_2}$.

3.3 The scattering matrix $T_{\mathbf{kk'}}$

In chapter 2 we have already defined the transition matrix $T(E)$, eq. (2.17), relating the wave function $|\psi\rangle$ of a perturbed system to the wave function $|\psi_0\rangle$ of the unperturbed system [72]. We will now consider $T(E)$ in its reciprocal-space representation, i.e. $T_{\mathbf{kk'}}$, where it represents the scattering amplitude from one state characterized by the state vector $\mathbf{k'}$ to a second state described by $\mathbf{k}$. For the purposes of this thesis, $T_{\mathbf{kk'}}$ is of central importance, since all physical quantities, i.e. the momentum scattering times, the surface state lifetimes as well as surface residual resistivities calculated later-on are derived from $T_{\mathbf{kk'}}$. Although scattering might have several reasons such as electron-electron or electron-phonon coupling, we will deal with impurity or defect scattering only. In this case, the scattering matrix $T_{\mathbf{kk'}}$ is defined as

$$\begin{aligned} T_{\mathbf{kk'}} &= \int d^3r \ \psi^\star_{\mathbf{k'}}(\mathbf{r}; E) \Delta V(\mathbf{r}) \psi^{\mathrm{imp}}_{\mathbf{k}}(\mathbf{r}; E) \\ &= \sum_n \int_{\mathrm{cell}\ n} d^3r \ \psi^\star_{\mathbf{k'}}(\mathbf{r} + \mathbf{R}^n; E) \Delta V^n(r) \psi^{\mathrm{imp}}_{\mathbf{k}}(\mathbf{r} + \mathbf{R}^n; E) \ , \end{aligned} \tag{3.67}$$

where the sum is to be understood as the sum over all perturbed cells/sites included in the impurity calculations.

In the following, we will simplify the latter expression and express the scattering matrix in terms of the coefficients $c_{\mathbf{k}L}$ and $c^{\mathrm{imp}}_{\mathbf{k}L}$, the structural Green function of the impurity $G^{\mathrm{imp},nn'}_{LL'}$ as well as the atomic scattering t-matrix $\Delta t_{LL'}$ and the related Δ-matrix $\Delta_{LL'}$. As in the previous sections, we will start with the atomic sphere approximation and then proceed with the full-potential treatment.

3.3.1 Spherical potential

In the ASA, inserting the expansion of the wave functions eq. (3.53) in the definition of $T_{\mathbf{kk}'}$, eq. (3.67) leads to the expression

$$
T_{\mathbf{kk}'} = \sum_n \int_{\text{cell } n} d^3r
$$
$$
\sum_L c_{\mathbf{k}'L}^{n\star} R_l^{n\star}(r; E) Y_L(\hat{r}) \Delta V^n(r) \sum_{L'} c_{\mathbf{k}L'}^{\text{imp},n} R_{l'}^{\text{imp},n}(r; E) Y_{L'}(\hat{r}) . \quad (3.68)
$$

Integration over the spherical coordinates yields

$$
T_{\mathbf{kk}'} = \sum_n \sum_L c_{\mathbf{k}'L}^{n\star} c_{\mathbf{k}L}^{\text{imp},n} \int_{\text{cell } n} r^2 dr \; R_l^{n\star}(r; E) \Delta V^n(r) R_l^{\text{imp},n}(r; E) . \quad (3.69)
$$

In the present form the remaining integral cannot be replaced by the atomic scattering matrix $\Delta t_l(E)$, since in the definition of $\Delta t_l(E)$, eqs. (A.34) and (A.35), the wavefunction of the homogeneous system appears and not its complex conjugate $R_l^{n\star}(r; E)$. Therefore, we define the above integral as Δ-matrix

$$
\Delta_l(E) := \int_{\text{cell } n} r^2 dr \; R_l^{n\star}(r; E) \Delta V^n(r) R_l^{\text{imp},n}(r; E) . \quad (3.70)
$$

There are several ways to proceed in order to calculate the Δ-matrix $\Delta_l(E)$. Of course, one possibility is to calculate the integral directly, which will be done later when the scattering matrix is calculated taking spin-orbit coupling into account.

However, if spin-orbit coupling is neglected, there are other possibilities to obtain $\Delta_l(E)$, too. The most simple one in the case of a pure spherical potential is to remember that the complex radial wave function $R_l^n(r; E)$ is real except a complex phase factor [73], thus $R_l^n(r; E) = \exp\left[i\delta_l\right] U_l^n(r; E)$, where $U_l^n(r; E)$ is real. Therefore, its complex conjugate is simply $R_l^{n\star}(r; E) = \exp\left[-2i\delta_l\right] R_l^n(r; E)$. The exponents δ_l are the l-dependent phase shifts which describe the difference in phase at the Wigner-Seitz radius of the wavefunction compared to the wavefunction of free space. The phase shifts can be obtained from the atomic t-matrix, since the relation

$$
t_l(E) = -\frac{1}{\sqrt{E}} \sin \delta_l(E) e^{i\delta_l} \quad (3.71)
$$

holds, thus

$$
\delta_l(E) = \frac{1}{2i} \ln\left[-2i\sqrt{E} t_l(E) + 1\right] . \quad (3.72)
$$

Then, the integral in eq. (3.69) can be identified with the Δt-matrix and the scattering matrix becomes

$$
T_{\mathbf{kk}'} = \sum_n \sum_L c_{\mathbf{k}'L}^{n\star} \exp\left[-2i\delta_l\right] \Delta t_l^n c_{\mathbf{k}L}^{\text{imp},n} . \quad (3.73)
$$

Inserting expression (3.57) for the impurity coefficients, the above relation becomes

$$
T_{\mathbf{kk}'} = \sum_{nn'} \sum_{LL'} c_{\mathbf{k}'L}^{n\star} \exp\left[-2i\delta_l\right] \Delta t_l^n \left(\delta_{LL'}\delta_{nn'} + G_{LL'}^{\text{imp},nn'}(E) \Delta t_{l'}^{n'}(E)\right) c_{\mathbf{k}L'}^{n'} . \quad (3.74)
$$

The scattering matrix $T_{\mathbf{kk}'}$ fulfills the optical theorem[1]

$$\sum_{\mathbf{k}'} |T_{\mathbf{kk}'}|^2 \delta(E_{\mathbf{k}} - E_{\mathbf{k}'}) = -\frac{1}{\pi} \mathrm{Im} T_{\mathbf{kk}} \, , \tag{3.75}$$

which will be useful when calculating the momentum relaxation time $\tau_{\mathbf{k}}$ of a state $\mathbf{k}$. An expression for $\tau_{\mathbf{k}}$ will be derived in section 3.5.

3.3.2 Full potential

Considering a non-spherical potential, expansion of the wavefunctions and the potential in the definition of the scattering matrix $T_{\mathbf{kk}'}$, eq. (3.67), yields

$$T_{\mathbf{kk}'} = \int d^3 r \sum_{L_1} c^{n\star}_{\mathbf{k}'L_1} R^{n\star}_{L_1}(\mathbf{r}, E) \sum_{L_2} \Delta V_{L_2}(r) Y_{L_2}(\hat{r}) \sum_{L_3} c^{\mathrm{imp},n}_{\mathbf{k}L_3} R^{\mathrm{imp},n}_{L_3}(\mathbf{r}, E) \, . \tag{3.76}$$

Integration over the solid angles leads to the same problem as in the previous section: the integral over the radial part cannot be identified with the atomic scattering matrix, since the complex conjugate of the host wavefunction appears in the integral. In order to trace it back to the definition of the Δt-matrix, we refer to the α-matrix $\alpha_{L_1 L_2}$ as defined in eq. (2.65). As explained in chapter 2, section 2.4, the inverse of the α-matrix transforms the regular (in general complex) wavefunctions $R_{L_1}(\mathbf{r})$ to real wavefunctions $U_{L_1}(\mathbf{r})$, eq. (2.66). Therefore, the complex conjugate can be rewritten as

$$R^{\star}_{L_1}(\mathbf{r}) = \left[\sum_{L_2} U_{L_2}(\mathbf{r}) \alpha_{L_2 L_1} \right]^{\star} = \sum_{L_2 L_3} R_{L_3}(\mathbf{r}) \alpha^{-1}_{L_3 L_2} \alpha^{\star}_{L_2 L_1} \, . \tag{3.77}$$

Inserting the above expression in eq. (3.76) we obtain

$$
\begin{aligned}
T_{\mathbf{kk}'} &= \int d^3 r \sum_{L_1} c^{n\star}_{\mathbf{k}'L_1} R^{n\star}_{L_1}(\mathbf{r}, E) \Delta V(\mathbf{r}) \sum_{L_2} c^{\mathrm{imp},n}_{\mathbf{k}L_2} R^{\mathrm{imp},n}_{L_2}(\mathbf{r}, E) \\
&= \sum_{L_1 L_2} c^{n\star}_{\mathbf{k}'L_1} c^{\mathrm{imp},n}_{\mathbf{k}L_2} \sum_{L_3 L_4} \alpha^{-1}_{L_4 L_3} \alpha^{\star}_{L_3 L_1} \int d^3 r \, R_{L_4}(\mathbf{r}) \Delta V(\mathbf{r}) R^{\mathrm{imp},n}_{L_2}(\mathbf{r}, E) \\
&= \sum_{L_1 L_2} c^{\star n}_{\mathbf{k}'L_1} c^{\mathrm{imp},n}_{\mathbf{k}L_2} \sum_{L_3 L_4} \alpha^{-1}_{L_4 L_3} \alpha^{\star}_{L_3 L_1} \Delta t_{L_4 L_2}(E) \, ,
\end{aligned} \tag{3.78}
$$

thus

$$T_{\mathbf{kk}'} = \sum_{L_1 L_2 L_3 L_4} c^{n\star}_{\mathbf{k}L_1} \alpha^{-1}_{L_3 L_2} \alpha^{\star}_{L_2 L_1} \Delta t_{L_3 L_4} c^{\mathrm{imp},n}_{\mathbf{k}'L_4} \, . \tag{3.79}$$

For a spherical potential, the above expression must reduce to eq. (3.73), which can be proven easily by inserting

$$
\begin{aligned}
\alpha_{L_1 L_2} &= \delta_{L_1 L_2} |\alpha_{L_1 L_2}| e^{i\delta_{l_1}} \qquad \text{and} \tag{3.80} \\
\Delta t_{L_1 L_2} &= \delta_{L_1 L_2} \Delta t_{l_1} \tag{3.81}
\end{aligned}
$$

in expression (3.79).

---

[1] In its original form, the optical theorem is $\frac{1}{2}(T^{\dagger} - T) = i\sqrt{E} T^{\dagger} T$, which in the case of atomic t-matrices simplifies to $1/2(t^{\star}_{L'L} - t_{LL'}) = i\sqrt{E} \sum_{L''} t^{\star}_{L''L} t_{L''L'}$. Knowing, that the atomic t-matrices $t_{LL'}$ are symmetric and setting $L = L'$ leads to the above form.

3.4 Wigner delay time

In order to analyze the time scale of the scattering process, it is useful to define the Wigner delay time t_{D} as

$$t_{\mathrm{D}} = 2\frac{d\delta_l}{dE} \,, \tag{3.82}$$

where δ_l denotes the phase shift as introduced in chapter 2 eq. (2.29). The above definition follows from the interpretation of the scattering process of a wave packet. The Wigner delay time t_{D} describes the delay of a scattered wave compared to an unperturbed one, or, in other words, the time which the electron spends at the impurity during the scattering process. More information and a detailed derivation of the Wigner delay time can be found in [60] and [72].

3.5 The lifetime $\tau_{\mathbf{k}}$

Having calculated the scattering matrix $T_{\mathbf{kk'}}$ and assuming elastic scattering, the microscopic scattering probability $P_{\mathbf{kk'}}$ can be found via the relation

$$P_{\mathbf{kk'}} = \frac{2\pi}{\hbar} Nc |T_{\mathbf{kk'}}|^2 \,\delta(E_{\mathbf{k}} - E_{\mathbf{k'}}) \,, \tag{3.83}$$

where N is the total number of atoms in the crystal and c is the impurity concentration – hence, Nc is the number of impurities present in the crystal. Assuming that each impurity scatters independently, the lifetime of a state $\mathbf{k}$ can be found by summing up the scattering probabilities for scattering of $\mathbf{k}$ into all states $\mathbf{k'}$

$$\tau_{\mathbf{k}}^{-1} = \sum_{\mathbf{k'}} P_{\mathbf{k'k}} = \frac{2\pi}{\hbar} Nc \sum_{\mathbf{k'}} |T_{\mathbf{k'k}}|^2 \,\delta(E_{\mathbf{k}} - E_{\mathbf{k'}}) \,. \tag{3.84}$$

The summation over $\mathbf{k'}$ can be transformed to an integral

$$\sum_{\mathbf{k'}} = \frac{V}{(2\pi)^3} \int d^3 k' \,, \tag{3.85}$$

where V is the volume of the crystal. The integration over $d^3 k'$ can be separated into an integral over surfaces with $E_{\mathbf{k'}} = \mathrm{const.}$ and an integration in the direction $k'_{\perp}$ perpendicular to them

$$\sum_{\mathbf{k'}} = \frac{V}{(2\pi)^3} \int_0^{E_{\max}} dE_{\mathbf{k'}} \int_{S(E_{\mathbf{k'}})} \frac{dS_{\mathbf{k'}}}{\hbar v_{\mathbf{k'}}} \,. \tag{3.86}$$

Therefore, the inverse lifetime (3.84) results in

$$\tau_{\mathbf{k}}^{-1} = \frac{1}{V_{\mathrm{BZ}}} \frac{2\pi Nc}{\hbar^2} \int_{S(E_{\mathrm{F}})} \frac{dS_{\mathbf{k'}}}{v_{\mathbf{k'}}} |T_{\mathbf{k'k}}|^2 \,, \tag{3.87}$$

replacing $(2\pi)^3/V$ by the volume of the Brillouin zone V_{BZ}, carrying out the integration over the energy $dE_{\mathbf{k'}}$ and setting $E_{\mathbf{k}} = E_{\mathrm{F}}$, since we are interested in lifetimes at the Fermi

energy E_F. If only the total momentum relaxation time should be calculated, the optical theorem

$$\frac{1}{V_{BZ}} \int_{S(E_F)} \frac{dS_{\mathbf{k}'}}{\hbar v_{\mathbf{k}'}} |T_{\mathbf{k}\mathbf{k}'}|^2 = -\frac{1}{\pi} \mathrm{Im} T_{\mathbf{k}\mathbf{k}} \tag{3.88}$$

can be used. Then, the integration over the Fermi surface can be omitted and the inverse momentum relaxation time is given by

$$\tau_{\mathbf{k}}^{-1} = -\frac{2}{\hbar} N c \, \mathrm{Im} T_{\mathbf{k}\mathbf{k}} \; . \tag{3.89}$$

3.6 Residual resistivity

In a metal, the mean free path $\Lambda_{\mathbf{k}}$ of an electron with wavevector $\mathbf{k}$ is given by the product

$$\Lambda_{\mathbf{k}} = \mathbf{v}_{\mathbf{k}} \tilde{\tau}_{\mathbf{k}} \; , \tag{3.90}$$

where $\mathbf{v}_{\mathbf{k}}$ is the Fermi velocity and $\tilde{\tau}_{\mathbf{k}}$ denotes the mean time between two scattering events. This so-called transport scattering time $\tilde{\tau}_{\mathbf{k}}$ does not equal the momentum relaxation time $\tau_{\mathbf{k}}$ calculated in the last section. It is obtained by a self-consistent solution of the Boltzmann equation [59]

$$\tilde{\tau}_{\mathbf{k}} v_{\mathbf{k}} \frac{N c \, V_n}{4\pi^2} \int_{S(E_F)} \frac{dS_{\mathbf{k}'}}{\hbar v_{\mathbf{k}'}} |T_{\mathbf{k}\mathbf{k}'}|^2 = v_{\mathbf{k}} + \frac{N c \, V_n}{4\pi^2} \int_{S(E_F)} \frac{dS_{\mathbf{k}'}}{\hbar v_{\mathbf{k}'}} \tilde{\tau}_{\mathbf{k}'} \frac{\mathbf{v}_{\mathbf{k}} \cdot \mathbf{v}_{\mathbf{k}'}}{v_{\mathbf{k}}} |T_{\mathbf{k}\mathbf{k}'}|^2 \; . \tag{3.91}$$

As in the last section, $N c$ denotes the number of impurities in the crystal, and V_n is the volume of a unit cell n. Once the transport scattering time $\tilde{\tau}_{\mathbf{k}}$ is known, the residual resistivity per impurity concentration $c\rho$ can be calculated. It is given by

$$\frac{1}{c\rho} = \frac{1}{3} \frac{e^2}{4\pi^3 \hbar} \int_{S(E_F)} dS_{\mathbf{k}} \, v_{\mathbf{k}} \tilde{\tau}_{\mathbf{k}} \; . \tag{3.92}$$

The factor $1/3$ is due to averaging the Fermi velocity over the three dimensions of space. If residual resistivities for 2-dimensional (host) systems such as thin films have to be calculated, the factor has to be replaced by $1/2$ and the residual resistivity per impurity concentration becomes

$$c\rho = \left[\frac{e^2}{8\pi^3 \hbar} \int_{S(E_F)} dS_{\mathbf{k}} \, v_{\mathbf{k}} \tilde{\tau}_{\mathbf{k}} \right]^{-1} \; . \tag{3.93}$$

In such two-dimensional systems, the integral over the Fermi surfaces reduces to a line integral.

Spin-orbit coupling

Spin-orbit coupling is the most important mechanism which couples the spin moment of an electron to its orbital motion. In the interplay with ordinary momentum relaxation, it determines the spin-relaxation time and the spin-flip lifetime for electrons, which is one of the major subjects of the present thesis. Therefore, at the beginning of this chapter a short introduction to the theoretical concept of spin-orbit interaction will be given. Up to now, the description of the scattering processes within the KKR-formalism has been done without spin-orbit coupling. In this chapter, we will extend the method to systems under the presence of spin-orbit coupling and describe its implementation within the KKR-formalism. However, we work in an approximation where the charge-density is calculated without spin-orbit coupling, while spin-orbit coupling is then included in the final step of wavefunction and t-matrix calculation for scattering properties.

We present a scheme to calculate the spin expectation operators and point out the problems arising when considering degenerated states. A simple model will be used to confirm that our unexpected results regarding this aspect are correct. Finally, the concept of momentum relaxation caused by impurity scattering is extended to systems where spin-orbit coupling effects are included and a formula for spin-relaxation times is derived.

4.1 Theory of spin-orbit coupling

Spin-orbit coupling denotes the interaction of a particle's spin with its motion. From a classical point of view, this can be understood by considering a moving electron in an electric field $\mathbf{E}$. A Lorentz transformation to the frame of reference of the moving electron leads to a magnetic field $\mathbf{B} \sim \mathbf{v} \times \mathbf{E}$ which couples to the magnetic moment of the electron. However, spin-orbit coupling is a purely relativistic effect, and therefore not inherent in the frame of the non-relativistic Schrödinger equation or even the scalar relativistic approach. The aim

of this section is to derive a correction term to the Schrödinger equation coupling the magnetic moment $\boldsymbol{\sigma}$ of the electron to its orbital momentum $\mathbf{L}$. Therefore, one has to start with the fully relativistic Dirac equation for an electron in an external scalar potential $V(\mathbf{r})$ and a vector potential $\mathbf{A}(\mathbf{r})$

$$H\boldsymbol{\Psi}(\mathbf{r}) = i\hbar\frac{\partial}{\partial t}\boldsymbol{\Psi}(\mathbf{r}) = E\boldsymbol{\Psi}(\mathbf{r}) \tag{4.1}$$

with the Hamiltonian

$$H = -eV(\mathbf{r}) + \beta mc^2 + \boldsymbol{\alpha} \cdot [c\mathbf{p} + e\mathbf{A}(\mathbf{r})] \tag{4.2}$$

for an electron with charge $-e$ and rest mass m.
The $\boldsymbol{\alpha}$-matrix is a vector of 4×4-matrices

$$\boldsymbol{\alpha} = \begin{pmatrix} 0 & \boldsymbol{\sigma} \\ \boldsymbol{\sigma} & 0 \end{pmatrix} \tag{4.3}$$

consisting of the Pauli spin matrices

$$\sigma_x = \begin{pmatrix} 0 & 1 \\ 1 & 0 \end{pmatrix}, \quad \sigma_y = \begin{pmatrix} 0 & -i \\ i & 0 \end{pmatrix} \text{ and } \quad \sigma_z = \begin{pmatrix} 1 & 0 \\ 0 & -1 \end{pmatrix}, \tag{4.4}$$

while β is a matrix of same rank, built of 2×2 unit matrices I_2

$$\beta = \begin{pmatrix} I_2 & 0 \\ 0 & -I_2 \end{pmatrix}. \tag{4.5}$$

The eigenfunctions $\boldsymbol{\Psi}(\mathbf{r})$ of (4.1) are four-component vectors usually written as

$$\boldsymbol{\Psi}(\mathbf{r}) = \begin{pmatrix} \psi(\mathbf{r}) \\ \xi(\mathbf{r}) \end{pmatrix}, \tag{4.6}$$

and the two-component vectors $\psi(\mathbf{r})$ and $\xi(\mathbf{r})$ are called large and small component of the wave function. Inserted into eq. (4.1) and using eq. (4.2), two differential equations coupling the large and small component are obtained

$$\left(E - 2mc^2 + eV(\mathbf{r})\right)\psi(\mathbf{r}) = \boldsymbol{\alpha} \cdot (c\mathbf{p} + e\mathbf{A}(\mathbf{r}))\xi(\mathbf{r}) \tag{4.7}$$

$$\left(E + 2mc^2 + eV(\mathbf{r})\right)\xi(\mathbf{r}) = \boldsymbol{\alpha} \cdot (c\mathbf{p} + e\mathbf{A}(\mathbf{r}))\psi(\mathbf{r}). \tag{4.8}$$

A substitution of eq. (4.8) in eq. (4.7) allows to formulate an equation for the large component, also denoted as Pauli-equation. For non-magnetic systems, the vector potential $\mathbf{A}(\mathbf{r}) = 0$ vanishes. Furthermore, in the non-relativistic limit, i.e. $v \ll c$, the Pauli-equation reduces to the Schrödinger equation but with the additional term

$$\frac{e\hbar}{2\left(M(r)c\right)^2}\boldsymbol{\sigma} \cdot (\nabla V(\mathbf{r}) \times \mathbf{p}), \tag{4.9}$$

comprising the coupling of the electron spin to the cross-product $\mathbf{E} \times \mathbf{p}$. Here, the relativistic mass $M(r)$ enters instead of the rest mass m. An expression for $M(r)$ will be given in the following section 4.2, eq. (4.20).

Then, the following transformation

$$
\begin{aligned}
\boldsymbol{\sigma} \cdot (\nabla V(\mathbf{r}) \times \mathbf{p}) &= \frac{1}{r} \frac{dV(r)}{dr} \boldsymbol{\sigma} \cdot (\mathbf{r} \times \mathbf{p}) \\
&= \frac{1}{r} \frac{dV(r)}{dr} \boldsymbol{\sigma} \cdot \mathbf{L}
\end{aligned}
\tag{4.10}
$$

is valid and leads to the sought-after coupling of the electron spin to its orbital momentum $\mathbf{L}$. Definition of the spin operator $\mathbf{S} = \boldsymbol{\sigma}/2$ yields the correction term

$$
V_{\text{SOC}} = \frac{e\hbar}{2M(r)^2 c^2} \frac{1}{r} \frac{dV(r)}{dr} \mathbf{L} \cdot \mathbf{S} \, ,
\tag{4.11}
$$

provided that the potential is spherical symmetric $V(\mathbf{r}) = V(r)$. This term is added to the non-relativistic or the scalar relativistic Hamiltonian H^{SRA}, respectively, and is often also denoted as spin-orbit Hamiltonian H_{SOC}. Then, the correction to the energy is obtained within first order perturbation theory.

In principle, the potential comprises contributions of all other electrons within the atom as well as the potential caused by the nucleus. In order to simplify calculations, this potential is replaced by a mean-field potential which is found during calculation, e.g. within density functional theory. The exact treatment of the potential in this thesis will be sketched in section 4.2.1. The strongest influence on the spin-orbit interaction comes from the strong nuclear field, whose derivative close to the core behaves as $1/r \, dV/dr \sim -Z|e|/r^3$; the dependence on the atomic number Z is also the reason why the influence of spin-orbit coupling is stronger in heavy atoms.

In the derivation of eq. (4.11), the definition of the angular momentum $\mathbf{L} = \mathbf{r} \times \mathbf{p}$ has been used. In the above form, it becomes evident that s-electrons do not contribute to spin-orbit coupling. The positive sign of the operator $\mathbf{L} \cdot \mathbf{S}$ indicates that spin- and orbital moment prefer to orient antiparallely giving rise to Hund's rule.

Although the spin-orbit Hamiltonian is proportional to L, p-electrons experience a stronger spin-orbit coupling than d- or f-electrons, since the p-wavefunction has a larger amplitude close to the nucleus (the wavefunctions of angular momentum l start off as $\sim r^l$), where the effect of spin-orbit coupling is largest (caused by the proportionality of the spin-orbit coupling Hamiltonian to $1/r^3$).

For further information, we refer to [74] or to any book on quantum mechanics, e.g. the books by Rose [75].

4.2 Evaluation of the spin-orbit Hamiltonian

The spin-orbit potential V_{SOC} as defined in eq. (4.11) is composed of a factor

$$
\xi(r) = \frac{e\hbar}{2M(r)^2 c^2} \frac{1}{r} \frac{dV(r)}{dr} \, ,
\tag{4.12}
$$

also called the spin-orbit coupling parameter, and the term $\mathbf{L} \cdot \mathbf{S}$. Whereas the parameter $\xi(r)$ determines the strength of the spin-orbit coupling, the term $\mathbf{L} \cdot \mathbf{S}$ accounts for the coupling of the orbital momenta to the spin. In order to include the term V_{SOC} in the KKR-formalism, we write eq. (4.11) in matrix notation

$$\begin{pmatrix} V_{\text{SOC}}^{\uparrow\uparrow}(r) & V_{\text{SOC}}^{\uparrow\downarrow}(r) \\ V_{\text{SOC}}^{\downarrow\uparrow}(r) & V_{\text{SOC}}^{\downarrow\downarrow}(r) \end{pmatrix} = \xi(r) \begin{pmatrix} (\mathbf{L} \cdot \mathbf{S})^{\uparrow\uparrow} & (\mathbf{L} \cdot \mathbf{S})^{\uparrow\downarrow} \\ (\mathbf{L} \cdot \mathbf{S})^{\downarrow\uparrow} & (\mathbf{L} \cdot \mathbf{S})^{\downarrow\downarrow} \end{pmatrix}, \tag{4.13}$$

where $\uparrow$ and $\downarrow$ denote the spin directions. In the following we will first make some remarks on the coupling constant $\xi(r)$ before evaluating the $\mathbf{L} \cdot \mathbf{S}$-matrix. The evaluation will be carried out in the basis of the real spherical harmonics

$$\begin{pmatrix} (\mathbf{L} \cdot \mathbf{S})_{LL'}^{\uparrow\uparrow} & (\mathbf{L} \cdot \mathbf{S})_{LL'}^{\uparrow\downarrow} \\ (\mathbf{L} \cdot \mathbf{S})_{LL'}^{\downarrow\uparrow} & (\mathbf{L} \cdot \mathbf{S})_{LL'}^{\downarrow\downarrow} \end{pmatrix} = \frac{1}{2} \left\langle Y_L(\hat{r}) \left| \begin{pmatrix} L_z & L_- \\ L_+ & -L_z \end{pmatrix} \right| Y_{L'}(\hat{r}) \right\rangle. \tag{4.14}$$

4.2.1 The spin-orbit coupling parameter $\xi(\mathbf{r})$

As already mentioned in the introduction, in principle the potential $V(\mathbf{r})$ entering in the spin-orbit coupling comprises the contributions of all other electrons as well as the nucleus. However, for a practical evaluation only the spherically symmetric component of the mean-field potential is taken. Both approximations lead to relatively good results since spin-orbit coupling is strong in the region close to the nucleus and negligibly weak in the interstitial region, where non-spherical terms appear (see figure 5.1 in chapter 5.

In order to calculate the derivative of the spherical potential $dV(r)/dr$ at r, the potential is split into two parts

$$V(r) = V(r)_{e-e} + V(r)_{Z-e}. \tag{4.15}$$

This is useful, since the contribution coming from the interaction of the nucleus with the electrons $V(r)_{Z-e}$ is known analytically

$$V_{Z-e}(r) = \begin{cases} -\frac{2Z}{r} & \text{for } r \geq R_{\text{N}} \\ -\frac{3Z}{R_{\text{N}}} + \frac{Zr^2}{R_{\text{N}}^3} & \text{for } r < R_{\text{N}}, \end{cases} \tag{4.16}$$

where R_{N} is the radius of the nucleus, approximated by [76]

$$R_{\text{N}} \approx 1.2 \cdot A^{1/3} \, 10^{-15} \text{Å} \approx \frac{1.2}{0.529177} \cdot A^{1/3} \, 10^{-5} \text{a.u.}. \tag{4.17}$$

Here, A is the total number of nucleons (protons and neutrons) contained inside the nucleus, which is assumed to have a homogeneous charge distribution.

The derivative of this contribution is hence

$$\frac{dV_{Z-e}(r)}{dr} = \begin{cases} \frac{2Z}{r^2} & \text{for } r \geq R_{\text{N}} \\ \frac{2Zr}{R_{\text{N}}^3} & \text{for } r < R_{\text{N}}. \end{cases} \tag{4.18}$$

The derivative of the electronic part has to be calculated numerically, and is simply calculated as the differential quotient at the position r

$$\frac{dV_{e-e}(r_i)}{dr} = \frac{1}{2}\left(\frac{V(r_{i+1}) - V(r_i)}{r_{i+1} - r_i} + \frac{V(r_i) - V(r_{i-1})}{r_i - r_{i-1}}\right), \tag{4.19}$$

where r_i are the radial points on which the potential is defined in the code. Inside the nuclear radius, the electronic part of the potential is much smaller than the first contribution, whereas it becomes important for increasing r.

In the evaluation of $\xi(r)$, the relativistic mass $M(r)$ has to be included, taking the mass enhancement close to the core into account. With the above considerations about the potential, $M(r)$ becomes

$$M(r) = m + \frac{1}{2c^2}\left(E - V_{e-e}(r) + 2\frac{Z}{r}\right). \tag{4.20}$$

Then, using atomic units, $e = 2m_e = \hbar = 1$, the spin-orbit coupling constant results in

$$\xi(r) = \frac{1}{2M(r)^2}\frac{1}{r}\frac{dV(r)}{dr}. \tag{4.21}$$

4.2.2 Evaluation of $\mathbf{L} \cdot \mathbf{S}$ in terms of real spherical harmonics

The term $\mathbf{L} \cdot \mathbf{S}$ can be decomposed according to

$$\mathbf{L} \cdot \mathbf{S} = L_x S_x + L_y S_y + L_z S_z. \tag{4.22}$$

Exploiting the definitions of the ladder operators

$$L_\pm = L_x \pm iL_y \tag{4.23}$$
$$S_\pm = S_x \pm iS_y, \tag{4.24}$$

the above decomposition can be written as

$$\mathbf{L} \cdot \mathbf{S} = \frac{1}{2}\left(L_+ S_- + L_- S_+\right) + L_z S_z. \tag{4.25}$$

The z-component of the spin operator measures the direction of the spin, thus

$$S_z \left|\uparrow\right\rangle = +\frac{1}{2}\left|\uparrow\right\rangle \qquad \text{and} \tag{4.26}$$

$$S_z \left|\downarrow\right\rangle = -\frac{1}{2}\left|\downarrow\right\rangle, \tag{4.27}$$

where $\left|\uparrow\right\rangle$ and $\left|\downarrow\right\rangle$ denote eigenstates of the spin operator with spin oriented in 'up'- and 'down'-direction, respectively.

On the contrary to S_z, the operators S_+ and S_- change the spin state according to

$$S_- \left|\uparrow\right\rangle = \left|\downarrow\right\rangle, \qquad S_- \left|\downarrow\right\rangle = 0, \tag{4.28}$$
$$S_+ \left|\downarrow\right\rangle = \left|\uparrow\right\rangle, \qquad S_+ \left|\uparrow\right\rangle = 0. \tag{4.29}$$

In matrix-form, equation (4.25) can then be rewritten as

$$
\begin{pmatrix} (\mathbf{L}\cdot\mathbf{S})^{\uparrow\uparrow} & (\mathbf{L}\cdot\mathbf{S})^{\uparrow\downarrow} \\ (\mathbf{L}\cdot\mathbf{S})^{\downarrow\uparrow} & (\mathbf{L}\cdot\mathbf{S})^{\downarrow\downarrow} \end{pmatrix} = \frac{1}{2}\left[\begin{pmatrix} 0 & 0 \\ L_+ & 0 \end{pmatrix} + \begin{pmatrix} 0 & L_- \\ 0 & 0 \end{pmatrix} \right] + \frac{1}{2}\begin{pmatrix} L_z & 0 \\ 0 & -L_z \end{pmatrix}
$$

$$
= \frac{1}{2}\begin{pmatrix} L_z & L_- \\ L_+ & -L_z \end{pmatrix}, \tag{4.30}
$$

where, in the basis set of spherical harmonics, L_+, L_- and L_z are matrices of the size $2l+1$. For the evaluation within the KKR-formalism we require the above matrix in the basis set of the real spherical harmonics denoted with $Y_L(\hat{r})$

$$
\begin{pmatrix} (\mathbf{L}\cdot\mathbf{S})^{\uparrow\uparrow}_{LL'} & (\mathbf{L}\cdot\mathbf{S})^{\uparrow\downarrow}_{LL'} \\ (\mathbf{L}\cdot\mathbf{S})^{\downarrow\uparrow}_{LL'} & (\mathbf{L}\cdot\mathbf{S})^{\downarrow\downarrow}_{LL'} \end{pmatrix} = \frac{1}{2}\left\langle Y_L(\hat{r}) \left| \begin{pmatrix} L_z & L_- \\ L_+ & -L_z \end{pmatrix} \right| Y_{L'}(\hat{r}) \right\rangle. \tag{4.31}
$$

However, we start with the evaluation of the $\mathbf{L}\cdot\mathbf{S}$-matrix in complex spherical harmonics $\mathcal{Y}_L(\hat{r}) = \mathcal{Y}_{lm}(\hat{r})$, since they are eigenfunctions to the L_z-operator and also simplify the application of the ladder operators.

The projection $\langle \mathcal{Y}_{lm}|L_z|\mathcal{Y}_{l'm'}\rangle$ is diagonal, i.e.

$$
\langle \mathcal{Y}_{lm}|L_z|\mathcal{Y}_{l'm'}\rangle = \delta_{ll'}\delta_{mm'}m, \tag{4.32}
$$

or, written in matrix notation,

$$
\langle \mathcal{Y}_{lm}|L_z|\mathcal{Y}_{lm'}\rangle = \begin{pmatrix} -l & 0 & \cdots & & & 0 \\ 0 & -l+1 & \cdots & & & \\ & & \ddots & & & \\ \vdots & & & 0 & & \vdots \\ & & & & \ddots & \\ & & \cdots & & l-1 & 0 \\ 0 & & \cdots & & 0 & l \end{pmatrix}. \tag{4.33}
$$

The ladder operators L_+ and L_- change m, thus the z-component of the angular momentum following

$$
L_\pm|\mathcal{Y}_{lm}\rangle = \sqrt{l(l+1)-m(m\pm1)}\,|\mathcal{Y}_{lm\pm1}\rangle, \tag{4.34}
$$

or,

$$
\langle \mathcal{Y}_{lm}|L_+|\mathcal{Y}_{lm'}\rangle = \begin{pmatrix} 0 & & & \cdots & & & 0 \\ \sqrt{2l} & 0 & & & & & \\ 0 & \sqrt{4l-2} & & & & & \\ & & \ddots & \ddots & & & \\ \vdots & & & \sqrt{l(l+1)} & & & \vdots \\ & & & & \ddots & & \\ & & & & \sqrt{4l-2} & 0 & \\ 0 & & & \cdots & & 0 & \sqrt{2l} & 0 \end{pmatrix} \tag{4.35}
$$

and

$$\langle \mathcal{Y}_{lm}|L_-|\mathcal{Y}_{lm'}\rangle = \begin{pmatrix} 0 & \sqrt{2l} & 0 & \cdots & & & & 0 \\ 0 & 0 & \sqrt{4l+2} & & & & & \\ & & & \ddots & & \ddots & & \\ \vdots & & & & \sqrt{l(l+1)} & & & \vdots \\ & & & & \ddots & & \ddots & \\ & & & & & & \sqrt{4l+2} & 0 \\ & & & & & & 0 & \sqrt{2l} \\ 0 & & & \cdots & & & & 0 \end{pmatrix}, \quad (4.36)$$

respectively.

In order to calculate the action of the three operators L_z, L_+ and L_- on the set of basis functions of real spherical harmonics, the transformation of complex spherical harmonics to real spherical harmonics is required. Choosing $m > 0$, it is

$$\begin{aligned} Y_{l,-m} &= \frac{i}{\sqrt{2}} \left[\mathcal{Y}_{l,-m} - (-1)^m \mathcal{Y}_{lm} \right] \\ Y_{l,0} &= \mathcal{Y}_{l,0} \\ Y_{l,m} &= \frac{1}{\sqrt{2}} \left[\mathcal{Y}_{l,-m} + (-1)^m \mathcal{Y}_{lm} \right], \quad m > 0. \end{aligned} \qquad (4.37)$$

The inverse transformation yielding the complex spherical harmonics as linear combinations of the real spherical harmonics is given by

$$\begin{aligned} \mathcal{Y}_{l,-m} &= \frac{1}{\sqrt{2}} \left[Y_{l,m} - iY_{l,-m} \right] \\ \mathcal{Y}_{l,0} &= Y_{l,0} \\ \mathcal{Y}_{l,m} &= \frac{(-1)^m}{\sqrt{2}} \left[Y_{l,m} + iY_{l,-m} \right], \quad m > 0. \end{aligned} \qquad (4.38)$$

A detailed derivation of the action of L_z and the ladder operators L_+ and L_- on the real spherical harmonics can be found in Appendix B.

Inserting the results of Appendix B into eq. (4.30) allows to obtain the spin-orbit coupling matrix $\mathbf{L} \cdot \mathbf{S}$ in the appropriate basis set of real spherical harmonics.

In principle, another much easier way can be chosen: The $\mathbf{L} \cdot \mathbf{S}$-matrix could be evaluated in the relativistic κ-μ-basis set defined as

$$\kappa = \begin{cases} l & \text{for} \quad j = l - \frac{1}{2} \\ -l-1 & \text{for} \quad j = l + \frac{1}{2} \end{cases} \quad \text{and} \qquad (4.39)$$

$$\mu = L_z + S_z, \qquad (4.40)$$

where $j(j+1)$ is the expectation value of the squared total angular momentum operator. In this basis set, the $\mathbf{L} \cdot \mathbf{S}$-matrix is diagonal [75], and can be subsequently transformed to the basis set of real spherical harmonics. However, in the presence of non-spherical potentials, the κ-μ-representation does not have an important advantage any more.

4.3 Spin-orbit coupling in KKR formalism

4.3.1 The spin-dependent Lippmann-Schwinger equation

Taking spin-orbit coupling into account, the wavefunction becomes spin-dependent $(\psi^\uparrow(\mathbf{r}; E), \psi^\downarrow(\mathbf{r}; E))^T$ and is calculated as a perturbation of the spherical solution of the system without spin-orbit coupling characterized by $\psi_0^\uparrow(\mathbf{r}; E)$, $\psi_0^\downarrow(\mathbf{r}; E)$, $G_0^{\uparrow\uparrow}(\mathbf{r}, \mathbf{r}'; E)$ and $G_0^{\downarrow\downarrow}(\mathbf{r}, \mathbf{r}'; E)$[1]. Therefore, the Lippmann-Schwinger equation

$$
\begin{pmatrix} \psi^\uparrow(\mathbf{r}) \\ \psi^\downarrow(\mathbf{r}) \end{pmatrix} = \begin{pmatrix} \psi_0^\uparrow(\mathbf{r}) \\ \psi_0^\downarrow(\mathbf{r}) \end{pmatrix}
$$
$$
+ \int d^3 r' \begin{pmatrix} G_0^{\uparrow\uparrow}(\mathbf{r}, \mathbf{r}') & 0 \\ 0 & G_0^{\downarrow\downarrow}(\mathbf{r}, \mathbf{r}') \end{pmatrix} \begin{pmatrix} V_{\text{SOC}}(\mathbf{r}')^{\uparrow\uparrow} & V_{\text{SOC}}(\mathbf{r}')^{\uparrow\downarrow} \\ V_{\text{SOC}}(\mathbf{r}')^{\downarrow\uparrow} & V_{\text{SOC}}(\mathbf{r}')^{\downarrow\downarrow} \end{pmatrix} \begin{pmatrix} \psi^\uparrow(\mathbf{r}') \\ \psi^\downarrow(\mathbf{r}') \end{pmatrix} \quad (4.41)
$$

is solved, which is identical to the solution of the full-potential problem, eq. (2.76), as described in chapter 2, section 2.4. To simplify the notation, the dependence of the wavefunction and the Green function on the energy E is omitted.

The perturbation potential is the spin-orbit correction term V_{SOC} as defined in eq. (4.11), which couples the two spin components. If full-potential calculations are performed, the non-spherical components $\Delta V_{\text{non-sph.}}^{\uparrow\uparrow}(\mathbf{r})$ and $\Delta V_{\text{non-sph.}}^{\downarrow\downarrow}(\mathbf{r})$ of the potential are added to the terms diagonal in spin space to the perturbation Hamiltonian. Therefore, V_{SOC} is replaced by ΔV in eq. (4.41) which is defined as

$$
\begin{pmatrix} \Delta V(\mathbf{r})^{\uparrow\uparrow} & \Delta V(\mathbf{r})^{\uparrow\downarrow} \\ \Delta V(\mathbf{r})^{\downarrow\uparrow} & \Delta V(\mathbf{r})^{\downarrow\downarrow} \end{pmatrix} =
$$
$$
\begin{pmatrix} V_{\text{SOC}}(\mathbf{r})^{\uparrow\uparrow} & V_{\text{SOC}}(\mathbf{r})^{\uparrow\downarrow} \\ V_{\text{SOC}}(\mathbf{r})^{\downarrow\uparrow} & V_{\text{SOC}}(\mathbf{r})^{\downarrow\downarrow} \end{pmatrix} + \begin{pmatrix} \Delta V_{\text{non-sph.}}^{\uparrow\uparrow}(\mathbf{r}) & 0 \\ 0 & \Delta V_{\text{non-sph.}}^{\downarrow\downarrow}(\mathbf{r}) \end{pmatrix}. \quad (4.42)
$$

For non-magnetic systems, the equality $\Delta V_{\text{non-sph.}}^{\uparrow\uparrow}(\mathbf{r}) = \Delta V_{\text{non-sph.}}^{\downarrow\downarrow}(\mathbf{r})$ holds. In the following, we assume that the incoming wave has only one spin component, thus

$$
\begin{pmatrix} \psi_0^\uparrow(\mathbf{r}) \\ \psi_0^\downarrow(\mathbf{r}) \end{pmatrix} = \begin{pmatrix} \psi_0^\uparrow(\mathbf{r}) \\ 0 \end{pmatrix} \quad (4.43)
$$

or

$$
\begin{pmatrix} \psi_0^\uparrow(\mathbf{r}) \\ \psi_0^\downarrow(\mathbf{r}) \end{pmatrix} = \begin{pmatrix} 0 \\ \psi_0^\downarrow(\mathbf{r}) \end{pmatrix}. \quad (4.44)
$$

The total wavefunctions, i.e. the solutions of the Lippmann-Schwinger equation (4.41) with incoming wave in up direction (4.43) will be denoted by

$$
\begin{pmatrix} \psi^{\uparrow\uparrow}(\mathbf{r}) \\ \psi^{\downarrow\uparrow}(\mathbf{r}) \end{pmatrix}, \quad (4.45)
$$

---

[1]In a non-magnetic system, $\psi_0^\uparrow(\mathbf{r}; E)$ and $\psi_0^\downarrow(\mathbf{r}; E)$ (or $G_0^{\uparrow\uparrow}(\mathbf{r}, \mathbf{r}'; E)$ and $G_0^{\downarrow\downarrow}(\mathbf{r}, \mathbf{r}'; E)$, respectively) are even the same.

and by

$$\begin{pmatrix} \psi^{\uparrow\downarrow}(\mathbf{r}) \\ \psi^{\downarrow\downarrow}(\mathbf{r}) \end{pmatrix} \tag{4.46}$$

for an incoming wave in down direction.

The two different choices lead to the two Lippmann-Schwinger equations

$$\begin{pmatrix} \psi^{\uparrow\uparrow}(\mathbf{r}) \\ \psi^{\downarrow\uparrow}(\mathbf{r}) \end{pmatrix} = \begin{pmatrix} \psi_0^{\uparrow}(\mathbf{r}) \\ 0 \end{pmatrix}$$
$$+ \int d^3r' \begin{pmatrix} G_0^{\uparrow\uparrow}(\mathbf{r},\mathbf{r}') & 0 \\ 0 & 0 \end{pmatrix} \begin{pmatrix} \Delta V^{\uparrow\uparrow}(\mathbf{r}') & \Delta V^{\uparrow\downarrow}(\mathbf{r}') \\ \Delta V^{\downarrow\uparrow}(\mathbf{r}') & \Delta V^{\downarrow\downarrow}(\mathbf{r}') \end{pmatrix} \begin{pmatrix} \psi^{\uparrow\uparrow}(\mathbf{r}') \\ \psi^{\downarrow\uparrow}(\mathbf{r}') \end{pmatrix} \tag{4.47}$$

and

$$\begin{pmatrix} \psi^{\uparrow\downarrow}(\mathbf{r}) \\ \psi^{\downarrow\downarrow}(\mathbf{r}) \end{pmatrix} = \begin{pmatrix} 0 \\ \psi_0^{\downarrow}(\mathbf{r}) \end{pmatrix}$$
$$+ \int d^3r' \begin{pmatrix} 0 & 0 \\ 0 & G_0^{\downarrow\downarrow}(\mathbf{r},\mathbf{r}') \end{pmatrix} \begin{pmatrix} \Delta V^{\uparrow\uparrow}(\mathbf{r}') & \Delta V^{\uparrow\downarrow}(\mathbf{r}') \\ \Delta V^{\downarrow\uparrow}(\mathbf{r}') & \Delta V^{\downarrow\downarrow}(\mathbf{r}') \end{pmatrix} \begin{pmatrix} \psi^{\uparrow\downarrow}(\mathbf{r}') \\ \psi^{\downarrow\downarrow}(\mathbf{r}') \end{pmatrix}. \tag{4.48}$$

The above two equations are not only valid for the wavefunctions $(\psi^{\uparrow\uparrow}(\mathbf{r}), \psi^{\downarrow\uparrow}(\mathbf{r}))^T$ and $(\psi^{\uparrow\downarrow}(\mathbf{r}), \psi^{\downarrow\downarrow}(\mathbf{r}))^T$, but can be analogously formulated for the basis functions, the regular solutions of the Schrödinger equation $R_L^{\uparrow n}(\mathbf{r})$ and $R_L^{\downarrow n}(\mathbf{r})$.

Merging the two equations (4.47) and (4.48) into one matrix equation and replacing the full wavefunctions with the regular wavefunctions as explained above, we obtain the full Lippmann-Schwinger equation

$$\begin{pmatrix} R_L^{\uparrow\uparrow}(\mathbf{r}) & R_L^{\uparrow\downarrow}(\mathbf{r}) \\ R_L^{\downarrow\uparrow}(\mathbf{r}) & R_L^{\downarrow\downarrow}(\mathbf{r}) \end{pmatrix} = \begin{pmatrix} R_L^{0,\uparrow}(\mathbf{r}) & 0 \\ 0 & R_L^{0,\downarrow}(\mathbf{r}) \end{pmatrix}$$
$$+ \int d^3r' \begin{pmatrix} G_0^{\uparrow\uparrow}(\mathbf{r},\mathbf{r}') & 0 \\ 0 & G_0^{\downarrow\downarrow}(\mathbf{r},\mathbf{r}') \end{pmatrix} \begin{pmatrix} \Delta V^{\uparrow\uparrow}(\mathbf{r}') & \Delta V^{\uparrow\downarrow}(\mathbf{r}') \\ \Delta V^{\downarrow\uparrow}(\mathbf{r}') & \Delta V^{\downarrow\downarrow}(\mathbf{r}') \end{pmatrix} \begin{pmatrix} R_L^{\uparrow\uparrow}(\mathbf{r}') & R_L^{\uparrow\downarrow}(\mathbf{r}') \\ R_L^{\downarrow\uparrow}(\mathbf{r}') & R_L^{\downarrow\downarrow}(\mathbf{r}') \end{pmatrix} \tag{4.49}$$

for the regular wavefunctions.

In order to solve this equation, it is helpful to expand the variables $G_0^{\sigma\sigma}(\mathbf{r},\mathbf{r}')$, $\Delta V^{\sigma\sigma'}(\mathbf{r})$ and $R_L^{\sigma\sigma'}(\mathbf{r})$ in terms of spherical harmonics $Y_L(\hat{r})$[2]

$$G_0^{\sigma\sigma}(\mathbf{r},\mathbf{r}') = \sum_{L'} Y_{L'}(\hat{r}) G_{0,l'}^{\sigma\sigma}(r,r') Y_{L'}(\hat{r}') \tag{4.50}$$

$$\Delta V^{\sigma\sigma'}(\mathbf{r}) = \sum_L \Delta V^{\sigma\sigma'}(r) Y_L(\hat{r}) \tag{4.51}$$

$$R_L^{\sigma\sigma'}(\mathbf{r}) = \sum_{L'} R_{L'L}^{\sigma\sigma'}(r) Y_{L'}(\hat{r}) \qquad \text{and} \tag{4.52}$$

$$R_L^{0,\uparrow(\downarrow)}(\mathbf{r}) = \sum_{L'} R_{L'L}^{0,\uparrow(\downarrow)}(r) Y_{L'} \delta_{L'L}(\hat{r}). \tag{4.53}$$

---

[2] As we start from the spherical solution of the host system, $G_{0,L'}^{\sigma\sigma}(r,r') = G_{0,l'}^{\sigma\sigma}(r,r')$ and the regular wavefunctions $R_{L'L}^{0,\uparrow(\downarrow)}(r)$ are diagonal in L.

Inserting the above expressions in the Lippmann-Schwinger equation (4.49), a system of coupled equations is obtained. In a first step this yields

$$
\sum_{L'} Y_{L'}(\hat{r}) \begin{pmatrix} R_{L'L}^{\uparrow\uparrow}(r) & R_{L'L}^{\uparrow\downarrow}(r) \\ R_{L'L}^{\downarrow\uparrow}(r) & R_{L'L}^{\downarrow\downarrow}(r) \end{pmatrix} = \sum_{L'} Y_{L'}(\hat{r}) \left[\begin{pmatrix} R_{L'L}^{0,\uparrow}(r)\delta_{L'L} & 0 \\ 0 & R_{L'L}^{0,\downarrow}(r)\delta_{L'L} \end{pmatrix} + \right.
$$
$$
\int d^3r' \begin{pmatrix} G_{0,l'}^{\uparrow\uparrow}(r,r') & 0 \\ 0 & G_{0,l'}^{\downarrow\downarrow}(r,r') \end{pmatrix} Y_{L'}(\hat{r}') \sum_{L''} Y_{L''}(\hat{r}') \begin{pmatrix} \Delta V_{L''}^{\uparrow\uparrow}(r') & \Delta V_{L''}^{\uparrow\downarrow}(r') \\ \Delta V_{L''}^{\downarrow\uparrow}(r') & \Delta V_{L''}^{\downarrow\downarrow}(r') \end{pmatrix}
$$
$$
\left. \sum_{L'''} Y_{L'''}(\hat{r}') \begin{pmatrix} R_{L'''L}^{\uparrow\uparrow}(r') & R_{L'''L}^{\uparrow\downarrow}(r') \\ R_{L'''L}^{\downarrow\uparrow}(r') & R_{L'''L}^{\downarrow\downarrow}(r') \end{pmatrix} \right]. \quad (4.54)
$$

The linear independence of the spherical harmonics $Y_{L'}(\hat{r})$ allows to omit the summation over L', and the above equation can be simplified to

$$
\begin{pmatrix} R_{L'L}^{\uparrow\uparrow}(r) & R_{L'L}^{\uparrow\downarrow}(r) \\ R_{L'L}^{\downarrow\uparrow}(r) & R_{L'L}^{\downarrow\downarrow}(r) \end{pmatrix} = \begin{pmatrix} R_{L'L}^{0,\uparrow}(r)\delta_{L'L} & 0 \\ 0 & R_{L'L}^{0,\downarrow}(r)\delta_{L'L} \end{pmatrix}
$$
$$
+ \sum_{L''L'''} \int d\Omega' Y_{L'}(\hat{r}') Y_{L''}(\hat{r}') Y_{L'''}(\hat{r}') \int r'^2 dr'
$$
$$
\begin{pmatrix} G_{0,l'}^{\uparrow\uparrow}(r,r') & 0 \\ 0 & G_{0,l'}^{\downarrow\downarrow}(r,r') \end{pmatrix} \begin{pmatrix} \Delta V_{L''}^{\uparrow\uparrow}(r') & \Delta V_{L''}^{\uparrow\downarrow}(r') \\ \Delta V_{L''}^{\downarrow\uparrow}(r') & \Delta V_{L''}^{\downarrow\downarrow}(r') \end{pmatrix} \begin{pmatrix} R_{L'''L}^{\uparrow\uparrow}(r') & R_{L'''L}^{\uparrow\downarrow}(r') \\ R_{L'''L}^{\downarrow\uparrow}(r') & R_{L'''L}^{\downarrow\downarrow}(r') \end{pmatrix}.
$$
$$
(4.55)
$$

The integral over the angular part $\int d\Omega' \ Y_{L'}(\hat{r}')Y_{L''}(\hat{r}')Y_{L'''}(\hat{r}')$ can be identified with the Gaunt coefficients $C_{L'L'''L''}$ (see eq. (2.49)). Defining the double-indexed perturbation Hamiltonian as

$$
\sum_{L''} C_{L'L'''L''} \Delta V_{L''}^{\sigma\sigma'}(r') = \Delta V_{L'L'''}^{\sigma\sigma'}(r') , \quad (4.56)
$$

finally results in

$$
\begin{pmatrix} R_{L'L}^{\uparrow\uparrow}(r) & R_{L'L}^{\uparrow\downarrow}(r) \\ R_{L'L}^{\downarrow\uparrow}(r) & R_{L'L}^{\downarrow\downarrow}(r) \end{pmatrix} = \begin{pmatrix} R_{L'L}^{0,\uparrow}(r)\delta_{L'L} & 0 \\ 0 & R_{L'L}^{0,\downarrow}(r)\delta_{L'L} \end{pmatrix}
$$
$$
+ \int r'^2 dr' \begin{pmatrix} G_{0,l'}^{\uparrow\uparrow}(r,r') & 0 \\ 0 & G_{0,l'}^{\downarrow\downarrow}(r,r') \end{pmatrix} \quad (4.57)
$$
$$
\sum_{L'''} \begin{pmatrix} \Delta V_{L'L'''}^{\uparrow\uparrow}(r') & \Delta V_{L'L'''}^{\uparrow\downarrow}(r') \\ \Delta V_{L'L'''}^{\downarrow\uparrow}(r') & \Delta V_{L'L'''}^{\downarrow\downarrow}(r') \end{pmatrix} \begin{pmatrix} R_{L'''L}^{\uparrow\uparrow}(r') & R_{L'''L}^{\uparrow\downarrow}(r') \\ R_{L'''L}^{\downarrow\uparrow}(r') & R_{L'''L}^{\downarrow\downarrow}(r') \end{pmatrix}.
$$

The above equation comprises only a one-dimensional integral over r' instead of the three-dimensional integral in eq. (4.49) and is solved iteratively. The procedure followed in this work will be sketched in the next paragraph.

Solution of the Lippmann-Schwinger equation for the regular wavefunctions

For the solution of the Lippmann-Schwinger equation (4.57) for the regular wavefunctions,

the radial Green function of the spherical potential $G_{0,l}^{\uparrow\uparrow(\downarrow\downarrow)}(r,r')$ is expressed in terms of the known radial solutions $R_l^0(r)$ and $H_l^0(r)$

$$G_{0,l}^{\uparrow\uparrow(\downarrow\downarrow)}(r,r') = -i\sqrt{E}R_l^{0,\uparrow(\downarrow)}(r_<)H_l^{0,\uparrow(\downarrow)}(r_>) \tag{4.58}$$

with

$$r_> = \max(r,r') \quad \text{and} \quad r_< = \min(r,r'). \tag{4.59}$$

This leads to a decomposition of the regular wavefunctions

$$
\begin{pmatrix} R_{L'L}^{\uparrow\uparrow}(r) & R_{L'L}^{\uparrow\downarrow}(r) \\ R_{L'L}^{\downarrow\uparrow}(r) & R_{L'L}^{\downarrow\downarrow}(r) \end{pmatrix} = \begin{pmatrix} A_{L'L}^{\uparrow\uparrow}(r) & A_{L'L}^{\uparrow\downarrow}(r) \\ A_{L'L}^{\downarrow\uparrow}(r) & A_{L'L}^{\downarrow\downarrow}(r) \end{pmatrix} \begin{pmatrix} R_{L'L}^{0,\uparrow}(r)\delta_{L'L} & 0 \\ 0 & R_{L'L}^{0,\downarrow}(r)\delta_{L'L} \end{pmatrix}
$$
$$
+ \begin{pmatrix} B_{L'L}^{\uparrow\uparrow}(r) & B_{L'L}^{\uparrow\downarrow}(r) \\ B_{L'L}^{\downarrow\uparrow}(r) & B_{L'L}^{\downarrow\downarrow}(r) \end{pmatrix} \begin{pmatrix} H_{L'L}^{0,\uparrow}(r)\delta_{L'L} & 0 \\ 0 & H_{L'L}^{0,\downarrow}(r)\delta_{L'L} \end{pmatrix} \tag{4.60}
$$

with

$$
\begin{pmatrix} A_{L'L}^{\uparrow\uparrow}(r) & A_{L'L}^{\uparrow\downarrow}(r) \\ A_{L'L}^{\downarrow\uparrow}(r) & A_{L'L}^{\downarrow\downarrow}(r) \end{pmatrix} = \begin{pmatrix} \delta_{L'L} & 0 \\ 0 & \delta_{L'L} \end{pmatrix} - i\sqrt{E} \int_r^{r_{\max}} r'^2 dr' \begin{pmatrix} H_{L'L}^{0,\uparrow}(r')\delta_{L'L} & 0 \\ 0 & H_{L'L}^{0,\downarrow}(r')\delta_{L'L} \end{pmatrix}
$$
$$
\sum_{L'''} \begin{pmatrix} \Delta V_{L'L'''}^{\uparrow\uparrow}(r') & \Delta V_{L'L'''}^{\uparrow\downarrow}(r') \\ \Delta V_{L'L'''}^{\downarrow\uparrow}(r') & \Delta V_{L'L'''}^{\downarrow\downarrow}(r') \end{pmatrix} \begin{pmatrix} R_{L'''L}^{\uparrow\uparrow}(r') & R_{L'''L}^{\uparrow\downarrow}(r') \\ R_{L'''L}^{\downarrow\uparrow}(r') & R_{L'''L}^{\downarrow\downarrow}(r') \end{pmatrix} \tag{4.61}
$$

and

$$
\begin{pmatrix} B_{L'L}^{\uparrow\uparrow}(r) & B_{L'L}^{\uparrow\downarrow}(r) \\ B_{L'L}^{\downarrow\uparrow}(r) & B_{L'L}^{\downarrow\downarrow}(r) \end{pmatrix} = -i\sqrt{E} \int_0^r r'^2 dr' \begin{pmatrix} R_{L'L}^{0,\uparrow}(r')\delta_{L'L} & 0 \\ 0 & R_{L'L}^{0,\downarrow}(r')\delta_{L'L} \end{pmatrix} \cdot
$$
$$
\sum_{L'''} \begin{pmatrix} \Delta V_{L'L'''}^{\uparrow\uparrow}(r') & \Delta V_{L'L'''}^{\uparrow\downarrow}(r') \\ \Delta V_{L'L'''}^{\downarrow\uparrow}(r') & \Delta V_{L'L'''}^{\downarrow\downarrow}(r') \end{pmatrix} \begin{pmatrix} R_{L'''L}^{\uparrow\uparrow}(r') & R_{L'''L}^{\uparrow\downarrow}(r') \\ R_{L'''L}^{\downarrow\uparrow}(r') & R_{L'''L}^{\downarrow\downarrow}(r') \end{pmatrix}. \tag{4.62}
$$

Equations (4.60), (4.61) and (4.62) can now be solved iteratively starting from the spherical solution without spin-orbit coupling

$$
\begin{pmatrix} R_{L'L}^{\uparrow\uparrow}(r) & R_{L'L}^{\uparrow\downarrow}(r) \\ R_{L'L}^{\downarrow\uparrow}(r) & R_{L'L}^{\downarrow\downarrow}(r) \end{pmatrix} = \begin{pmatrix} R_{L'L}^{0,\uparrow}(r)\delta_{L'L} & 0 \\ 0 & R_{L'L}^{0,\downarrow}(r)\delta_{L'L} \end{pmatrix}. \tag{4.63}
$$

The iteration scheme described above is the so-called Fredholm-method [77]. Another way to solve the equations yielding the same results makes use of the Volterra method [66].

Relation to the Δt-matrix Once the matrices **A** and **B** are known, the correction to the atomic scattering matrix $\Delta t^{\sigma\sigma'}$ can be calculated. The current paragraph deals with establishing a relation of the Δt-matrix to the matrices **A** and **B**.

Outside the range of the potential, for $r > r_{\max}$, the second term of equation (4.61) becomes zero

$$
\begin{pmatrix} A_{L'L}^{\uparrow\uparrow}(r) & A_{L'L}^{\uparrow\downarrow}(r) \\ A_{L'L}^{\downarrow\uparrow}(r) & A_{L'L}^{\downarrow\downarrow}(r) \end{pmatrix} = \begin{pmatrix} \delta_{L'L} & 0 \\ 0 & \delta_{L'L} \end{pmatrix} \tag{4.64}
$$

and thus (4.60) reduces to

$$\begin{pmatrix} R^{\uparrow\uparrow}_{L'L}(r) & R^{\uparrow\downarrow}_{L'L}(r) \\ R^{\downarrow\uparrow}_{L'L}(r) & R^{\downarrow\downarrow}_{L'L}(r) \end{pmatrix} = \begin{pmatrix} R^{0,\uparrow}_{L'L}(r)\delta_{L'L} & 0 \\ 0 & R^{0,\downarrow}_{L'L}(r)\delta_{L'L} \end{pmatrix}$$
$$+ \begin{pmatrix} B^{\uparrow\uparrow}_{L'L}(S) & B^{\uparrow\downarrow}_{L'L}(S) \\ B^{\downarrow\uparrow}_{L'L}(S) & B^{\downarrow\downarrow}_{L'L}(S) \end{pmatrix} \begin{pmatrix} H^{0,\uparrow}_{L'L}(r)\delta_{L'L} & 0 \\ 0 & H^{0,\downarrow}_{L'L}(r)\delta_{L'L} \end{pmatrix}. \quad (4.65)$$

A comparison of the last equation with the definition of the Δt-matrix (see eq. (2.37) for the ASA or eq. (2.73) for the case of a full potential), Δt can be identified as

$$\begin{pmatrix} \Delta t^{\uparrow\uparrow}_{L'L}(E) & \Delta t^{\uparrow\downarrow}_{L'L}(E) \\ \Delta t^{\downarrow\uparrow}_{L'L}(E) & \Delta t^{\downarrow\downarrow}_{L'L}(E) \end{pmatrix} = \frac{i}{\sqrt{E}} \begin{pmatrix} B^{\uparrow\uparrow}_{L'L}(S) & B^{\uparrow\downarrow}_{L'L}(S) \\ B^{\downarrow\uparrow}_{L'L}(S) & B^{\downarrow\downarrow}_{L'L}(S) \end{pmatrix}. \quad (4.66)$$

Hence, according to eq. (4.62), Δt can be explicitly calculated as

$$\begin{pmatrix} \Delta t^{\uparrow\uparrow}_{L'L}(E) & \Delta t^{\uparrow\downarrow}_{L'L}(E) \\ \Delta t^{\downarrow\uparrow}_{L'L}(E) & \Delta t^{\downarrow\downarrow}_{L'L}(E) \end{pmatrix} = \int_0^{r_{max}} r'^2 dr' \begin{pmatrix} R^{0,\uparrow}_{L'L}(r')\delta_{L'L} & 0 \\ 0 & R^{0,\downarrow}_{L'L}(r')\delta_{L'L} \end{pmatrix}$$
$$\sum_{L'''} \begin{pmatrix} \Delta V^{\uparrow\uparrow}_{L'L'''}(r') & \Delta V^{\uparrow\downarrow}_{L'L'''}(r') \\ \Delta V^{\downarrow\uparrow}_{L'L'''}(r') & \Delta V^{\downarrow\downarrow}_{L'L'''}(r') \end{pmatrix} \begin{pmatrix} R^{\uparrow\uparrow}_{L'''L}(r') & R^{\uparrow\downarrow}_{L'''L}(r') \\ R^{\downarrow\uparrow}_{L'''L}(r') & R^{\downarrow\downarrow}_{L'''L}(r') \end{pmatrix}. \quad (4.67)$$

4.3.2 The spinor wavefunctions including spin-orbit coupling

In the presence of spin-orbit interaction, the **k**-dependent wavefunction as defined in eq. (3.32) has to be generalized to

$$\begin{pmatrix} \psi^{\uparrow}_{\mathbf{k}}(\mathbf{r} + \mathbf{R}^n; E) \\ \psi^{\downarrow}_{\mathbf{k}}(\mathbf{r} + \mathbf{R}^n; E) \end{pmatrix} = \sum_L c^{\uparrow n}_{\mathbf{k}L} \begin{pmatrix} R^{\uparrow\uparrow n}_L(\mathbf{r}; E) \\ R^{\downarrow\uparrow n}_L(\mathbf{r}; E) \end{pmatrix} + \sum_L c^{\downarrow n}_{\mathbf{k}L} \begin{pmatrix} R^{\uparrow\downarrow n}_L(\mathbf{r}; E) \\ R^{\downarrow\downarrow n}_L(\mathbf{r}; E) \end{pmatrix}. \quad (4.68)$$

Hence, it becomes a spinor with the two components $\psi^{\uparrow}_{\mathbf{k}}(\mathbf{r} + \mathbf{R}^n; E)$ and $\psi^{\downarrow}_{\mathbf{k}}(\mathbf{r} + \mathbf{R}^n; E)$, which are referred to as spin-up and spin-down components.
In the above expansion (4.68), the radial wavefunction

$$R^{\uparrow n}_L(\mathbf{r}; E) = \begin{pmatrix} R^{\uparrow\uparrow n}_L(\mathbf{r}; E) \\ R^{\downarrow\uparrow n}_L(\mathbf{r}; E) \end{pmatrix} \quad (4.69)$$

denotes the spinor wavefunction of an incoming wave only containing a spin up component

$$\begin{pmatrix} j_L(\mathbf{r}; E) \\ 0 \end{pmatrix} = j_L(\sqrt{E}r)Y_L(\hat{r}) \begin{pmatrix} 1 \\ 0 \end{pmatrix}, \quad (4.70)$$

whereas

$$R^{\downarrow n}_L(\mathbf{r}; E) = \begin{pmatrix} R^{\uparrow\downarrow n}_L(\mathbf{r}; E) \\ R^{\downarrow\downarrow n}_L(\mathbf{r}; E) \end{pmatrix} \quad (4.71)$$

is the spinor wavefunction of an incoming wave only comprising a spin down component, respectively

$$\begin{pmatrix} 0 \\ j_L(\mathbf{r}; E) \end{pmatrix} = j_L(\sqrt{E}r)Y_L(\hat{r})\begin{pmatrix} 0 \\ 1 \end{pmatrix}. \tag{4.72}$$

In eq. (4.68), the second spin index denotes the boundary condition, thus the spin state of the incoming wave while the first index refers to the scattered, outgoing wave.
Expanding the regular wavefunctions $R_L^{\sigma\sigma'n}(\mathbf{r}; E)$ in their orbital components, equation (4.68) becomes

$$\begin{pmatrix} \psi_{\mathbf{k}}^{\uparrow}(\mathbf{r} + \mathbf{R}^n; E) \\ \psi_{\mathbf{k}}^{\downarrow}(\mathbf{r} + \mathbf{R}^n; E) \end{pmatrix} = \sum_{LL'}\left[c_{\mathbf{k}L}^{\uparrow n}\begin{pmatrix} R_{L'L}^{\uparrow\uparrow n}(\mathbf{r}; E) \\ R_{L'L}^{\downarrow\uparrow n}(\mathbf{r}; E) \end{pmatrix} + c_{\mathbf{k}L}^{\downarrow n}\begin{pmatrix} R_{L'L}^{\uparrow\downarrow n}(\mathbf{r}; E) \\ R_{L'L}^{\downarrow\downarrow n}(\mathbf{r}; E) \end{pmatrix}\right]Y_{L'}(\hat{r}) \tag{4.73}$$

or, rewriting the wavefunctions in matrices

$$\begin{pmatrix} \psi_{\mathbf{k}}^{\uparrow}(\mathbf{r} + \mathbf{R}^n; E) \\ \psi_{\mathbf{k}}^{\downarrow}(\mathbf{r} + \mathbf{R}^n; E) \end{pmatrix} = \sum_{LL'}\left[\begin{pmatrix} R_{L'L}^{\uparrow\uparrow n}(\mathbf{r}; E) & R_{L'L}^{\uparrow\downarrow n}(\mathbf{r}; E) \\ R_{L'L}^{\downarrow\uparrow n}(\mathbf{r}; E) & R_{L'L}^{\downarrow\downarrow n}(\mathbf{r}; E) \end{pmatrix}\begin{pmatrix} c_{\mathbf{k}L}^{\uparrow n} \\ c_{\mathbf{k}L}^{\downarrow n} \end{pmatrix}\right]Y_{L'}(\hat{r}). \tag{4.74}$$

Again, as for the spin index in eq. (4.68), the second index L indicates the boundary condition, thus the orbital momentum of the incoming wave while the first index L' refers to the scattered, outgoing wave.

4.4 The coefficients $c_{\mathbf{k}L}^{n,\uparrow}$ and $c_{\mathbf{k}L}^{n,\downarrow}$

In order to evaluate the full, spin-dependent Bloch wavefunction including spin-orbit coupling

$$\begin{pmatrix} \psi_{\mathbf{k}}^{\uparrow}(\mathbf{r}) \\ \psi_{\mathbf{k}}^{\downarrow}(\mathbf{r}) \end{pmatrix} = \sum_L c_{\mathbf{k}L}^{\uparrow n}\begin{pmatrix} R_L^{\uparrow\uparrow n}(\mathbf{r}) \\ R_L^{\downarrow\uparrow n}(\mathbf{r}) \end{pmatrix} + \sum_L c_{\mathbf{k}L}^{\downarrow n}\begin{pmatrix} R_L^{\uparrow\downarrow n}(\mathbf{r}) \\ R_L^{\downarrow\downarrow n}(\mathbf{r}) \end{pmatrix}, \tag{4.75}$$

not only the regular wavefunctions whose calculation has been described in the previous section, but also the coefficients $c_{\mathbf{k}L}^{n,\uparrow}$ and $c_{\mathbf{k}L}^{n,\downarrow}$ are needed. They can be evaluated using the Lippmann-Schwinger equation for the full wavefunction (4.41). As reference system, we choose in analogy to the derivation of the coefficients without spin-orbit coupling in section 3.1.3 the system of repulsive potential defined in section 2.5. Under these conditions, the Lippmann-Schwinger equation is homogeneous and reduces to

$$\begin{pmatrix} \psi^{\uparrow}(\mathbf{r}) \\ \psi^{\downarrow}(\mathbf{r}) \end{pmatrix} = \int d^3r'\begin{pmatrix} G_0^{\uparrow\uparrow}(\mathbf{r}, \mathbf{r}') & 0 \\ 0 & G_0^{\downarrow\downarrow}(\mathbf{r}, \mathbf{r}') \end{pmatrix}\begin{pmatrix} \Delta V^{\uparrow\uparrow}(\mathbf{r}') & \Delta V^{\uparrow\downarrow}(\mathbf{r}') \\ \Delta V^{\downarrow\uparrow}(\mathbf{r}') & \Delta V^{\downarrow\downarrow}(\mathbf{r}') \end{pmatrix}\begin{pmatrix} \psi^{\uparrow}(\mathbf{r}') \\ \psi^{\downarrow}(\mathbf{r}') \end{pmatrix}, \tag{4.76}$$

or, using expansions (4.68) and (4.50),

$$
\sum_{LL'} \left[c_{\mathbf{k}L'}^{\uparrow n} \begin{pmatrix} R_{LL'}^{\uparrow\uparrow n}(\mathbf{r}) \\ R_{LL'}^{\downarrow\uparrow n}(\mathbf{r}) \end{pmatrix} + c_{\mathbf{k}L'}^{\downarrow n} \begin{pmatrix} R_{LL'}^{\uparrow\downarrow n}(\mathbf{r}) \\ R_{LL'}^{\downarrow\downarrow n}(\mathbf{r}) \end{pmatrix} \right] Y_L(\hat{r}) = \sum_L Y_L(\hat{r}) \Bigg[
$$

$$
\int d^3 r' \begin{pmatrix} G_{0,l}^{\uparrow\uparrow}(r,r') & 0 \\ 0 & G_{0,l}^{\downarrow\downarrow}(r,r') \end{pmatrix} Y_L(\hat{r}') \sum_{L'} Y_{L'}(\hat{r}') \begin{pmatrix} \Delta V_{L'}^{\uparrow\uparrow}(r') & \Delta V_{L'}^{\uparrow\downarrow}(r') \\ \Delta V_{L'}^{\downarrow\uparrow}(r') & \Delta V_{L'}^{\downarrow\downarrow}(r') \end{pmatrix}
$$

$$
\sum_{L''L'''} \left[c_{\mathbf{k}L''}^{\uparrow n} \begin{pmatrix} R_{L'''L''}^{\uparrow\uparrow n}(r') \\ R_{L'''L''}^{\downarrow\uparrow n}(r') \end{pmatrix} + c_{\mathbf{k}L''}^{\downarrow n} \begin{pmatrix} R_{L'''L''}^{\uparrow\downarrow n}(r') \\ R_{L'''L''}^{\downarrow\downarrow n}(r') \end{pmatrix} \right] Y_{L'''}(\hat{r}')
$$

$$
+ \int d^3 r' \sum_{L''''} \begin{pmatrix} R_l^{\uparrow}(r) G_{0,LL''''}^{\uparrow\uparrow} R_{l''''}^{\uparrow}(r') & 0 \\ 0 & R_l^{\downarrow}(r) G_{0,LL''''}^{\downarrow\downarrow} R_{l''''}^{\downarrow}(r') \end{pmatrix} Y_{L''''}(\hat{r}')
$$

$$
\sum_{L'} Y_{L'}(\hat{r}') \begin{pmatrix} \Delta V_{L'}^{\uparrow\uparrow}(r') & \Delta V_{L'}^{\uparrow\downarrow}(r') \\ \Delta V_{L'}^{\downarrow\uparrow}(r') & \Delta V_{L'}^{\downarrow\downarrow}(r') \end{pmatrix}
$$

$$
\sum_{L''L'''} \left[c_{\mathbf{k}L''}^{\uparrow n} \begin{pmatrix} R_{L'''L''}^{\uparrow\uparrow n}(r') \\ R_{L'''L''}^{\downarrow\uparrow n}(r') \end{pmatrix} + c_{\mathbf{k}L''}^{\downarrow n} \begin{pmatrix} R_{L'''L''}^{\uparrow\downarrow n}(r') \\ R_{L'''L''}^{\downarrow\downarrow n}(r') \end{pmatrix} \right] Y_{L'''}(\hat{r}') \Bigg].
$$

(4.77)

Here, the first term on the right side results from the single-site scattering, whereas the second term is the back-scattering term. $G_{LL'}^{\sigma\sigma'}$ is the structural Green function of the reference system, which does not imply spin-orbit coupling. As in the derivation in section 4.3.1, the summation over L can be omitted. For each summand the integral over the spherical coordinates results in the Gaunt coefficients, and with the transformation of the spin-orbit Hamiltonian according to (4.56), the above equation yields

$$
\sum_{L'} \left[c_{\mathbf{k}L'}^{\uparrow n} \begin{pmatrix} R_{LL'}^{\uparrow\uparrow n}(\mathbf{r}) \\ R_{LL'}^{\downarrow\uparrow n}(\mathbf{r}) \end{pmatrix} + c_{\mathbf{k}L'}^{\downarrow n} \begin{pmatrix} R_{LL'}^{\uparrow\downarrow n}(\mathbf{r}) \\ R_{LL'}^{\downarrow\downarrow n}(\mathbf{r}) \end{pmatrix} \right] =
$$

$$
\int r'^2 dr' \begin{pmatrix} G_{0,l}^{\uparrow\uparrow}(r,r') & 0 \\ 0 & G_{0,l}^{\downarrow\downarrow}(r,r') \end{pmatrix} \sum_{L'''L''} \begin{pmatrix} \Delta V_{LL'''}^{\uparrow\uparrow}(r') & \Delta V_{LL'''}^{\uparrow\downarrow}(r') \\ \Delta V_{LL'''}^{\downarrow\uparrow}(r') & \Delta V_{LL'''}^{\downarrow\downarrow}(r') \end{pmatrix}
$$

$$
\left[c_{\mathbf{k}L''}^{\uparrow n} \begin{pmatrix} R_{L'''L''}^{\uparrow\uparrow n}(r') \\ R_{L'''L''}^{\downarrow\uparrow n}(r') \end{pmatrix} + c_{\mathbf{k}L''}^{\downarrow n} \begin{pmatrix} R_{L'''L''}^{\uparrow\downarrow n}(r') \\ R_{L'''L''}^{\downarrow\downarrow n}(r') \end{pmatrix} \right]
$$

(4.78)

$$
+ \int r'^2 dr' \sum_{L''''} \begin{pmatrix} R_l^{0\uparrow}(r) G_{0,LL''''}^{\uparrow\uparrow} R_{l''''}^{0\uparrow}(r') & 0 \\ 0 & R_l^{0\downarrow}(r) G_{LL''''}^{\downarrow\downarrow} R_{l''''}^{0\downarrow}(r') \end{pmatrix}
$$

$$
\sum_{L''L'''} \begin{pmatrix} \Delta V_{L''''L'''}^{\uparrow\uparrow}(r') & \Delta V_{L''''L'''}^{\uparrow\downarrow}(r') \\ \Delta V_{L''''L'''}^{\downarrow\uparrow}(r') & \Delta V_{L''''L'''}^{\downarrow\downarrow}(r') \end{pmatrix}
$$

$$
\left[c_{\mathbf{k}L''}^{\uparrow n} \begin{pmatrix} R_{L'''L''}^{\uparrow\uparrow n}(r') \\ R_{L'''L''}^{\downarrow\uparrow n}(r') \end{pmatrix} + c_{\mathbf{k}L''}^{\downarrow n} \begin{pmatrix} R_{L'''L''}^{\uparrow\downarrow n}(r') \\ R_{L'''L''}^{\downarrow\downarrow n}(r') \end{pmatrix} \right].
$$

The first term on the right side can be summed up with the left side, since the regular solutions $\left(R_{LL'}^{n,\uparrow\uparrow(\uparrow\downarrow)}(r), R_{LL'}^{n,\downarrow\uparrow(\downarrow\downarrow)}(r) \right)^T$ fulfill the Lippmann-Schwinger equations (see eq. (4.57))

$$
\begin{pmatrix} R_{L'L}^{\uparrow\uparrow}(r) \\ R_{L'L}^{\downarrow\uparrow}(r) \end{pmatrix} = \begin{pmatrix} R_{L'L}^{0,\uparrow}(r)\delta_{L'L} \\ 0 \end{pmatrix} + \int r'^2 dr' \begin{pmatrix} G_{0,l'}^{\uparrow\uparrow}(r,r') & 0 \\ 0 & G_{0,l'}^{\downarrow\downarrow}(r,r') \end{pmatrix} \cdot
$$
$$
\sum_{L'''} \begin{pmatrix} \Delta V_{L'L'''}^{\uparrow\uparrow}(r') & \Delta V_{L'L'''}^{\uparrow\downarrow}(r') \\ \Delta V_{L'L'''}^{\downarrow\uparrow}(r') & \Delta V_{L'L'''}^{\downarrow\downarrow}(r') \end{pmatrix} \begin{pmatrix} R_{L'''L}^{\uparrow\uparrow}(r') \\ R_{L'''L}^{\downarrow\uparrow}(r') \end{pmatrix} \quad (4.79)
$$

and

$$
\begin{pmatrix} R_{L'L}^{\uparrow\downarrow}(r) \\ R_{L'L}^{\downarrow\downarrow}(r) \end{pmatrix} = \begin{pmatrix} 0 \\ R_{L'L}^{0,\downarrow}(r)\delta_{L'L} \end{pmatrix} + \int r'^2 dr' \begin{pmatrix} G_{0,l'}^{\uparrow\uparrow}(r,r') & 0 \\ 0 & G_{0,l'}^{\downarrow\downarrow}(r,r') \end{pmatrix} \cdot
$$
$$
\sum_{L'''} \begin{pmatrix} \Delta V_{L'L'''}^{\uparrow\uparrow}(r') & \Delta V_{L'L'''}^{\uparrow\downarrow}(r') \\ \Delta V_{L'L'''}^{\downarrow\uparrow}(r') & \Delta V_{L'L'''}^{\downarrow\downarrow}(r') \end{pmatrix} \begin{pmatrix} R_{L'''L}^{\uparrow\downarrow}(r') \\ R_{L'''L}^{\downarrow\downarrow}(r') \end{pmatrix} . \quad (4.80)
$$

Therefore, equation (4.78) can be simplified to

$$
\sum_{L'} \left[c_{\mathbf{k}L'}^{\uparrow n} \begin{pmatrix} R_{LL'}^{0,\uparrow n}(r)\delta_{LL'} \\ 0 \end{pmatrix} + c_{\mathbf{k}L'}^{\downarrow n} \begin{pmatrix} 0 \\ R_{LL'}^{0,\downarrow n}(r)\delta_{LL'} \end{pmatrix} \right] =
$$
$$
\int r'^2 dr' \sum_{L''''} \begin{pmatrix} R_l^{0\uparrow}(r)G_{0,LL''''}^{\uparrow\uparrow}R_{l''''}^{\uparrow}(r') & 0 \\ 0 & R_l^{0\downarrow}(r)G_{0,LL''''}^{\downarrow\downarrow}R_{l''''}^{\downarrow}(r') \end{pmatrix} \cdot
$$
$$
\sum_{L''L'''} \begin{pmatrix} \Delta V_{L''''L'''}^{\uparrow\uparrow}(r') & \Delta V_{L''''L'''}^{\uparrow\downarrow}(r') \\ \Delta V_{L''''L'''}^{\downarrow\uparrow}(r') & \Delta V_{L''''L'''}^{\downarrow\downarrow}(r') \end{pmatrix} \left[c_{\mathbf{k}L''}^{\uparrow n} \begin{pmatrix} R_{L'''L''}^{\uparrow\uparrow n}(r') \\ R_{L'''L''}^{\downarrow\uparrow n}(r') \end{pmatrix} + c_{\mathbf{k}L''}^{\downarrow n} \begin{pmatrix} R_{L'''L''}^{\uparrow\downarrow n}(r') \\ R_{L'''L''}^{\downarrow\downarrow n}(r') \end{pmatrix} \right] . \quad (4.81)
$$

Using the definition of the Δt-matrix (4.67), one obtains

$$
\begin{pmatrix} R_l^{0\uparrow}(r) & 0 \\ 0 & R_l^{0\downarrow}(r) \end{pmatrix} \begin{pmatrix} c_{\mathbf{k}L}^{\uparrow n} \\ c_{\mathbf{k}L}^{\downarrow n} \end{pmatrix} = \sum_{L''L''''} \begin{pmatrix} R_l^{0\uparrow}(r) & 0 \\ 0 & R_l^{0\downarrow}(r) \end{pmatrix} \begin{pmatrix} G_{0,LL''''}^{\uparrow\uparrow} & 0 \\ 0 & G_{0,LL''''}^{\downarrow\downarrow} \end{pmatrix} \cdot
$$
$$
\left[c_{\mathbf{k}L''}^{\uparrow n} \begin{pmatrix} \Delta t_{L''''L''}^{\uparrow\uparrow n}(E) \\ \Delta t_{L''''L''}^{\downarrow\uparrow n}(E) \end{pmatrix} + c_{\mathbf{k}L''}^{\downarrow n} \begin{pmatrix} \Delta t_{L''''L''}^{\uparrow\downarrow n}(E) \\ \Delta t_{L''''L''}^{\downarrow\downarrow n}(E) \end{pmatrix} \right] \quad (4.82)
$$

and thus

$$
\begin{pmatrix} c_{\mathbf{k}L}^{\uparrow n} \\ c_{\mathbf{k}L}^{\downarrow n} \end{pmatrix} = \sum_{L''L''''} \begin{pmatrix} G_{0,LL''''}^{\uparrow\uparrow} & 0 \\ 0 & G_{0,LL''''}^{\downarrow\downarrow} \end{pmatrix} \begin{pmatrix} \Delta t_{L''''L''}^{\uparrow\uparrow n}(E) & \Delta t_{L''''L''}^{\uparrow\downarrow n}(E) \\ \Delta t_{L''''L''}^{\downarrow\uparrow n}(E) & \Delta t_{L''''L''}^{\downarrow\downarrow n}(E) \end{pmatrix} \begin{pmatrix} c_{\mathbf{k}L''}^{\uparrow n} \\ c_{\mathbf{k}L''}^{\downarrow n} \end{pmatrix} . \quad (4.83)
$$

Finally, the coefficients $\left(c_{\mathbf{k}L''}^{\uparrow n}, c_{\mathbf{k}L''}^{\downarrow n} \right)^T$ can be calculated following

$$
\sum_{L'L''} \left[\begin{pmatrix} \delta_{LL'}\delta_{L'L''} & 0 \\ 0 & \delta_{LL'}\delta_{L'L''} \end{pmatrix} - \begin{pmatrix} G_{0,LL'}^{\uparrow\uparrow} & 0 \\ 0 & G_{0,LL'}^{\downarrow\downarrow} \end{pmatrix} \begin{pmatrix} \Delta t_{L'L''}^{\uparrow\uparrow n}(E) & \Delta t_{L'L''}^{\uparrow\downarrow n}(E) \\ \Delta t_{L'L''}^{\downarrow\uparrow n}(E) & \Delta t_{L'L''}^{\downarrow\downarrow n}(E) \end{pmatrix} \right] \cdot
$$
$$
\begin{pmatrix} c_{\mathbf{k}L''}^{\uparrow n} \\ c_{\mathbf{k}L''}^{\downarrow n} \end{pmatrix} = 0. \quad (4.84)
$$

The above equation is the KKR secular equation for systems including non-spherical components of the potential as well as spin-orbit coupling, as it is eq. (3.49) for systems without spin-orbit coupling. It can be used for band structure calculations and for the calculation of the Fermi surface, i.e. the $\mathbf{k}$-points at the Fermi energy E_F, as well as the corresponding coefficients $\left(c_{\mathbf{k}L''}^{\uparrow n}, c_{\mathbf{k}L''}^{\downarrow n}\right)^T$.

The method used to calculate the Fermi surface is the same as already described in chapter 3 and the Appendix, sections A.2 and 3.1.4 for systems without spin-orbit coupling.

In order to obtain the final, correctly scaled coefficients $c_{\mathbf{k}L}^{n\uparrow}$ and $c_{\mathbf{k}L}^{n\downarrow}$, the norm of the full wavefunctions must be calculated which is discussed in the following paragraph.

Normalization of the wavefunctions $\left(\psi_{\mathbf{k}}^{\uparrow}(\mathbf{r}+\boldsymbol{\chi}^{\mu}), \psi_{\mathbf{k}}^{\downarrow}(\mathbf{r}+\boldsymbol{\chi}^{\mu})\right)^T$ In order to normalize the wavefunctions comprising an up- and down-component, the coefficients $c_{\mathbf{k}L}^{\mu\uparrow}$ and $c_{\mathbf{k}L}^{\mu\downarrow}$ must be chosen such that

$$\sum_{\mu=1}^{N_\mathrm{at}} \int_{V_\mu} d^3r \left(\left|\psi_{\mathbf{k}}^{\uparrow}(\mathbf{r}+\boldsymbol{\chi}^{\mu})\right|^2 + \left|\psi_{\mathbf{k}}^{\downarrow}(\mathbf{r}+\boldsymbol{\chi}^{\mu})\right|^2\right) = 1 \tag{4.85}$$

for each $\mathbf{k}$, which is achieved by choosing an appropriate prefactor of $\left(c_{\mathbf{k}L}^{\mu\uparrow},\ c_{\mathbf{k}L}^{\mu\downarrow}\right)^T$. Again, we have dropped the index n, indicating the lattice site while introducing the index μ, which accounts for the number of atoms N_at in the unit cell. The procedure is similar to that followed in the case of the full potential (see chapter 3, section 3.1.2). Hence, the integration in eq. (4.85) has to be performed over non-spherical Wigner-Seitz cells and the shapefunction $\Theta(\mathbf{r})$ has to be introduced

$$\sum_{\mu=1}^{N_\mathrm{at}} \int d^3r\, \Theta^\mu(\mathbf{r}) \left(\left|\psi_{\mathbf{k}}^{\uparrow}(\mathbf{r}+\boldsymbol{\chi}^{\mu})\right|^2 + \left|\psi_{\mathbf{k}}^{\downarrow}(\mathbf{r}+\boldsymbol{\chi}^{\mu})\right|^2\right) = 1 \ . \tag{4.86}$$

The square of the absolute value of the wavefunction $\left|\psi_{\mathbf{k}}^{\uparrow}(\mathbf{r}+\boldsymbol{\chi}^{\mu})\right|^2$ and $\left|\psi_{\mathbf{k}}^{\downarrow}(\mathbf{r}+\boldsymbol{\chi}^{\mu})\right|^2$ is

$$\begin{aligned}
&\left|\psi_{\mathbf{k}}^{\uparrow}(\mathbf{r}+\boldsymbol{\chi}^{\mu})\right|^2 + \left|\psi_{\mathbf{k}}^{\downarrow}(\mathbf{r}+\boldsymbol{\chi}^{\mu})\right|^2 \\
&\quad = \begin{pmatrix}\psi_{\mathbf{k}}^{\uparrow}(\mathbf{r}+\boldsymbol{\chi}^{\mu}) \\ \psi_{\mathbf{k}}^{\downarrow}(\mathbf{r}+\boldsymbol{\chi}^{\mu})\end{pmatrix}^{\dagger} \begin{pmatrix}\psi_{\mathbf{k}}^{\uparrow}(\mathbf{r}+\boldsymbol{\chi}^{\mu}) \\ \psi_{\mathbf{k}}^{\downarrow}(\mathbf{r}+\boldsymbol{\chi}^{\mu})\end{pmatrix} \\
&\quad = \sum_{L_1' L_1} \left[\begin{pmatrix}c_{\mathbf{k}L_1}^{\uparrow\mu\star} & c_{\mathbf{k}L_1}^{\downarrow\mu\star}\end{pmatrix} \begin{pmatrix}R_{L_1' L_1}^{\uparrow\uparrow\mu\star}(r) & R_{L_1' L_1}^{\downarrow\uparrow\mu\star}(r) \\ R_{L_1' L_1}^{\uparrow\downarrow\mu\star}(r) & R_{L_1' L_1}^{\downarrow\downarrow\mu\star}(r)\end{pmatrix}\right] Y_{L_1'}^{\star}(\hat{r}) \\
&\qquad\qquad \sum_{L_2' L_2} \left[\begin{pmatrix}R_{L_2' L_2}^{\uparrow\uparrow\mu}(r) & R_{L_2' L_2}^{\uparrow\downarrow\mu}(r) \\ R_{L_2' L_2}^{\downarrow\uparrow\mu}(r) & R_{L_2' L_2}^{\downarrow\downarrow\mu}(r)\end{pmatrix} \begin{pmatrix}c_{\mathbf{k}L_2}^{\uparrow\mu} \\ c_{\mathbf{k}L_2}^{\downarrow\mu}\end{pmatrix}\right] Y_{L_2'}(\hat{r}) \\
&\quad = \sum_{L_1 L_2} \sum_{L_1' L_2'} Y_{L_1'}^{\star}(\hat{r}) Y_{L_2'}(\hat{r}) \\
&\qquad\qquad \sum_{\sigma\sigma'} \left[c_{\mathbf{k}L_1'}^{\sigma\mu\star} c_{\mathbf{k}L_2'}^{\sigma'\mu} \left(R_{L_1 L_1'}^{\uparrow\sigma\mu\star}(r) R_{L_2 L_2'}^{\uparrow\sigma'\mu}(r) + R_{L_1 L_1'}^{\downarrow\sigma\mu\star}(r) R_{L_2 L_2'}^{\downarrow\sigma'\mu}(r)\right)\right] .
\end{aligned}$$

$$\tag{4.87}$$

Similar to the procedure used for systems without spin-orbit coupling the definition

$$\rho_{L_1 L_2}^{\mu \sigma \sigma'} = \int_0^{r_{\max}} r^2 dr \sum_{L_1' L_2' L_3} \Theta_{L_3}^{\mu}(r) C_{L_1' L_2' L_3} \sum_{\sigma''} R_{L_1' L_1}^{\mu \star \sigma'' \sigma}(r) R_{L_2' L_2}^{\mu \sigma'' \sigma'}(r) \tag{4.88}$$

allows to rewrite the normalization condition (4.85) as

$$\sum_{\mu=1}^{N_{\text{at}}} \int d^3 r \Theta^{\mu}(\mathbf{r}) \left(\left| \psi_{\mathbf{k}}^{\uparrow}(\mathbf{r} + \boldsymbol{\chi}^{\mu}) \right|^2 + \left| \psi_{\mathbf{k}}^{\downarrow}(\mathbf{r} + \boldsymbol{\chi}^{\mu}) \right|^2 \right) = \sum_{\mu} \sum_{\sigma \sigma'} \sum_{L_1 L_2} c_{\mathbf{k} L_1}^{\mu \star \sigma} c_{\mathbf{k} L_2}^{\mu \sigma'} \rho_{L_1 L_2}^{\mu \sigma \sigma'}$$

$$= 1. \tag{4.89}$$

The quantity $\rho_{L_1 L_2}^{\mu \sigma \sigma'}$ calculates similarly to $\rho_{L_1 L_2}^{\mu}$ described in section 3.1.2.
Finally, the correctly scaled coefficients $c_{\mathbf{k} L}^{\mu \uparrow}$ and $c_{\mathbf{k} L}^{\mu \downarrow}$, which fulfill the normalization condition (4.85) are given by

$$c_{\mathbf{k} L}^{\mu \sigma} \to \left[\sum_{\mu} \sum_{\sigma \sigma'} \sum_{L_1 L_2} c_{\mathbf{k} L_1}^{\mu \star \sigma} c_{\mathbf{k} L_2}^{\mu \sigma'} \rho_{L_1 L_2}^{\mu \sigma \sigma'} \right]^{-\frac{1}{2}} c_{\mathbf{k} L}^{\mu \sigma}. \tag{4.90}$$

4.5 Expectation values of the spin operators

For a number of applications it is necessary to calculate the expectation values $S_{\mathbf{k}}^x$, $S_{\mathbf{k}}^y$ and $S_{\mathbf{k}}^z$ of the spin operators $\mathbf{S}^i$, $i = x, y, z$ at the Bloch states $\mathbf{k}$. We will deal with this subject here because of two reasons: First, the scheme to calculate them is very similar to that of the normalization of the coefficients, which was the subject of the previous section. Secondly, the spin expectation values are required for the determination of the coefficients $c_{\mathbf{k} L}^{\uparrow \mu}$ and $c_{\mathbf{k} L}^{\downarrow \mu}$ in the case of spin degeneracy. The latter is explained in the next section.
For each point $\mathbf{k}$ on the Fermi surface, the expectation value of the spin is determined by $\mathbf{S} = 1/2 \hbar \, \boldsymbol{\sigma}$, i.e. in atomic units ($\hbar = 1$),

$$S_{\mathbf{k}}^x = \frac{1}{2} \langle \psi_{\mathbf{k}} | \sigma^x | \psi_{\mathbf{k}} \rangle \, , \tag{4.91}$$

$$S_{\mathbf{k}}^y = \frac{1}{2} \langle \psi_{\mathbf{k}} | \sigma^y | \psi_{\mathbf{k}} \rangle \, , \tag{4.92}$$

$$S_{\mathbf{k}}^z = \frac{1}{2} \langle \psi_{\mathbf{k}} | \sigma^z | \psi_{\mathbf{k}} \rangle \, , \tag{4.93}$$

where σ^x, σ^y and σ^z are the Pauli matrices as defined in eq. (4.4).
Hence, $S_{\mathbf{k}}^x$, $S_{\mathbf{k}}^y$ and $S_{\mathbf{k}}^z$ can be calculated according to

$$S_{\mathbf{k}}^{x,\mu} = \frac{1}{2} \int_{V_{\mu}} d^3 r \begin{pmatrix} \psi_{\mathbf{k}}^{\uparrow}(\mathbf{r} + \boldsymbol{\chi}^{\mu}) \\ \psi_{\mathbf{k}}^{\downarrow}(\mathbf{r} + \boldsymbol{\chi}^{\mu}) \end{pmatrix}^{\dagger} \begin{pmatrix} 0 & 1 \\ 1 & 0 \end{pmatrix} \begin{pmatrix} \psi_{\mathbf{k}}^{\uparrow}(\mathbf{r} + \boldsymbol{\chi}^{\mu}) \\ \psi_{\mathbf{k}}^{\downarrow}(\mathbf{r} + \boldsymbol{\chi}^{\mu}) \end{pmatrix}$$

$$= \frac{1}{2} \int_{V_{\mu}} d^3 r \left[\psi_{\mathbf{k}}^{\uparrow \star}(\mathbf{r} + \boldsymbol{\chi}^{\mu}) \psi_{\mathbf{k}}^{\downarrow}(\mathbf{r} + \boldsymbol{\chi}^{\mu}) + \psi_{\mathbf{k}}^{\downarrow \star}(\mathbf{r} + \boldsymbol{\chi}^{\mu}) \psi_{\mathbf{k}}^{\uparrow}(\mathbf{r} + \boldsymbol{\chi}^{\mu}) \right], \tag{4.94}$$

$$S_{\mathbf{k}}^{y,\mu} = \frac{1}{2} \int_{V_\mu} d^3r \begin{pmatrix} \psi_{\mathbf{k}}^\uparrow(\mathbf{r}+\boldsymbol{\chi}^\mu) \\ \psi_{\mathbf{k}}^\downarrow(\mathbf{r}+\boldsymbol{\chi}^\mu) \end{pmatrix}^\dagger \begin{pmatrix} 0 & -i \\ i & 0 \end{pmatrix} \begin{pmatrix} \psi_{\mathbf{k}}^\uparrow(\mathbf{r}+\boldsymbol{\chi}^\mu) \\ \psi_{\mathbf{k}}^\downarrow(\mathbf{r}+\boldsymbol{\chi}^\mu) \end{pmatrix}$$

$$= \frac{1}{2} \int_{V_\mu} d^3r \left[(-i)\psi_{\mathbf{k}}^{\uparrow\star}(\mathbf{r}+\boldsymbol{\chi}^\mu)\psi_{\mathbf{k}}^\downarrow(\mathbf{r}+\boldsymbol{\chi}^\mu) + i\psi_{\mathbf{k}}^{\downarrow\star}(\mathbf{r}+\boldsymbol{\chi}^\mu)\psi_{\mathbf{k}}^\uparrow(\mathbf{r}+\boldsymbol{\chi}^\mu) \right], \quad (4.95)$$

and

$$S_{\mathbf{k}}^{z,\mu} = \frac{1}{2} \int_{V_\mu} d^3r \begin{pmatrix} \psi_{\mathbf{k}}^{\uparrow\star}(\mathbf{r}+\boldsymbol{\chi}^\mu) \\ \psi_{\mathbf{k}}^{\downarrow\star}(\mathbf{r}+\boldsymbol{\chi}^\mu) \end{pmatrix}^\dagger \begin{pmatrix} 1 & 0 \\ 0 & 1 \end{pmatrix} \begin{pmatrix} \psi_{\mathbf{k}}^\uparrow(\mathbf{r}+\boldsymbol{\chi}^\mu) \\ \psi_{\mathbf{k}}^\downarrow(\mathbf{r}+\boldsymbol{\chi}^\mu) \end{pmatrix}$$

$$= \frac{1}{2} \int_{V_\mu} d^3r \left[\left|\psi_{\mathbf{k}}^\uparrow(\mathbf{r}+\boldsymbol{\chi}^\mu)\right|^2 - \left|\psi_{\mathbf{k}}^\downarrow(\mathbf{r}+\boldsymbol{\chi}^\mu)\right|^2 \right]. \quad (4.96)$$

In a more general form, the above equations can be subsumed to

$$S_{\mathbf{k}}^{i,\mu} = \frac{1}{2} \int_{V_\mu} d^3r \sum_{L,L'} \left[\begin{pmatrix} R_L^{\uparrow\uparrow\mu}(\mathbf{r}) & R_L^{\uparrow\downarrow\mu}(\mathbf{r}) \\ R_L^{\downarrow\uparrow\mu}(\mathbf{r}) & R_L^{\downarrow\downarrow\mu}(\mathbf{r}) \end{pmatrix} \begin{pmatrix} c_{\mathbf{k}L}^{\uparrow\mu} \\ c_{\mathbf{k}L}^{\downarrow\mu} \end{pmatrix} \right]^\dagger$$
$$\begin{pmatrix} \sigma_{11}^i & \sigma_{12}^i \\ \sigma_{21}^i & \sigma_{22}^i \end{pmatrix} \begin{pmatrix} R_{L'}^{\uparrow\uparrow\mu}(\mathbf{r}) & R_{L'}^{\uparrow\downarrow\mu}(\mathbf{r}) \\ R_{L'}^{\downarrow\uparrow\mu}(\mathbf{r}) & R_{L'}^{\downarrow\downarrow\mu}(\mathbf{r}) \end{pmatrix} \begin{pmatrix} c_{\mathbf{k}L'}^{\uparrow\mu} \\ c_{\mathbf{k}L'}^{\downarrow\mu} \end{pmatrix} \quad (4.97)$$

or

$$S_{\mathbf{k}}^{i,\mu} = \frac{1}{2} \sum_{L,L'} \begin{pmatrix} c_{\mathbf{k}L}^{\uparrow\mu} & c_{\mathbf{k}L}^{\downarrow\mu} \end{pmatrix}^\star \begin{pmatrix} \Sigma_{LL'}^{\uparrow\uparrow\mu,i} & \Sigma_{LL'}^{\uparrow\downarrow\mu,i} \\ \Sigma_{LL'}^{\downarrow\uparrow\mu,i} & \Sigma_{LL'}^{\downarrow\downarrow\mu,i} \end{pmatrix} \begin{pmatrix} c_{\mathbf{k}L'}^{\uparrow\mu} \\ c_{\mathbf{k}L'}^{\downarrow\mu} \end{pmatrix}, \quad i = x, y, z, \quad (4.98)$$

where the notation

$$\begin{pmatrix} \Sigma_{LL'}^{\uparrow\uparrow\mu,i} & \Sigma_{LL'}^{\uparrow\downarrow\mu,i} \\ \Sigma_{LL'}^{\downarrow\uparrow\mu,i} & \Sigma_{LL'}^{\downarrow\downarrow\mu,i} \end{pmatrix} = \int_{V_\mu} d^3r \begin{pmatrix} R_L^{\uparrow\uparrow\mu}(\mathbf{r}) & R_L^{\uparrow\downarrow\mu}(\mathbf{r}) \\ R_L^{\downarrow\uparrow\mu}(\mathbf{r}) & R_L^{\downarrow\downarrow\mu}(\mathbf{r}) \end{pmatrix}^\dagger \begin{pmatrix} \sigma_{11}^i & \sigma_{12}^i \\ \sigma_{21}^i & \sigma_{22}^i \end{pmatrix} \begin{pmatrix} R_{L'}^{\uparrow\uparrow\mu}(\mathbf{r}) & R_{L'}^{\uparrow\downarrow\mu}(\mathbf{r}) \\ R_{L'}^{\downarrow\uparrow\mu}(\mathbf{r}) & R_{L'}^{\downarrow\downarrow\mu}(\mathbf{r}) \end{pmatrix} \quad (4.99)$$

has been introduced. The expectation values of the total spin components are

$$S_{\mathbf{k}}^x = \sum_{\mu=1}^{N_{\mathrm{at}}} S_{\mathbf{k}}^{x,\mu},$$

$$S_{\mathbf{k}}^y = \sum_{\mu=1}^{N_{\mathrm{at}}} S_{\mathbf{k}}^{y,\mu},$$

$$S_{\mathbf{k}}^z = \sum_{\mu=1}^{N_{\mathrm{at}}} S_{\mathbf{k}}^{z,\mu} \quad (4.100)$$

and thus

$$S_{\mathbf{k}}^{\mathrm{tot}} = \sqrt{\left(S_{\mathbf{k}}^x\right)^2 + \left(S_{\mathbf{k}}^y\right)^2 + \left(S_{\mathbf{k}}^z\right)^2}. \quad (4.101)$$

4.6 The coefficients $c_\mathbf{k}$ for the case of Kramers degeneracy

In non-magnetic systems with inversion symmetry, for example in fcc copper, silver or gold crystals, all states on the Fermi surface belonging to $(\mathbf{k}_{\mathrm{F}}, E_{\mathrm{F}})$ are twofold degenerate. In

this case, there are two eigenfunctions $\psi_{\mathbf{k}}^1(\mathbf{r})$ and $\psi_{\mathbf{k}}^2(\mathbf{r})$ which are orthogonal to each other and have opposite spin expectation values

$$\left\langle \psi_{\mathbf{k}}^1 | \sigma^i | \psi_{\mathbf{k}}^1 \right\rangle = -\left\langle \psi_{\mathbf{k}}^2 | \sigma^i | \psi_{\mathbf{k}}^2 \right\rangle, \quad i = x, y, z \, ; \tag{4.102}$$

this is known as Kramers degeneracy. However, the coefficients $c_{\mathbf{k}L}^{1,2}$ belonging to the two wavefunctions $\psi_{\mathbf{k}}^1(\mathbf{r})$ and $\psi_{\mathbf{k}}^2(\mathbf{r})$ do not always initially fulfill the above condition, since they are calculated as eigenvectors of the KKR-matrix (see section 3.1.4) using the Lapack-routine [78] ZGEEV, which computes the eigenvalues and, optionally, the left and/or right eigenvectors of nonsymmetric complex matrices. Therefore, an explicit orthogonalization is necessary

$$\begin{pmatrix} \tilde{c}_{\mathbf{k}}^{2,\uparrow} \\ \tilde{c}_{\mathbf{k}}^{2,\downarrow} \end{pmatrix} = \begin{pmatrix} c_{\mathbf{k}}^{2,\uparrow} \\ c_{\mathbf{k}}^{2,\downarrow} \end{pmatrix} - \frac{\left[\begin{pmatrix} c_{\mathbf{k}}^{1,\uparrow} & c_{\mathbf{k}}^{1,\downarrow} \end{pmatrix}^{\star} \cdot \begin{pmatrix} c_{\mathbf{k}}^{2,\uparrow} \\ c_{\mathbf{k}}^{2,\downarrow} \end{pmatrix} \right]}{\left[\begin{pmatrix} c_{\mathbf{k}}^{1,\uparrow} & c_{\mathbf{k}}^{1,\downarrow} \end{pmatrix}^{\star} \cdot \begin{pmatrix} c_{\mathbf{k}}^{1,\uparrow} \\ c_{\mathbf{k}}^{1,\downarrow} \end{pmatrix} \right]} \begin{pmatrix} c_{\mathbf{k}}^{1,\uparrow} \\ c_{\mathbf{k}}^{1,\downarrow} \end{pmatrix}, \tag{4.103}$$

which reduces to

$$\begin{pmatrix} \tilde{c}_{\mathbf{k}}^{2,\uparrow} \\ \tilde{c}_{\mathbf{k}}^{2,\downarrow} \end{pmatrix} = \begin{pmatrix} c_{\mathbf{k}}^{2,\uparrow} \\ c_{\mathbf{k}}^{2,\downarrow} \end{pmatrix} - \left[\begin{pmatrix} c_{\mathbf{k}}^{1,\uparrow} & c_{\mathbf{k}}^{1,\downarrow} \end{pmatrix}^{\star} \cdot \begin{pmatrix} c_{\mathbf{k}}^{2,\uparrow} \\ c_{\mathbf{k}}^{2,\downarrow} \end{pmatrix} \right] \begin{pmatrix} c_{\mathbf{k}}^{1,\uparrow} \\ c_{\mathbf{k}}^{1,\downarrow} \end{pmatrix} \tag{4.104}$$

if $\left(c_{\mathbf{k}}^{1,\uparrow}, \ c_{\mathbf{k}}^{1,\downarrow} \right)^T$ is normalized. The orthogonality can be easily proven by multiplying $\left(\tilde{c}_{\mathbf{k}}^{2,\uparrow}, \ \tilde{c}_{\mathbf{k}}^{2,\downarrow} \right)^T$ with $\left(c_{\mathbf{k}}^{1,\uparrow\star}, \ c_{\mathbf{k}}^{1,\downarrow\star} \right)$. Note that the above operation does not conserve the norm and a normalization of $\left(\tilde{c}_{\mathbf{k}}^{2,\uparrow}, \ \tilde{c}_{\mathbf{k}}^{2,\downarrow} \right)^T$ is necessary.

Although the wavefunctions $\psi_{\mathbf{k}}^1(\mathbf{r})$ and $\psi_{\mathbf{k}}^2(\mathbf{r})$ are now orthogonal, the degeneracy allows any linear combination of the two wavefunctions. The appropriate linear combination is determined by the particular physical problem at hand in each case. For the problem of spin relaxation that is investigated in the present thesis, two types of linear combination are most interesting: one that maximizes $S_{\mathbf{k}}^z$ and one that gives $S_{\mathbf{k}}^x = S_{\mathbf{k}}^y = 0$ for all $\mathbf{k}$. The two choices are not equivalent and correspond to different, though similar, experimental situations. The former condition would correspond to the creation of a spin population by acting with an external B-field along the z-axis, which is then switched off, while the latter corresponds to the case when electrons, which are polarized exactly in the z-direction are injected to the material from an external source, e.g. a ferromagnet.

We continue now to seek a linear combination of the degenerate coefficients $\mathbf{c}_{\mathbf{k}}^1$ and $\mathbf{c}_{\mathbf{k}}^2$, which is constructed such that it fulfills the required conditions. To simplify the notation, we write

$$\psi_{\mathbf{k}}^{1,2} = \underline{\underline{R}} \cdot \mathbf{c}_{\mathbf{k}}^{1,2} \tag{4.105}$$

instead of

$$\begin{pmatrix} \psi_{\mathbf{k}}^{1,2\uparrow}(\mathbf{r} + \boldsymbol{\chi}^\mu) \\ \psi_{\mathbf{k}}^{1,2\downarrow}(\mathbf{r} + \boldsymbol{\chi}^\mu) \end{pmatrix} = \sum_\mu \sum_L \left[\begin{pmatrix} R_L^{\uparrow\uparrow\mu}(\mathbf{r}) & R_L^{\uparrow\downarrow\mu}(\mathbf{r}) \\ R_L^{\downarrow\uparrow\mu}(\mathbf{r}) & R_L^{\downarrow\downarrow\mu}(\mathbf{r}) \end{pmatrix} \begin{pmatrix} c_{\mathbf{k}L}^{1,2\uparrow\mu} \\ c_{\mathbf{k}L}^{1,2\downarrow\mu} \end{pmatrix} \right] \tag{4.106}$$

and, likewise

$$S_{\mathbf{k}}^{i,1,2} = \frac{1}{2} \left\langle \psi_{\mathbf{k}}^{1,2} | \boldsymbol{\sigma}^i | \psi_{\mathbf{k}}^{1,2} \right\rangle = \mathbf{c}_{\mathbf{k}}^{1,2\dagger} \underline{\underline{\Sigma}}^i \mathbf{c}_{\mathbf{k}}^{1,2}, \quad i = x, y, z \tag{4.107}$$

for the spin expectation values (4.98) with

$$\underline{\underline{\Sigma}}^i = \frac{1}{2} \int d^3r \, \underline{\underline{R}}^\dagger \boldsymbol{\sigma}^i \underline{R} \, . \tag{4.108}$$

The coefficients of the linear combination can be expressed as

$$\mathbf{d}_\mathbf{k}^{1,2} = f_\mathbf{k}^{1,2} \mathbf{c}_\mathbf{k}^1 + g_\mathbf{k}^{1,2} \mathbf{c}_\mathbf{k}^2 \tag{4.109}$$

with $f_\mathbf{k}^{1,2}, g_\mathbf{k}^{1,2} \in \mathbb{C}$ and

$$\left| f_\mathbf{k}^{1,2} \right|^2 + \left| g_\mathbf{k}^{1,2} \right|^2 = 1. \tag{4.110}$$

Since the phase of $\mathbf{d}_\mathbf{k}^{1,2}$ is irrelevant, one of the parameters $f_\mathbf{k}^{1,2}, g_\mathbf{k}^{1,2}$, e.g. $f_\mathbf{k}^1$ can be chosen to be a real number. Due to condition (4.110), we can set

$$
\begin{aligned}
f_\mathbf{k}^1 &= \cos\frac{\alpha_\mathbf{k}}{2} \quad \text{and} \\
g_\mathbf{k}^1 &= \sin\frac{\alpha_\mathbf{k}}{2} \, e^{i\beta_\mathbf{k}} \, ,
\end{aligned}
\tag{4.111}
$$

resulting in

$$\mathbf{d}_\mathbf{k}^1 = \cos\frac{\alpha_\mathbf{k}}{2} \mathbf{c}_\mathbf{k}^1 + \sin\frac{\alpha_\mathbf{k}}{2} \, e^{i\beta_\mathbf{k}} \mathbf{c}_\mathbf{k}^2. \tag{4.112}$$

The orthogonality of the $\mathbf{c}_\mathbf{k}^{1,2}$ as well as the new coefficients $\mathbf{d}_\mathbf{k}^{1,2}$

$$\mathbf{d}_\mathbf{k}^{m\dagger} \cdot \mathbf{d}_\mathbf{k}^n = \delta_{mn}, \quad m, n = 1, 2 \tag{4.113}$$

then leads to

$$\mathbf{d}_\mathbf{k}^2 = -\sin\frac{\alpha_\mathbf{k}}{2} \mathbf{c}_\mathbf{k}^1 + \cos\frac{\alpha_\mathbf{k}}{2} \, e^{i\beta_\mathbf{k}} \mathbf{c}_\mathbf{k}^2 \, . \tag{4.114}$$

For simplicity, we will skip the index $\mathbf{k}$ in the following discussion. Nevertheless, all parameters, coefficients and spin expectation values depend on $\mathbf{k}$.

An evaluation of the spin expectation value $S_{d_1}^i = \mathbf{d}_\mathbf{k}^{1\dagger} \underline{\underline{\Sigma}}^i \mathbf{d}_\mathbf{k}^1$ in terms of the old coefficients and spin expectation values yields

$$
\begin{aligned}
S_{d_1}^i &= \left(\cos\frac{\alpha}{2}\right)^2 S_{c_1}^i + \left(\sin\frac{\alpha}{2}\right)^2 S_{c_2}^i + \left(\sin\frac{\alpha}{2}\right)\left(\cos\frac{\alpha}{2}\right)\left[e^{i\beta}\mathbf{c}^{1\dagger}\Sigma^i\mathbf{c}^2 + e^{-i\beta}\mathbf{c}^{2\dagger}\Sigma^i\mathbf{c}^1\right] \\
&= \left(\cos\frac{\alpha}{2}\right)^2 S_{c_1}^i + \left(\sin\frac{\alpha}{2}\right)^2 S_{c_2}^i + \left(\sin\frac{\alpha}{2}\right)\left(\cos\frac{\alpha}{2}\right) 2\mathrm{Re}\left[e^{i\beta}\mathbf{c}^{1\dagger}\Sigma^i\mathbf{c}^2\right] \\
&= \cos\alpha \, S_{c_1}^i + \sin\alpha \, \mathrm{Re}\left[e^{i\beta}\mathbf{c}^{1\dagger}\Sigma^i\mathbf{c}^2\right].
\end{aligned}
\tag{4.115}
$$

In the last step, we have used eq. (4.102) as well as the double-angle formulae for trigonometric functions. Defining

$$S_{c_1,c_2}^i = \mathbf{c}^{1\dagger}\Sigma^i\mathbf{c}^2 \quad i = x, y, z \tag{4.116}$$

in accordance with eq. (4.107), the expectation value (4.115) results in

$$S_{d_1}^i = \cos\alpha \, S_{c_1}^i + \sin\alpha \, \mathrm{Re}\left[e^{i\beta} S_{c_1,c_2}^i\right] \quad i = x, y, z. \tag{4.117}$$
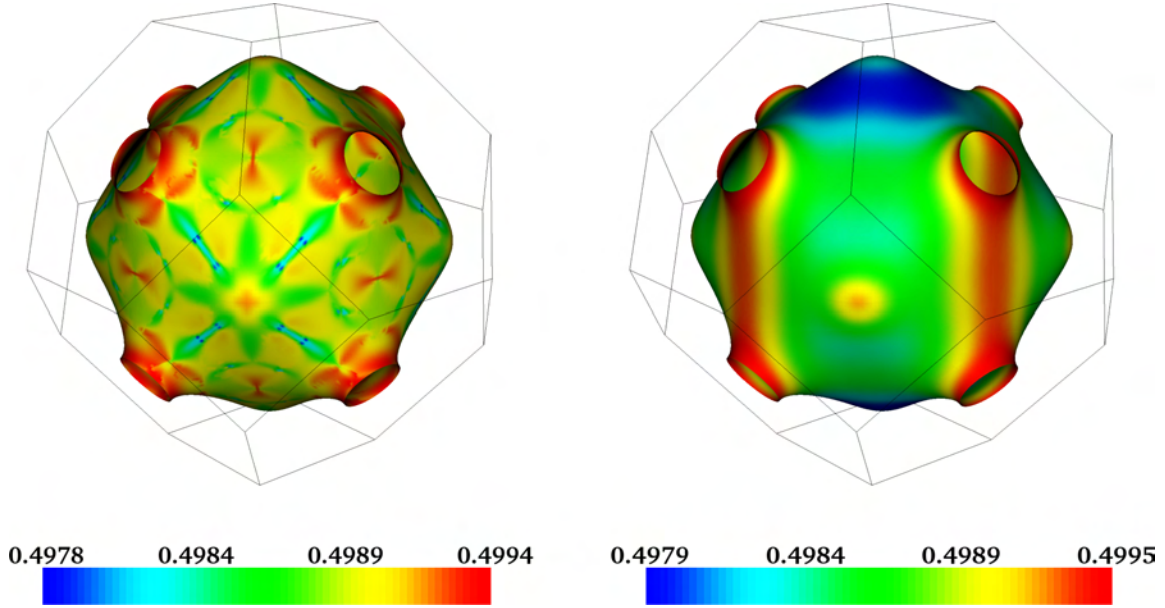
Figure 4.1.: Total spin expectation values $S_{\mathbf{k}}^{\text{tot}}$ for a copper fcc crystal on the Fermi surface. While the left panel shows $S_{\mathbf{k}}^{\text{tot}}$ for an arbitrary reference system for each $\mathbf{k}$ (i.e. the initial 'choice', taking the orthogonalized coefficients such as they result from the eigenvalue routine), the right panel represents the total spin expectation values for linear combinations of $\mathbf{c_k}$ such that the z-component $S_{\mathbf{k}}^z$ is maximized.

At this point, one has to decide which condition the spin expectation values in the new reference system should fulfill. As already indicated, the z-axis will be chosen as spin quantization axis, but this choice might either be understood as

$$S_{d_1}^z = \text{max.} \tag{4.118}$$

or

$$S_{d_1}^x = S_{d_1}^y = 0 \,. \tag{4.119}$$

In the following, both cases will be considered. We start with the first one, hence maximizing $S_{d_1}^z$. The two parameters α and β are then determined by the conditions

$$
\begin{aligned}
\frac{\partial S_{d_1}^z}{\partial \alpha} &= 0 \quad \text{and} \\
\frac{\partial S_{d_1}^z}{\partial \beta} &= 0,
\end{aligned}
\tag{4.120}
$$

which result in the two equations

$$
\begin{aligned}
-\sin\alpha\, S_{c_1}^z + \cos\alpha\, \text{Re}\left[e^{i\beta} S_{c_1,c_2}^z\right] &= 0 \quad \text{and} \\
\sin\alpha\, \text{Im}\left[e^{i\beta} S_{c_1,c_2}^z\right] &= 0.
\end{aligned}
\tag{4.121}
$$

Then, α and β are given by

$$
\begin{aligned}
\beta &= \arg S_{c_1,c_2}^z \\
\alpha &= \tan^{-1}\left[\frac{\mathrm{Re}\left[e^{i\beta} S_{c_1,c_2}^z \right]}{S_{c_1}^z} \right].
\end{aligned}
\tag{4.122}
$$

In contrast, condition (4.119) leads to

$$
\begin{aligned}
\beta &= \frac{1}{2i}\ln\left[-\frac{S_{c_1}^x S_{c_1,c_2}^{y\star} - S_{c_1}^y S_{c_1,c_2}^{x\star}}{S_{c_1}^x S_{c_1,c_2}^y - S_{c_1}^y S_{c_1,c_2}^x} \right] \\
\alpha &= -\tan^{-1}\left[\frac{S_{c_1}^x}{\mathrm{Re}\left[e^{i\beta} S_{c_1,c_2}^x \right]} \right] = -\tan^{-1}\left[\frac{S_{c_1}^y}{\mathrm{Re}\left[e^{i\beta} S_{c_1,c_2}^y \right]} \right].
\end{aligned}
\tag{4.123}
$$

The total spin expectation value $S_{\mathbf{k}}^{\mathrm{tot}}$ is different in the two cases although the difference is very small and not visible in a figure. However, the distribution of the spin expectation values S_c^{tot} on the Fermi surface for the initial coefficients $c_{\mathbf{k}}$ differ remarkably from that of S_d^{tot} for one of the choices $S^x = S^y = 0$ or $S^z = \mathrm{max.}$. This is illustrated in figure 4.1 for copper. The integrated difference for copper and gold crystals can be found in table 4.1 and will be analyzed in the next subsection. In addition, we will average the spin expectation values over the Fermi surface and compare our results to other numerical data.
As a further test of our findings, we constructed a simple model in order to show that the two conditions are not equivalent. This issue will be the subject of the section after the next 4.6.2.

4.6.1 Comparison of the spin-expectation value S^{tot} of copper and gold to other numerical data

In the previous section we derived linear combinations of the degenerate coefficients $c_{\mathbf{k}}^1$ and $c_{\mathbf{k}}^2$ such that either the condition $S^z = \mathrm{max.}$ or $S^x = S^y = 0$ is fulfilled. Now, a quantitative analysis of the two possible choices for copper and gold fcc crystals is presented. The results are subsumed in table 4.1.
Apparently, the choice of $S^z = \mathrm{max.}$ leads to non-vanishing spin-components S^x and S^y. While this is only a small effect for copper, lower than 1 per mille, for a gold crystal the average of S^x and S^y over the Fermi surface is of the order of about 1% of the total spin expectation value S^{tot}. In addition, the total spin expectation value (averaged over the Fermi surface) is affected, too; the maximization of S^z leads to slightly higher values of S^{tot}. However, as already stated in the last section, the difference is very small and would not be visible in a figure. In all calculations of momentum- and spin-relaxation times in this thesis which are presented in chapter 6 for bulk systems and in chapter 8 for thin films, the second condition (4.119) $S^x = S^y = 0$ is chosen.
Comparing the distribution of the spin expectation value for copper in the right panel of figure 4.2 to the distribution shown in [79], a good agreement is found. For a more accurate

		ASA		FP	
		S^z = max.	$S^x = S^y = 0$	S^z = max.	$S^x = S^y = 0$
Cu	S^x	$2.5 \cdot 10^{-4}$	0	$2.2 \cdot 10^{-4}$	0
	S^y	$3.6 \cdot 10^{-4}$	0	$2.8 \cdot 10^{-4}$	0
	S^z	0.4988682	0.4988679	0.49901815	0.4990179
	S^{tot}	0.4988685	0.4988679	0.49901835	0.4990179
Au	S^x	$1.3 \cdot 10^{-2}$	0	$0.6 \cdot 10^{-2}$	0
	S^y	$1.3 \cdot 10^{-2}$	0	$1.0 \cdot 10^{-2}$	0
	S^z	0.4678345	0.4673311	0.4782259	0.4779915
	S^{tot}	0.4684714	0.4673311	0.47846055	0.4779915

Table 4.1.: Spin expectation values $\mathbf{S} = \langle \mathbf{S_k} \rangle_{\text{FS}}$ (with $\mathbf{S_k} = 1/2 \ \langle \psi_\mathbf{k} | \boldsymbol{\sigma} | \psi_\mathbf{k} \rangle$) and $S^{\text{tot}} = \langle \mathbf{S_k^{\text{tot}}} \rangle_{\text{FS}}$ of copper and gold averaged over the Fermi surface for the two different conditions S^z = max. and $S^x = S^y = 0$. While the total spin expectations S^{tot} for the latter condition equal the expectation value of S_z, choosing the first one leads to finite, non negligible spin expectation values of the x and y spin components. For gold, a difference in the total spin expectation values between the two possible conditions averaged over the Fermi surface of the order of 1% is found.

comparison, we introduce the parameters $a_\mathbf{k}$ and $b_\mathbf{k}$ defined as

$$|a_\mathbf{k}|^2 \ = \ \sum_{\mu=1}^{N_{\text{at}}} \int_{V_\mu} d^3r \ \psi_\mathbf{k}^{\uparrow\star}(\mathbf{r} + \boldsymbol{\chi}^\mu)\psi_\mathbf{k}^\uparrow(\mathbf{r} + \boldsymbol{\chi}^\mu) \qquad \text{and} \qquad (4.124)$$

$$|b_\mathbf{k}|^2 \ = \ \sum_{\mu=1}^{N_{\text{at}}} \int_{V_\mu} d^3r \ \psi_\mathbf{k}^{\downarrow\star}(\mathbf{r} + \boldsymbol{\chi}^\mu)\psi_\mathbf{k}^\downarrow(\mathbf{r} + \boldsymbol{\chi}^\mu), \qquad (4.125)$$

which are often used to quantify the strength of spin-orbit coupling e.g. in [14]. The quantity $|b_\mathbf{k}|^2$ is called spin-mixing parameter or Elliott-Yafet parameter (see section 6.1.1 in chapter 6). As one can easily prove, the relation of $|a_\mathbf{k}|^2$ and $|b_\mathbf{k}|^2$ to the normalization of the wavefunction and the spin expectation value $S_\mathbf{k}^z$ is given by

$$|a_\mathbf{k}|^2 + |b_\mathbf{k}|^2 \ = \ 1 \qquad \text{and} \qquad (4.126)$$

$$|a_\mathbf{k}|^2 - |b_\mathbf{k}|^2 \ = \ 2S_\mathbf{k}^z, \qquad (4.127)$$

being equivalent to

$$|a_\mathbf{k}|^2 \ = \ \frac{1}{2} + S_\mathbf{k}^z \qquad \text{and} \qquad (4.128)$$

$$|b_\mathbf{k}|^2 \ = \ \frac{1}{2} - S_\mathbf{k}^z. \qquad (4.129)$$

0.0005   0.0009   0.0013   0.0021   0.0103   0.0168   0.0274   0.0446
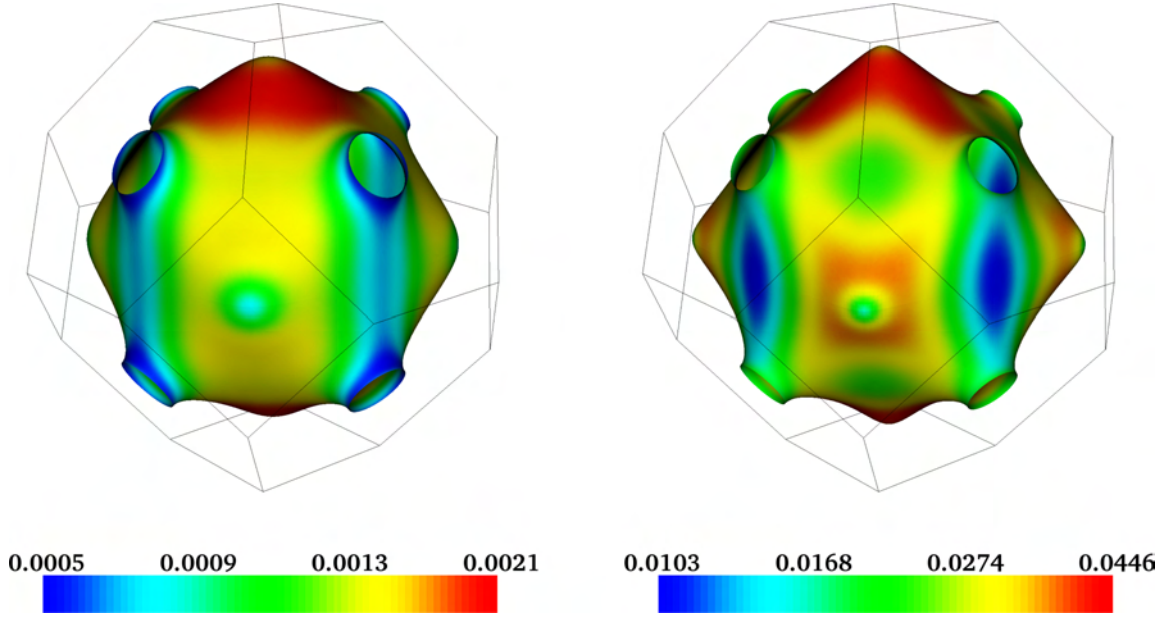
Figure 4.2.: Spin-mixing parameters $|b_{\mathbf{k}}|^2$ for copper (*left*) and gold (*right*) fcc bulk crystals after a linear combination of the degenerate coefficients $c_{\mathbf{k}}^1$ and $c_{\mathbf{k}}^2$ such that the condition $S^x = S^y = 0$ is fulfilled. While the distributions for copper and gold are qualitatively similar to each other, the order of magnitude of the absolute values of $|b_{\mathbf{k}}|^2$ differs strongly. As expected, the effect of spin-orbit coupling is much larger for gold than for copper. To compare, for copper, the distribution of the spin expectation value $S_{\mathbf{k}}^z = 1/2 - |b_{\mathbf{k}}|^2$ after the maximization of S^z is shown in figure 4.1.

Furthermore, the strength of spin-orbit coupling is often quantified by $\rho^{\uparrow\downarrow}$ [79], which is also denoted as spin-mixing parameter and defined as

$$\rho^{\uparrow\downarrow} = \langle 1 - 2|S_{\mathbf{k}}^z| \rangle_{\text{FS}} \ . \tag{4.130}$$

Similar to $b_{\mathbf{k}}$, it should vanish in the absence of spin-orbit coupling. It is related to the averages of $|a_{\mathbf{k}}|^2$ and $|b_{\mathbf{k}}|^2$ over the Fermi surface according to

$$\left\langle |a_{\mathbf{k}}|^2 \right\rangle_{\text{FS}} = 1 - \frac{\rho^{\uparrow\downarrow}}{2} \qquad \text{and} \tag{4.131}$$

$$\left\langle |b_{\mathbf{k}}|^2 \right\rangle_{\text{FS}} = \frac{\rho^{\uparrow\downarrow}}{2}. \tag{4.132}$$

However, in this thesis we use the first definition of the spin-mixing parameter, i.e. $b_{\mathbf{k}}$.
The distributions of $|b_{\mathbf{k}}|^2$ on the Fermi surfaces of copper and gold are shown in figure 4.2; whereas a qualitative similarity can be observed for copper and gold, the order of magnitude of the absolute values differs strongly. As expected, the effect of spin-orbit coupling is much larger for gold than for copper.
Furthermore, we have calculated the spin-mixing parameter $\left\langle |b_{\mathbf{k}}|^2 \right\rangle_{\text{FS}} = \rho^{\uparrow\downarrow}/2$ averaged over the Fermi surface. The results for calculations within the atomic sphere approximation as

		ASA		FP	
		S^z = max.	$S^x = S^y = 0$	S^z = max.	$S^x = S^y = 0$
Cu	our results	$1.13 \cdot 10^{-3}$	$1.13 \cdot 10^{-3}$	$9.81 \cdot 10^{-4}$	$9.82 \cdot 10^{-4}$
	other calc.		$1.5 \cdot 10^{-3}$		
Au	our results	$3.16 \cdot 10^{-2}$	$3.27 \cdot 10^{-2}$	$2.15 \cdot 10^{-2}$	$2.20 \cdot 10^{-2}$
	other calc.		$3.0 \cdot 10^{-2}$		

Table 4.2.: Spin-mixing parameters $\left\langle |b_{\mathbf{k}}|^2 \right\rangle_{\mathrm{FS}} = \rho^{\uparrow\downarrow}/2$ averaged over the Fermi surface of copper and gold. Comparison of our results to numerical data from ref. [79]. Note that in ref. [79], data are given in $\rho^{\uparrow\downarrow}$ and are therefore twice as large as the values specified here.

well as full-potential calculations can be found in table 4.2 together with numerical data from [79][3]; especially for gold, large differences between the full potential calculation and that within the atomic sphere approximation can be observed. Considering this argument, the agreement of our spin mixing parameters with those from reference [79] is reasonable.

4.6.2 Inequivalence of the conditions S^z = max. and $S^x = S^y = 0$ in a simple model

In order to demonstrate that the two conditions eq. (4.118) and eq. (4.119) do not lead to the same result we construct a simple model system consisting of two bands $E_>(\mathbf{k})$ and $E_<(\mathbf{k})$, where the latter one is chosen to have a lower energy. The states around each $\mathbf{k}$-point are linear combinations of the s-orbital s_0 and the three p-orbitals ϕ_x, ϕ_y and ϕ_z. Without spin-orbit coupling, the wavefunction at $\mathbf{k}$ in the upper band is

$$|\psi_0\rangle = a_\psi\phi_x + b_\psi\phi_y + c_\psi\phi_z + d_\psi s_0 \,, \tag{4.133}$$

and in the lower band

$$|\chi_0\rangle = a_\chi\phi_x + b_\chi\phi_y + c_\chi\phi_z + d_\chi s_0, \tag{4.134}$$

respectively. Treating spin-orbit coupling as a perturbation to first order in the spirit of Elliott [9] we obtain the perturbed states

$$|\chi^+\rangle = \begin{pmatrix} |\chi_0\rangle + \frac{\lambda}{2\Delta E}\langle\psi_0|L_z|\chi_0\rangle|\psi_0\rangle \\ \frac{\lambda}{2\Delta E}\langle\psi_0|L_x + iL_y|\chi_0\rangle|\psi_0\rangle \end{pmatrix} \tag{4.135}$$

and

$$|\chi^-\rangle = \begin{pmatrix} -\frac{\lambda}{2\Delta E}\langle\psi_0|L_x - iL_y|\chi_0\rangle|\psi_0\rangle \\ |\chi_0\rangle - \frac{\lambda}{2\Delta E}\langle\psi_0|L_z|\chi_0\rangle|\psi_0\rangle \end{pmatrix} \tag{4.136}$$

[3]Note that in ref. [79], data are given in terms of $\rho^{\uparrow\downarrow}$ and are therefore twice as large as the values specified in table 4.2.

with $\Delta E(\mathbf{k}) = E_>(\mathbf{k}) - E_<(\mathbf{k})$. Inserting the explicit forms of the wavefunctions $|\psi_0\rangle$ and $|\chi_0\rangle$ and applying the momentum operators L_x, L_y and L_z leads to

$$|\chi^+\rangle = \begin{pmatrix} |\chi_0\rangle + \frac{\lambda}{2\Delta E} i\gamma \, |\psi_0\rangle \\ \frac{\lambda}{2\Delta E} \left(\eta + i\zeta\right) |\psi_0\rangle \end{pmatrix} \tag{4.137}$$

and

$$|\chi^-\rangle = \begin{pmatrix} \frac{\lambda}{2\Delta E} \left(-\eta + i\zeta\right) |\psi_0\rangle \\ |\chi_0\rangle - \frac{\lambda}{2\Delta E} i\gamma \, |\psi_0\rangle \end{pmatrix}, \tag{4.138}$$

where the abbreviations

$$\eta \;=\; a_\psi^\star c_\chi - c_\psi^\star a_\chi \tag{4.139}$$

$$\zeta \;=\; b_\psi^\star c_\chi - c_\psi^\star b_\chi \tag{4.140}$$

$$\gamma \;=\; b_\psi^\star a_\chi - a_\psi^\star b_\chi \tag{4.141}$$

have been introduced. Naturally, expressions equivalent to eqs. (4.137, 4.138) can be found for $|\psi^+\rangle$ and $|\psi^-\rangle$ just by interchanging the two states χ and ψ. The two perturbed states $|\chi^+\rangle$ and $|\chi^-\rangle$ (or $|\psi^+\rangle$ and $|\psi^-\rangle$, respectively) are not normalized to 1, but they fulfill the conditions

$$\langle \chi^+|\chi^+\rangle \;=\; \langle \chi^-|\chi^-\rangle \qquad\qquad \text{and} \tag{4.142}$$

$$\langle \chi^+|\chi^-\rangle \;=\; \langle \chi^-|\chi^+\rangle = 0. \tag{4.143}$$

As can be easily shown, they have the same energy.
In the following, linear combinations of $|\chi^+\rangle$ and $|\chi^-\rangle$ are introduced, in the form

$$|\tilde{\chi}^+\rangle \;=\; +\cos\frac{\alpha}{2}\,|\chi^+\rangle + \sin\frac{\alpha}{2}e^{i\beta}\,|\chi^-\rangle \qquad\qquad \text{and} \tag{4.144}$$

$$|\tilde{\chi}^-\rangle \;=\; -\sin\frac{\alpha}{2}\,|\chi^+\rangle + \cos\frac{\alpha}{2}e^{i\beta}\,|\chi^-\rangle\,, \tag{4.145}$$

with α and β determined according to eqs. (4.121) such that the new states $|\tilde{\chi}\rangle$ fulfill the condition of S_z being maximal

$$\beta \;=\; \arg S^z_{\chi^+,\chi^-}$$

$$\alpha \;=\; \tan^{-1}\left[\frac{\mathrm{Re}\left[e^{i\beta} S^z_{\chi^+,\chi^-}\right]}{S^z_{\chi^+}}\right]. \tag{4.146}$$

Here, in analogy to eqs. (4.107) and (4.116) we have used the definitions of the expectation values

$$S^i_{\chi^\pm} \;=\; \langle \chi^\pm|\sigma^i|\chi^\pm\rangle \qquad\qquad \text{and} \tag{4.147}$$

$$S^i_{\chi^+,\chi^-} \;=\; \langle \chi^+|\sigma^i|\chi^-\rangle \qquad \text{for } i = x, y, z\,. \tag{4.148}$$

In the following, we will show that these new states do <u>not</u> fulfill

$$S^x_{\chi^+} + \tan\alpha\,\mathrm{Re}\left[e^{i\beta} S^x_{\chi^+,\chi^-}\right] = 0, \tag{4.149}$$

which is equivalent to eq. (4.123), i.e., the new states do no fulfill $S_x = S_y = 0$. The proof will be carried out by assuming that eqs. (4.146) and (4.149) are simultaneously fulfilled and by thus ending in a contradiction.

With

$$e^{i\beta} = \sqrt{\frac{S^{z\star}_{\chi^+,\chi^-}}{S^z_{\chi^+,\chi^-}}} \tag{4.150}$$

and

$$\tan\alpha = \frac{\mathrm{Re}\left[e^{i\beta} S^z_{\chi^+,\chi^-}\right]}{S^z_{\chi^+}} = \frac{\mathrm{Re}\left[\sqrt{\frac{S^{z\star}_{\chi^+,\chi^-}}{S^z_{\chi^+,\chi^-}}} S^z_{\chi^+,\chi^-}\right]}{S^z_{\chi^+}}, \tag{4.151}$$

equation (4.149) becomes

$$0 = S^x_{\chi^+} + \frac{\mathrm{Re}\left[\sqrt{S^{z\star}_{\chi^+,\chi^-} \cdot S^z_{\chi^+,\chi^-}}\right]}{S^z_{\chi^+}} \mathrm{Re}\left[\sqrt{\frac{S^{z\star}_{\chi^+,\chi^-}}{S^z_{\chi^+,\chi^-}}} S^x_{\chi^+,\chi^-}\right]. \tag{4.152}$$

Multiplication with $S^z_{\chi^+}$ yields

$$\begin{aligned}
0 &= S^x_{\chi^+} S^z_{\chi^+} + \left|S^z_{\chi^+,\chi^-}\right| \frac{1}{2}\left[\sqrt{\frac{S^{z\star}_{\chi^+,\chi^-}}{S^z_{\chi^+,\chi^-}}} S^x_{\chi^+,\chi^-} + \left(\sqrt{\frac{S^{z\star}_{\chi^+,\chi^-}}{S^z_{\chi^+,\chi^-}}}\right)^\star S^{x\star}_{\chi^+,\chi^-}\right] \\
&= S^x_{\chi^+} S^z_{\chi^+} + \frac{1}{2}\left[S^{z\star}_{\chi^+,\chi^-} S^x_{\chi^+,\chi^-} + S^z_{\chi^+,\chi^-} S^{x\star}_{\chi^+,\chi^-}\right]. \tag{4.153}
\end{aligned}$$

In order to demonstrate that the above equation is not fulfilled, the expectation values $S^z_{\chi^+,\chi^-} = \langle\chi^+|\sigma^z|\chi^-\rangle$, $S^z_{\chi^+} = \langle\chi^+|\sigma^z|\chi^+\rangle$, $S^x_{\chi^+,\chi^-} = \langle\chi^+|\sigma^x|\chi^-\rangle$ and $S^x_{\chi^+} = \langle\chi^+|\sigma^x|\chi^+\rangle$ must be determined explicitly. In terms of η, ζ and γ the expectation values are

$$\begin{aligned}
S^z_{\chi^+,\chi^-} = \langle\chi^+|\sigma^z|\chi^-\rangle &= \chi^{+\uparrow\star}\chi^{-\uparrow} - \chi^{+\downarrow\star}\chi^{-\downarrow} \tag{4.154} \\
&= \left(\frac{\lambda}{2\Delta E}\right)^2 \left[2\,\mathrm{Re}\left[\gamma^\star\zeta\right] + 2i\,\mathrm{Re}\left[\eta\gamma^\star\right]\right],
\end{aligned}$$

$$\begin{aligned}
S^z_{\chi^+,\chi^+} = \langle\chi^+|\sigma^z|\chi^+\rangle &= \chi^{+\uparrow\star}\chi^{+\uparrow} - \chi^{+\downarrow\star}\chi^{+\downarrow} \tag{4.155} \\
&= 1 + \left(\frac{\lambda}{2\Delta E}\right)^2 \left[|\gamma|^2 - |\eta|^2 - |\zeta|^2\right] \\
&= -\langle\chi^-|\sigma^z|\chi^-\rangle,
\end{aligned}$$

$$\begin{aligned}
S^x_{\chi^+,\chi^-} = \langle\chi^+|\sigma^x|\chi^-\rangle &= \chi^{+\uparrow\star}\chi^{-\downarrow} + \chi^{+\downarrow\star}\chi^{-\uparrow} \tag{4.156} \\
&= 1 - \left(\frac{\lambda}{2\Delta E}\right)^2 \left[|\gamma|^2 + |\eta|^2 - |\zeta|^2 - 2i\,\mathrm{Re}\left[\eta^\star\zeta\right]\right]
\end{aligned}$$

and

$$
\begin{aligned}
S^x_{\chi^+,\chi^+} = \langle \chi^+ | \sigma^x | \chi^+ \rangle &= \chi^{+\uparrow\star} \chi^{+\downarrow} + \chi^{+\downarrow\star} \chi^{+\uparrow} \qquad\qquad (4.157) \\
&= \left(\frac{\lambda}{2\Delta E} \right)^2 \left[2\,\mathrm{Re}\left[\zeta^\star \gamma \right] - 2\,\mathrm{Im}\left[\eta^\star \gamma \right] \right] \\
&= \left(\frac{\lambda}{2\Delta E} \right)^2 \left[2\,\mathrm{Re}\left[\zeta^\star \gamma \right] \right] \\
&= -\langle \chi^- | \sigma^x | \chi^- \rangle \,.
\end{aligned}
$$

The term $\mathrm{Im}\left[\eta^\star \gamma \right] = 0$ because the parameters η and γ represent expectation values of the angular momenta l_x and l_z which must be real.

Inserting the results of eqs. (4.155) to (4.158) in eq. (4.153) results in

$$
S^x_{\chi^+} S^z_{\chi^+} + \frac{1}{2} \left[S^{z\star}_{\chi^+,\chi^-} S^x_{\chi^+,\chi^-} + S^z_{\chi^+,\chi^-} S^{x\star}_{\chi^+,\chi^-} \right] = \left(\frac{\lambda}{2\Delta E} \right)^2 4\,\mathrm{Re}\left[\gamma^\star \zeta \right] \qquad (4.158)
$$

which in terms of the amplitudes a_χ, b_χ, c_χ and a_ψ, b_ψ, c_ψ becomes

$$
\left(\frac{\lambda}{2\Delta E} \right)^2 4\,\mathrm{Re}\left[\gamma^\star \zeta \right] =
$$
$$
\left(\frac{\lambda}{2\Delta E} \right)^2 4\,\mathrm{Re}\left[|b_\psi|^2 a^\star_\chi c_\chi + |b_\chi|^2 a^\star_\psi c_\psi - b_\psi b_\chi a^\star_\chi c^\star_\psi - b^\star_\psi b^\star_\chi a_\chi c_\psi \right]. \quad (4.159)
$$

For non-vanishing amplitudes and spin-orbit coupling parameter $\lambda \neq 0$ the above expression does not vanishes; therefore, we have proven that even in this simple model the two conditions $S^x = S^y = 0$ and $S^z = \max$ are not equivalent.

4.7 Impurity scattering within the presence of spin-orbit coupling

Finally, we want to consider scattering processes at an impurity in a system with spin-orbit coupling. In this case, both the scattering wavefunction due to the impurity

$$
\begin{aligned}
\begin{pmatrix} \psi^{\mathrm{imp}\uparrow}_{\mathbf{k}}(\mathbf{r}+\mathbf{R}^n; E) \\ \psi^{\mathrm{imp}\downarrow}_{\mathbf{k}}(\mathbf{r}+\mathbf{R}^n; E) \end{pmatrix} &= \sum_L \left[c^{\mathrm{imp}\uparrow n}_{\mathbf{k}L} \begin{pmatrix} R^{\mathrm{imp}\uparrow\uparrow n}_L(\mathbf{r}; E) \\ R^{\mathrm{imp}\downarrow\uparrow n}_L(\mathbf{r}; E) \end{pmatrix} + c^{\mathrm{imp}\downarrow n}_{\mathbf{k}L} \begin{pmatrix} R^{\mathrm{imp}\uparrow\downarrow n}_L(\mathbf{r}; E) \\ R^{\mathrm{imp}\downarrow\downarrow n}_L(\mathbf{r}; E) \end{pmatrix} \right] \\
&= \sum_{LL'} \begin{pmatrix} R^{\mathrm{imp}\uparrow\uparrow n}_{L'L}(r; E) & R^{\mathrm{imp}\uparrow\downarrow n}_{L'L}(r; E) \\ R^{\mathrm{imp}\downarrow\uparrow n}_{L'L}(r; E) & R^{\mathrm{imp}\downarrow\downarrow n}_{L'L}(r; E) \end{pmatrix} \begin{pmatrix} c^{\mathrm{imp}\uparrow n}_{\mathbf{k}L} \\ c^{\mathrm{imp}\downarrow n}_{\mathbf{k}L} \end{pmatrix} Y_{L'}(\hat{r})
\end{aligned} \qquad (4.160)
$$

and the wavefunction of the host system

$$
\begin{pmatrix} \psi^{\uparrow}_{\mathbf{k}}(\mathbf{r}+\mathbf{R}^n; E) \\ \psi^{\downarrow}_{\mathbf{k}}(\mathbf{r}+\mathbf{R}^n; E) \end{pmatrix} = \sum_{LL'} \begin{pmatrix} R^{\uparrow\uparrow n}_{L'L}(r; E) & R^{\uparrow\downarrow n}_{L'L}(r; E) \\ R^{\downarrow\uparrow n}_{L'L}(r; E) & R^{\downarrow\downarrow n}_{L'L}(r; E) \end{pmatrix} \begin{pmatrix} c^{\uparrow n}_{\mathbf{k}L} \\ c^{\downarrow n}_{\mathbf{k}L} \end{pmatrix} Y_{L'}(\hat{r}) \qquad (4.161)
$$

are spin-dependent. In order to establish a relation between the coefficients $\left(c_{\mathbf{k}L}^{\mathrm{imp}\uparrow n}, c_{\mathbf{k}L}^{\mathrm{imp}\downarrow n}\right)^T$ and $\left(c_{\mathbf{k}L}^{\uparrow n}, c_{\mathbf{k}L}^{\downarrow n}\right)^T$, the spin-dependent Lippmann-Schwinger equation has to be considered

$$
\begin{pmatrix} \psi_{\mathbf{k}}^{\mathrm{imp}\uparrow}(\mathbf{r} + \mathbf{R}^n; E) \\ \psi_{\mathbf{k}}^{\mathrm{imp}\downarrow}(\mathbf{r} + \mathbf{R}^n; E) \end{pmatrix} = \begin{pmatrix} \psi_{\mathbf{k}}^{\uparrow}(\mathbf{r} + \mathbf{R}^n; E) \\ \psi_{\mathbf{k}}^{\downarrow}(\mathbf{r} + \mathbf{R}^n; E) \end{pmatrix}
$$
$$
+ \sum_{n'} \int d^3 r' \begin{pmatrix} G^{\uparrow\uparrow}(\mathbf{r} + \mathbf{R}^n, \mathbf{r}' + \mathbf{R}^{n'}; E) & G^{\uparrow\downarrow}(\mathbf{r} + \mathbf{R}^n, \mathbf{r}' + \mathbf{R}^{n'}; E) \\ G^{\downarrow\uparrow}(\mathbf{r} + \mathbf{R}^n, \mathbf{r}' + \mathbf{R}^{n'}; E) & G^{\downarrow\downarrow}(\mathbf{r} + \mathbf{R}^n, \mathbf{r}' + \mathbf{R}^{n'}; E) \end{pmatrix}
$$
$$
\cdot \begin{pmatrix} \Delta V^{\uparrow\uparrow}(\mathbf{r}') & \Delta V^{\uparrow\downarrow}(\mathbf{r}') \\ \Delta V^{\downarrow\uparrow}(\mathbf{r}') & \Delta V^{\downarrow\downarrow}(\mathbf{r}') \end{pmatrix} \begin{pmatrix} \psi_{\mathbf{k}}^{\mathrm{imp}\uparrow}(\mathbf{r}' + \mathbf{R}^{n'}; E) \\ \psi_{\mathbf{k}}^{\mathrm{imp}\downarrow}(\mathbf{r}' + \mathbf{R}^{n'}; E) \end{pmatrix}. \quad (4.162)
$$

The Green function has now non-zero off-diagonal elements, both the single-site term and the back-scattering term, if spin-orbit effects in the host are taken into account, too. The single-site term can be written as

$$
\begin{pmatrix} G^{\mathrm{s.s.}\uparrow\uparrow}(\mathbf{r} + \mathbf{R}^n, \mathbf{r}' + \mathbf{R}^{n'}; E) & G^{\mathrm{s.s.}\uparrow\downarrow}(\mathbf{r} + \mathbf{R}^n, \mathbf{r}' + \mathbf{R}^{n'}; E) \\ G^{\mathrm{s.s.}\downarrow\uparrow}(\mathbf{r} + \mathbf{R}^n, \mathbf{r}' + \mathbf{R}^{n'}; E) & G^{\mathrm{s.s.}\downarrow\downarrow}(\mathbf{r} + \mathbf{R}^n, \mathbf{r}' + \mathbf{R}^{n'}; E) \end{pmatrix}
$$
$$
= \sum_{LL'} Y_L(\hat{r}) \begin{pmatrix} G_{LL'}^{\mathrm{s.s.}\uparrow\uparrow}(r, r'; E) & G_{LL'}^{\mathrm{s.s.}\uparrow\downarrow}(r, r'; E) \\ G_{LL'}^{\mathrm{s.s.}\downarrow\uparrow}(r, r'; E) & G_{LL'}^{\mathrm{s.s.}\downarrow\downarrow}(r, r'; E) \end{pmatrix} Y_{L'}(\hat{r}') \quad (4.163)
$$

with

$$
G_{LL'}^{\mathrm{s.s.}\sigma\sigma'}(r, r'; E) = -i\sqrt{E} \begin{cases} \sum_{L''} \sum_{\sigma''} R_{LL''}^{\sigma\sigma''}(r; E) H_{L'L''}^{\sigma''\sigma'}(r'; E) & \text{for } r \leq r' \\ \sum_{L''} \sum_{\sigma''} H_{LL''}^{\sigma\sigma''}(r; E) R_{L'L''}^{\sigma''\sigma'}(r'; E) & \text{for } r > r' \end{cases}. \quad (4.164)
$$

The back-scattering term is

$$
\begin{pmatrix} G^{\mathrm{b.s.}\uparrow\uparrow}(\mathbf{r} + \mathbf{R}^n, \mathbf{r}' + \mathbf{R}^{n'}; E) & G^{\mathrm{b.s.}\uparrow\downarrow}(\mathbf{r} + \mathbf{R}^n, \mathbf{r}' + \mathbf{R}^{n'}; E) \\ G^{\mathrm{b.s.}\downarrow\uparrow}(\mathbf{r} + \mathbf{R}^n, \mathbf{r}' + \mathbf{R}^{n'}; E) & G^{\mathrm{b.s.}\downarrow\downarrow}(\mathbf{r} + \mathbf{R}^n, \mathbf{r}' + \mathbf{R}^{n'}; E) \end{pmatrix} \quad (4.165)
$$
$$
= \sum_{LL'} \sum_{\sigma\sigma'} \begin{pmatrix} R_L^{\uparrow\sigma}(\mathbf{r}) G_{LL'}^{\sigma\sigma'nn'}(E) R_{L'}^{\uparrow\sigma'}(\mathbf{r}') & R_L^{\uparrow\sigma}(\mathbf{r}) G_{LL'}^{\sigma\sigma'nn'}(E) R_{L'}^{\downarrow\sigma'}(\mathbf{r}') \\ R_L^{\downarrow\sigma}(\mathbf{r}) G_{LL'}^{\sigma\sigma'nn'}(E) R_{L'}^{\uparrow\sigma'}(\mathbf{r}') & R_L^{\downarrow\sigma}(\mathbf{r}) G_{LL'}^{\sigma\sigma'nn'}(E) R_{L'}^{\downarrow\sigma'}(\mathbf{r}') \end{pmatrix}
$$
$$
= \sum_{LL'} \sum_{L''L'''} \sum_{\sigma\sigma'} Y_{L''}(\hat{r}) Y_{L'''}(\hat{r}')
$$
$$
\begin{pmatrix} R_{L''L}^{\uparrow\sigma}(r) G_{LL'}^{\sigma\sigma'nn'}(E) R_{L'''L'}^{\uparrow\sigma'}(r') & R_{L''L}^{\uparrow\sigma}(r) G_{LL'}^{\sigma\sigma'nn'}(E) R_{L'''L'}^{\downarrow\sigma'}(r') \\ R_{L''L}^{\downarrow\sigma}(r) G_{LL'}^{\sigma\sigma'nn'}(E) R_{L'''L'}^{\uparrow\sigma'}(r') & R_{L''L}^{\downarrow\sigma}(r) G_{LL'}^{\sigma\sigma'nn'}(E) R_{L'''L'}^{\downarrow\sigma'}(r') \end{pmatrix}.
$$

For the following derivation, it will be helpful to decompose the last matrix in a product of three matrices

$$
\sum_{\sigma\sigma'} \begin{pmatrix} R_{L''L}^{\uparrow\sigma}(r) G_{LL'}^{\sigma\sigma'nn'}(E) R_{L'''L'}^{\uparrow\sigma'}(r') & R_{L''L}^{\uparrow\sigma}(r) G_{LL'}^{\sigma\sigma'nn'}(E) R_{L'''L'}^{\downarrow\sigma'}(r') \\ R_{L''L}^{\downarrow\sigma}(r) G_{LL'}^{\sigma\sigma'nn'}(E) R_{L'''L'}^{\uparrow\sigma'}(r') & R_{L''L}^{\downarrow\sigma}(r) G_{LL'}^{\sigma\sigma'nn'}(E) R_{L'''L'}^{\downarrow\sigma'}(r') \end{pmatrix} =
$$
$$
\begin{pmatrix} R_{L''L}^{\uparrow\uparrow}(r) & R_{L''L}^{\uparrow\downarrow}(r) \\ R_{L''L}^{\downarrow\uparrow}(r) & R_{L''L}^{\downarrow\downarrow}(r) \end{pmatrix} \cdot \begin{pmatrix} G_{LL'}^{\uparrow\uparrow nn'}(E) & G_{LL'}^{\uparrow\downarrow nn'}(E) \\ G_{LL'}^{\downarrow\uparrow nn'}(E) & G_{LL'}^{\downarrow\downarrow nn'}(E) \end{pmatrix} \cdot \begin{pmatrix} R_{L'''L'}^{\uparrow\uparrow}(r') & R_{L'''L'}^{\uparrow\downarrow}(r') \\ R_{L'''L'}^{\downarrow\uparrow}(r') & R_{L'''L'}^{\downarrow\downarrow}(r') \end{pmatrix} \cdot
$$
$$
\quad (4.166)
$$

The matrix containing the difference in potential is given by

$$
\begin{pmatrix} \Delta V^{\uparrow\uparrow}(\mathbf{r'}) & \Delta V^{\uparrow\downarrow}(\mathbf{r'}) \\ \Delta V^{\downarrow\uparrow}(\mathbf{r'}) & \Delta V^{\downarrow\downarrow}(\mathbf{r'}) \end{pmatrix} = \begin{pmatrix} V_{\mathrm{imp}}^{\uparrow\uparrow}(\mathbf{r'}) & V_{\mathrm{imp}}^{\uparrow\downarrow}(\mathbf{r'}) \\ V_{\mathrm{imp}}^{\downarrow\uparrow}(\mathbf{r'}) & V_{\mathrm{imp}}^{\downarrow\downarrow}(\mathbf{r'}) \end{pmatrix} - \begin{pmatrix} V^{\uparrow\uparrow}(\mathbf{r'}) & V^{\uparrow\downarrow}(\mathbf{r'}) \\ V^{\downarrow\uparrow}(\mathbf{r'}) & V^{\downarrow\downarrow}(\mathbf{r'}) \end{pmatrix}. \quad (4.167)
$$

Hence, it is the difference between the system including an impurity and spin-orbit coupling and the host system under the presence of spin-orbit coupling.

In order to derive the coefficients of the impurity wavefunction in terms of the coefficients of the host, one has to proceed like in the case of a full-potential wavefunction described in section 3.2, but taking the two spin components into account. Inserting the orbital expansions (4.160), (4.161), (4.163) and (4.165) in the Lippmann-Schwinger equation (4.162), integrating over the spherical coordinates and using the Lippmann-Schwinger equation of the radial wavefunction of the impurity

$$
\begin{pmatrix} R_{L_1L}^{\mathrm{imp}\uparrow\uparrow n}(r;E) & R_{L_1L}^{\mathrm{imp}\uparrow\downarrow n}(r;E) \\ R_{L_1L}^{\mathrm{imp}\downarrow\uparrow n}(r;E) & R_{L_1L}^{\mathrm{imp}\downarrow\downarrow n}(r;E) \end{pmatrix} = \begin{pmatrix} R_{L_1L}^{\uparrow\uparrow n}(r;E) & R_{L_1L}^{\uparrow\downarrow n}(r;E) \\ R_{L_1L}^{\downarrow\uparrow n}(r;E) & R_{L_1L}^{\downarrow\downarrow n}(r;E) \end{pmatrix} +
$$

$$
\int r'^2 dr' \sum_{L_2} \begin{pmatrix} G_{L_1L_2}^{\mathrm{s.s.}\uparrow\uparrow}(r,r';E) & G_{L_1L_2}^{\mathrm{s.s.}\uparrow\downarrow}(r,r';E) \\ G_{L_1L_2}^{\mathrm{s.s.}\downarrow\uparrow}(r,r';E) & G_{L_1L_2}^{\mathrm{s.s.}\downarrow\downarrow}(r,r';E) \end{pmatrix} \sum_{L_4} \begin{pmatrix} \Delta V_{L_2L_4}^{\uparrow\uparrow}(r') & \Delta V_{L_2L_4}^{\uparrow\downarrow}(r') \\ \Delta V_{L_2L_4}^{\downarrow\uparrow}(r') & \Delta V_{L_2L_4}^{\downarrow\downarrow}(r') \end{pmatrix}
$$

$$
\begin{pmatrix} R_{L_4L}^{\mathrm{imp}\uparrow\uparrow n}(r';E) & R_{L_4L}^{\mathrm{imp}\uparrow\downarrow n}(r';E) \\ R_{L_4L}^{\mathrm{imp}\downarrow\uparrow n}(r';E) & R_{L_4L}^{\mathrm{imp}\downarrow\downarrow n}(r';E) \end{pmatrix} \quad (4.168)
$$

as well as the expression for the Δt-matrix

$$
\begin{pmatrix} \Delta t_{L_1L_2}^{n\uparrow\uparrow}(E) & \Delta t_{L_1L_2}^{n\uparrow\downarrow}(E) \\ \Delta t_{L_1L_2}^{n\downarrow\uparrow}(E) & \Delta t_{L_1L_2}^{n\downarrow\downarrow}(E) \end{pmatrix} = \int r^2 dr \sum_{L_3} \begin{pmatrix} R_{L_3L_1}^{n\uparrow\uparrow}(r;E) & R_{L_3L_1}^{n\uparrow\downarrow}(r;E) \\ R_{L_3L_1}^{n\downarrow\uparrow}(r;E) & R_{L_3L_1}^{n\downarrow\downarrow}(r;E) \end{pmatrix}
$$

$$
\sum_{L_5} \begin{pmatrix} \Delta V_{L_3L_5}^{n\uparrow\uparrow}(r) & \Delta V_{L_3L_5}^{n\uparrow\downarrow}(r) \\ \Delta V_{L_3L_5}^{n\downarrow\uparrow}(r) & \Delta V_{L_3L_5}^{n\downarrow\downarrow}(r) \end{pmatrix} \begin{pmatrix} R_{L_5L_2}^{\mathrm{imp}\uparrow\uparrow n}(r;E) & R_{L_5L_2}^{\mathrm{imp}\uparrow\downarrow n}(r;E) \\ R_{L_5L_2}^{\mathrm{imp}\downarrow\uparrow n}(r;E) & R_{L_5L_2}^{\mathrm{imp}\downarrow\downarrow n}(r;E) \end{pmatrix} \quad (4.169)
$$

yields the simplified equation

$$
\sum_L \begin{pmatrix} R_{L_1L}^{\uparrow\uparrow n}(r;E) & R_{L_1L}^{\uparrow\downarrow n}(r;E) \\ R_{L_1L}^{\downarrow\uparrow n}(r;E) & R_{L_1L}^{\downarrow\downarrow n}(r;E) \end{pmatrix} \begin{pmatrix} c_{\mathbf{k}L}^{\mathrm{imp}\uparrow n} \\ c_{\mathbf{k}L}^{\mathrm{imp}\downarrow n} \end{pmatrix} =
$$

$$
\sum_L \begin{pmatrix} R_{L_1L}^{\uparrow\uparrow n}(r;E) & R_{L_1L}^{\uparrow\downarrow n}(r;E) \\ R_{L_1L}^{\downarrow\uparrow n}(r;E) & R_{L_1L}^{\downarrow\downarrow n}(r;E) \end{pmatrix} \begin{pmatrix} c_{\mathbf{k}L}^{\uparrow n} \\ c_{\mathbf{k}L}^{\downarrow n} \end{pmatrix}
$$

$$
+ \sum_{n'} \sum_{L_2L_3L} \begin{pmatrix} R_{L_1L_3}^{\uparrow\uparrow}(r) & R_{L_1L_3}^{\uparrow\downarrow}(r) \\ R_{L_1L_3}^{\downarrow\uparrow}(r) & R_{L_1L_3}^{\downarrow\downarrow}(r) \end{pmatrix} \begin{pmatrix} G_{L_3L_2}^{\uparrow\uparrow nn'}(E) & G_{L_3L_2}^{\uparrow\downarrow nn'}(E) \\ G_{L_3L_2}^{\downarrow\uparrow nn'}(E) & G_{L_3L_2}^{\downarrow\downarrow nn'}(E) \end{pmatrix} \quad (4.170)
$$

$$
\cdot \begin{pmatrix} \Delta t_{L_2L}^{\uparrow\uparrow}(E) & \Delta t_{L_2L}^{\uparrow\downarrow}(E) \\ \Delta t_{L_2L}^{\downarrow\uparrow}(E) & \Delta t_{L_2L}^{\downarrow\downarrow}(E) \end{pmatrix} \begin{pmatrix} c_{\mathbf{k}L}^{\mathrm{imp}\uparrow n} \\ c_{\mathbf{k}L}^{\mathrm{imp}\downarrow n} \end{pmatrix}.
$$

The above eq. (4.170) can be reduced to

$$
\begin{pmatrix} c_{\mathbf{k}L}^{\text{imp}\uparrow n} \\ c_{\mathbf{k}L}^{\text{imp}\downarrow n} \end{pmatrix} = \begin{pmatrix} c_{\mathbf{k}L}^{\uparrow n} \\ c_{\mathbf{k}L}^{\downarrow n} \end{pmatrix}
$$
$$
+ \sum_{n'} \sum_{L_2 L_3} \begin{pmatrix} G_{LL_2}^{\uparrow\uparrow nn'}(E) & G_{LL_2}^{\uparrow\downarrow nn'}(E) \\ G_{LL_2}^{\downarrow\uparrow nn'}(E) & G_{LL_2}^{\downarrow\downarrow nn'}(E) \end{pmatrix} \begin{pmatrix} \Delta t_{L_2 L_3}^{\uparrow\uparrow}(E) & \Delta t_{L_2 L_3}^{\uparrow\downarrow}(E) \\ \Delta t_{L_2 L_3}^{\downarrow\uparrow}(E) & \Delta t_{L_2 L_3}^{\downarrow\downarrow}(E) \end{pmatrix} \begin{pmatrix} c_{\mathbf{k}L_3}^{\text{imp}\uparrow n} \\ c_{\mathbf{k}L_3}^{\text{imp}\downarrow n} \end{pmatrix}, \quad (4.171)
$$

which finally leads to the sought-after relation between the impurity coefficients $\begin{pmatrix} c_{\mathbf{k}L}^{\text{imp}\uparrow n} \\ c_{\mathbf{k}L}^{\text{imp}\downarrow n} \end{pmatrix}$

and the host coefficients $\begin{pmatrix} c_{\mathbf{k}L}^{\uparrow n} \\ c_{\mathbf{k}L}^{\downarrow n} \end{pmatrix}$

$$
\begin{pmatrix} c_{\mathbf{k}L}^{\uparrow n} \\ c_{\mathbf{k}L}^{\downarrow n} \end{pmatrix} = \sum_{n'} \sum_{L'L''} \left[\begin{pmatrix} \delta_{nn'}\delta_{LL'}\delta_{LL''} & 0 \\ 0 & \delta_{nn'}\delta_{LL'}\delta_{LL''} \end{pmatrix} \right.
$$
$$
\left. - \begin{pmatrix} G_{LL'}^{\uparrow\uparrow nn'}(E) & G_{LL'}^{\uparrow\downarrow nn'}(E) \\ G_{LL'}^{\downarrow\uparrow nn'}(E) & G_{LL'}^{\downarrow\downarrow nn'}(E) \end{pmatrix} \begin{pmatrix} \Delta t_{L'L''}^{\uparrow\uparrow} & \Delta t_{L'L''}^{\uparrow\downarrow} \\ \Delta t_{L'L''}^{\downarrow\uparrow} & \Delta t_{L'L''}^{\downarrow\downarrow} \end{pmatrix} \right] \begin{pmatrix} c_{\mathbf{k}L''}^{\text{imp}\uparrow n'} \\ c_{\mathbf{k}L''}^{\text{imp}\downarrow n'} \end{pmatrix}. \quad (4.172)
$$

In a simplified matrix notation, the above result can be written as

$$
\begin{pmatrix} \mathbf{c}_{\mathbf{k}}^{\text{imp}\uparrow} \\ \mathbf{c}_{\mathbf{k}}^{\text{imp}\downarrow} \end{pmatrix} = \left[\begin{pmatrix} 1 & 0 \\ 0 & 1 \end{pmatrix} - \begin{pmatrix} G^{\uparrow\uparrow}(E) & G^{\uparrow\downarrow}(E) \\ G^{\downarrow\uparrow}(E) & G^{\downarrow\downarrow}(E) \end{pmatrix} \begin{pmatrix} \Delta t^{\uparrow\uparrow} & \Delta t^{\uparrow\downarrow} \\ \Delta t^{\downarrow\uparrow} & \Delta t^{\downarrow\downarrow} \end{pmatrix} \right]^{-1} \begin{pmatrix} \mathbf{c}_{\mathbf{k}}^{\uparrow} \\ \mathbf{c}_{\mathbf{k}}^{\downarrow} \end{pmatrix}. \quad (4.173)
$$

or, skipping the spin indices, as

$$
\mathbf{c}_{\mathbf{k}}^{\text{imp}} = \left[1 - \mathbf{G}(E) \cdot \Delta t \right]^{-1} \mathbf{c}_{\mathbf{k}}. \quad (4.174)
$$

In analogy to the impurity coefficients without spin-orbit coupling, section 3.2, eq. (3.65), the latter relation can be formulated in terms of the structural Green function of the impurity $G^{\text{imp}}(E)$

$$
\mathbf{c}_{\mathbf{k}}^{\text{imp}} = \left[1 + \mathbf{G}^{\text{imp}}(E) \cdot \Delta t \right] \mathbf{c}_{\mathbf{k}}, \quad (4.175)
$$

which is used in the calculations of this thesis.

4.8 The spin-dependent scattering matrix $T_{\mathbf{kk}'}^{\sigma\sigma'}$

In the last section, we have used the Lippmann-Schwinger equation to establish a relation between the wavefunction of an arbitrary host system under the presence of spin-orbit coupling and the same system perturbed by an impurity. Therefore, these two systems differ in their potentials $\Delta V(\mathbf{r})$, which is a 2×2-matrix in spin-space. Using the relations of the previous section allows us to find the spin-dependent scattering matrix $T_{\mathbf{kk}'}^{\sigma\sigma'}$ for scattering processes mediated by the potential difference $\Delta V(\mathbf{r})$, quantifying the scattering amplitude

for scattering from a state characterized by $\mathbf{k}'$ with spin σ' to another state of momentum $\mathbf{k}$ and spin σ. In particular, we have in mind that the Fermi surface of the host shows a Kramers degeneracy as described in section 4.6. Then, the host states at $\mathbf{k}$ have to be chosen by a criterion, e.g. $S_x = S_y = 0$. An additional quantum number $\sigma = (\uparrow, \downarrow)$ indicates then the choice of $S_z > 0$ or $S_z < 0$. This particular σ enters in the definition of the scattering matrix $T_{\mathbf{k}\mathbf{k}'}^{\sigma\sigma'}$. In case of absence of spin-orbit coupling in the host, σ is reduced to a pure spin quantum number. For a deeper analysis, we refer the reader to chapter 6.

Hence, the spin-dependent scattering matrix $T_{\mathbf{k}\mathbf{k}'}^{\sigma\sigma'}$ yields

$$
\begin{aligned}
T_{\mathbf{k}\mathbf{k}'}^{\sigma\sigma'} &= \int d^3r \begin{pmatrix} \psi_{\mathbf{k}}^{\sigma',\uparrow}(\mathbf{r};E) \\ \psi_{\mathbf{k}}^{\sigma',\downarrow}(\mathbf{r};E) \end{pmatrix}^{\dagger} \begin{pmatrix} \Delta V^{\uparrow\uparrow}(\mathbf{r}) & \Delta V^{\uparrow\downarrow}(\mathbf{r}) \\ \Delta V^{\downarrow\uparrow}(\mathbf{r}) & \Delta V^{\downarrow\downarrow}(\mathbf{r}) \end{pmatrix} \begin{pmatrix} \psi_{\mathbf{k}'}^{\mathrm{imp},\sigma,\uparrow}(\mathbf{r};E) \\ \psi_{\mathbf{k}'}^{\mathrm{imp},\sigma,\downarrow}(\mathbf{r};E) \end{pmatrix} \qquad (4.176)\\[2mm]
&= \sum_n \int_{V_n} d^3r \sum_{LL'} \left[\begin{pmatrix} R_{L'L}^{\uparrow\uparrow n}(r;E) & R_{L'L}^{\uparrow\downarrow n}(r;E) \\ R_{L'L}^{\downarrow\uparrow n}(r;E) & R_{L'L}^{\downarrow\downarrow n}(r;E) \end{pmatrix} \begin{pmatrix} c_{\mathbf{k}L}^{\sigma',\uparrow n} \\ c_{\mathbf{k}L}^{\sigma',\downarrow n} \end{pmatrix} \right]^{\dagger} Y_{L'}(\hat{r})\\[2mm]
&\qquad \sum_{L''} \begin{pmatrix} \Delta V_{L''}^{n\uparrow\uparrow}(r) & \Delta V_{L''}^{n\uparrow\downarrow}(r) \\ \Delta V_{L''}^{n\downarrow\uparrow}(r) & \Delta V_{L''}^{n\downarrow\downarrow}(r) \end{pmatrix} Y_{L''}(\hat{r})\\[2mm]
&\qquad \sum_{L'''L''''} \begin{pmatrix} R_{L'''L'''}^{\mathrm{imp}\uparrow\uparrow n}(r;E) & R_{L'''L'''}^{\mathrm{imp}\uparrow\downarrow n}(r;E) \\ R_{L'''L'''}^{\mathrm{imp}\downarrow\uparrow n}(r;E) & R_{L'''L'''}^{\mathrm{imp}\downarrow\downarrow n}(r;E) \end{pmatrix} \begin{pmatrix} c_{\mathbf{k}'L'''}^{\mathrm{imp},\sigma,\uparrow n} \\ c_{\mathbf{k}'L'''}^{\mathrm{imp},\sigma,\downarrow n} \end{pmatrix} Y_{L''''}(\hat{r})\\[2mm]
&= \sum_n \int r^2 dr \sum_{LL'L'''L''''} \begin{pmatrix} c_{\mathbf{k}L}^{*,\sigma',\uparrow,n} & c_{\mathbf{k}L}^{*,\sigma',\downarrow,n} \end{pmatrix} \begin{pmatrix} R_{L'L}^{*\uparrow\uparrow n}(r;E) & R_{L'L}^{*\downarrow\uparrow n}(r;E) \\ R_{L'L}^{*\uparrow\downarrow n}(r;E) & R_{L'L}^{*\downarrow\downarrow n}(r;E) \end{pmatrix}\\[2mm]
&\qquad \begin{pmatrix} \Delta V_{L'L''''}^{n\uparrow\uparrow}(r) & \Delta V_{L'L''''}^{n\uparrow\downarrow}(r) \\ \Delta V_{L'L''''}^{n\downarrow\uparrow}(r) & \Delta V_{L'L''''}^{n\downarrow\downarrow}(r) \end{pmatrix} \begin{pmatrix} R_{L'''L'''}^{\mathrm{imp}\uparrow\uparrow n}(r;E) & R_{L'''L'''}^{\mathrm{imp}\uparrow\downarrow n}(r;E) \\ R_{L'''L'''}^{\mathrm{imp}\downarrow\uparrow n}(r;E) & R_{L'''L'''}^{\mathrm{imp}\downarrow\downarrow n}(r;E) \end{pmatrix} \begin{pmatrix} c_{\mathbf{k}'L'''}^{\mathrm{imp},\sigma,\uparrow n} \\ c_{\mathbf{k}'L'''}^{\mathrm{imp},\sigma,\downarrow n} \end{pmatrix}.
\end{aligned}
$$

By defining the Δ-matrix (in analogy to the definition (3.70) in section 3.3) as

$$
\begin{aligned}
\begin{pmatrix} \Delta_{LL'}^{\uparrow\uparrow n}(r;E) & \Delta_{LL'}^{\uparrow\downarrow n}(r;E) \\ \Delta_{LL'}^{\downarrow\uparrow n}(r;E) & \Delta_{LL'}^{\downarrow\downarrow n}(r;E) \end{pmatrix} &= \int r^2 dr \sum_{L''L'''} \begin{pmatrix} R_{L''L}^{*\uparrow\uparrow n}(r;E) & R_{L''L}^{*\downarrow\uparrow n}(r;E) \\ R_{L''L}^{*\uparrow\downarrow n}(r;E) & R_{L''L}^{*\downarrow\downarrow n}(r;E) \end{pmatrix}\\[2mm]
&\quad \begin{pmatrix} \Delta V_{L''L'''}^{n\uparrow\uparrow}(r) & \Delta V_{L''L'''}^{n\uparrow\downarrow}(r) \\ \Delta V_{L''L'''}^{n\downarrow\uparrow}(r) & \Delta V_{L''L'''}^{n\downarrow\downarrow}(r) \end{pmatrix} \begin{pmatrix} R_{L'''L'}^{\mathrm{imp}\uparrow\uparrow n}(r;E) & R_{L'''L'}^{\mathrm{imp}\uparrow\downarrow n}(r;E) \\ R_{L'''L'}^{\mathrm{imp}\downarrow\uparrow n}(r;E) & R_{L'''L'}^{\mathrm{imp}\downarrow\downarrow n}(r;E) \end{pmatrix},
\end{aligned}
$$

the above relation can be simplified to

$$
T_{\mathbf{k}\mathbf{k}'}^{\sigma\sigma'} = \sum_n \sum_{LL'} \begin{pmatrix} c_{\mathbf{k}L}^{*,\sigma',\uparrow,n} & c_{\mathbf{k}L}^{*,\sigma',\downarrow,n} \end{pmatrix} \begin{pmatrix} \Delta_{LL'}^{\uparrow\uparrow n}(E) & \Delta_{LL'}^{\uparrow\downarrow n}(E) \\ \Delta_{LL'}^{\downarrow\uparrow n}(E) & \Delta_{LL'}^{\downarrow\downarrow n}(E) \end{pmatrix} \begin{pmatrix} c_{\mathbf{k}'L'}^{\mathrm{imp},\sigma,\uparrow n} \\ c_{\mathbf{k}'L'}^{\mathrm{imp},\sigma,\downarrow n} \end{pmatrix}. \qquad (4.177)
$$

4.9 Momentum- and spin-relaxation times τ and T_1

In the same way as presented for systems without spin-orbit coupling in chapter 3, section 3.5, the transition probability for scattering from a state characterized by $\mathbf{k}$, σ into a state with $\mathbf{k}'$, σ' is given by

$$
P_{\mathbf{k}'\mathbf{k}}^{\sigma'\sigma} = \frac{2\pi}{\hbar} N c \left| T_{\mathbf{k}'\mathbf{k}}^{\sigma'\sigma} \right|^2 \delta(E_{\mathbf{k}} - E_{\mathbf{k}'}). \qquad (4.178)
$$

The inverse of the spin-conserving scattering times $\tau_{\mathbf{k}}^{\uparrow\uparrow}$, $\tau_{\mathbf{k}}^{\downarrow\downarrow}$ and the spin-flip scattering times $\tau_{\mathbf{k}}^{\uparrow\downarrow}$, $\tau_{\mathbf{k}}^{\downarrow\uparrow}$ are then determined by summation over all states $\mathbf{k}'$

$$
\begin{aligned}
\left(\tau_{\mathbf{k}}^{\sigma'\sigma}\right)^{-1} &= \sum_{\mathbf{k}'} P_{\mathbf{k}'\mathbf{k}}^{\sigma'\sigma} \\
&= \frac{2\pi N c}{V_{\mathrm{BZ}}\hbar^2} \int_{S(E_{\mathrm{F}})} \frac{dS_{\mathbf{k}'}}{v_{\mathbf{k}'}} \left|T_{\mathbf{k}'\mathbf{k}}^{\sigma'\sigma}\right|^2 .
\end{aligned}
\tag{4.179}
$$

The relaxation times averaged over the Fermi surface are then obtained via

$$
\frac{1}{\tau^{\sigma'\sigma}} = \frac{1}{V_{\mathrm{BZ}}} \int_{S(E_{\mathrm{F}})} \frac{dS_{\mathbf{k}}}{\hbar v_{\mathbf{k}}} \tau_{\mathbf{k}}^{\sigma'\sigma} .
\tag{4.180}
$$

In accordance with reference [80] we define the momentum-relaxation time τ by

$$
\tau = 2 \left(\frac{1}{\tau^{\uparrow\uparrow}} + \frac{1}{\tau^{\downarrow\downarrow}}\right)^{-1}
\tag{4.181}
$$

and the spin-relaxation time T_1 by

$$
T_1 = \left(\frac{1}{\tau^{\uparrow\downarrow}} + \frac{1}{\tau^{\downarrow\uparrow}}\right)^{-1} .
\tag{4.182}
$$

Implementation and testing of the spin-orbit coupling

5.1 Computational details

As illustrated in chapter 4, section 4.3.1, the calculation of the wavefunctions including spin-orbit coupling requires the solution of the Lippmann-Schwinger equation. The Lippmann-Schwinger equation can be either solved in a Born series by a relatively simple iteration, or, better, by making use of the so-called Volterra method [66]. The Volterra method also implies an iteration scheme, and it is already implemented to solve the Lippmann-Schwinger equation for full-potential calculations, eq. (2.76).

In both methods each iteration step comprises integrations over products of the wavefunctions and the spin-orbit Hamiltonian[1]. However, for calculations within the scalar-relativistic approximation (SRA), small numerical instabilities arising from the product of the large spin-orbit Hamiltonian for small r with the very small value of the regular wavefunctions lead to strong fluctuations of numerical origin after a couple of iterations, and therefore to a divergence of the Born series. This problem does not appear in the full-potential problem without spin-orbit coupling, because the perturbation caused by the non-spherical components of the potential vanishes close to the nucleus.

In order to solve this numerical problem and achieve convergence of the Lippmann-Schwinger equation including spin-orbit coupling, the following trick has been used, which is also physically motivated. We avoid the divergence of the spin-orbit Hamiltonian for $r \to 0$ by replacing the potential inside the nucleus by its analytical form

$$V_{Z-e}(r) = \begin{cases} -\frac{2Z}{r} & \text{for } r \geq R_\text{N} \\ -\frac{3Z}{R_\text{N}} + \frac{Zr^2}{R_\text{N}^3} & \text{for } r < R_\text{N} \, , \end{cases} \tag{5.1}$$

---

[1] For the Born series, this is demonstrated in eq. (4.62) and (4.61).
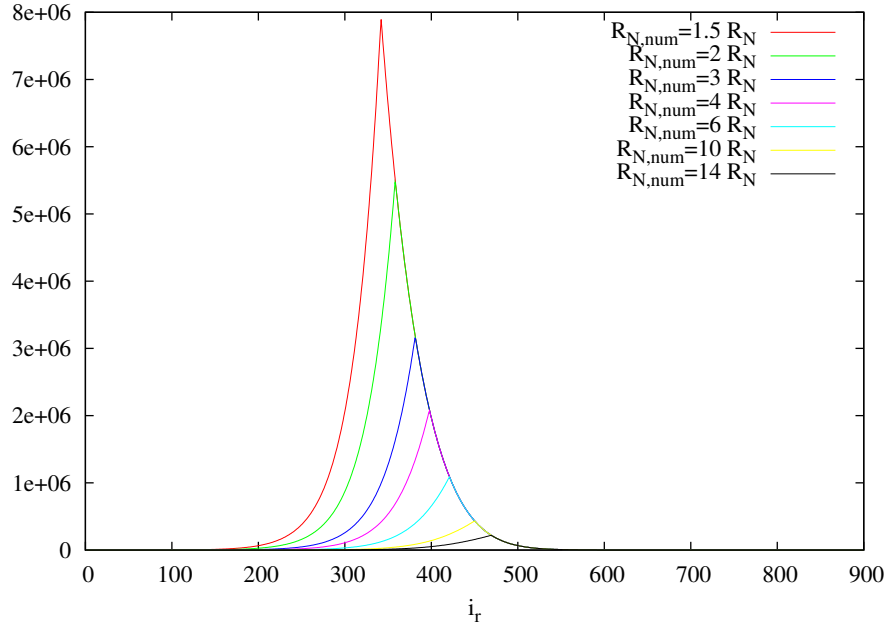
Figure 5.1.: Prefactor of the spin-orbit Hamiltonian $1/(2M(r)^2)\frac{1}{r}\frac{dV}{dr}$ in atomic units for different nuclear radii $R_{\mathrm{N,num}}$ as a function of radial point index i_{r}. The points are not equidistant. Due to a exponential radial mesh, the point $i_r = 500$ is still very close to the origin.

assuming a homogeneous charge distribution in a spherical nucleus of radius R_{N}. This was already illustrated in chapter 4, section 4.2.1, and leads to a kink in the spin-orbit Hamiltonian as shown in figure 5.1. For $r < R_{\mathrm{N}}$, a further divergence of the Hamiltonian is prevented. However, tests have shown that in the SRA for many elements even the inclusion of the correct nuclear radius does not lead to convergence of the Lippmann-Schwinger equation. Therefore, a larger radius than given by eq. (4.17) is chosen; the minimal required value of $R_{\mathrm{num,N}}$, for which the Lippmann-Schwinger equation converges depends also on the number of radial points used for the integration. Using more radial points, lower nuclear radii are needed.

This numerical trick can be justified by showing that the size of the nuclear radius for not too large radii hardly affects the resulting wavefunctions and the t-matrix. In order to estimate the errors made by this approximation we have calculated

$$\sum_{LL'} \left| t_{LL'} - t_{LL'}^{\mathrm{ref}} \right|^2 \ , \tag{5.2}$$

where we have taken the t-matrix using 901 radial points and the minimal radius $R_{\mathrm{num,N}} = 1.5\, R_{\mathrm{N}}$, which lead to convergence, as reference t-matrix t^{ref}.

The results are shown in figure 5.2 for a cutoff of $l_{\max} = 2$. All test calculations in this section have been performed for gold in the SRA. Even for nuclear radii, which are 20 times larger than the correct one and 353 radial points the integrated errors are still very small. This behavior hardly changes when going to $l_{\max} = 3$ or full potential calculations (see figure
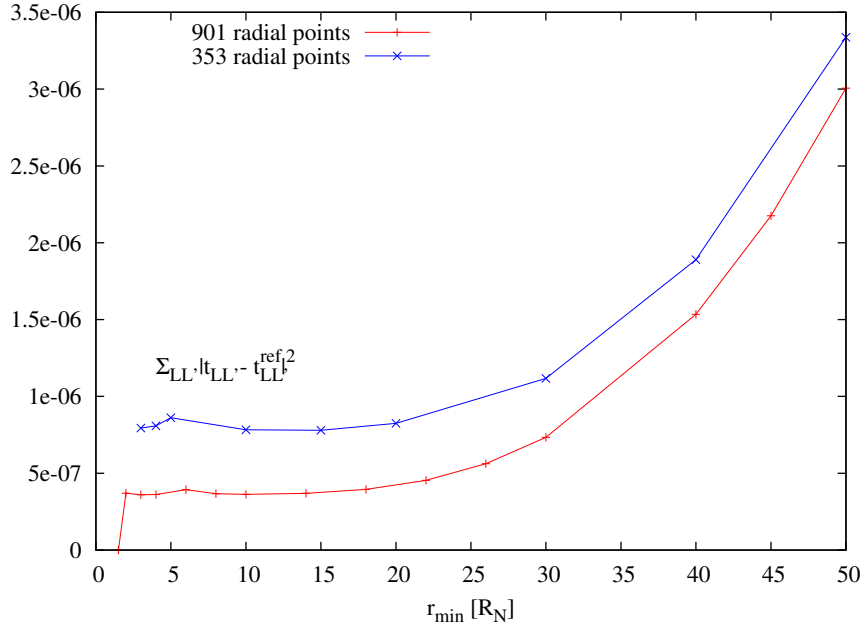
Figure 5.2.: $\sum_{LL'} \left| t_{LL'} - t_{LL'}^{\text{ref}} \right|^2$ for different nuclear radii, ASA calculations, $E = 0.415\text{Ryd}$ and $l_{\max} = 2$. As reference t-matrix $t_{LL'}^{\text{ref}}$, the t-matrix for 901 radial points and the smallest nuclear radius $R_{\text{num,N}} = 1.5 \, R_{\text{N}}$, leading to convergence of the Lippmann-Schwinger equation, has been taken. The blue curve shows the integrated differences $\sum_{LL'} \left| t_{LL'} - t_{LL'}^{\text{ref}} \right|^2$ from the t-matrix which has been obtained from 353 radial points, which is the number of points usually chosen for calculations in the atomic sphere approximation.

5.3). Choosing a larger nuclear radius drastically reduces the number of iterations needed to solve the Lippmann-Schwinger equation. This dependence is shown in the upper panel of figure 5.4 for $l_{\max} = 2$ and ASA calculations. For a nuclear radius which is chosen to be 20 times larger than it would be according to eq. (4.17), 20 iterations are sufficient, while the error in the t-matrix is still small (see figure 5.2). For all calculations performed in this thesis, a numerical nuclear radius $R_{\text{num,N}} = 10 \, R_{\text{N}}$ has been chosen, because deviations for other elements than gold might be larger.

Before closing this section, we come to another aspect already mentioned at the beginning of this section. In contrast to the non-spherical components of the potential, the spin-orbit Hamiltonian decays fast with increasing r. Therefore, it is necessary to include the spin-orbit Hamiltonian only within a sphere with radius $r_{\text{SOC,max}}$, for which the spin-orbit coupling is relevant. In order to check how large this radius has to be chosen, we have calculated the t-matrix for different $r_{\text{SOC,max}}$. The error in the t-matrix is shown in the lower panel of figure 5.4. However, since in most cases we have included the non-spherical components of the potential together with the spin-orbit Hamiltonian and treated them on the same footing, this cutoff has not been used.
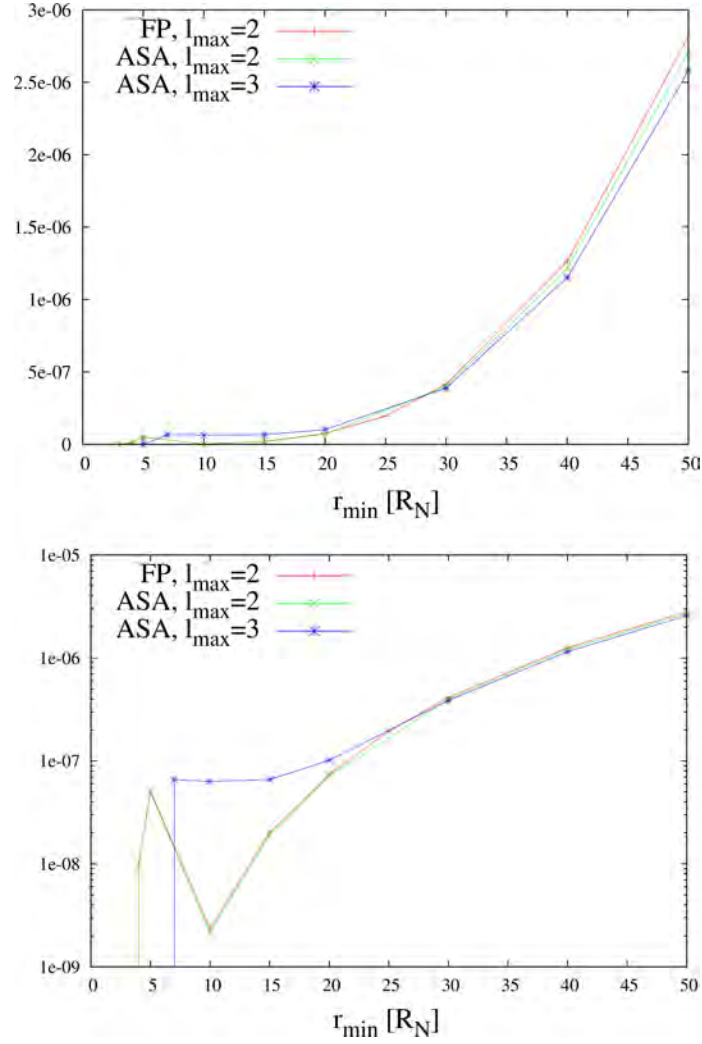
Figure 5.3.: *Top:* $\sum_{LL'} \left| t_{LL'} - t_{LL'}^{\mathrm{ref}} \right|^2$ for different nuclear radii. The reference t-matrix is for all curves the t-matrix for $r_{\min} = 3R_{\mathrm{N}}$ and 901 radial points. *Bottom:* The same as in the left panel but using a logarithmic scale.

5.2 Test of the atomic scattering matrix

In order to check the accuracy of the t-matrix including spin-orbit coupling, we compared the t-matrix for ASA calculations to the t-matrix calculated with a KKR-code in which the Dirac equation is solved for spherical potentials [81]. The comparison was made after transforming the t-matrix to the relativistic κ-μ-basis, which brings the t-matrix into a diagonal form if the potential is spherically symmetric. The results for platinum, gold and lead are shown in figure 5.5. We have plotted the real as well as the imaginary part of the t-matrix for the s, p and d-orbitals, thus $t_s(E)$, $t_p(E)$ and $t_d(E)$ for energies ranging from -1 to 1 Rydberg. For almost all elements and energies, a very good agreement is obtained; ex-
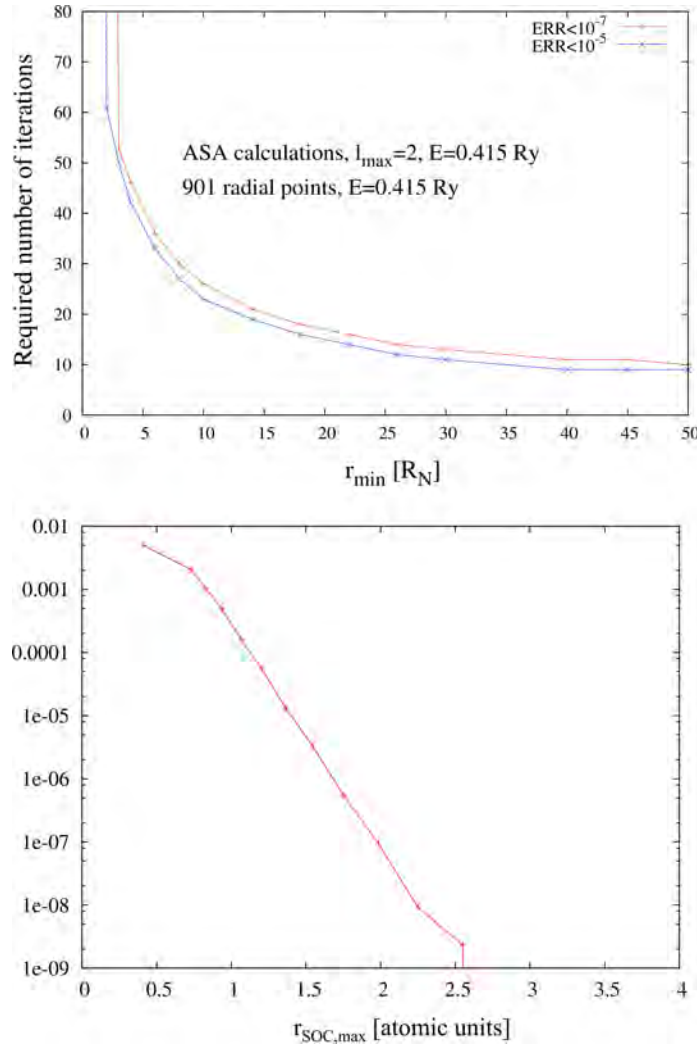
Figure 5.4.: *Top:* Number of iterations needed to solve the Lippmann-Schwinger equation up to the accuracy of 10^{-7} (*red curve*) and 10^{-5} (*blue curve*) as function of the nuclear radius. *Bottom:* $\sum_{LL'} \left| t_{LL'} - t_{LL'}^{\text{ref}} \right|^2$ as a function of $r_{\text{SOC,max}}$ in atomic units, for which the spin-orbit Hamiltonian $H_{\text{SOC}}(r)$ in atomic units is included. To compare, the radius for the ASA-spheres amounts to $r_{\text{ASA}} = 3.01$ a.u.. Note that a logarithmic scale has been used.

clusively for lead differences in the imaginary part of the t-matrix have been found for low energies.
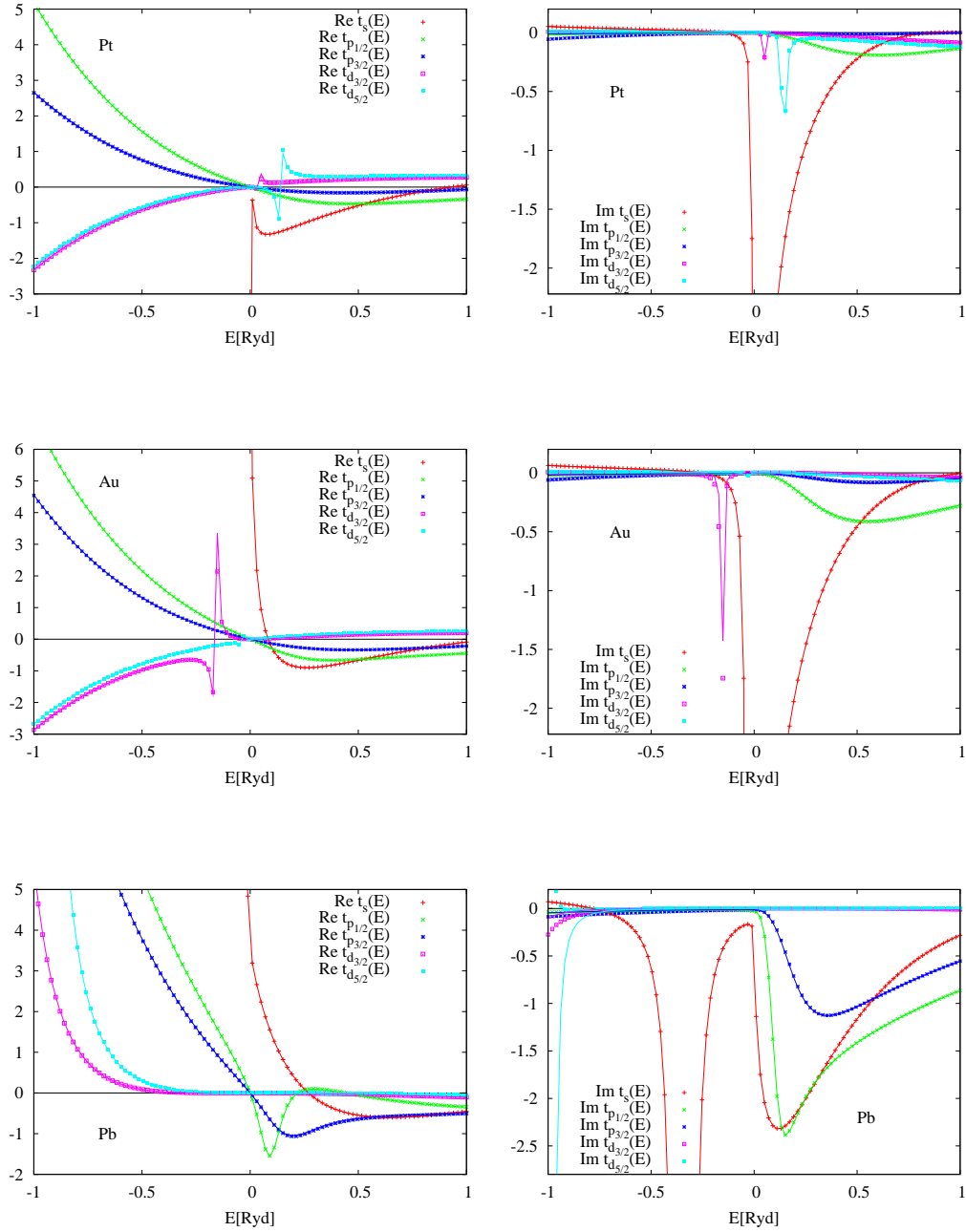
Figure 5.5.: Comparison of the real and imaginary part of the t-matrix for the s, p and d-orbitals for platinum (*top*), gold (*middle*) and lead (*bottom*). The lines are the results obtained with the Dirac equation [81], while the points represent the results calculated with the newly developed code. The agreement is very good with the exception of lead at low energies, where there are deviations in the imaginary part of the t-matrix.

CHAPTER 6

Spin relaxation in noble metals

At low temperatures, when the electron-phonon and electron-electron scattering are frozen out, scattering at impurity atoms is the most serious source of resistivity in metals. These scattering processes result in a rapid loss of momentum coherence, which for metals has been found in experimental studies [7] to be typically in the order of ten femtoseconds. Compared to this momentum relaxation time τ – the average time a carrier loses its original momentum due to a scattering event – electrons have a relatively persistent spin, i.e. long spin-relaxation time T_1. T_1 describes the time after which a system reaches an equilibrium spin population by exchanging energy, momentum and angular momentum with the lattice, and can amount to several nanoseconds. The mobility of electrons as well as the fact that spin coherence can survive quite long bear a promise on the ability of transferring information by electron spins and making spintronics a viable potential technology. Therefore, significant effort has gone into the investigation of the dominant spin-relaxation mechanisms. The ultimate goal is the reduction of spin relaxation in order to keep T_1 as long as possible. In this thesis we contribute to this research by investigating spin relaxation due to impurity scattering in the noble metals copper and gold.

Spin relaxation is caused by many different effects and mechanisms [7]. Thus, it strongly depends on the material, specific characteristics of the sample (e.g. the sample size, the type and the concentration of impurities) and experimental details such as the temperature or the density of excited spins. Despite of the great variety of mechanisms causing spin-flip scattering processes, for the noble metals one mechanism appears to be dominant: the Elliott-Yafet mechanism [9, 82] based on momentum scattering at impurities, phonons and electrons. In addition, there exists a mechanism of spin-flip scattering due to the impurity spin-orbit coupling. If structural inversion symmetry is broken and e.g. surfaces or semiconductors [7] are investigated, a supplementary mechanism, the so-called D'yakonov-Perel mechanism [10] becomes important. Since the latter is absent in the investigated bulk materials, it will be discussed in chapter 8 along with spin-relaxation at

surfaces.

In the current chapter, the effects of spin-orbit coupling due to impurity scattering in the noble metals copper and gold will be discussed. While in the first section the predominant spin-flip mechanisms are described, the second section deals with some numerical aspects of the calculations. Unexpected deviations from expected symmetries are presented and the obtained results are compared to calculations performed by other groups and to experimental data.

Finally, in the third section momentum- and spin-relaxation times for $3d$, $4sp$, $4d$, $5sp$, $5d$ and $6sp$ impurities in fcc copper and gold bulk crystals are studied systematically. Additionally, interference effects in scattering between two impurities are investigated.

6.1   Dominant mechanisms of spin relaxation in noble metals

As sketched in the introduction, in noble metals mainly two mechanisms account for spin relaxation, the Elliott-Yafet mechanism and spin-flip scattering due to spin-orbit coupling of impurities. In the following, the theoretical concepts of these two mechanisms will be shortly presented. For more details about the Elliott-Yafet mechanism we refer to [8].

6.1.1 Elliott-Yafet mechanism

The Elliott-Yafet mechanism is the predominant source of spin-relaxation in materials with structure inversion symmetry and comes along with momentum scattering. It is based on the fact that in the presence of spin-orbit coupling the degenerate electronic Bloch states $\Psi_{\mathbf{k}}^{\uparrow}$ and $\Psi_{\mathbf{k}}^{\downarrow}$ have no pure spin character anymore. Instead, they are a mixture of spin up and spin down states

$$\Psi_{\mathbf{k}}^{\uparrow} \;\; = \;\; \left[a_{\mathbf{k}}(\mathbf{r}) \begin{pmatrix} 1 \\ 0 \end{pmatrix} + b_{\mathbf{k}}(\mathbf{r}) \begin{pmatrix} 0 \\ 1 \end{pmatrix} \right] e^{i\mathbf{k}\cdot\mathbf{r}} \tag{6.1}$$

$$\Psi_{\mathbf{k}}^{\downarrow} \;\; = \;\; \left[a_{-\mathbf{k}}^{\star}(\mathbf{r}) \begin{pmatrix} 0 \\ 1 \end{pmatrix} - b_{-\mathbf{k}}^{\star}(\mathbf{r}) \begin{pmatrix} 1 \\ 0 \end{pmatrix} \right] e^{i\mathbf{k}\cdot\mathbf{r}}. \tag{6.2}$$

Here, $a_{\mathbf{k}}(\mathbf{r})$ and $b_{\mathbf{k}}(\mathbf{r})$ are complex functions, having the periodicity of the lattice and $\Psi_{\mathbf{k}}^{\uparrow}$ and $\Psi_{\mathbf{k}}^{\downarrow}$ are chosen to be polarized along the z-direction, such that

$$\left\langle \Psi_{\mathbf{k}}^{\uparrow} | S_z | \Psi_{\mathbf{k}}^{\uparrow} \right\rangle \;\; = \;\; - \left\langle \Psi_{\mathbf{k}}^{\downarrow} | S_z | \Psi_{\mathbf{k}}^{\downarrow} \right\rangle \qquad \text{and} \tag{6.3}$$

$$\left\langle \Psi_{\mathbf{k}}^{\uparrow} | S_z | \Psi_{\mathbf{k}}^{\downarrow} \right\rangle \;\; = \;\; - \left\langle \Psi_{\mathbf{k}}^{\downarrow} | S_z | \Psi_{\mathbf{k}}^{\uparrow} \right\rangle = 0 \quad . \tag{6.4}$$

Since in most cases the average a of $a_{\mathbf{k}}$ over the whole Fermi surface is close to unity and $b \ll 1$, it is still reasonable to denote $\Psi_{\mathbf{k}}^{\uparrow}$ and $\Psi_{\mathbf{k}}^{\downarrow}$ as 'up' and 'down' states.

Ordinarily, spin-conserving scattering at phonons and impurities induces transitions between two states with the same spin character but a different $\mathbf{k}$, hence scattering from $\Psi_{\mathbf{k}}^{\sigma}$ to

$\Psi_{\mathbf{k}'}^{\sigma}$. For states with non-vanishing $b_{\mathbf{k}}$ transitions also occur between states of opposite spin direction, i.e. scattering from $\Psi_{\mathbf{k}}^{\sigma}$ to $\Psi_{\mathbf{k}'}^{-\sigma}$. In the following, the perturbation which causes the scattering is denoted with δH. It is assumed that the spin-orbit coupling of the impurity is insignificant, i.e. $\langle \uparrow | \delta H | \downarrow \rangle \approx \langle \downarrow | \delta H | \uparrow \rangle \approx 0$, where the notations

$$|\uparrow\rangle = \begin{pmatrix} 1 \\ 0 \end{pmatrix} \quad \text{and} \quad |\downarrow\rangle = \begin{pmatrix} 0 \\ 1 \end{pmatrix} \tag{6.5}$$

have been used. The probability of a scattering event in a first approximation is given by the square of the expectation values

$$P_{\mathbf{kk}'}^{\uparrow\uparrow} = \frac{2\pi}{\hbar} \left| \left\langle \Psi_{\mathbf{k}}^{\uparrow} \left| \delta H \right| \Psi_{\mathbf{k}'}^{\uparrow} \right\rangle \right|^2 \tag{6.6}$$

$$= \frac{2\pi}{\hbar} \left| \left\langle a_{\mathbf{k}} e^{i\mathbf{k}\cdot\mathbf{r}} \left| \delta H \right| a_{\mathbf{k}'} e^{i\mathbf{k}'\cdot\mathbf{r}} \right\rangle + \left\langle b_{\mathbf{k}} e^{i\mathbf{k}\cdot\mathbf{r}} \left| \delta H \right| b_{\mathbf{k}'} e^{i\mathbf{k}'\cdot\mathbf{r}} \right\rangle \right|^2 \quad \text{or}$$

$$P_{\mathbf{kk}'}^{\uparrow\downarrow} = \frac{2\pi}{\hbar} \left| \left\langle \Psi_{\mathbf{k}}^{\uparrow} \left| \delta H \right| \Psi_{\mathbf{k}'}^{\downarrow} \right\rangle \right|^2 \tag{6.7}$$

$$= \frac{2\pi}{\hbar} \left| - \left\langle a_{\mathbf{k}} e^{i\mathbf{k}\cdot\mathbf{r}} \left| \delta H \right| b_{-\mathbf{k}'}^{\star} e^{i\mathbf{k}'\cdot\mathbf{r}} \right\rangle + \left\langle b_{\mathbf{k}} e^{i\mathbf{k}\cdot\mathbf{r}} \left| \delta H \right| a_{-\mathbf{k}'}^{\star} e^{i\mathbf{k}'\cdot\mathbf{r}} \right\rangle \right|^2 \quad ,$$

respectively.

While the probability for spin-conserving scattering is of the order of $|a|^4$, the probability for spin-flip scattering is proportional to the factor $|a|^2|b|^2$ and therefore the ratio between spin-flip and spin-conserving scattering approximately yields

$$\frac{P_{\mathbf{kk}'}^{\uparrow\downarrow}}{P_{\mathbf{kk}'}^{\uparrow\uparrow}} \approx \frac{|b|^2}{|a|^2} \approx \left(\frac{\langle \xi \rangle}{\Delta} \right)^2 . \tag{6.8}$$

In the last step, the results of first-order perturbation theory have been used [9], according to which $|b| / |a| \approx \xi/\Delta$, where ξ corresponds to the strength of the spin-orbit coupling entering as a perturbation parameter and Δ is the interband distance (see also eqs. (4.137) and (4.138)).

The explicit values of the ratio $(\langle \xi \rangle / \Delta)^2$ span a wide range. For light metals, the value of $(\langle \xi \rangle / \Delta)^2$ is very small (e.g. 10^{-10} for Li), whereas for heavy metals it might be in comparison very large (e.g. 10^{-2} for Cs) or even 0.8 for Au [15].

6.1.2 Spin-flip scattering due to impurity spin-orbit coupling

Spin-flip scattering due to impurity spin-orbit coupling has been neglected in the previous section. Naturally, the approximation breaks down if its spin-orbit coupling becomes relevant. Generally, this spin-flip scattering cannot be treated independently from the Elliott-Yafet mechanism, since every spin-flip process induced by the impurity spin-orbit coupling can be reverted by the Elliott-Yafet mechanism and vice versa. In calculations, this interference must be considered by adding up the amplitudes of both effects and not the probabilities.

	single impurity		two impurities	
SOC	in imp. only	in imp. and host	in imp. only	in imp. and host
Cu host				
$(\Delta\tau^{\sigma\sigma})^2$	$5.1 \cdot 10^{-6}$	$2.0 \cdot 10^{-3}$	$3.3 \cdot 10^{-4}$	$6.7 \cdot 10^{-4}$
$(\Delta\tau^{\sigma-\sigma})^2$	$5.0 \cdot 10^{-4}$	$2.0 \cdot 10^{-2}$	$3.0 \cdot 10^{-2}$	$2.5 \cdot 10^{-2}$
Au host				
$(\Delta\tau^{\sigma\sigma})^2$	$9.9 \cdot 10^{-4}$	$4.6 \cdot 10^{-4}$	$1.3 \cdot 10^{-3}$	$1.9 \cdot 10^{-3}$
$(\Delta\tau^{\sigma-\sigma})^2$	$7.9 \cdot 10^{-3}$	$1.0 \cdot 10^{-2}$	$2.0 \cdot 10^{-2}$	$2.7 \cdot 10^{-2}$

Table 6.1.: Mean square difference of $\tau_{\mathbf{k}}^{\uparrow\uparrow}$ and $\tau_{\mathbf{k}}^{\downarrow\downarrow}$ or $\tau_{\mathbf{k}}^{\uparrow\downarrow}$ and $\tau_{\mathbf{k}}^{\downarrow\uparrow}$, averaged over the Fermi surface for one and two nickel impurities in a copper and a gold host, full potential calculations. $\Delta\tau^{\sigma\sigma}$ and $\Delta\tau^{\sigma-\sigma}$ are defined in eqs. (6.10). In the calculation of the scattering matrix (and therefore evidently of the relaxation times, too), all nearest neighbours are included. Note that for a single impurity and single-site calculations in the atomic sphere approximation, the differences become negligible. To compare the mean square errors with the absolute values of the scattering times see table 6.2 and 6.3.

Generally, all impurities are considered to scatter independently from each other. However, correlated-scattering effects might become important if the impurity concentration becomes high or if impurities tend to cluster. We will investigate this aspect at the end of the current chapter, section 6.5.1.

6.2 Unexpected deviations

Before analyzing our numerical results for relaxation times due to impurity scattering, we present some observations made during the calculation process.
From time-reversal symmetry one would intuitively expect that the $\mathbf{k}$-dependent spin-conserving anisotropic scattering times $\tau_{\mathbf{k}}^{\uparrow\uparrow}$ and $\tau_{\mathbf{k}}^{\downarrow\downarrow}$ as well as the spin-relaxation times $\tau_{\mathbf{k}}^{\uparrow\downarrow}$ and $\tau_{\mathbf{k}}^{\downarrow\uparrow}$ as defined in chapter 4, eq. (4.180), behave according to

$$\begin{aligned} \tau_{\mathbf{k}}^{\uparrow\downarrow} &= \tau_{-\mathbf{k}}^{\downarrow\uparrow} \quad \text{and} \\ \tau_{\mathbf{k}}^{\uparrow\uparrow} &= \tau_{-\mathbf{k}}^{\downarrow\downarrow} . \end{aligned} \tag{6.9}$$

This is because the time-reversal operation changes $\mathbf{k}$ to $-\mathbf{k}$ and the spin σ to $-\sigma$. However, an explicit derivation starting from the expression for $T_{\mathbf{k}\mathbf{k}'}^{\sigma\sigma'}$, $\sigma, \sigma' \in (\uparrow, \downarrow)$ occurs to be not trivial. Therefore, we proceed with a numerical evaluation of eq. (6.10), which, as we find,
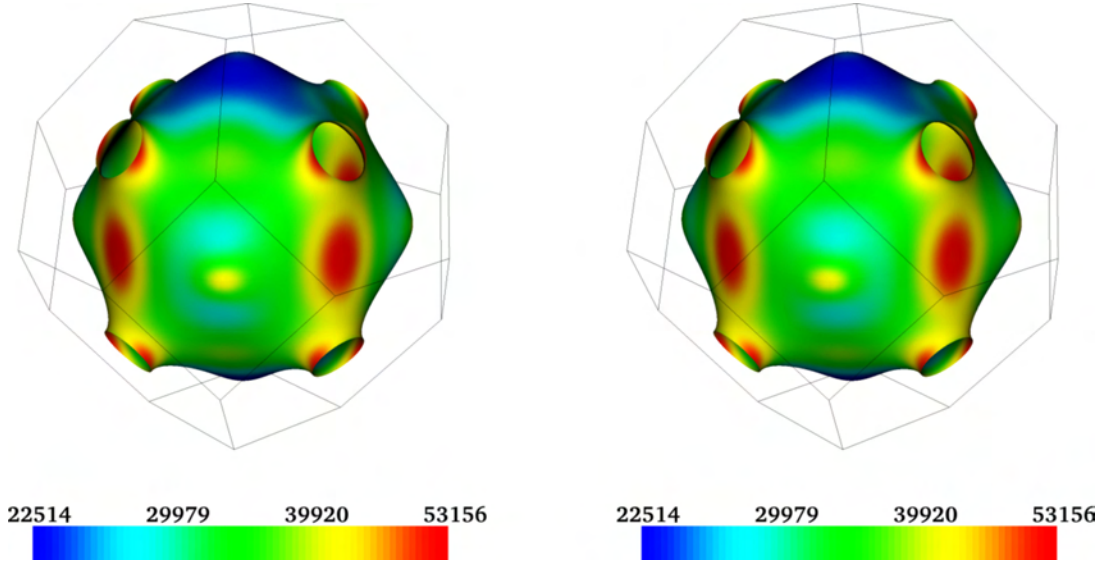
Figure 6.1.: Spin relaxations times $\tau_{\mathbf{k}}^{\uparrow\downarrow}$ (*left*) and $\tau_{\mathbf{k}}^{\downarrow\uparrow}$ (*right*) for a Ga impurity in fs per 1% in copper bulk. Spin-orbit coupling is present both in the host and the impurity potential. A small difference between the two distributions can be seen, manifesting in a light blue 'C' in the middle of the Fermi surface in the left panel or an inverted 'C' in the right panel, respectively. After averaging the inverse of $\tau_{\mathbf{k}}^{\uparrow\downarrow}$ and $\tau_{\mathbf{k}}^{\downarrow\uparrow}$ according to eq. (6.11) and plotting $T_{1\mathbf{k}}$ as in figure 6.2, the anisotropy vanishes.

is not always fulfilled.

Especially for systems with more than one impurity the differences between $\tau_{\mathbf{k}}^{\uparrow\uparrow}$ and $\tau_{\mathbf{k}}^{\downarrow\downarrow}$ (or $\tau_{\mathbf{k}}^{\uparrow\downarrow}$ and $\tau_{\mathbf{k}}^{\downarrow\uparrow}$) can be quite large. To give an impression of the order of magnitude of the deviations, we define the root mean-square errors $\Delta\tau^{\sigma\sigma}$ and $\Delta\tau^{\sigma-\sigma}$ as

$$\Delta\tau^{\sigma\sigma} \quad := \quad \left(\frac{1}{V_{\mathrm{BZ}}}\int\frac{dS_{\mathbf{k}}}{\hbar v_{\mathbf{k}}}\left|\tau_{\mathbf{k}}^{\uparrow\uparrow}-\tau_{\mathbf{k}}^{\downarrow\downarrow}\right|^2\right)^{\frac{1}{2}} \tag{6.10}$$

$$\Delta\tau^{\sigma-\sigma} \quad := \quad \left(\frac{1}{V_{\mathrm{BZ}}}\int\frac{dS_{\mathbf{k}}}{\hbar v_{\mathbf{k}}}\left|\tau_{\mathbf{k}}^{\uparrow\downarrow}-\tau_{\mathbf{k}}^{\downarrow\uparrow}\right|^2\right)^{\frac{1}{2}} .$$

Exemplarily, table 6.1 gives $(\Delta\tau^{\sigma\sigma})^2$ and $(\Delta\tau^{\sigma-\sigma})^2$ for nickel impurities embedded in a copper and a gold host for systems with one and two impurities. In all calculations, scattering within a cluster comprising the nearest neighbours is included. Apart from that, results are presented for two different scenarios: First, spin-orbit coupling is taken into account in the impurity potential only and secondly, spin-orbit coupling is present in the host as well as in the impurity potential. The deviations appear for both cases, and except for a single impurity in a Cu host, they are approximately of the same order of magnitude. Additionally, in figure 6.1 the distribution of $\tau_{\mathbf{k}}^{\uparrow\downarrow}$ and $\tau_{\mathbf{k}}^{\downarrow\uparrow}$ for a single Ga impurity in copper bulk is presented. The small anisotropy manifests in a visible light blue 'C' in the middle of the Fermi surface in the left panel and the inverted 'C' in the right panel, which disappears

when calculating the average spin relaxation time

$$T_{1\mathbf{k}} = \left(1/\tau_{\mathbf{k}}^{\uparrow\downarrow} + 1/\tau_{\mathbf{k}}^{\downarrow\uparrow}\right)^{-1} , \tag{6.11}$$

presented in figure 6.2.

Averaging the momentum-relaxation times $\tau_{\mathbf{k}}^{\uparrow\uparrow}$, $\tau_{\mathbf{k}}^{\downarrow\downarrow}$ and the spin-relaxation times $\tau_{\mathbf{k}}^{\uparrow\downarrow}$, $\tau_{\mathbf{k}}^{\downarrow\uparrow}$ over the Fermi surface yields

$$\begin{aligned} \tau^{\uparrow\uparrow} &= \tau^{\downarrow\downarrow} \\ \tau^{\uparrow\downarrow} &= \tau^{\downarrow\uparrow} \end{aligned} \tag{6.12}$$

up to a relative numerical accuracy of about 10^{-12}.

After extensive checking we act on the assumption that the deviations are not caused by a numerical problem, since qualitatively, the same deviations appear within the frame of a simple tight-binding model, too. The model and the tests are documented in Appendix C. The physics which provokes the asymmetry still has to be understood.

6.3 Comparison to other numerical and experimental data

In this section we compare the obtained relaxation times for some of the calculated systems to other calculations [13, 80, 83] and experimental data obtained with conduction electron spin resonance (CESR) [16].

As a first step, the distributions of the momentum relaxation time $\tau_{\mathbf{k}}$ and the spin relaxation time $T_{1\mathbf{k}}$ for Ni, Zn and Ga impurities in copper bulk on the Fermi surface are considered. The results shown in figures 6.2 agree very well with the distributions shown in [80, 83]. Small deviations can be explained by differences in the methods. Although the calculations in references [80, 83] have been performed within the KKR formalism, too, a fully relativistic approach solving the Dirac equation has been chosen there. On the other hand, in our calculations the full potential is included, while the calculations of references [80, 83] have been performed within the atomic sphere approximation neglecting the non-spherical components of the potential. Furthermore, a different size of the region where charge relaxation is allowed has been chosen: In contrast to [80, 83], where four nearest-neighbor shells, hence 55 atoms, around the interstitial impurity have been included in the calculations, we have restricted this region to a cluster of 13 atoms, corresponding to all nearest neighbors. The cutoff of the orbital momentum $l_{\max}$ in the expansion of the wavefunctions and the Green function as well as the lattice constant might play a role, too. These two values are not specified in the respective references. In our calculations, we have used the cutoff $l_{\max} = 3$ and the experimental lattice constants $a = 3.62$ Å for copper and $a = 4.08$ Å for gold.

Examining the distributions of the momentum relaxation times for the three impurities Ni, Ga and Zn on the Fermi surface of copper in the three figures in the left column of figure 6.2, we observe that $\tau_{\mathbf{k}}$ has the full symmetry of the Brillouin zone (48-fold O_h), while $T_{1\mathbf{k}}$ has a reduced symmetry (C_{4v}, rotations around the z-axis and reflections). This is due to
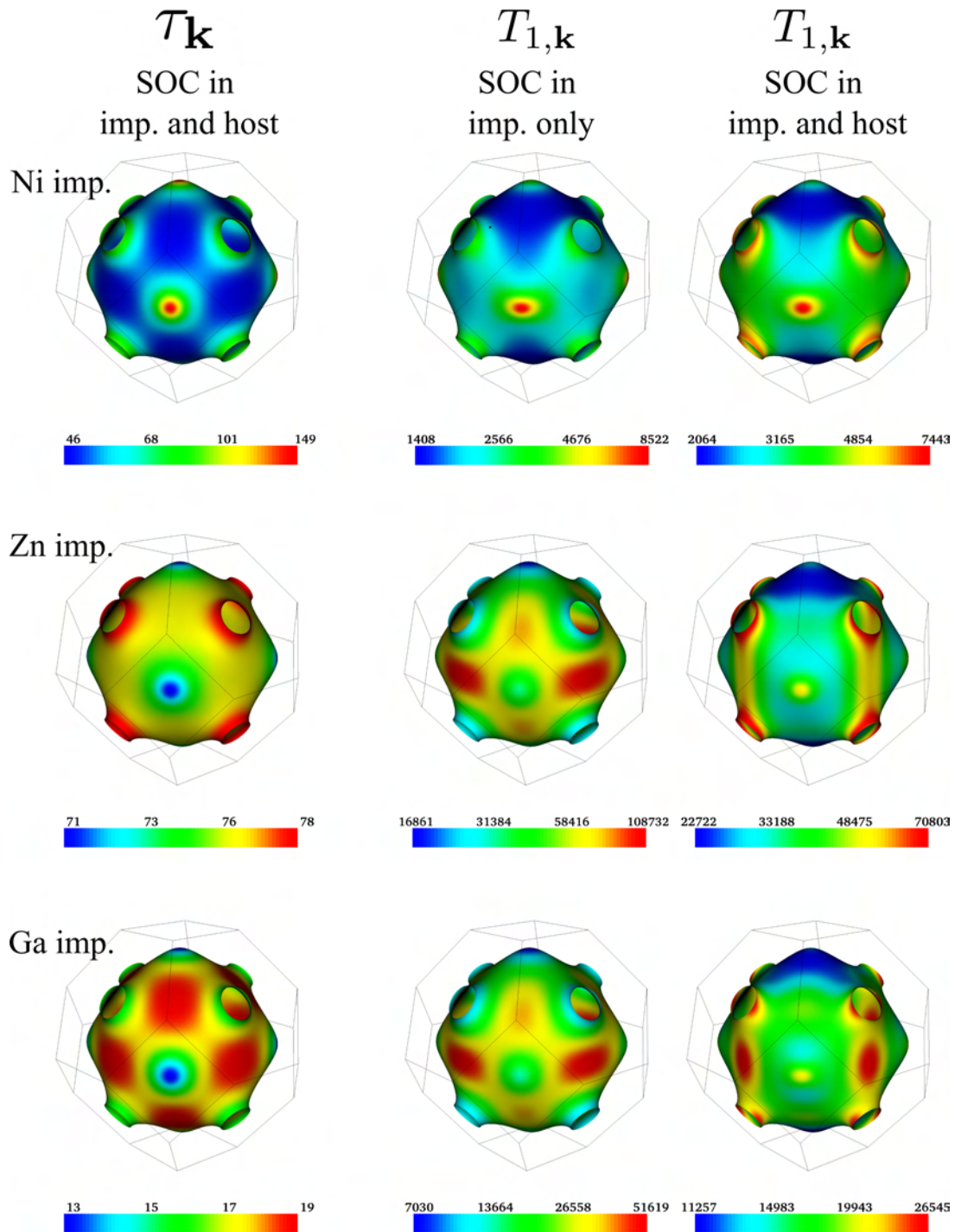
Figure 6.2.: Distribution of the momentum relaxation times $\tau_{\mathbf{k}}$ for spin-conserving scattering (*left*) and spin-flip scattering $T_{1,\mathbf{k}}$ (*middle* and *right*) for Ni (*top*), Zn (*center*) and Ga (*bottom*) impurities in fs at a concentration of 1% impurities embedded in a fcc copper host crystal. The three figures in the second column represent the situation of spin-orbit coupling included in the impurity potential only while the three figures in the third column are results for spin-orbit coupling in the host and the impurity. For $\tau_{\mathbf{k}}$, only very small differences are found if spin-orbit coupling is included in the host or not.

impurity type	SOC in imp. only	SOC in imp. and host	other calculations [80]
K	$1.0 \cdot 10^{-2}$	$1.0 \cdot 10^{-2}$	
Ca	$1.3 \cdot 10^{-2}$	$1.3 \cdot 10^{-2}$	
Sc	$1.0 \cdot 10^{-2}$	$1.0 \cdot 10^{-2}$	
Ti	$5.1 \cdot 10^{-3}$	$5.1 \cdot 10^{-3}$	
V	$3.6 \cdot 10^{-3}$	$3.6 \cdot 10^{-3}$	
Cr	$3.3 \cdot 10^{-3}$	$3.3 \cdot 10^{-3}$	
Mn	$3.8 \cdot 10^{-3}$	$3.9 \cdot 10^{-3}$	
Fe	$5.8 \cdot 10^{-3}$	$5.9 \cdot 10^{-3}$	
Co	$1.3 \cdot 10^{-2}$	$1.3 \cdot 10^{-2}$	
Ni	$5.7 \cdot 10^{-2}$	$5.6 \cdot 10^{-2}$	$5.7 \cdot 10^{-2}$
Zn	$7.6 \cdot 10^{-2}$	$7.6 \cdot 10^{-2}$	$7.8 \cdot 10^{-2}$
Ga	$1.7 \cdot 10^{-2}$	$1.7 \cdot 10^{-2}$	$1.7 \cdot 10^{-2}$
Ge	$7.4 \cdot 10^{-2}$	$7.5 \cdot 10^{-3}$	$7.2 \cdot 10^{-3}$
As	$3.3 \cdot 10^{-3}$	$3.3 \cdot 10^{-3}$	$4.3 \cdot 10^{-3}$
Se	$3.6 \cdot 10^{-3}$	$3.7 \cdot 10^{-3}$	
Au	0.14	0.15	
(ASA)		0.16	0.48

Table 6.2.: Momentum relaxation times $\tau = 2\left(1/\tau^{\uparrow\uparrow} + 1/\tau^{\downarrow\downarrow}\right)$ in ps for $3d$ and $4sp$ impurities in a fcc copper host, assuming an impurity concentration of 1%. All calculations are non spin-polarized and have been performed including a cluster of 13 atoms, corresponding to the nearest neighbors. The momentum relaxation times merely change when spin-orbit coupling in the cluster is neglected or not. The other calculations are done by M. Gradhand et al. [80].

the assumption that the incoming state is prepared with a spin along the z-axis.

Furthermore, differences between the three impurities Ni, Ga and Zn become obvious. The reason for this discrepancy can be found in the different scattering properties of the three elements: While Ni is a typical d-scatterer, Zn and Ga are sp-scatterers, among which Zn s-scattering is dominant and for Ga scattering mostly occurs in the p-channel. For Ni, the momentum scattering rate is observed to be lowest in [100] direction (the momentum relaxation time is longest). In contrast, for Zn and Ga scattering in this direction is maximal and therefore leads to short momentum relaxation times. For Zn, momentum relaxation times are highest in regions close to the necks, whereas Ga shows the longest momentum-relaxation times between the necks, in the [110] directions.

Considering the spin-relaxation times for spin-orbit coupling being included in the impurity potential only (second column of the same figure 6.2), the qualitative distribution of

impurity type	our calculations		other calc. [80]		experimental data [16]
	SOC in		SOC in		
	imp. only	imp. + host	imp. only	imp. + host	
K	122.7	7.9			
Ca	142.5	7.2			
Sc	137.6	5.5			
Ti	22.6	3.5			
V	2.4	1.7			
Cr	0.59	0.63			
Mn	0.29	0.32			
Fe	0.26	0.29			
Co	0.45	0.54			
Ni	2.0	3.1	1.6	3.9	2.2 ± 0.2
Zn	48.2	34.6	49	41	64 ± 9
Ga	21.0	16.7	22	16	30 ± 4
Ge	9.0	8.6	10	7.1	14 ± 2
As	4.7	2.2	5.7	4.6	8.6 ± 0.7
Se	2.8	1.8			
Au	0.35	0.45	0.56	0.47	0.62 ± 0.21
(ASA)		0.47			

Table 6.3.: Spin relaxation times $T_1 = \left(1/\tau^{\uparrow\downarrow} + 1/\tau^{\downarrow\uparrow}\right)^{-1}$ in ps per atomic percent for $3d$ and $4sp$ impurities in fcc copper bulk, non spin-polarized calculations.

$T_{1\mathbf{k}}$ is similar to that of $\tau_{\mathbf{k}}$ for Ni impurities. In contrast, the spin-relaxation time $T_{1\mathbf{k}}$ for Zn and Ga impurities shows a completely different behavior. Obviously, the parts of the Fermi surface where ordinary momentum scattering is strong are not the same as for spin-flip scattering. This is reasonable for s-scattering, since s-orbitals ($l = 0$) do not participate in the spin-orbit coupling. For p-scattering, however, spin-orbit coupling effects are expected to be stronger than in the d-channel, since p-electrons are generally located closer to the nucleus and therefore 'feel' the nuclear potential more strongly (see chapter 4). That this not the case also manifests in the comparison of the momentum relaxation time and the spin-relaxation time for the whole series of $3d$ and $4sp$ impurities in figure 6.3. While the inverse momentum-relaxation time for the $4sp$ impurities increases up to the maximum of the $3d$ series, the spin-flip scattering rate remains very weak. This apparent paradox persists, as we will see, in the case of $4d$ and $5sp$ as wells as $5d$ and $6sp$ impurities. We will see how it is resolved in sections 6.4 and 6.5.

The distribution of the spin-relaxation time is shown in the third column of figure 6.2.
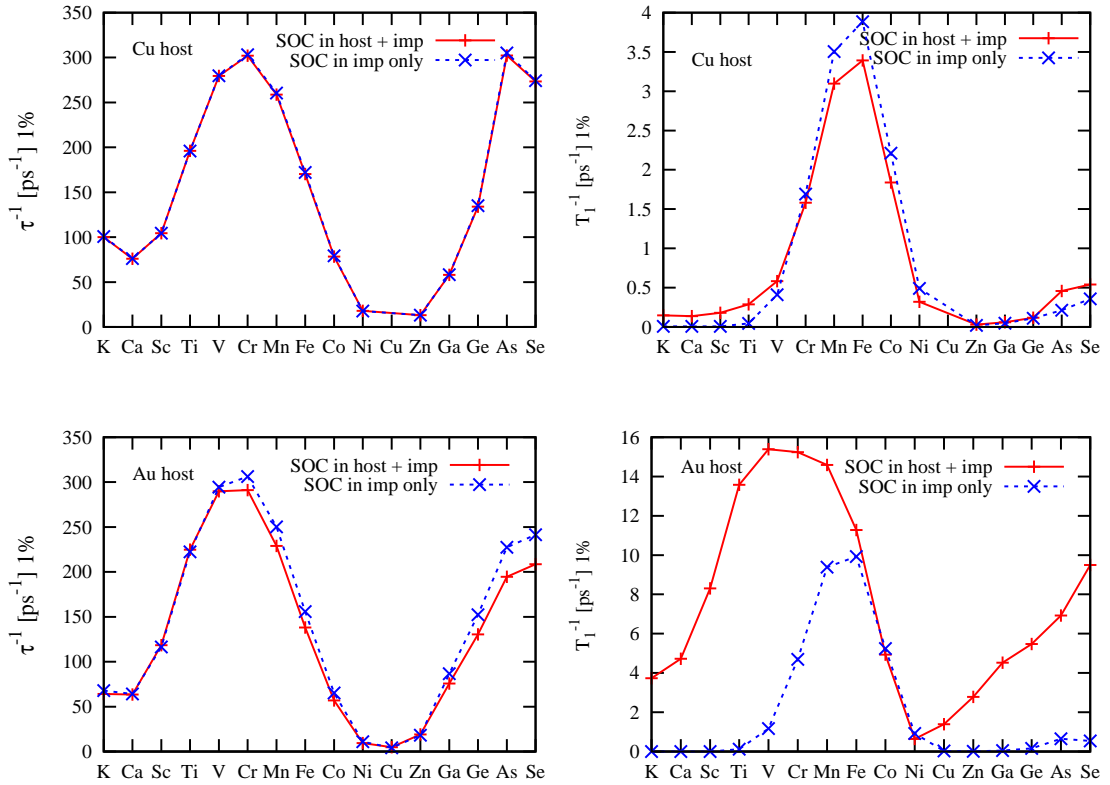
Figure 6.3.: Inverse momentum-relaxation times τ^{-1} for spin-conserving scattering (*left*) and spin-relaxation times T_1^{-1} (*right*) in ps^{-1} per atomic percent for a copper (*upper panels*) and a gold (*lower panels*) host bulk crystal. The blue curves represent the scattering rate under the presence of spin-orbit coupling in the impurity only, whereas the red curves are lifetime calculations for spin-orbit coupling in the host and in the cluster. For both curves scattering within a cluster including the thirteen nearest neighbours is taken into account.

There, spin-orbit coupling is included in the whole system, thus in the impurity and the host. Especially for the Zn and the Ga impurities, the distributions strongly differ from those of the situation, when spin-orbit coupling effects are included in the host only. Comparing the latter two contributions with the spin expectation values of the copper host (see figures 4.1 and 4.2 in chapter 4), it becomes obvious that this change is due to the spin-orbit effects of the host. In [001] direction, where the spin expectation values are lowest, spin-orbit coupling effects of the host are the largest and therefore spin-flip scattering in this direction is enhanced. On the other hand, in a stripe between the necks spin-orbit coupling of the host is lowest and the characteristics of the distribution of $T_{1\mathbf{k}}$ on the Fermi surface are determined by the properties of the impurity.

Having analyzed the distribution of the momentum- and spin-relaxation times on the Fermi

surface exemplarily for three impurities, we continue the comparison of our results to those of references [13], [80] and [83]. Additionally, in table 6.2 and figure 6.3 the results of different calculations for anisotropic momentum-relaxation times for $3d$ and $4sp$ impurities are presented[1]. Obviously, for a copper host, the momentum-relaxation times hardly differ when spin-orbit coupling is included in the copper host or not. Comparing our results with those from reference [83], one notices that the agreement is very good for Ni, Zn, Ga and Ge impurities, while for Au the deviation is considerable. The reason for that deviation might be due to the high relaxation time, i.e. weak scattering. In such a case, small differences can lead to large discrepancies. In order to check whether this is due to the difference of full potential and atomic sphere approximation, we have repeated our calculations in the latter approximation. As can be seen in table 6.2, this turns out not to be the reason, since our result in ASA hardly differ. As expected, for the momentum-relaxation times the treatment of spin-orbit coupling effects in the host does not determine the momentum-relaxation time. On the contrary, for a gold host, where spin-orbit coupling effects are much larger, a small difference can be observed (compare left panel of figure 6.3).

Regarding the spin-relaxation times (see table 6.3 and figure 6.3), even for a copper host the differences between the calculations with and without spin-orbit coupling in the host are more pronounced. Especially for the early $4sp$-$3d$ elements such as K, Ca, Sc and Ti, which are mainly s-scatterers and therefore have a very low spin-orbit coupling, spin-relaxation times are essentially determined by the host spin-orbit coupling.

It is interesting to compare the effects of spin-orbit coupling in the host for the three elements Ni, Zn and Ga. While in the presence of spin-orbit coupling in the host, the spin-relaxation time for a Ni impurity is increased, it is reduced for Zn and Ga impurities. Hence, apparently for Ni impurities spin-orbit coupling effects of the host interfere destructively with the ones of the impurity. In the picture of the Elliott-Yafet mechanism, a spin-flip induced by the impurity can be reverted by a spin-flip of the host and vice versa. That this happens for Ni impurities but not for Zn and Ga impurities, might be due to the distribution of the momentum-relaxation times and the spin-orbit effects on the Fermi surface. While for Ni impurities momentum scattering is highest in the same part of the Fermi surface where the spin-orbit coupling effect of the host is maximal, favoring the interference in those regions, for Zn and Ga impurities these two effects dominate in different parts of the Fermi surface, and thus can be considered as non-interfering, so that the relaxation rates are additive.

For a gold host (see the lower panels of figure 6.3), the differences in the spin-relaxation times between calculations where spin-orbit coupling is present in the impurity only and those where it is present also in the host, are much more pronounced. The effect of the host is most distinct for the sp-scatterers. The maximum of the scattering rate is shifted from Fe when the spin-orbit coupling of the host is neglected to V when spin-orbit coupling is regarded both in the host and the impurity. The reason is that the spin-flip in a gold host with spin-orbit coupling is largely determined by the momentum scattering (i.e. it happens due to the Elliott-Yafet mechanism) and for V and Cr the strongest momentum relaxation

---

[1]All calculations are performed within a shell of the 13 nearest neighbors. This is assumed to be enough, since even single-site calculations – which are not shown here – almost lead to the same results.

is observed.

Comparing the absolute scattering rates of momentum scattering and spin-relaxation in the two different hosts, the expected strength of the spin-orbit coupling of Au becomes obvious: While the momentum-relaxation rate is almost the same, the spin-relaxation rate for Au is much larger (approximately by a factor of 4), since spin-flip processes occur more often.

6.4 Relation of T_1 to Wigner delay times t_D

We will now come back to the paradox that the spin-relaxation rate for the $4sp$ impurities is very low, although the momentum scattering rate is high and the spin-orbit coupling effects are expected to be stronger for p-electrons than for d-electrons[2].

In order to explain this paradox, we use an approximative formula for the inverse spin-relaxation time T_1

$$T_1^{-1} = \frac{2v_\mathrm{F}c}{V_0} \frac{2}{3} \frac{4\pi}{E_\mathrm{F}} \sum_{l>0} \frac{l(l+1)}{2l+1} \sin^2\left[\delta_{l+1/2} - \delta_{l-1/2}\right] , \qquad (6.13)$$

giving the spin relaxation rate in terms of the generalized phase shifts δ_j, where $j = l \pm 1/2$ is the total momentum quantum number. The above formula is exact for a free electron host, and exclusively accounts for the spin-orbit induced scattering from the impurity potential. Hence, spin-orbit effects of the host are not included. Equation (6.13) is obtained by relating the spin-flip scattering cross section σ_SF from reference [12, 84]

$$\sigma_\mathrm{SF} = \frac{2}{3} \frac{4\pi}{E_\mathrm{F}} \sum_{l>0} \frac{l(l+1)}{2l+1} \sin^2\left[\delta_{l+1/2} - \delta_{l-1/2}\right] \qquad (6.14)$$

with the spin relaxation time T_1 via [85]

$$\sigma_\mathrm{SF} = \frac{V_0}{2v_\mathrm{F}c} T_1^{-1} . \qquad (6.15)$$

The difference of the phase shifts $\delta_{l+1/2} - \delta_{l-1/2}$, entering in eq. (6.13), can be rewritten in terms of the energy-splitting of the $(l+1/2)$- and the $(l-1/2)$-orbital and the Wigner delay times t_D defined in section 3.4, eq. (3.82)

$$\delta_{l+1/2} - \delta_{l-1/2} \approx \left(E_{l+1/2} - E_{l-1/2}\right) \frac{d\delta_l}{dE} = \frac{1}{2} \Delta E_{l+1/2,l-1/2}\, t_D . \qquad (6.16)$$

Here, it is assumed that $\delta_{l+1/2}(E)$ and $\delta_{l-1/2}(E)$ have the same functional form, $\delta_l(E)$, but mutually displaced in the energy axis by $\Delta E_{l+1/2,l-1/2}$. Calculations show this to be approximately correct.

Using the identity $\sin x^2 = 1/2\,(1 - \cos 2x)$, we obtain

$$T_1^{-1} \approx \frac{2v_\mathrm{F}c}{V_0} \frac{2}{3} \frac{4\pi}{E_\mathrm{F}} \sum_{l>0} \frac{l(l+1)}{2l+1} \frac{1}{2} \left[1 - \cos \Delta E t_D\right] . \qquad (6.17)$$

---

[2]For the $4d$, $5sp$ and the $5d$, $6sp$ impurities a similar behavior is observed as can be seen in figures 6.7 and 6.8.
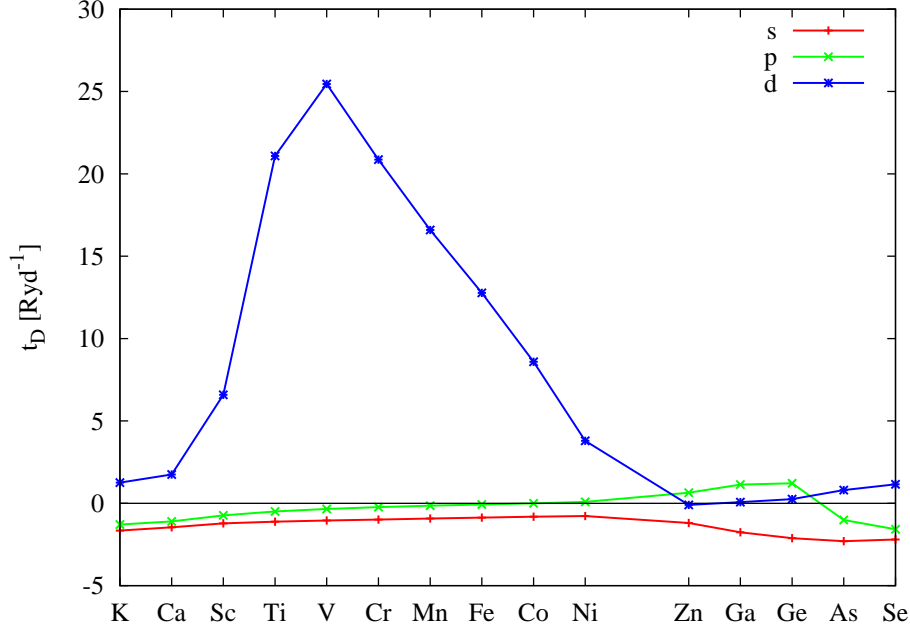
Figure 6.4.: Wigner delay time t_D in atomic units (Ryd^{-1}) for $3d$ and $4sp$ impurities in copper bulk, calculated from s, p and d orbital momenta. The delay-times for the d-orbitals are much larger than those for the s- and p-orbitals, for which even negative delay times have been calculated. These negative times can be interpreted such that the first waves of a wavepacket have already left the impurity site, while the last ones have not yet entered.

This equation allows the following physical interpretation of the spin-flip scattering process induced by momentum scattering: The electron wavepacket enters the impurity and 'feels' the spin-orbit induced splitting of the energy levels $l + 1/2$ and $l - 1/2$ due to the spin-orbit coupling of the impurity potential; this energy splitting causes a precession of the electron spin. The second quantity entering in eq. (6.17) is the Wigner delay time t_D. It denotes the time the electron requires for the (momentum) scattering process and remains at the impurity site. Hence, if the delay-time is long, the electron is exposed to the impurity spin-orbit coupling. The term $1 - \cos \Delta E \, t_D$ is typical for a beating effect between two states – here $l - 1/2$ and $l + 1/2$ – split by an energy ΔE, for a time interval t_D. It is obvious that, in the presence of resonant scattering, when t_D becomes long, the precession will be significant.

A calculation of the Wigner delay times t_D for the s-, p- and d-partial waves of the $3d$ and $4sp$ impurities in copper bulk, figure 6.4, shows that the delay times for the d-partial waves are much longer than those of the s- and p-orbitals. This is because transition elements cause resonant d-wave scattering, as is well known, and explains why spin-relaxation due to d-scattering is much stronger compared to that of p-scattering. For a qualitative explanation
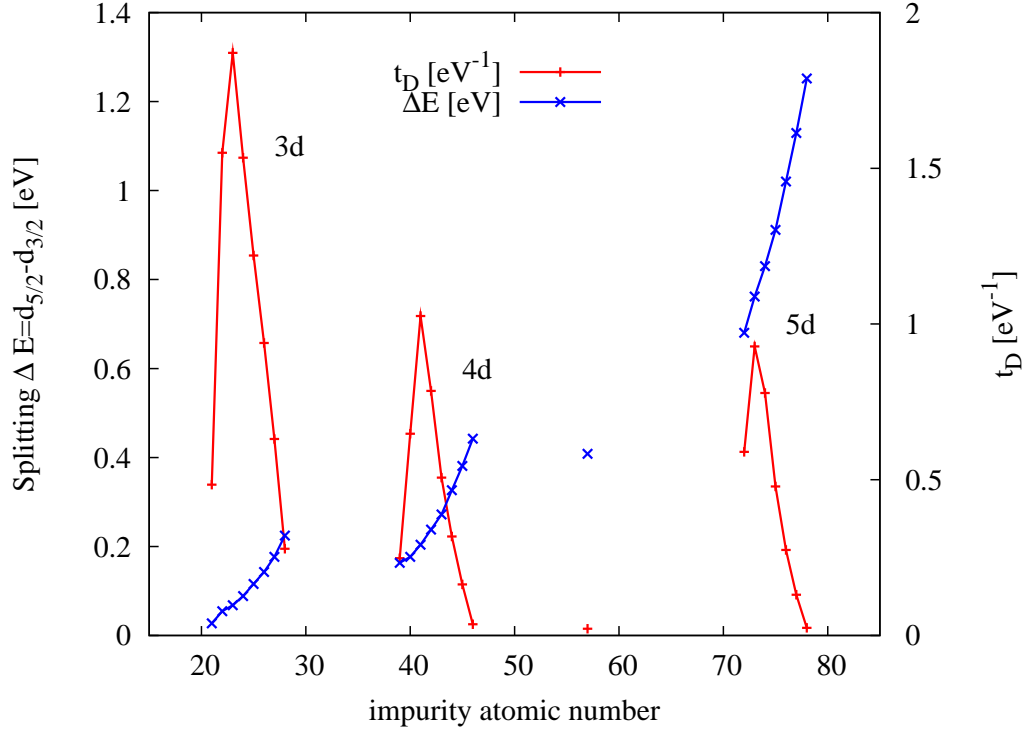
Figure 6.5.: Wigner delay times t_D in eV^{-1} and splitting of the two energy levels $E_{5/2}$ and $E_{3/2}$ in eV induced by spin-orbit coupling at the Fermi level E_F. While the splittings $\Delta\omega$ increase with the filling of the d-shell as well as the principal quantum number, the delay times have a peak for almost half-filled d-shells. To convert the values of t_D given in eV^{-1} to SI-units, note that $1\mathrm{eV}^{-1} \approx 0.66\mathrm{fs}$.

it is sufficient to approximate the Cu host by a free electron gas and use the phase shifts δ_l obtained for the spherical part of the potential. For some elements, t_D calculated from the s- and p-orbitals becomes negative. According to Newton [60], small negative delay times for wave packets are possible. An interpretation is that the front part of the wave packet already leaves the impurity while the rear part has not yet arrived. In this case, the absolute value of the delay time is also called advancement time.

In order to attest our interpretation, we have applied this simple model to the $3d$, $4d$ and $5d$ impurities in copper bulk. Therefore, we have only taken into account the splitting of the d-partial wave, i.e. $\Delta E = (E_{d_{5/2}} - E_{d_{3/2}})$, because for the d impurities it is expected to
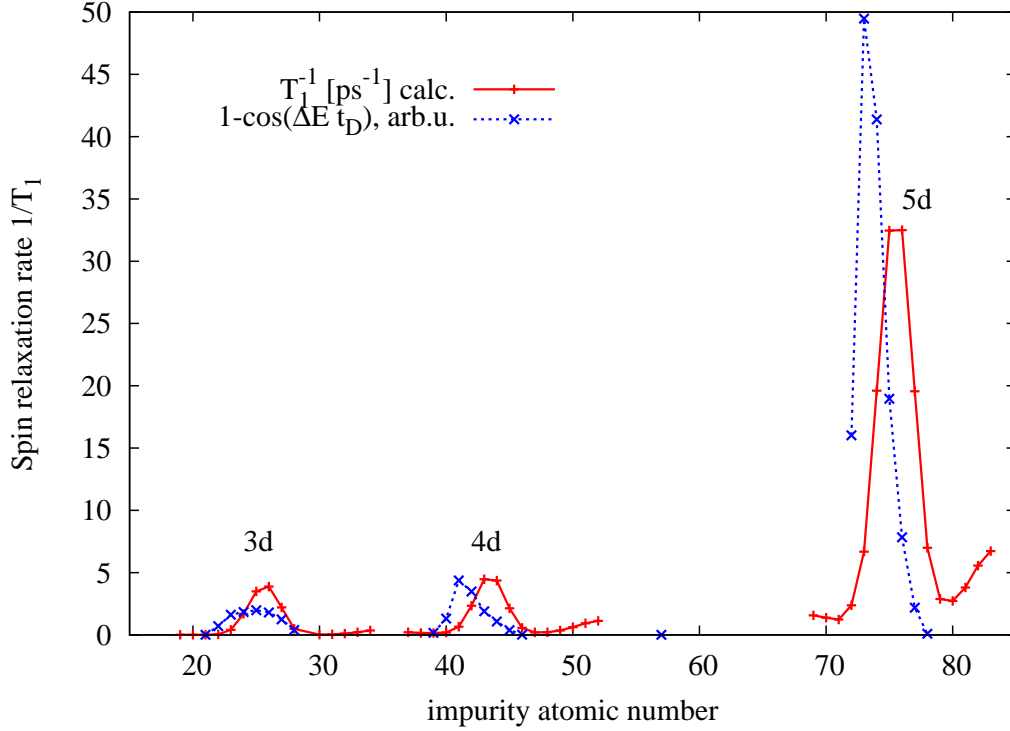
Figure 6.6.: Inverse spin relaxation times T_1^{-1} for the $3d$, $4d$ and $5d$ impurities in a copper host. Numerical data (in ps^{-1}) are compared to those obtained within the approximation using the Wigner delay times t_D and the spin-orbit induced splittings of the energy level $d_{5/2}$ and $d_{3/2}$ shown in figure 6.5.

provide the main contribution to the scattering rate. Thus,

$$T_1^{-1} \propto \sin^2\left[\delta_{5/2} - \delta_{3/2}\right]$$
$$\propto 1 - \cos \Delta E \, t_D \, .$$
(6.18)

Whereas the splittings ΔE and the Wigner delay times t_D for the $3d$, $4d$ and $5d$ impurities in copper bulk are shown in figure 6.5, the approximated results using eq. (6.18) are compared to our numerical data in figure 6.6. The splitting of the energy levels increases both with the filling of the d-shell as the d-wavefunctions are retracted towards the nucleus, and the principal quantum number as the impurity atoms are heavier. In contrast, the trends of the Wigner delay times have a peaked structure with maxima for V, Nb and Ta, which are in the same column of the periodic table. The trends obtained for the approximated inverse spin relaxation times T_1^{-1}, figure 6.6, qualitatively agree with the numerical results, although the maximum of the three trends has shifted to impurities with a lower atomic number (from Fe to Mn for the $3d$ impurities, Tc to Nb for the $4d$ impurities, and from Re to Ta for the

$5d$ impurities). This might be due to the approximations made in this model such as the assumption of a free electron host and the use of the phase shifts of the spherical part of the potential and not the generalized ones. However, qualitatively the model explains very well the different behavior of the d- and the sp-scatterers and shows the general importance of resonant scattering for spin relaxation.

6.5 Momentum- and spin-relaxation times for $3d$, $4sp$, $4d$, $5sp$, $5d$ and $6sp$ impurities in copper and gold fcc bulk

6.5.1 Scattering at single impurities

After having compared and discussed the momentum- and spin-relaxation times for the $3d$ and $4sp$ elements in copper and gold hosts for single impurities we will take a look at the $4d$, $5sp$, $5d$ and $6sp$ elements (see the red curves of figures 6.7 and 6.8). Basically, the trends for the $4d$ and $5d$ series are similar to the curves of the $3d$ and $4sp$ series: Both momentum- and spin-flip scattering rates have a peak in the middle of the d series; additionally, momentum scattering is strong for the late sp elements while the spin-flip scattering rate is low. For a gold host, an increase of T_1^{-1} for the late elements is observed, originating from the spin-orbit effects of the host (see the two curves in figure 6.3). This is again a manifestation of the Elliott-Yafet mechanism , i.e., momentum scattering becomes important again, due to the strong spin mixing of the Au Fermi surface. Comparing the order of magnitude of the three rows for the copper host, almost no difference can be noticed between the $3d$ and $4d$ impurities, or the $4sp$ and $5sp$ impurities, respectively. However, for the $5d$ and $6sp$ elements, the spin-relaxation rate is much higher, while the momentum scattering rate does not increase. This is due to the higher atomic numbers of these elements which yield a higher spin-orbit coupling since $H_{\mathrm{SO}} \propto Z$. For a gold host, qualitatively the same behavior is observed, while quantitatively the values of the spin-flip scattering rates are larger.

It is instructive to analyze the ratio T_1/τ, which corresponds to the number of momentum scattering events per spin-flip event. The results are presented in figure 6.9 for copper and gold hosts. In a copper host, the ratio T_1/τ covers a wide range: While for the early sp-scatterer more than 10^4 scattering events occur before one spin flips, throughout the $3d$ series the ratio strongly decreases, ending up with a minimum for Ni; for a Ni impurity, one flip occurs approximately every 55 momentum scattering events. For the $4sp$ elements, T_1/τ increases again, i.e., the spin-flip scattering rate is low in comparison to the momentum scattering rate. This follows from our considerations in the last section, where we have found, that the $4sp$ impurities exhibit a strong momentum scattering, but a weak spin-flip scattering, as the s- and p-wave scattering is not resonant.

Comparing the trends for impurities of the three periods in copper, a qualitative similarity is observed. However, quantitatively, large differences can be noticed: as one moves lower in the periodic table, i.e. consider impurities with higher atomic numbers, the ratio T_1/τ decreases. Hence, the relative number of spin-flip scattering events rises. Again, this behavior is due to the spin-orbit Hamiltonian being proportional Z.
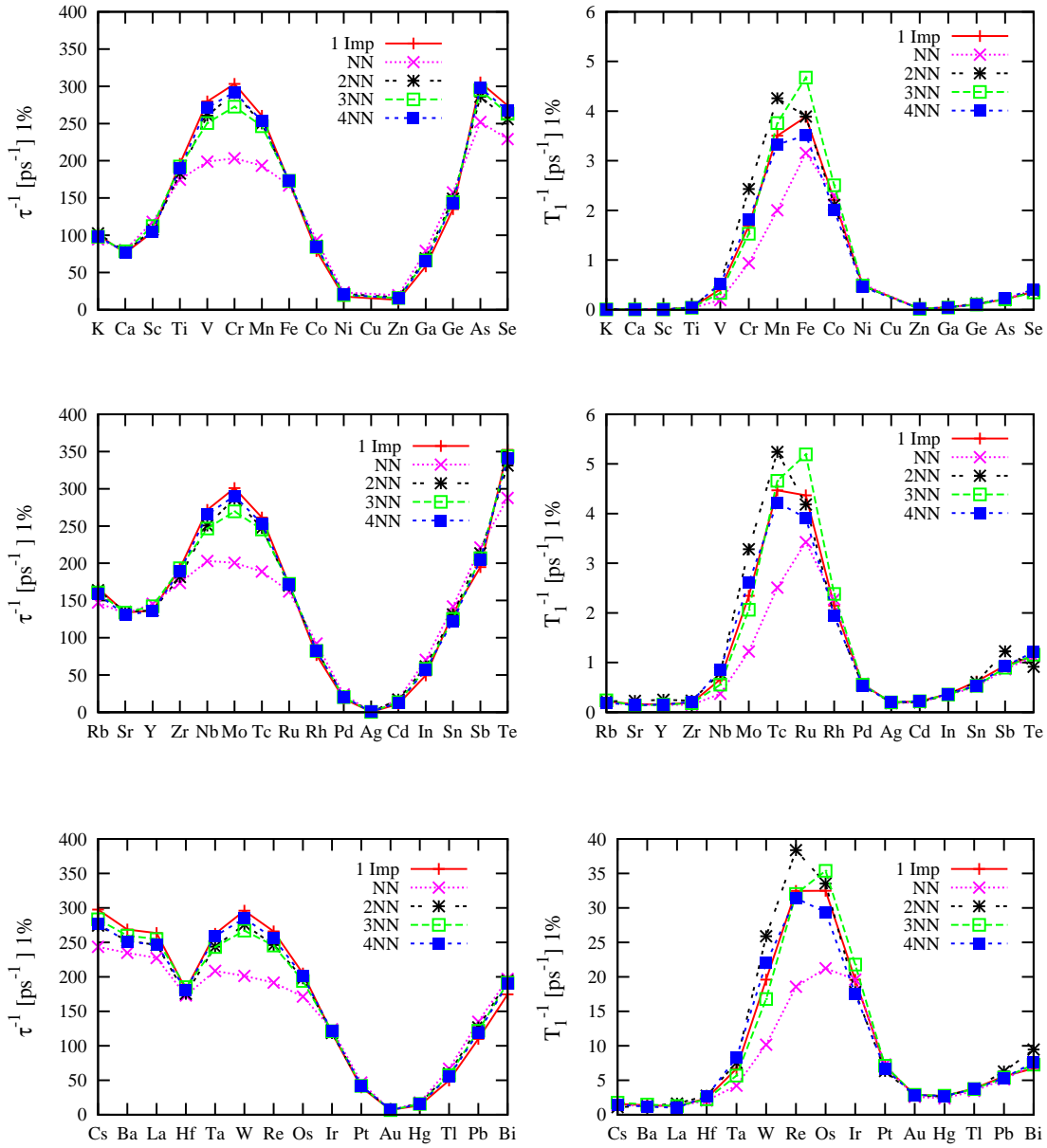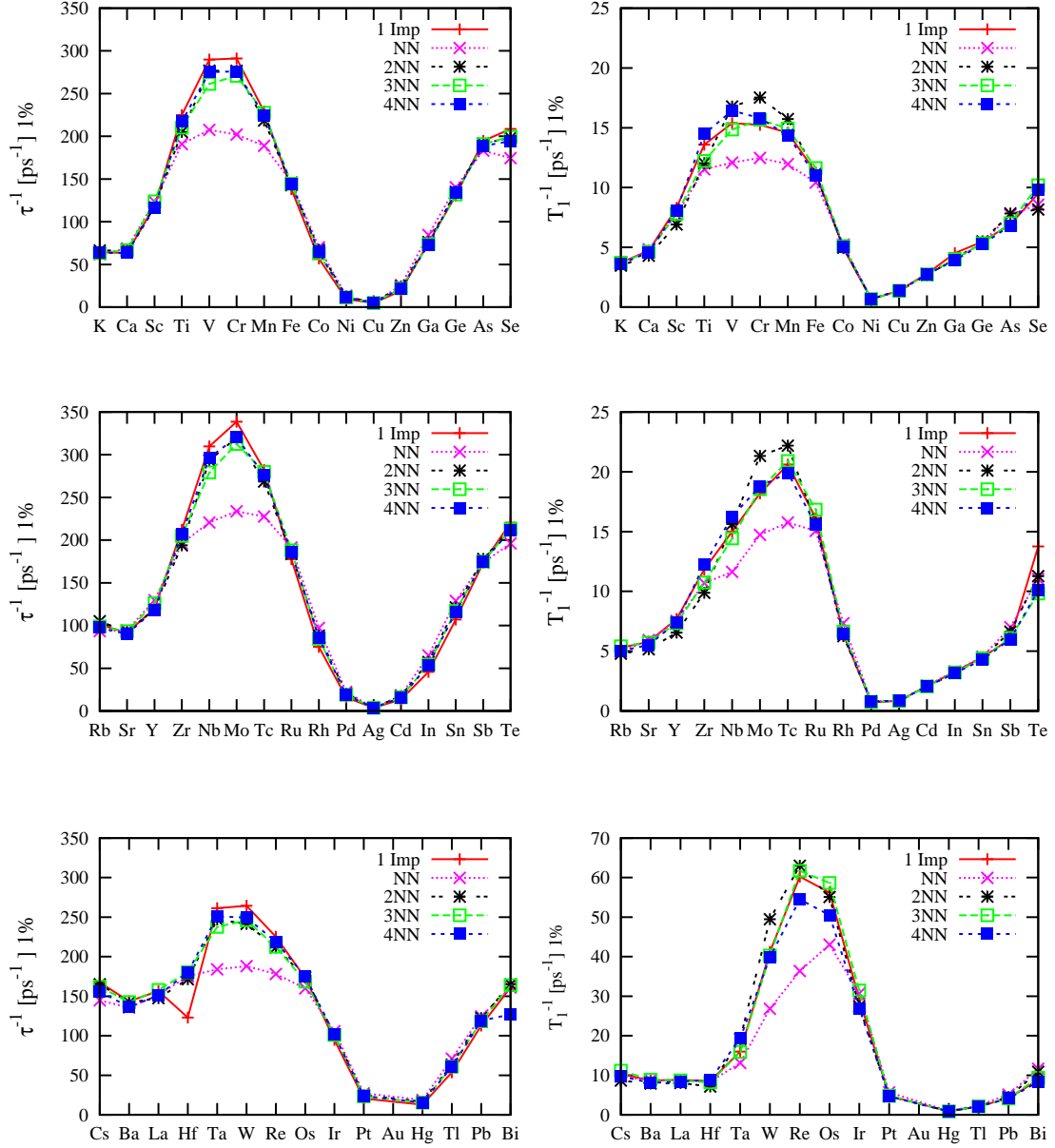
Figure 6.7.: Inverse momentum relaxation time τ^{-1} for spin-conserving scattering (*left*) and spin-flip scattering relaxation rates T_1^{-1} (*right*) in ps^{-1} per 1% impurity concentration in a copper host crystal. While the red curves represent calculations for single impurities, all other values ($\tau_{\mathrm{dimer}}^{-1}/2$ and $T_{1\,\mathrm{dimer}}^{-1}/2$) have been obtained for two correlated impurities, placed at nearest neighboring (magenta curve) and second (black curve), third (green curve) and forth (blue curve) nearest neighboring sites. The greatest deviation from the result of a single impurity (i.e. $\tau_{\mathrm{dimer}}^{-1}/2 - \tau^{-1}$ or $T_{1\,\mathrm{dimer}}^{-1}/2 - T_1^{-1}$, respectively) can be observed for two impurities being nearest neighbors. The positions of nearest neighbors, second, third and forth nearest neighbors are demonstrated in figure 6.10.

Figure 6.8.: Inverse momentum relaxation time τ^{-1} for spin-conserving scattering (*left*) and spin-flip scattering relaxation rates T_1^{-1} (*right*) in ps^{-1} per 1% in a gold host crystal. As for a copper host shown in figure 6.7, effects of interaction between two impurities are studied.
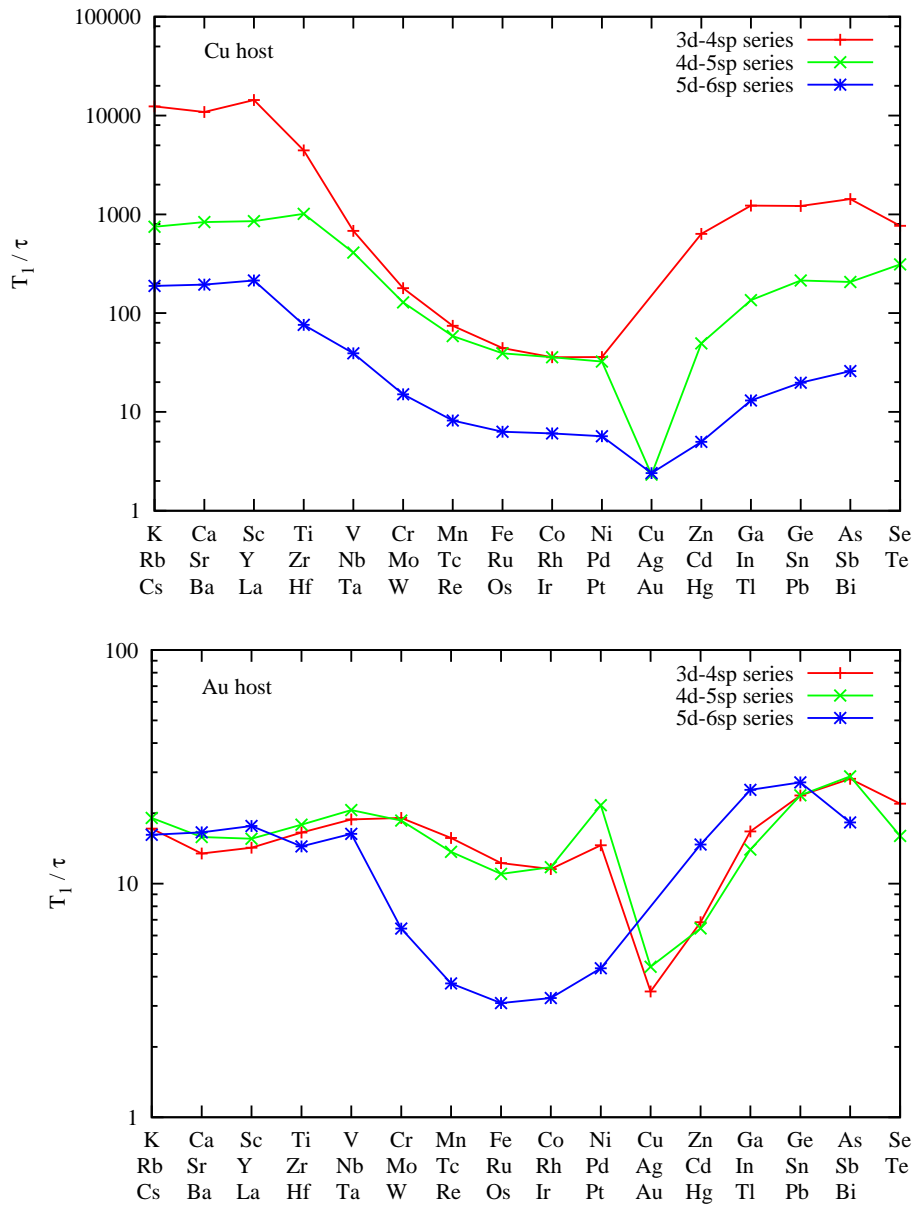
Figure 6.9.: Ratio of the spin-relaxation time versus the momentum relaxation time T_1/τ, i.e. number of spin-conserving scattering processes per one spin-flip event for copper (*upper panel*) and gold (*lower panel*). While in a copper host, T_1/τ strongly depends on the type of impurity and especially for the light s-scatterer more than 10^4 scattering processes are necessary before one spin-flip occurs, in gold maximally 30 momentum scattering events per one spin-flip event take place. This reflects the dominating role of the Au host in spin relaxation.
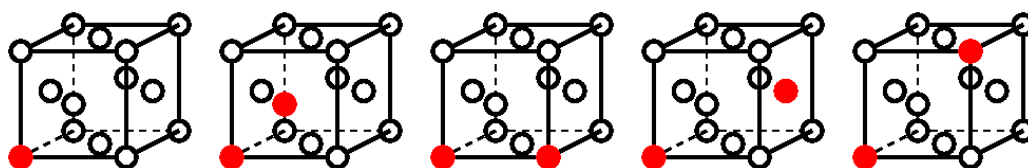
Figure 6.10.: Position of the single impurity in the fcc structure as well as the position of two impurities at nearest neighboring sites, second, third and forth nearest neighboring sites (from left to right).

Considering the lower panel of figure 6.9, which shows the ratio T_1/τ for impurities in a gold host, the picture strongly differs from that of the copper host; compared to copper, the trends throughout the three series are rather flat, the ratio T_1/τ only ranges from approximately 30 (for As, Sb, Pb) down to three scattering events per one spin-flip for Cu, Ag, Os, Ir impurities. In contrast to the behavior within a copper host, in a gold crystal the ratio T_1/τ is of the same order of magnitude for the impurities of the three different rows of the periodic table. The two latter observations (the low ratio in general as well as the rather small difference between different impurities) let us conclude that the ratio is mainly determined by the spin-orbit coupling effects induced by the gold host (Elliott-Yafet mechanism); apparently, the effects of impurity spin-orbit coupling play a minor role.

Furthermore, considering the trends in figure 6.9, a kink in the curve for silver and gold impurities in the copper host and for copper and silver impurities in the gold host are observed. This immediate decrease of the T_1/τ is due to the fact, that copper, silver and gold belong to the same column of the periodic table and therefore have a similar electron configuration, yielding a very low (momentum) scattering rate. Hence, almost all scattering processes are due to the different strength of spin-orbit coupling of the three noble metals, scaling with the atomic number. Therefore, for these impurities a very small number of momentum scattering processes occur before one spin flips.

After having analyzed scattering processes at single impurities we will proceed with the investigation of correlated scattering processes, which will be the subject of the next section.

6.5.2 Correlation between proximity of impurities and scattering

In the previous section the momentum and spin relaxation times at low impurity concentrations of 1% in copper and gold host crystals have been discussed, assuming that each impurity scatters independently. However, if the impurity concentration increases significantly or the impurities tend to cluster, this approximation breaks down and a correlation between impurity positioning and scattering rates must be investigated. In the picture of incoming and scattered waves, correlated scattering processes can be understood as follows: If several impurities are close to each other, interference between waves scattered at these impurities as well as multiple scattering events become possible. Such effects might lead to changes in the momentum- and spin-relaxation times.

Therefore, we have studied momentum- and spin-relaxation times for two impurities situ-

ated at close-by sites, i.e. at nearest neighboring positions, second, third, and forth-nearest neighboring sites (see figure 6.10). We included in our self-consistent calculations the nearest neighboring host sites of both impurities, leading to calculations with 20 sites for two impurities being nearest neighbors, and 22, 24 and 25 sites for 2nd, 3rd, and 4th nearest neighbors, respectively.

The results for the correlated scattering rates per impurity concentration for two impurities (i.e. $\tau_{\text{dimer}}^{-1}/2$ or $T_{1\,\text{dimer}}^{-1}/2$) are presented in figure 6.7 for a copper host and figure 6.8 for a gold host and compared to the scattering rates τ^{-1} and T_1^{-1} for single impurities. Apparently, for most elements $\tau_{\text{dimer}}^{-1}/2 \approx \tau^{-1}$ (or $T_{1\,\text{dimer}}^{-1}/2 \approx T_1^{-1}$, respectively) is valid, hence no correlated scattering between two impurities is observed. The greatest difference can be seen for the $3d$, $4d$ and $5d$ scatterers, when impurities are placed at nearest neighboring positions.

An explanation can be given with the help of the density of states. As typical examples for d-scatterers and sp-scatterers, in figure 6.11 we present the density of states of Cr, Ni and Zn impurities in a copper host for a single impurity as well as nearest neighbors, second and third nearest neighbors. For (single) Cr and Ni impurities we observe a sharp peak in the density of states coming from the d-state, while for the Se impurity a broader, though less intense peak is observed. It mostly originates from a p-band. The position of the peak relative to the Fermi level E_{F} (or the absolute value of the density of states at $E = E_{\text{F}}$, respectively) determines the scattering properties of the system including the impurities, since only electrons at the Fermi level can participate at scattering processes. The higher the density of states, the larger is the number of electrons which can participate in the scattering process. Therefore, the Cr impurity causes a much stronger scattering than e.g. a Ni impurity.

We focus now on the density of states for the systems with two impurities: For all three types of impurities a splitting of the peak can be noticed, which is most pronounced for the system, for which the two impurities are placed at nearest neighboring sites. This splitting corresponds to a hybridization of the d-states of the two neighboring impurities for Cr and Ni and the p-states for Se. However, the hybridization occurs mostly close to the center of the peak. For elastic scattering processes, mainly the situation at the Fermi energy plays a role. This explains the fact that only for the Cr impurities considerable correlation effects can be observed, since only for Cr impurities the hybridization takes place at the Fermi level. Although we have shown the density of states of three types of impurities only, their behavior is typical also for the others.

6.6 Conclusion

In the current chapter a systematic study of momentum-relaxation and spin-relaxation times for $3d$, $4sp$, $4d$, $5sp$, $5d$ and $6sp$ impurities in the noble metals copper and gold was presented. We started giving a short introduction into the two dominant spin-relaxation mechanisms at low temperatures, namely the Elliott-Yafet mechanism and spin-relaxation due to impurity spin-orbit coupling. After that, some unexpected findings have been com-
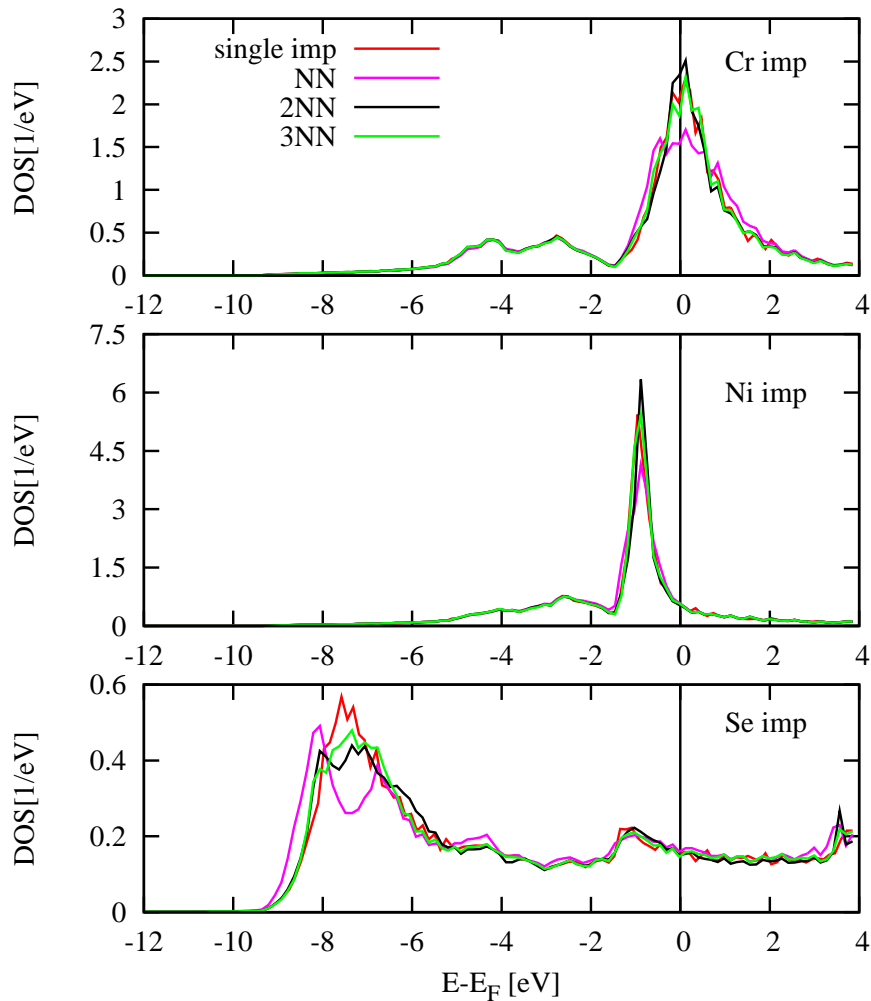
Figure 6.11.: Density of states for Cr (*top*), Ni (*middle*) and Se (*bottom*) impurities in copper bulk for a single impurity (red curve), two impurities placed at nearest neighboring positions (magenta curve), second (black curve) and third (green curve) nearest neighbor sites.

mented on. We compared some of our results for the momentum-relaxation and spin-relaxation times to other numerical and experimental data. The agreement was quite good. Analyzing the distribution of the momentum- and spin-relaxation times for Ni, Zn, and Ga impurities on the Fermi surface of copper, large differences have been observed. They were traced back to the different scattering properties of the three elements.

A comparison of the trends for the momentum-relaxation rate with that of the spin-relaxation rate for the whole series of $3d$ and $4sp$ elements (as well $4d$ and $5sp$, $5d$ and $6sp$) led to the conclusion that strong momentum scattering does not necessarily entail strong spin-flip

scattering. Whereas for the d-scattering elements both momentum and spin relaxation are large, for the sp-scatterers having a large momentum-relaxation rate spin relaxation is very low. An explanation for that different behavior was given by a consideration of the Wigner delay times; for those impurities, where resonant d-scattering is dominant, the Wigner delay time occurs to be an order of magnitude longer than that for the sp-scatterers[3]. Hence, electrons scattering at the $3d$, $4d$ and $5d$ impurities have much more time to 'feel' the impurity spin-orbit coupling and therefore exhibit a much stronger spin relaxation. This has consequences especially in a copper host, because the spin-orbit coupling of the copper host is weak. However, for the late sp-scatterers in a gold host the spin-flip scattering rate also increases due to the spin-orbit coupling of the gold host. Furthermore, we have shown that the approximate formula for the spin relaxation as a function of the Wigner delay time and the spin-orbit induced splitting of the energy-levels for the $3d$, $4d$ and $5d$ impurities in the copper host leads to results, which qualitatively agree well with our numerical data.

The trends for $3d$, $4sp$, $4d$, $5sp$, $5d$, and $6sp$ impurities qualitatively showed the same behavior in copper and gold hosts. However, while the ordinary momentum scattering rate is of the same order of magnitude, spin relaxation is significantly enhanced in the case of a gold host.

The dominating role for spin relaxation of the gold host also manifests in the ratio $T_1/\tau_{\mathbf{k}}$. While for copper $T_1/\tau_{\mathbf{k}}$ strongly depends on the type of the impurity (and its strength of spin-orbit coupling), ranging from 3 to more than 10^4 momentum scattering processes per one spin-flip, in gold even for the light impurities with very low spin-flip scattering rate only 30 momentum scattering processes occur before one spin flips. For copper, a clear minimum of the quotient is reached for the late d-scatterers, while the early s-scatterers (especially K, Ca and Sc) exhibit the largest values of $T_1/\tau_{\mathbf{k}}$, i.e. the lowest relative spin-flip scattering.

Finally, a correlation between the proximity of impurities and scattering has been investigated. Significant changes in the spin-conserving and the spin-flip scattering have been observed for the d impurities with approximately half-filled d-shells, when the two impurities are nearest neighbors. An analysis of the density of states of three impurities, chosen exemplarily, let us conclude that correlation effects are due to resonance-splitting and can be seen only for those impurities whose d-resonance is close to the Fermi energy.

---

[3]We have demonstrated this behavior for the example of the $3d$ and the $4sp$ impurities in the copper host.

Lifetime reduction of surface states caused by impurity scattering in simple metals

In order to describe the dynamics of charge transport, localization and quantum information on metal surfaces, it is of crucial importance to understand the temporal evolution of quasiparticles (electrons and holes) in surface states, characterized by a momentum-dependent lifetime $\tau_{\mathbf{k}}$. Understanding these lifetimes is quite complicated, because they reflect the properties of the correlated many-electron system and depend on a variety of parameters both of intrinsic and extrinsic nature. The field of research is very wide because of the great variety of mechanisms and materials which can be investigated as well as the number of experimental and theoretical techniques which can be employed. Therefore, in the last years much theoretical and experimental effort has been spent for a better understanding, and though a lot of questions are still open, tremendous progress has been made [23].

The lifetime of surface states is limited because the quasiparticles are scattered off the many-particle system, loosing energy and changing their momentum. In metallic systems, mainly three different types of scattering processes dominate (assuming the quasiparticles to be electrons): electron-electron scattering, electron-phonon scattering and scattering of quasi-particles at defects, impurities and grain boundaries. Which one of the three processes is most important depends on many criteria such as the temperature, the crystal and electronic structure of the material, the characteristic of the considered surface state, and the presence of disorder in the material, i.e. the concentration of defects and impurities.

Experimentally, surface-state lifetimes can be measured by three different techniques: Angle-resolved photoemission and scanning tunneling microscopy and spectroscopy, that provide indirect measurements via the broadening of linewidth, and two-photon photoemission that allows a direct measurement of lifetimes in the time domain. The advantage of scanning tunneling microscopy and spectroscopy is the possibility to avoid impurities or to probe them on an atomic scale, whereas photoemission experiments integrate over a com-

paratively large sample area with all its defects, impurities and other imperfections of the surface. This might be the reason for the observed discrepancies in the linewidth of the noble metal surface states obtained in these two experimental setups [27].

The first type of interaction, i.e. electron-electron scattering, reflects the intrinsic properties of the considered surface state. Close to the Fermi energy, electron-electron scattering is small due to the limited phase space of the end states, whereas it becomes important at higher energies[1]. An investigation of the electron-electron correlation of the (111) surface state of noble metals with photoemission experiments can be found in [27].

Electron-phonon interaction results in elastic or almost elastic scattering, because phonons carry relatively low energy[2]. The strength of phonon-scattering strongly depends on the temperature; at low temperatures the contribution of phonons can be neglected, since they are almost frozen. In order to estimate the contribution of electron-phonon scattering to the total lifetime reduction of a specific material, experimental studies are done at different temperatures but in a given temperature range where electron-phonon scattering is assumed to be dominating; then, a linear dependence of the linewidth on the temperature is assumed, which allows for an extrapolation of the phonon-contribution to a given temperature [86, 87]. Lifetime reduction of the noble metal surface states due to scattering at phonons has been both studied in photoemission spectroscopy [86, 87, 88] as well as with scanning tunneling microscopy (STM) and spectroscopy (STS) [22, 24, 89]. A general overview about the investigation of surface-state lifetimes with STM and STS is provided by [90], while in [23] all theoretical and experimental investigations of the last few years are treated. Finally, a lifetime measurement for different concentrations of Co adatoms on the Cu (001) surface with two-photon photoemission can be found in [91].

As a consequence of the above considerations about the contributions of electron-electron and electron-phonon scattering to lifetime reduction, we can conclude that, at low temperatures and energies close to the Fermi level, both are negligible; however, scattering at defects and impurities often is the limiting factor because the creation of a small number of surface defects cannot be avoided. It is therefore worthwhile to provide a systematic theoretical study of lifetime reduction due to impurity scattering, which is the topic of this chapter. The systems investigated are the (111) surfaces of the noble metals Cu, Ag and Au, where the surface states appear in the projected energy gap of the bulk bands. Lifetime reduction due to scattering at $3d$ and $4sp$ impurities below, in and on top of the first surface layer are investigated.

In the first part of the chapter we will discuss some numerical aspects of the calculation before analyzing the considered Cu, Ag and Au (111) surfaces and their corresponding Fermi surfaces. Then, we proceed comparing surface-state lifetimes for scattering at $3d$ and $4sp$ impurities in the surface and at adatoms for copper surfaces. The latter trend, i.e. scattering at adatoms, is investigated in more detail before a systematic study of lifetime reduction in Cu, Ag and Au films for different thicknesses is provided.

For the sake of completeness, trends of scattering rates at magnetic impurities will be dis-

---

[1]At the noble metal surfaces a Fermi liquid behavior is expected, hence the electron-electron scattering rate scales as $\left(E - E_{\mathrm{F}} \right)^2$.

[2]The Debye temperature usually does not exceed a few hundred Kelvin, corresponding to a few tens of meV.
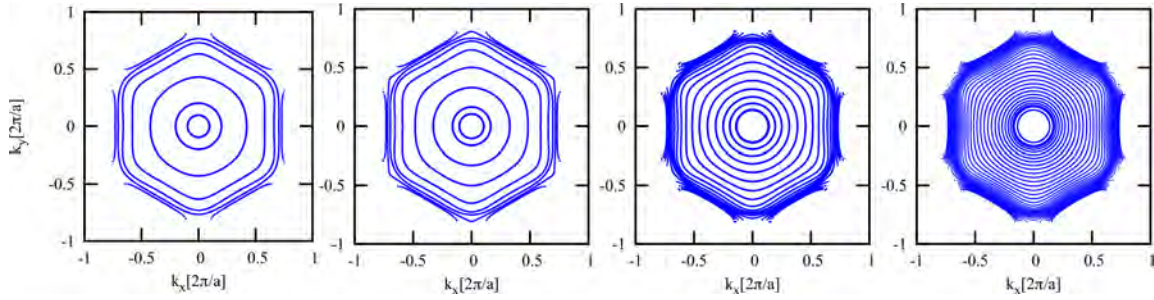
Figure 7.1.: Fermi surfaces of Cu films oriented in [111] direction for 6, 10, 18 and 40 layers (from *left* to *right*). For the calculations three 'vacuum layers' have been added on each side. The calculations have been performed within the atomic sphere approximation (ASA). The splitting between the two surface states (represented by the two innermost rings) decreases with the number of layers. Absolute values for the splittings are given in table 7.1.

cussed.

Finally, for copper films, surface resistivities are investigated, being closely related to the topic of surface-state lifetimes. Trends for different film thicknesses are compared to each other as well as to the trends obtained for surface-state lifetimes.

7.1 Computational and numerical aspects of the calculations

Comparable calculations for residual resistivities and momentum scattering times in bulk systems [69, 92] have been performed within the spherical potential approximation. As demonstrated in chapter 3, the formalism as well as the computational effort in ASA is much lower than for full potential (FP) calculations. However, at surfaces, where the symmetry is broken, it is reasonable that non-spherical components of the potential might play an important role. Especially, scattering at adatoms are expected to be sensitive on the FP/ASA treatment. Therefore, the first part of the current chapter deals with the comparison of surface-state lifetimes for ASA and FP calculations.

In our calculations a finite-thickness film is always considered. The situation of a half-infinite crystal with a single surface is approximated by increasing the film thickness. Furthermore, the vacuum region is described by empty atomic sites at 3 (or in some calculations 4) layers above the surface; these are called 'vacuum layers'.

7.1.1 Fermi surfaces of copper, silver and gold (111) films

Before investigating surface-state lifetimes, we shortly present the Fermi surfaces of the considered films, which are all crystallized in the fcc structure and oriented in [111] direction. The investigated materials are the three noble metals copper, silver and gold, whose elec-

number of layers	$\Delta \mathbf{k}[2\pi/a](\mathrm{a.u.})]$	$\Delta E[\mathrm{Ryd}]$
6	$1.1 \cdot 10^{-1}$	$4.9 \cdot 10^{-2}$
10	$2.8 \cdot 10^{-2}$	$1.3 \cdot 10^{-2}$
18	$4.4 \cdot 10^{-3}$	$2.3 \cdot 10^{-3}$
40	$4.5 \cdot 10^{-5}$	$2.4 \cdot 10^{-5}$

Table 7.1.: Splittings of the two surface states for symmetric Cu films as a function of the number of layers in atomic units. The splitting $\Delta \mathbf{k}$ on the Fermi surface corresponds to a splitting in energy given by $\Delta E(\mathbf{k}) = (\partial E_{\mathbf{k}}/\partial \mathbf{k}) \cdot \Delta \mathbf{k}$. All results have been obtained within the atomic sphere approximation.

tronic structure and Fermi surfaces are very similar to each other. As these systems are characterized by a two-dimensional periodicity, the Fermi surface consists of one-dimensional curves that in this case forms ring-like structures. The number of rings on the Fermi surface scales linearly with the number of layers, which can be seen in figure 7.1 for the example of a copper (111) Fermi surface for films with 6, 10, 18 and 40 copper layers (from left to right). The two innermost rings represent the so-called surface states which are formed in the gap of the surface-projected band-structure due to the boundary condition of a surface [93]. Surface states are localized at the atom layers close to the surface as can be seen in figures 7.2 and 7.10 and decay exponentially into the bulk and into the vacuum. Since in a finite film there are two surfaces, also two surface states appear. For finite films, they form a bonding and an anti-bonding state. The coupling of these two states manifests in a splitting between the two inner rings of the Fermi surfaces, decreasing with increasing film thickness since the overlap of the two surface states decreases exponentially. For 40 layers, the splitting of the two states almost vanishes. Absolute values of the splittings for copper surfaces obtained within the atomic sphere approximation are given in table 7.1.

In figure 7.2, the charge per atom for two $\mathbf{k}$-points belonging to the two different surface states is shown as function of the layer for films with 6 (left panel) and 40 (right panel) layers of copper[3]. Whereas for 6 layers the charge density of the surface states is still high in the center of the film, it is receded to a very low value at the center of the film consisting of 40 copper layers. The highest charge density of the surface states can be observed in the first surface layer; apart from that, it is still very high in the second surface layer as well as in the first vacuum layer.

Considering the Fermi surfaces of silver and gold films (see figure 7.3), a peculiarity for silver can be noticed. In the case of the silver films, the bottom of the band of the surface state is located only slightly below the Fermi energy, such that the coupling of the two surface states for thin films pushes one of the them above the Fermi level. Therefore, for silver films with 6 and 10 layers only one surface state appears as a ring on the Fermi surface. As it will be shown in section 7.3, this has consequences for the resulting surface state lifetimes, too.

---

[3]The two $\mathbf{k}$-points are chosen in [010] direction on the Fermi surface, but because the inner part of the Fermi surface is isotropic, this choice does not affect the results.
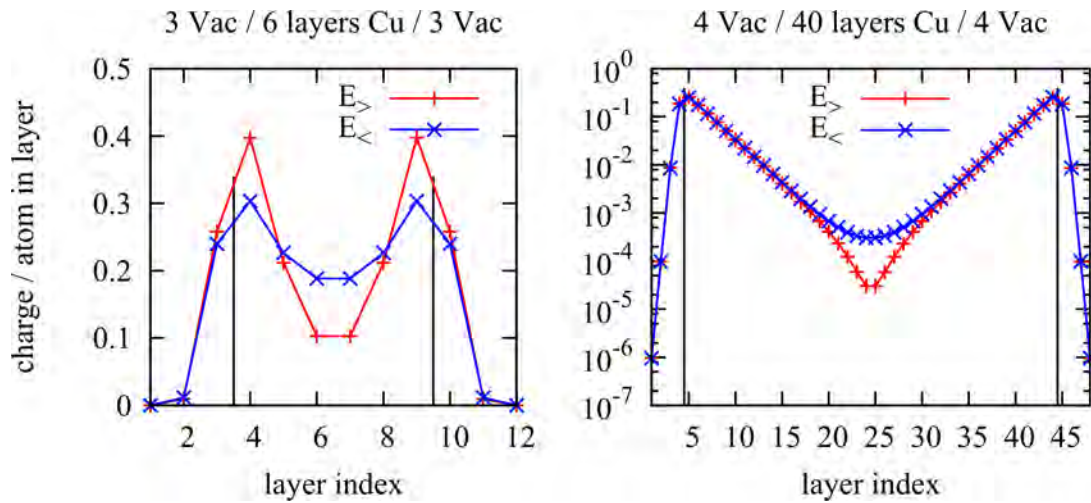
Figure 7.2.: Charge per layer at the Fermi energy E_F of the two surface states as a function of the layer index for films with six layers (*left*) and forty layers (*right*) of copper. The two selected **k**-points on the innermost ring or the second inner ring, respectively, are representative for the whole ring and chosen in [010] direction. The vertical black lines in the figures indicate the position of the surfaces. Note the different scales of the two diagrams. Whereas for the film with six copper layers the density of states for the two surface states in the center of the film is still large, in the case of 40 layers it is almost zero; therefore, the coupling of the two surface states is weak and almost no splitting on the Fermi surface is observed. The sum over all layers for each **k**-points equals one, due to normalization of wavefunctions. $E_>$ and $E_<$, respectively, denote the innermost and the second-innermost Fermi-ring.

7.1.2 The optical theorem

After having calculated the Fermi surfaces, we can now proceed with the investigation of lifetime reduction due to impurity scattering. Therefore, we place impurities in the surface layer, one layer below the surface as well as in adatom positions on top of the surface at the fcc threefold-hollow site. To calculate the surface-state lifetimes as described in chapter 3, we use the same scheme which we have already applied to bulk systems to calculate the momentum relaxation times $\tau_{\mathbf{k}}$. The perturbed region, where charge relaxation is allowed, generally is restricted in our calculations to a cluster of 13 sites, thus the shell of nearest neighbors[4]. All scattering rates, i.e. inverse lifetimes $\tau_{\mathbf{k}}^{-1}$, are given in units of ps per atomic percent of impurities, adatoms or defects.

Contrary to the case of the bulk systems investigated in chapter 6, there are no numerical or experimental references to compare our results. Although in principle surface-state lifetimes of copper, silver and gold (111) surfaces have been measured, they have not been

---

[4]In section 7.1.4, it will be shown that this choice is sufficient to obtain reasonable results.
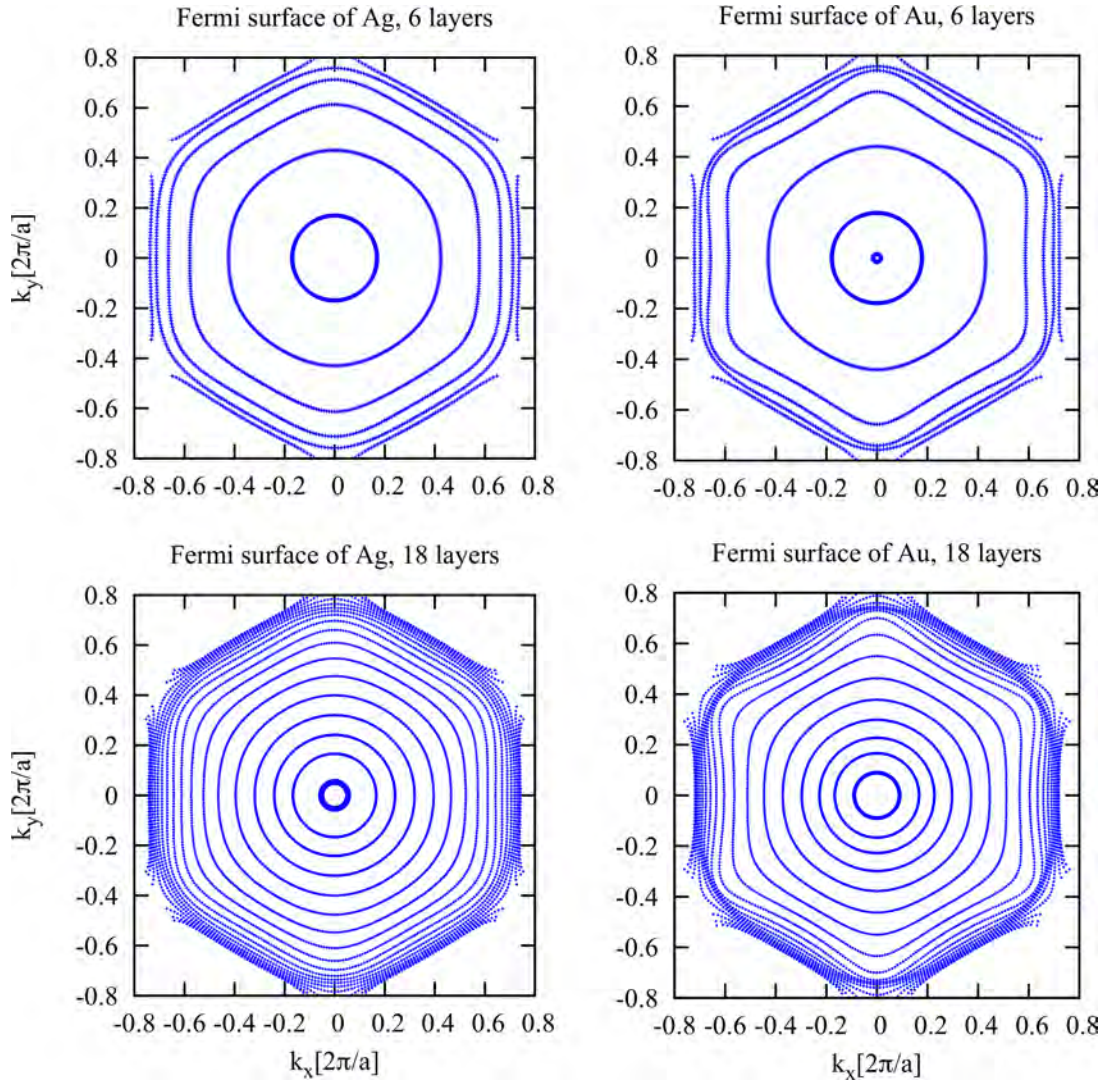
Figure 7.3.: Fermi surfaces of films with six layers (*upper panels*) and 18 layers (*lower panels*) of silver (*left*) and gold (*right*), oriented in [111] direction. For the Fermi surface of the film consisting of six layers of silver, only one surface state appears; this is due to the localization of the surface state only slightly below the Fermi energy and the large coupling of the two states for thin films. For 18 layers, the splitting is much smaller and the surface state with the higher energy again appears on the Fermi surface.

investigated under the aspect of impurity scattering. Impurity scattering has been preferably avoided.

However, another possibility to attest the numerical correctness of the results is given by the optical theorem. According to the optical theorem (see section 3.5, eq. (3.88)), the imagi-

nary part of the diagonal elements of the scattering matrix must obey

$$-\frac{2Nc}{\hbar}\mathrm{Im}\,T_{\mathbf{kk}} = \frac{2\pi Nc}{V_{\mathrm{BZ}}\hbar}\int_{S(E_{\mathbf{k}})}\frac{dS_{\mathbf{k}'}}{\hbar v_{\mathbf{k}'}}\,|T_{\mathbf{kk}'}|^2 \equiv \tau_{\mathbf{k}}^{-1}\,. \tag{7.1}$$

Both sides of the above equation are shown in figure 7.4 for a non spin-polarized calculation of Fe impurities in the first surface layer (left panel) and Fe adatoms (right panel) on top of a film consisting of six layers of copper. Additionally, in the same figure results obtained within the atomic sphere approximation (upper panels) as well as for taking the full potential (lower panels) into account are presented. For a better view, the inverse lifetimes $\tau_{\mathbf{k}}^{-1}$ are presented for all $\mathbf{k}$-points in the irreducible part of the Fermi surface (which is $1/12$ of the full Brillouin zone for systems without spin-orbit coupling) as a function of a $\mathbf{k}$-point index, following circle by circle, starting from the innermost ring to the outer boundary of the Brillouin zone. Thus, the two surface states are those with the smallest indices. The agreement of the two sides is very good, although for the two surface states in the case of Fe adatoms calculated within full potential calculations, a small difference can be observed. To obtain the above accuracy especially for the latter case (adatom and full potential calculations), a meticulous convergence of numerical parameters has been necessary. For example, it occurs that four vacuum layers on each side of the film are required instead of three which lead to good results for calculations performed within the atomic sphere approximation. Additionally, a very large number of $\mathbf{k}$-points for the calculation of the structural Green function, eq. (2.47), is required. Further comparisons of scattering rates obtained within ASA and FP calculations follow in a later part of this section and of surface resistivities in section 7.5.

A supplementary check of the results has been done by calculating the average of the inverse lifetimes $\left\langle\tau_{\mathbf{k}}^{-1}\right\rangle$ over the bulk states for Fe impurities in the surface layer as well as one layer below the surface; scaling it with the number of layers N, the average $N\cdot\left\langle\tau_{\mathbf{k}}^{-1}\right\rangle$ results in a value comparable to that obtained for an Fe impurity in copper bulk.

7.1.3 Comparison of ASA and FP calculations

Now, we return to the question whether there are deviations between inverse surface-state lifetimes $\tau_{\mathbf{k}}^{-1}$ obtained within ASA and FP calculations. As we have seen in chapter 6, section 6.3, for impurities in bulk systems, the calculated scattering rates agree very well; however, this might be different for systems with broken symmetry such as surfaces, where non-spherical components of the potential become more important.

In order to compare the two calculation schemes, inverse surface-state lifetimes for the whole series of $3d$ elements for adatoms and impurities in the surface of a copper film consisting of 6 layers are investigated. For simplicity, only one surface state (the innermost ring) will be considered. The results are presented in figure 7.5. In the two panels of the left column, the scattering rates for single-site calculations are presented, while in the two figures of the right column the shell consisting of the nearest neighbors (hence 13 atoms) has been included. For impurities in the first surface layer (the results are shown in the
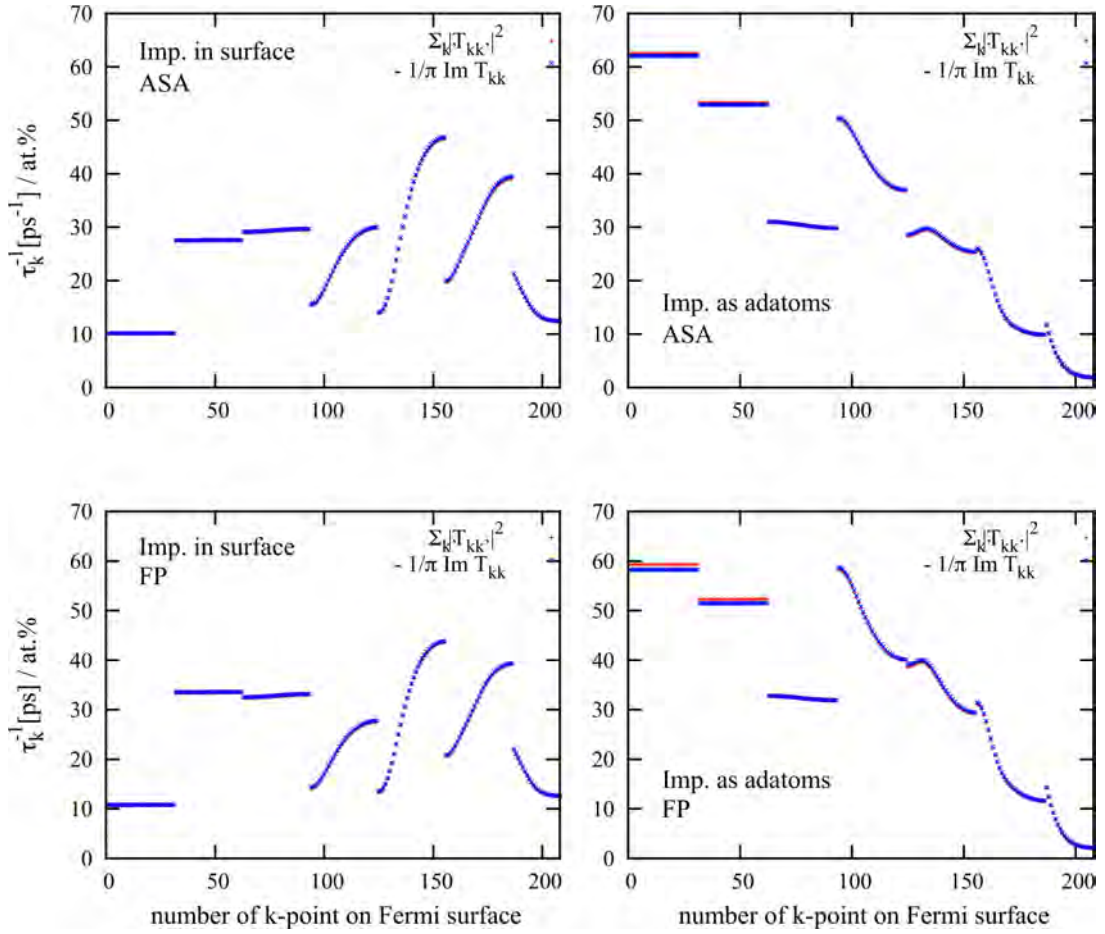
Figure 7.4.: Scattering rates $\tau_\mathbf{k}^{-1}$ for Fe impurities in the first surface layer (*left panels*) and Fe adatoms (*right panels*) in/on a film of 6 layers of copper as a function of the index of the $\mathbf{k}$-point on the Fermi surface in $1/12$ of the Brillouin zone, representing the irreducible part for systems without spin-orbit coupling. In order to check the correctness of the calculations, both sides of the optical-theorem equation are shown. The agreement is very good, only for the case of Fe adatoms and full potential calculations a small deviation for the two surface states can be observed. In this case, the obtained results are very sensitive to the chosen numerical parameters, and a careful convergence has been necessary.

two upper panels), the agreement of the two different calculation schemes is very good, both for single-site calculations and calculations where the nearest neighbors have been included. This is not the case for adatoms as can be observed in the two lower panels of figure 7.5; a considerable deviation is visible, even when a cluster including all nearest neighbors is taken into account. However, although a quantitative difference can be observed, the trends are similar.

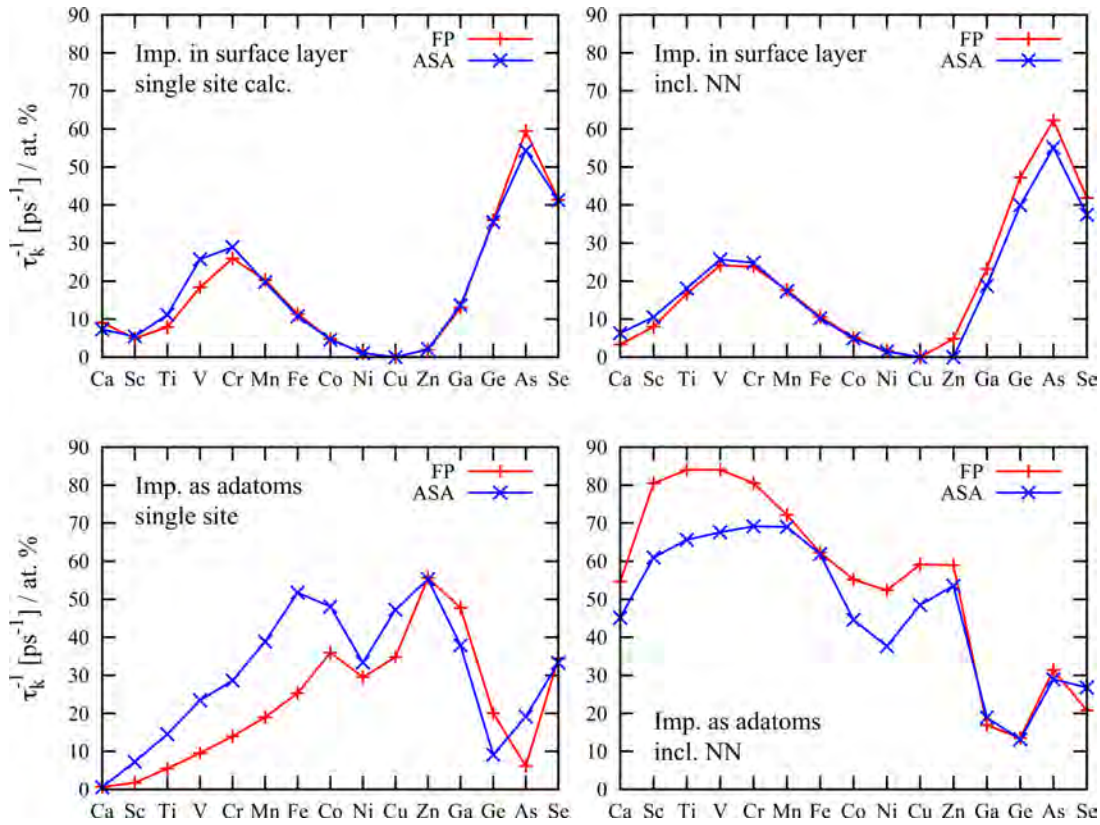Comparing the scattering rate at impurities in the surface layer (shown in the upper panels

Figure 7.5.: Scattering rates $\tau_{\mathbf{k}}^{-1}$ for impurities in the first surface layer (*upper panels*) and adatoms (*lower panels*) obtained within the atomic sphere approximation and full-potential calculations. While the agreement between the two calculations is very good for impurities in the first surface layer, for adatoms the two calculation schemes lead to qualitatively similar but quantitatively different results. Additionally, in the left panels the comparison has been done for single-site calculations, while in the right panels results for calculations are shown for which a cluster of the nearest neighbors has been included.

of figure 7.5) to the scattering at adatoms (lower panels of the same figure), a significant qualitative difference is evident. While the trend for impurities in the first surface layer resembles that which we have found for scattering at impurities in bulk, figure 6.7 in chapter 6, the trend for the scattering rate at adatoms does not. Additionally, for the latter case a large difference between single-site calculations (left panels) and those including nearest neighbors (right panels) can be observed. An analysis of these aspects follows in a later part of this chapter.

We conclude that quantitative differences between full potential calculations and calculations performed within the atomic sphere approximation are observed. However, in the following qualitative analysis we will restrict ourselves to ASA calculations. This can be justified by the fact that the observed trends qualitatively are the same for both calculations.
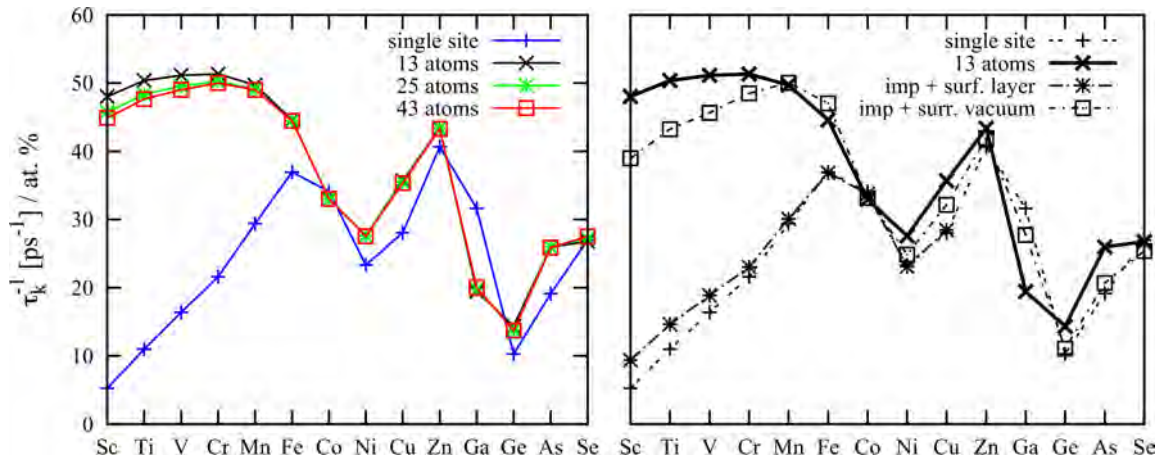
Figure 7.6.: *Left*: Scattering rates $\tau_{\mathbf{k}}^{-1}$ for adatoms in a film of 40 copper layers for different cluster sizes (ASA calculations). While a large difference between single-site calculations and those including nearest neighbors can be observed, larger cluster sizes hardly change the obtained scattering rates. *Right*: Scattering rates $\tau_{\mathbf{k}}^{-1}$ for adatoms on a film of 40 copper layers. Presented are single-site calculations, calculations including the adatom with the neighboring sites ('13 atoms'), calculations including the adatom and the surrounding vacuum sites only, and calculations including the adatom and the surface nearest neighbors only. We observe that especially for the early $3d$ elements, the surrounding vacuum strongly influences the scattering rate.

7.1.4 Convergence with cluster size

In the previous section, we have already seen that for adatoms large differences between single-site calculations and those including a cluster of nearest neighbors are observed. The above finding raises the question whether the cluster consisting of nearest neighbors only is large enough to obtain converged results. Therefore, calculations including additionally the shells of the second nearest neighbors and the third-nearest neighboring sites in the first vacuum layer (25 atoms) and third nearest neighbors (43 atoms) are performed. The results are presented in the left panel of figure 7.6; when including more than nearest neighbors, scattering rates hardly change. Therefore, in the following we restrict ourselves to the shell of nearest neighbors.

7.2 Analysis of surface-state lifetimes for adatoms

Considering the trend of the inverse surface-state lifetimes for scattering at adatoms (see e.g. figure 7.12) it catches one's eye that the observed trend remarkably differs from the one obtained for impurities in the first surface layer as well as from the trends for the scattering rates at impurities in bulk systems (see chapter 6, e.g. figure 6.7). The main reason for this
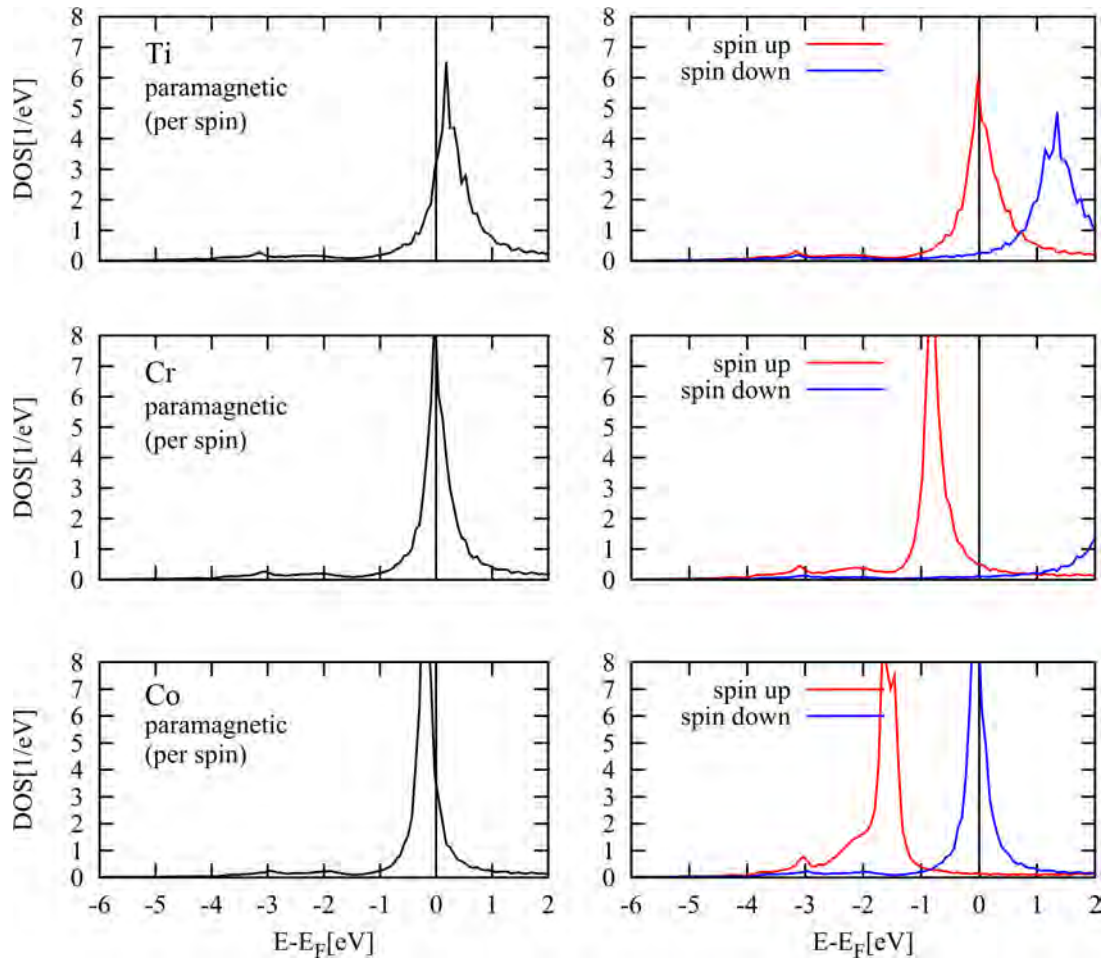
Figure 7.7.: Density of states per spin for paramagnetic (*left panels*) and magnetic (*right panels*) Ti, Cr and Co adatoms on a copper film consisting of 40 layers of copper. In the case of paramagnetic adatoms, for Ti (and all elements with smaller atomic numbers than Cr) the d-resonance is above the Fermi energy, while for all elements with larger atomic numbers than Cr the d-resonance is below E_F. For impurities in the surface, this explains why scattering has a maximum for a Cr impurity. In contrast, for magnetic adatoms two maxima are observed corresponding to the d-resonances of the two spin channels crossing the Fermi energy.

different behavior is that the perturbation caused by an adatom is totally different from the situation of an impurity in the surface layer or in a bulk lattice. While in the latter case only a copper atom is replaced by a different, foreign atom, the addition of an adatom on top of the surface changes the geometry of the total system. Then, the strength of scattering depends on parameters such as the size and the delocalization of the adatom (because of the lack of surrounding atoms in the vacuum layer) as well as on the reduced overlap with the bulk states.

The difference between the trends for adatoms and impurities in the first surface layer is

most striking for the first elements of the row (such as Sc, Ti, V) and the sp scatterers Ga and As. For the latter ones, the scattering rate is maximal if they are placed in the surface but minimal when positioned as adatoms.

In contrast, while the scattering rate for Sc, Ti and V is low for impurities in the surface and in the bulk, the inverse scattering rate for surface states is at the same level as for the d scatterer with half-filled d-shells. Additionally, as already stated in the previous section, for these light elements the deviation between single-site calculations and those where nearest neighbors are included is relatively large. Apparently, for these elements the scattering rate cannot be explained with their density of states, which is shown (for Ti, Cr and Co adatoms) in the left panels of figure 7.7.

However, the densities of states help to explain the results obtained for impurities in the surface and – at least partly – the results of the single-site calculations. The trend calculated for impurities in the first surface layer resembles the trend of the momentum scattering times in bulk systems and is therefore what is expected. For the d scatterer, the scattering rate is determined by the position (in energy) of the d-resonance relative to the Fermi energy. The maximal scattering rate is obtained for V and Cr impurities, for which the d-resonance is centered at the Fermi level (see figure 7.7); for the earlier elements, the peak is at higher energies, whereas for elements with higher atomic numbers the resonance is below the Fermi energy[5] and the scattering rate decreases and obviously vanishes for Cu. For the sp scatterer it increases again, according to Linde's rule [94, 95].

In order to understand the trend of $\tau_{\mathbf{k}}^{-1}$ calculated for scattering at adatoms, we start from the observation already made in the previous section that the single-site results remarkably differ from those obtained within a cluster of nearest neighbors. This lead us to the question which sites of the cluster contribute most to the scattering rate. Therefore, we have performed calculations where we have included – apart from the adatom – the surrounding vacuum sites only, or, the surface nearest neighbors only, respectively. The results are presented in the left panel of figure 7.6. While the surface-state scattering rates at the adatom together with the copper atoms in the first surface layer hardly differ from the single-site results, the inclusion of the surrounding vacuum sites leads to scattering rates which are already close to those obtained for scattering within the whole shell consisting of all nearest neighbors. Hence, the largest contribution arises from the surrounding vacuum potentials. This effect is relatively large for the early $3d$ scatterers and low for all other elements. A possible reason for this behavior is that these elements have a relatively large atomic radius (which is $r_{\mathrm{at}} = 1.62$ Å for Sc, 1.45 Å for Ti, 1.34 Å for V) [96] and therefore extend more into the vacuum than for example a Ga adatom with $r_{\mathrm{at}} = 1.22$ Å; apparently, the large extent entails stronger scattering rates because of the larger overlap of the perturbed region with the host wavefunctions.

In order to analyze and understand the single-site results for scattering at adatoms, orbital-momentum resolved scattering rates are investigated. Therefore, we define the scattering

---

[5]Although the densities of states are shown for adatoms the qualitative picture, i.e. the position of the resonances relative to the Fermi level does not change for impurities in the surface.
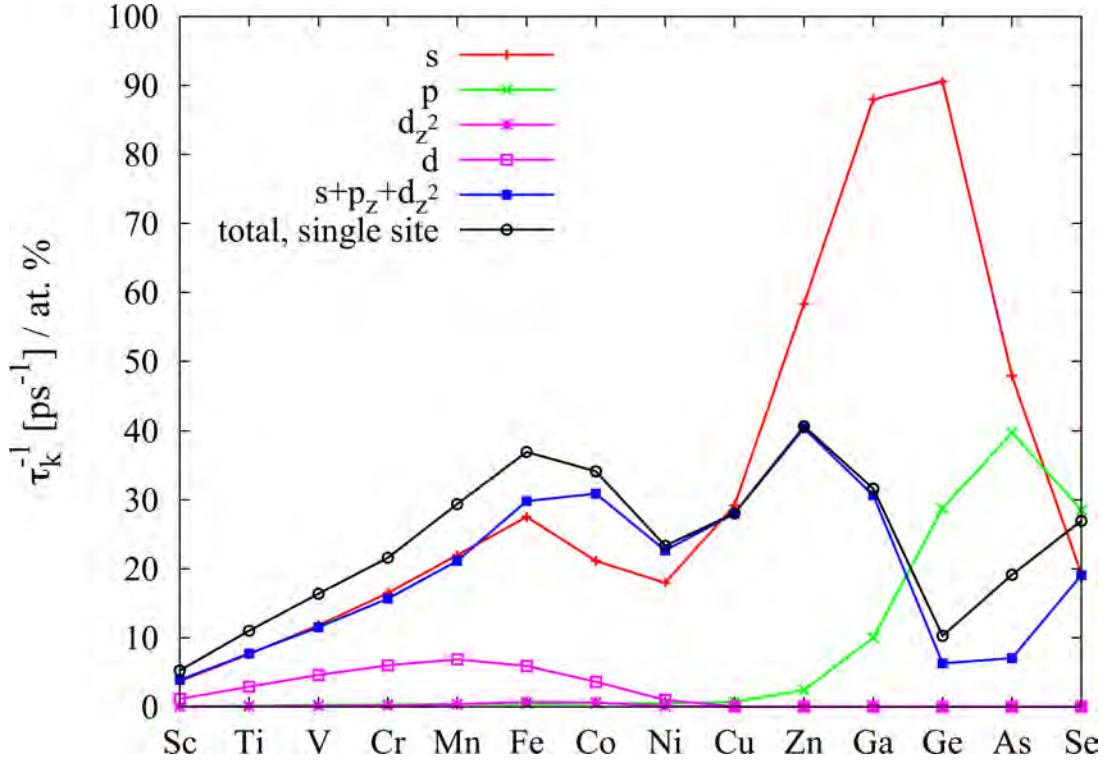
Figure 7.8.: Angular-momentum resolved scattering rates for adatoms on a film consisting of 40 layers of copper. The inclusion of the s, p_z and the d_{z^2} channel in the single-site scattering matrix $T_{LL'}^{00}$ (compare eq. (7.2)) describes the total scattering rate already well. For the early elements, s-scattering is dominant, while the consideration of only the s-channel for the sp scatterers Zn-As by far overestimates the total scattering. This behavior can be understood by the investigation of Friedel-oscillations (see figure 7.9), which verify the assumption of a constructive interference for a Co adatom and destructive interference for Ga and Ge adatoms.

matrix $T_{LL'}^{nn'}$ as[6]

$$T_{LL'}^{nn'} := \sum_{L''} \Delta_{LL''}^n \left(\delta_{L''L'}\delta_{nn'} + \sum_{L'''} G_{L''L'''}^{\text{imp},nn'} \Delta t_{L'''L'}^{n'} \right) \tag{7.2}$$

which is related to the scattering matrix $T_{\mathbf{k}\mathbf{k}'}$ in reciprocal space by

$$T_{\mathbf{k}\mathbf{k}'} = \sum_{nn'} \sum_{LL'} c_{\mathbf{k}L}^{n\star} T_{LL'}^{nn'} c_{\mathbf{k}'L'}^{n'} . \tag{7.3}$$

Then, the single-site contribution $n = n' = 0$ is resolved to different L-channels. The results are presented in figure 7.8 for T_{ss}^{00}, T_{pp}^{00}, $T_{d_{z^2}d_{z^2}}^{00}$, T_{dd}^{00} and $T_{sp_zd_{z^2},sp_zd_{z^2}}^{00}$ together with the total

---

[6]For a better understanding of expressions 7.2 and 7.3 compare the definition of $T_{\mathbf{k}\mathbf{k}'}$ in section 3.3.

single-site contribution. Due to the presence of the surface, which breaks the symmetry to some extent, we expect that interference is possible among s, p_z and d_{z^2} waves. As can be observed, the inclusion of the s-, p_z- and d_{z^2}-channel already leads to a curve similar to the total single-site result. For the first elements of the row, scattering in the s-channel is dominant, while for the sp scatterer (starting from Zn) the restriction of T^{00} to the s-channel only overestimates the whole scattering rate; thus, apparently, destructive interference occurs.

In order to analyze interference effects, we have calculated the Friedel oscillations for Co, Ga and Ge adatoms, i.e. the difference of the local density of states integrated over the ASA sphere in the vacuum on an axis parallel to the surface compared to that of the host vacuum site, i.e. $n_l(E_F) - n_l^{vac}(E_F)$. It is presented in figure 7.9 as function of the distance from the adatom site. For a Co adatom, the s-, p_z- (though being very small) and d_{z^2}-components of the waves are in phase and, in agreement with the orbital-resolved scattering rate in figure 7.8, a constructive interference can be observed. In contrast, for Ga and Ge adatoms the oscillations in the s- and p-channel are not in phase and interfere destructively. This explains why for these elements the high scattering observed in the s-channel does not lead to high total scattering rates.

7.2.1 Scattering to bulk and surface states

The method used to calculate the surface-state lifetimes given in section 3.5, eq. (3.87), allows to distinguish between scattering to bulk and to surface states. The total scattering rate of a (surface) state characterized by a wavevector $\mathbf{k}$ is composed of a contribution $\tau_{\mathbf{k}}^{surf}$ given by

$$\frac{1}{\tau_{\mathbf{k}}^{surf}} = \frac{2\pi Nc}{V_{BZ}\hbar} \int_{S(E_F),surf} \frac{dS_{\mathbf{k}'}}{\hbar v_{\mathbf{k}'}} |T_{\mathbf{k}\mathbf{k}'}|^2 \ , \tag{7.4}$$

where the integration is performed only over the surface states, and, analogously, a contribution $\tau_{\mathbf{k}}^{bulk}$, where only the bulk states of the Fermi surface are taken into account

$$\frac{1}{\tau_{\mathbf{k}}^{bulk}} = \frac{2\pi Nc}{V_{BZ}\hbar} \int_{S(E_F)bulk} \frac{dS_{\mathbf{k}'}}{\hbar v_{\mathbf{k}'}} |T_{\mathbf{k}\mathbf{k}'}|^2 \ . \tag{7.5}$$

Obviously, considering the definitions of $\tau_{\mathbf{k}}$, $\tau_{\mathbf{k}}^{surf}$ and $\tau_{\mathbf{k}}^{bulk}$, the relation

$$\frac{1}{\tau_{\mathbf{k}}} = \frac{1}{\tau_{\mathbf{k}}^{surf}} + \frac{1}{\tau_{\mathbf{k}}^{bulk}} \tag{7.6}$$

is fulfilled.

The two contributions have been calculated for films consisting of 6 and 40 layers of copper for impurities in the layer below the surface, in the surface layer as well as for adatoms and are presented in figure 7.11. For impurities in the surface layer and below the surface, scattering to bulk states is expected to be much larger than scattering to surface states. This is fulfilled very well for the $3d$ scatterers, but *not* for the sp scatterers. Even in the case of impurities below the surface, for the film with six copper layers (compare the panel at the
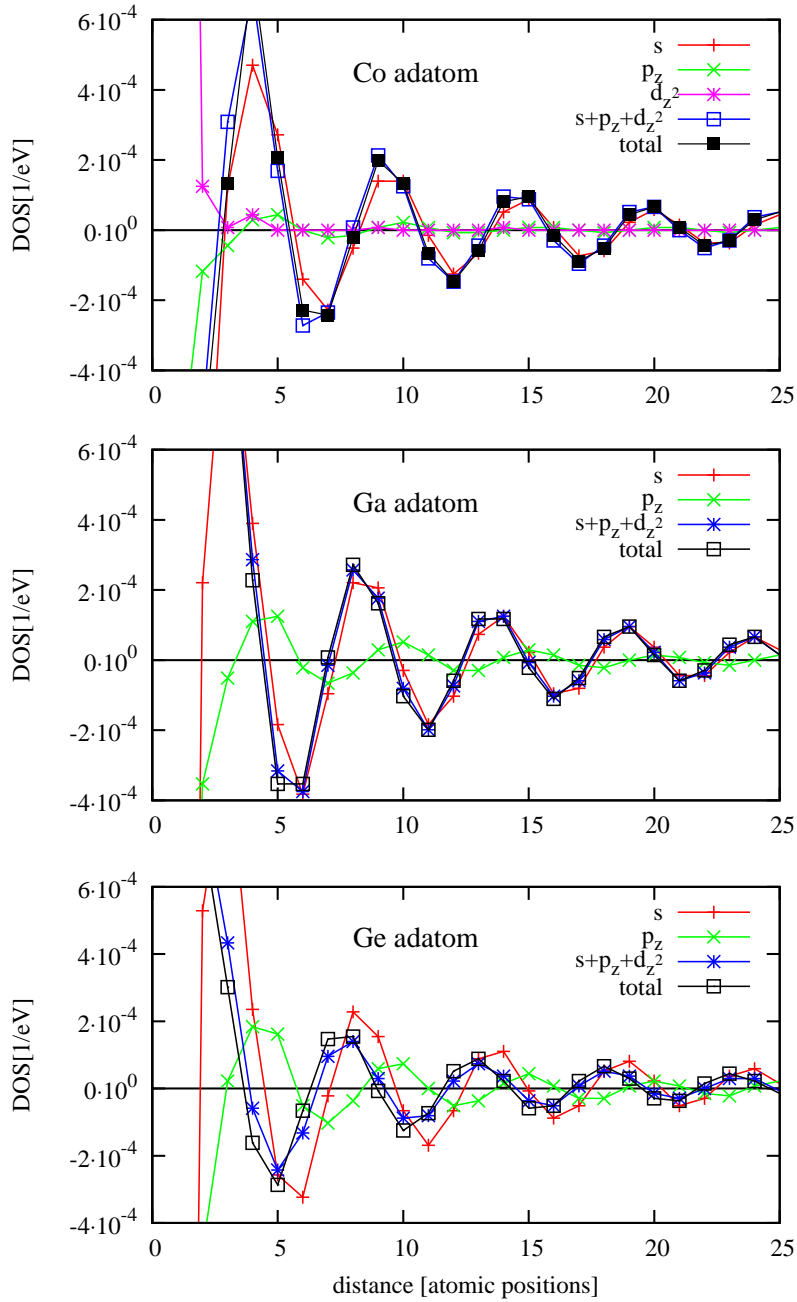
Figure 7.9.: Friedel-oscillations calculated for Co, Ga and Ge adatoms. The momentum-resolved difference of the local density of states as a function of distance to the adatom site is calculated, i.e. $n_l(E_F) - n_l^{\mathrm{vac}}(E_F)$, with $n_l^{\mathrm{vac}}(E_F)$ being the density of states of the vacuum site of the host and $n_l(E_F)$ the density of states, perturbed by the adatom. While for a Co adatom the s-, p_z- and d-channel oscillate in phase, for Ga and Ge adatoms a destructive interference of the s- and p_z-channel is observed. For Ga and Ge adatoms, d-scattering is very small and can be neglected.
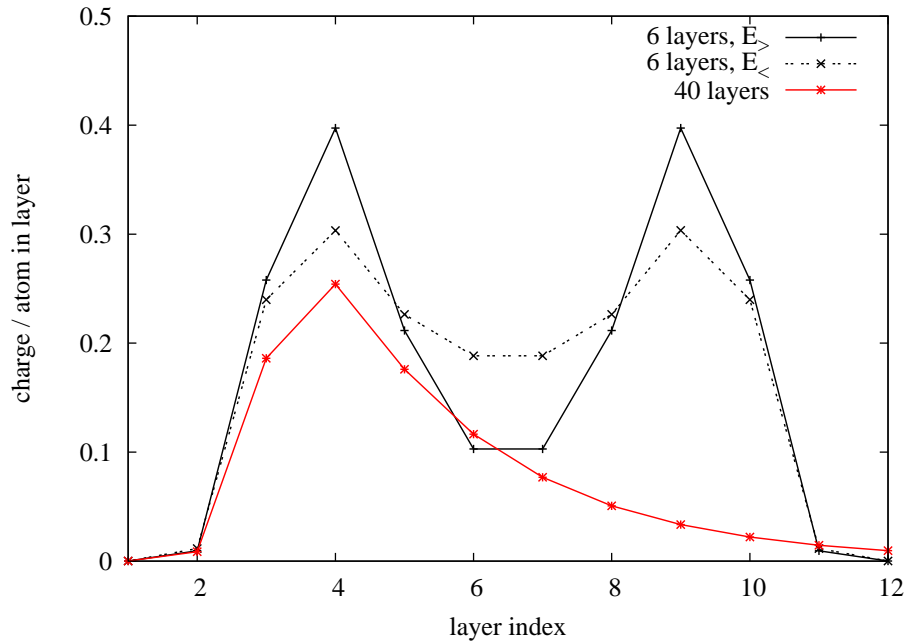
Figure 7.10.: Charge per atom in layer for the two surface states of a copper film with six layers and for one of the two surface states of a film with 40 copper layers. For the thinner film, the charge in each layer is larger than for the 40 layers-film, because the number of layers in which the surface states can penetrate is limited. This might be the reason for which scattering rates (for scattering at adatoms) increase with decreasing number of layers (compare figure 7.12).

left bottom of figure 7.11), the scattering rate to surface states at Ga, Ge and As impurities is higher than the scattering rate to bulk states. Interestingly, this is opposite to the film of 40 copper layers, where scattering to bulk states prevails. For the case of adatoms, the two contributions behave reversed; while the scattering at $3d$ adatoms is clearly dominated by scattering to other surface states, for sp-adatoms scattering to bulk states is lower than scattering to the two other surface states.

The reason for the different behavior of the scattering in 6 and 40 layers of copper is not fully understood. However, scattering to surface states in the thinner films might be higher than in the thicker films, because the localization of surface wavefunctions in the vacuum, surface and subsurface layer, where the impurity is placed, is larger in the thin films (see figure 7.10).

Finally, while the lifetimes $\tau_{\mathbf{k}}$ of the bulk states scale inversely with the number of layers, the surface-state lifetimes $\tau_{\mathbf{k}}$ with increasing number converge to a constant value (see figure 7.12), which is considerably smaller than the momentum scattering rate τ^{-1} for impurities in bulk. A possible reason for this decrease might be the delocalization of the surface state
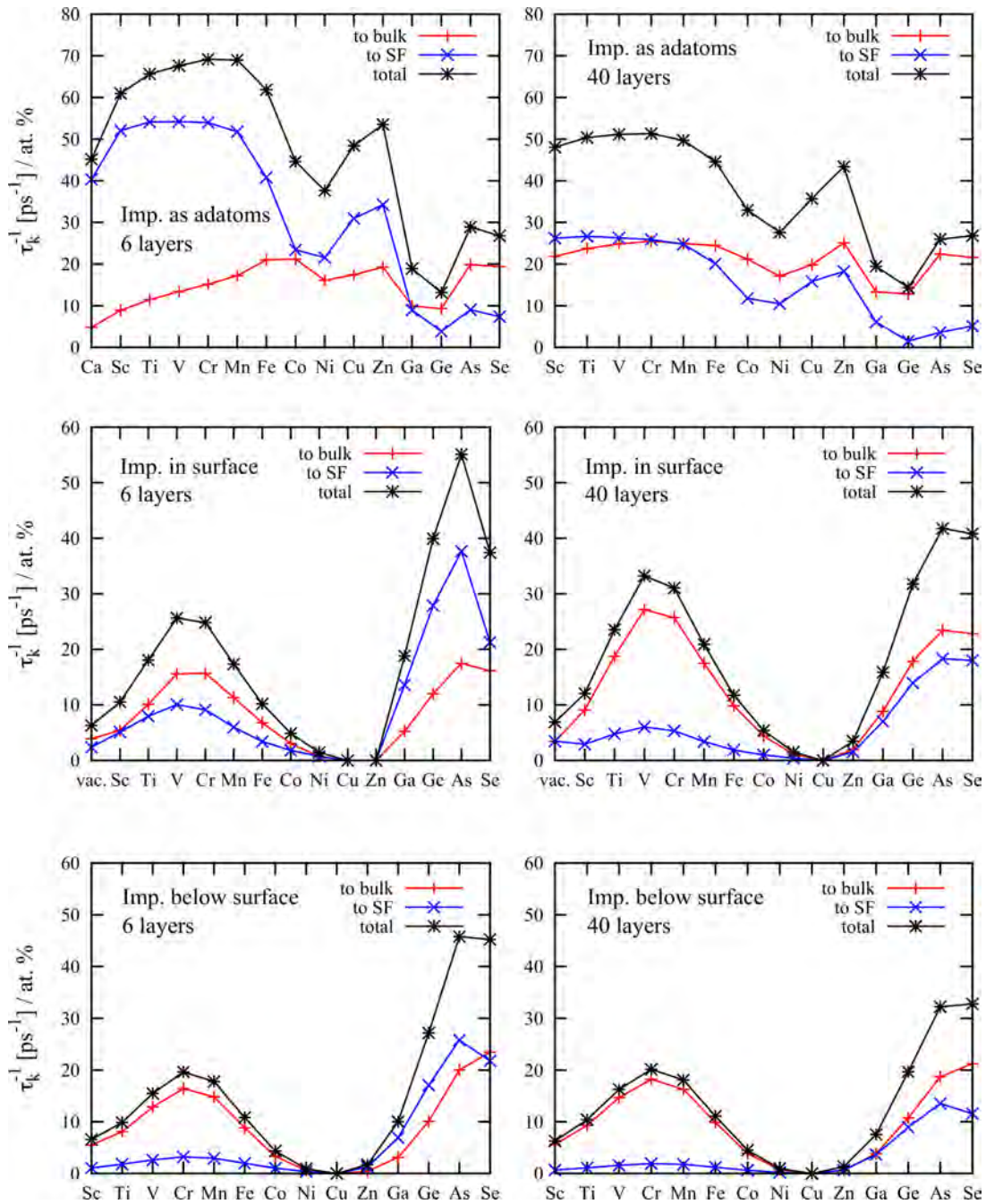
Figure 7.11.: Total inverse surface-state lifetimes $\tau_{\mathbf{k}}^{-1}$ for the innermost surface state together with the contributions of scattering rates to bulk and surface states $1/\tau_{\mathbf{k}}^{\text{bulk}}$ and $1/\tau_{\mathbf{k}}^{\text{surf}}$ for films with 6 layers of copper (*left panels*) and 40 copper layers (*right panels*) for adatoms (*top*), impurities in the first surface layer (*center*) and impurities in the layer below the surface (*bottom*).

mainly over three layers; the first two surface layers and the first vacuum layer. Assuming

that in the bulk there are N atoms, among them one impurity, then the overlap of a bulk
state with the impurity is given by $1/N$. In contrast, if N atoms are in the surface, the surface
state expands over a volume of $3N$ atoms and, therefore, has an overlap of $1/3N$ with the
adatom, leading to smaller scattering rates.

7.3 Surface-state lifetimes for Cu, Ag and Au films

Having analyzed the surface-state lifetimes for impurities in and on copper films, we inves-
tigate scattering rates for $3d$ and $4sp$ impurities and adatoms in/on silver and gold films.
Additionally, we compare inverse surface-state lifetimes for different numbers of layers[7].
The calculated data, shown in figure 7.12, are qualitatively similar for all three hosts. Scatter-
ing rates off adatoms are largest for the first elements of the row and remain almost constant
until Mn; just as in the case of the copper film (see previous section), this should be due to
the larger atomic radius entailing a larger extent of these elements into the vacuum. Fur-
thermore, all three host materials show a clear trend that scattering at adatoms on a film of
six layers is enhanced compared to that of larger numbers of layers. Again, the reason is the
higher localization of the surface state for thin films; the surface states extend over a smaller
number of layers, entailing a larger overlap with the impurities, and, therefore higher scat-
tering rates.
Concerning scattering at impurities in the surface, the situation is more complicated. Qual-
itatively, for all three host materials a clear maximal scattering rate for the $3d$ elements with
half-filled shells (V, Cr) is observed as well as high inverse lifetimes for the sp scatterer.
Hence, as expected, the global trend reflects the situation of scattering at impurities in the
bulk which has been already discussed in chapter 6 and in the previous section 7.2. How-
ever, large quantitative differences among the three host materials are observed when con-
sidering the thickness-dependency as well as the comparative scattering strength of $3d$ and
$4sp$ impurities. While for a copper host, the scattering rate does not depend much on the
film thickness, for silver films the thickness makes a big difference. Actually, the silver host
is expected to show a strong thickness dependence because of the relatively shallow position
of the surface state (starting below the Fermi energy). In thin films quantum-confinement
effects push one of the two surface states above E_{F}, resulting in a significant change of the
available phase space for scattering.
A comparison to other theoretical or experimental results is not possible because of the
lack of data; although the investigated surfaces and even surface states have been subject to
a lot of experiments, according to our knowledge no experiments have been performed in
which the surface-state lifetimes due to scattering at the specific impurities at the Fermi level
have been measured. However, the order of magnitude of scattering rates calculated in the
present thesis should allow for an experimental detection; to compare, in inverse photoe-
mission spectroscopy a linewidth of about $23\ \mathrm{meV} \approx 35\ \mathrm{ps}^{-1}\hbar$ for Cu, $6\ \mathrm{meV} \approx 9\ \mathrm{ps}^{-1}\hbar$ for
Ag and $21\ \mathrm{meV} \approx 33\ \mathrm{ps}^{-1}\hbar$ for Au for electron-electron scattering processes is measured.
A measurement for $1\ \%$ of defects should be, therefore, within the experimental resolution.

---

[7]Similar as in the previous section, for a qualitative analysis we restrict to ASA calculations.
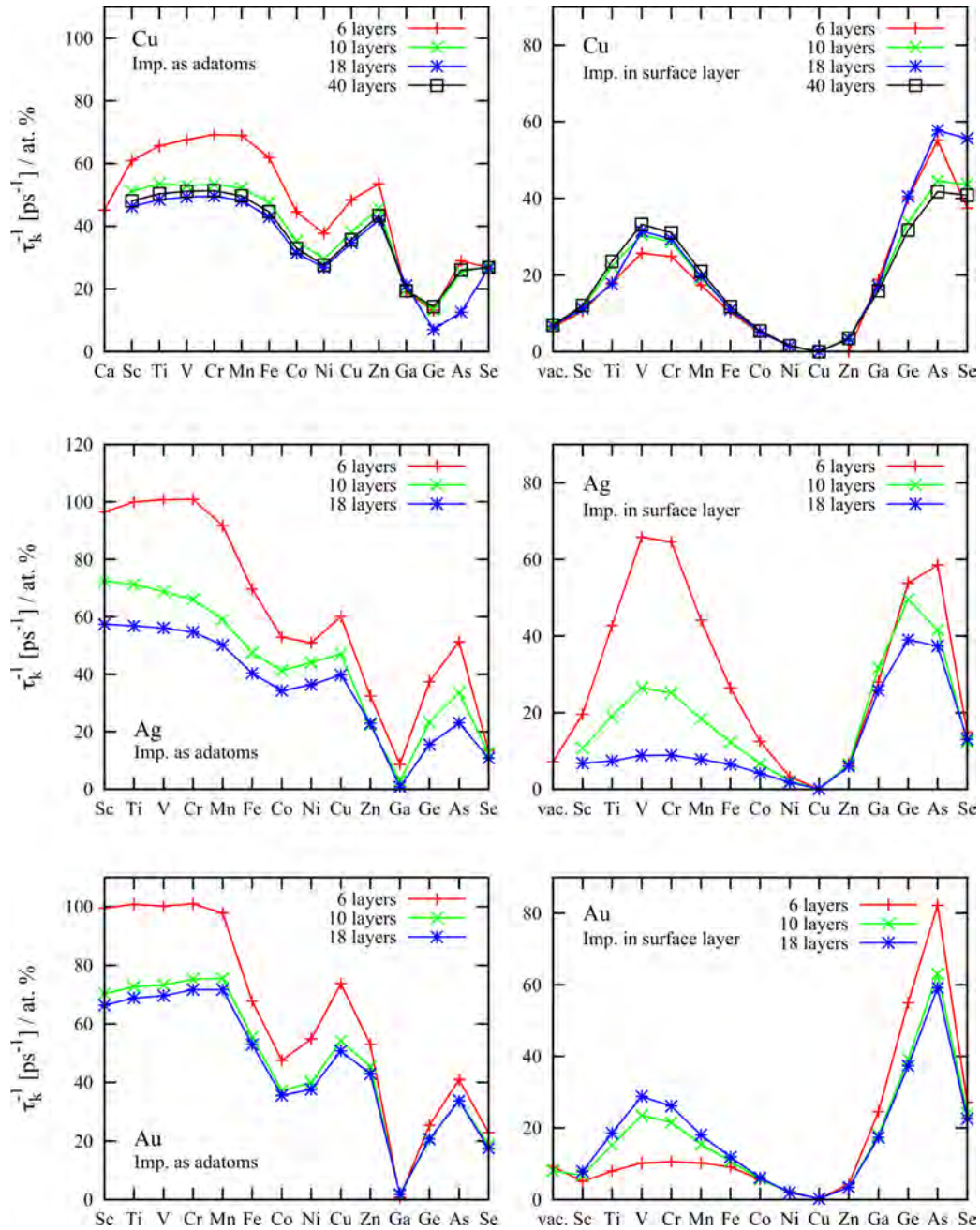
Figure 7.12.: Inverse surface-state lifetimes τ_k^{-1} for adatoms (*left panels*) and impurities in the first surface layer (*right panels*) for Cu, Ag and Au films with different number of layers. For all three host materials, the trend for scattering at impurities in the surface correspond to that already observed for scattering in the corresponding bulk metals; however, the dependency on the number of layers highly differ for silver films. While for copper and gold films a slight increase of τ_k^{-1} with increasing film thickness is observed, for silver films the inverse scattering rate decreases. This different behavior might be related to the fact that for silver films with 6 and 10 layers only one surface state accounts for scattering, since the other one is above the Fermi energy. The scattering rates for scattering at adatoms on silver and gold films show the same trend as on copper films.

7.4 Scattering at magnetic impurities

So far, only scattering at non-magnetic impurities and adatoms has been considered. However, above the Kondo temperature, some of the $3d$ impurities become magnetic and scattering at the two spin channels has to be treated separately. The resulting lifetimes are shown in figure 7.13. As adatoms, the $3d$ metals starting from Ti to Co are magnetic, while for impurities in the surface Ti is still paramagnetic. The $4sp$ elements are paramagnetic. The magnetism of the $3d$ elements leads to a double-peak structure in the trend of the surface-state lifetimes, which is already known e.g. for residual resistivity in bulk and originates from the offset of the d-resonance of the two spin channels, which is mutually shifted due to the exchange interaction. This becomes obvious when considering the density of states, shown in figure 7.7. As already stated for impurities in bulk and in the surface layer, scattering rates become large when the d-resonance crosses the Fermi energy. However, for magnetic impurities the d-resonance is shifted for the two spin channels, such that scattering becomes large twice, i.e. for each spin channel crossing the Fermi energy. Therefore, a first peak of the inverse lifetimes is observed for Ti, where the d-resonance of the spin-up channel is centered at the Fermi level, while a second peak appears for Fe/Co, where this is the case for the spin-down channel. For Cr impurities, where scattering rates are large in the case of paramagnetic impurities, the inverse lifetime is low since E_F is between the d-resonances of the two spin channels.

As already mentioned, the consideration of magnetic impurities/adatoms is valid only above the Kondo temperature. However, at high temperatures the phonon contribution becomes important, and, scaling linearly with temperature [86], at room temperature (for not too high impurity concentrations), dominates the reduction of lifetimes. Therefore, lifetime reduction caused by impurity scattering can be better observed at lower temperatures, where most impurities are non-magnetic. The Kondo temperature varies over orders of magnitude, depending exponentially on the position of the d-resonance and on the hybridization. Therefore, there is no 'unique' temperature above which all $3d$ impurities become simultaneously magnetic. At low temperature, however, they should all be non-magnetic. In this case, the non-magnetic density of states in the local-density approximation (see section 1.3) does not represent the physical density of states, except exactly at the Fermi energy E_F, where it is probably a good approximation. This follows from the fact that, as it has been shown in model calculations [97], the phase shift and density of states at E_F in the Kondo phase, at $T = 0$, coincide with the corresponding quantities calculated in the mean-field approximation when the electron correlation is ignored.

7.5 Residual resistivity

Surface-state lifetimes are strongly related to the concept of surface resistivity ρ_surf, defined as the ratio of a voltage drop per unit length to the surface current per unit width. Therefore, ρ_surf is a property of the material and does not (or at least should not) depend on the size of the sample.
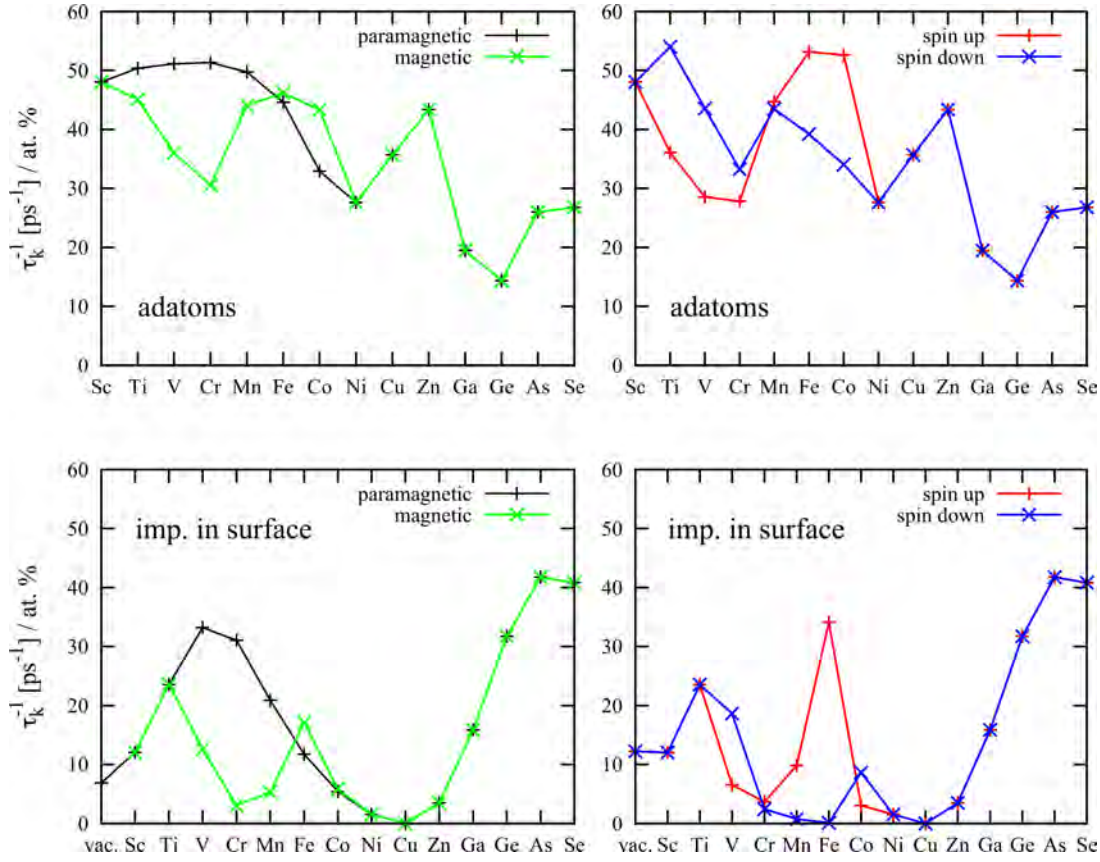
Figure 7.13.: Inverse lifetimes for scattering at magnetic adatoms (*top*) and impurities in the surface layer (*bottom*) of a copper film of 40 layers. The magnetism of the $3d$ elements leads to a double-peak structure of the inverse surface-state life-times $\tau_{\mathbf{k}}^{-1}$ because of the offset in the density of states of the two spin channels (see figure 7.7). The first maximum is reached for Ti, when the d-resonance of the spin-up channel crosses the Fermi level, while the second maximum corresponds to the localization of the d-resonance of the spin down channel at E_{F}.

Surface resistivities can be calculated in analogy to residual resistivities in bulk materials ρ_{bulk} as explained in section 3.6 using the Boltzmann equation (3.91) and eq. (3.92) or eq. (3.93), respectively. In order to attest the correctness of our calculations of surface resistivities and to compare ρ_{surf} with the values obtained for residual resistivities in bulk ρ_{bulk}, we start with a presentation of ρ_{bulk}, calculated for the $3d$ impurities in copper bulk.

7.5.1 Residual resistivity in copper bulk

In contrast to momentum relaxation times $\tau_{\mathbf{k}}$, residual resistivities due to scattering at $3d$ impurities in copper bulk have been measured and calculated within *ab initio* calculations
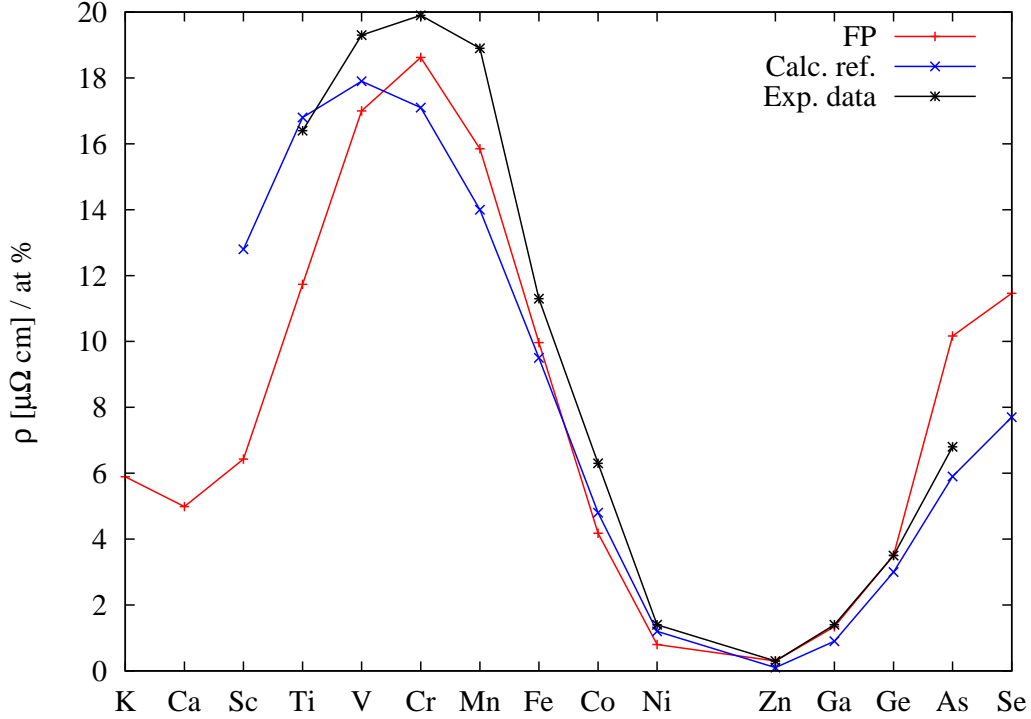
Figure 7.14.: Residual resistivities $\rho \, [\mu\Omega\ \mathrm{cm}]$ per one atomic percent of $3d$ and $4sp$ impurities in copper bulk. Our results for full potential calculations (FP) are compared to numerical results of reference [69, 92] obtained within the spherical potential approximation and experimental results from [98, 99, 100].

already 30 years ago. Therefore, in figure 7.14 we present our results of $\rho_{\mathrm{bulk}}[\mu\Omega\ \mathrm{cm}]/1\%$ together with numerical [69, 92] and experimental [98, 99, 100] data. The agreement of our results with those of the references is reasonable. Whereas we have been performed full potential calculations, the numerical results of [69, 92] have been obtained within a spherical potential approximation.

Comparing the residual resistivities with the inverse momentum relaxation times $\tau_{\mathbf{k}}^{-1}$ (see figure 6.7 in section 6.5), a difference in the curves can be observed: While the resistivity of the $4sp$ elements increases only to approximately half of the maximum of the $3d$-metals, the maximal inverse momentum relaxation time is of the same order for $3d$ and $4sp$ impurities. This is caused by the different relaxation times entering in ρ and τ^{-1}: While $\tau_{\mathbf{k}}$ is the momentum relaxation time, for the calculation of ρ the transport relaxation time is required. The difference stems from the fact that for the transport time, resulting from the Boltzmann equation 3.91, back-scattering is far more important than forward scattering, while for the lifetime they are equally important. The d-resonance contributes to back-scattering more than the p-states.
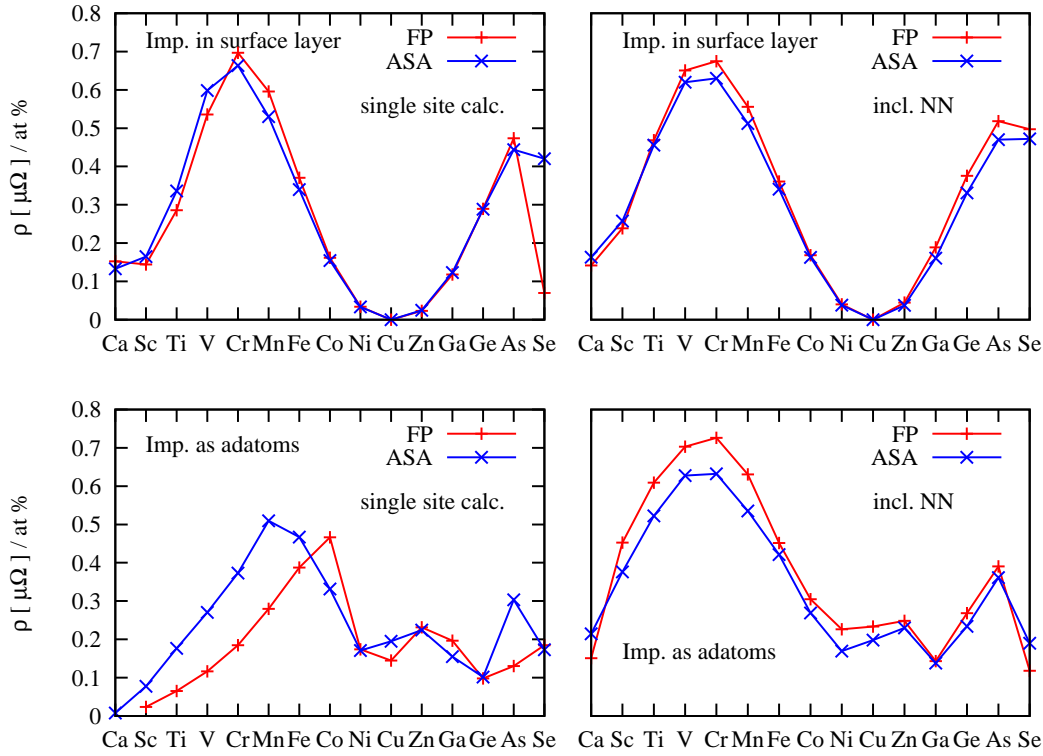
Figure 7.15.: Comparison of surface resistivities, measured in $\mu\Omega$ per atomic percent for impurities in the first surface layer (*top*) and on top of the surface (*bottom*). All calculations have been performed for a film consisting of 6 layers of copper. In the left panels single-site calculations are shown, while in the right panels a cluster of 13 sites, i.e. nearest neighbors have been included in the calculations.

7.5.2 Surface resistivity

In this section, we present surface resistivities due to scattering at $3d$ impurities in the first surface layer and positioned as adatoms on copper films. In contrast to resistivities in bulk, ρ_{surf} is given in Ω and not in Ωm.

Similar as for the surface-state lifetimes, in a first step, we have compared the surface resistivities obtained in ASA and FP calculations, respectively (see figure 7.15); furthermore, single-site results are compared to those where the nearest neighbors have been included. Afterwards, we have considered scattering processes for $3d$ and $4sp$ impurities and adatoms on copper surfaces for different numbers of layers, presented in figure 7.16.

Considering figure 7.15, we find similarities to the observations made for the surface-state lifetimes, figure 7.5 in section 7.1.3; whereas the surface resistivities obtained within ASA and full potential calculations for impurities in the first surface layer are very similar, de-
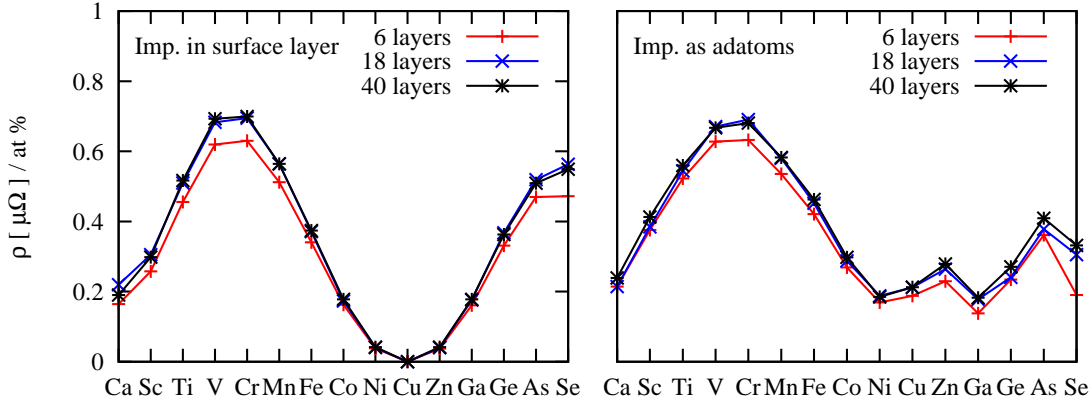
Figure 7.16.: Surface resistivities, measured in $\mu\Omega$ per atomic percent for impurities in the first surface layer (*left*) and on top of the surface (*right*), obtained within full potential calculations. Results are shown for different film thicknesses starting from 6 to 40 layers of copper. In contrast to the dependence on the number of layers for the surface-state lifetimes (compare figure 7.12), only a small deviation can be observed. All calculations have been performed within a cluster of 13 sites. For comparison, the surface resistivities ρ_{surf} have been scaled with the number of layers, otherwise $\rho_{\mathrm{surf}} \to 0$ for increasing slab thickness, since in the limit of very thick films a single impurity or adatom does not result in a finite resistivity.

viations of the order of 10 to 15% are found for adatoms; however, even within the ASA, the qualitative trend is correct. Contrarily, the surface resistivities calculated for adatoms within single-site calculations lead to very poor results; this is not the case for impurities in the first surface layer, where the agreement of calculations within a shell of nearest neighbors and single-site calculations is good.

The qualitative trend for the surface resistivities due to scattering at impurities in the first surface layer is very similar to that obtained for residual resistivities in bulk, presented in the previous subsection, figure 7.14. We observe a peak for the $3d$ scatterers (with a maximum for Cr impurities) and a high resistivity for the $4sp$ scatterers. Again, for the resistivities d-scattering gains importance compared to the trend obtained for the surface-state lifetimes, shown e.g. in figure 7.12. The same argument as for impurities in bulk holds; whereas for the surface-state lifetime forward- and back-scattering are equally important, for the transport relaxation time back-scattering has much more weight. Since the d-resonance contributes more to back-scattering than the p-states, larger resistivities are found. For the same reason, the plateau of the early sp- and d-adatoms, observed in the surface-state scattering rate $\tau_{\mathbf{k}}^{-1}$, disappears in the resistivity, and a peak shows up for the strong d scatterers (V and Cr).

Additionally, we have studied the dependence of the surface resistivity on film thickness; the results are presented in figure 7.16. We have calculated surface resistivities both for adatoms (right panel) and impurities in the first surface layer (left panel) for films with 6, 18 and 40 layers of copper. In order to compare the surface resistivities for different film thicknesses, we have scaled ρ_{surf} with the number of layers; otherwise, the surface resistivity due to single adatom or impurity, respectively, would converge to zero for increasing slab thickness.

This scaled quantity ρ_{surf} slightly increases with increasing film thickness, but compared to the behavior of surface-state lifetimes, figure 7.12, the dependency is rather weak. Additionally, whereas for inverse surface-state lifetimes a decrease is observed, surface resistivities behave inversely. The reason for this difference might be due to the splitting of surface states: While for the inverse lifetimes only the scattering rate obtained for the surface state corresponding to the innermost Fermi-ring is shown, the surface resistivity does not depend on a special $\mathbf{k}$-point and results from an integration over all states. Hence, also the contribution of the surface state with lower energy enters, whose scattering rate increases with increasing number of layers; this behavior is also related to the decrease of $|\mathbf{k}|$ of the innermost surface state with increasing number of layers, resulting in a shorter lifetime.

To conclude, surface resistivities are much less sensitive to parameters such as the number of layers or the approximation of the calculation method (ASA or FP) than inverse surface-state lifetimes. The trends for scattering at impurities in the surface and at adatoms show some differences for the $4sp$ elements, but the qualitative behavior for the $3d$ elements is similar. In this way, the results obtained for surface resistivities differ from the inverse surface-state lifetimes, because the latter show a trend for scattering at adatoms which is completely different from scattering at impurities in the surface.

7.6 Conclusion

Even though at low temperatures and energies close to the Fermi level impurity scattering at noble metal surfaces is assumed to provide the dominating contribution to the scattering rate, this effect has not been studied systematically in earlier works. In this chapter, surface-state lifetimes due to scattering at $3d$ and $4sp$ impurities below, in, and on top of the first surface layer of (111) copper, silver and gold films have been investigated.

While the calculated inverse lifetimes for scattering at impurities below and in the surfaces show basically the main characteristics which have already been observed for scattering at impurities in bulk materials, we have found unexpected results especially for scattering at adatoms. In contrast to all other results, the trend found for scattering at $3d$- and $4sp$-adatoms on Cu, Ag and Au surfaces does not directly reflect the position of the $3d$-resonance relative to the Fermi level, or, at least, this does not seem to be the dominating criterion. An analysis has revealed that the extent of the adatom into the surrounding vacuum plays a great role; the extent into the vacuum is related to the atomic radius, which is relatively large for the first elements of the row, and, therefore explains the high scattering rates for these adatoms.

Furthermore, an angular-momentum resolved study of the single-site scattering rates for adatoms has been presented, allowing for a scattering in specific L-channels of the single-site T-matrix $T^{00}_{LL'}$ only. While a constructive interference of the s- and the d-channel is observed for the $3d$ elements, for the $4sp$ scatterers the s- and the p_z-channel interfere destructively. The results are fortified and confirmed by a calculation of Friedel-oscillations for Co, Ga and Ge adatoms.

The applied method allows to distinguish between scattering to bulk and to surface states, and the contributions of the total inverse surface-state lifetimes for impurities below the surface, in and on top of the surface have been presented separately for different numbers of layers. As expected, scattering at adatoms leads to especially high contributions to other surface states, whereas scattering at impurities below the surface mostly occurs to bulk states. However, the dependency on layer thickness as well as differences observed for $3d$ and $4sp$ impurities is not obvious and still needs to be understood.

A comparison of inverse surface-state lifetimes for Cu, Ag and Au films shows trends very similar to each other, with the dominant features described in detail for copper films. However, when considering the dependency on film thickness, differences for silver films are revealed. This discrepancy might be due to the interplay of the position of the bottom of the surface band relative to the Fermi level and the large splitting of the two surface states for thin films. For silver, the bottom of the surface band is by far closest to the Fermi energy compared to copper and gold films. Therefore, for thin silver films only one surface state is present at the Fermi level.

Furthermore, we have calculated surface-state lifetimes for magnetic impurities. The obtained trend shows the double-peak structure caused by the d-resonances of the two spin channels crossing the Fermi level.

Finally, residual resistivities in copper bulk and surface resistivities for impurities in the surface layer and on top of the surface for copper films are presented. The resulting trends are compared to those obtained for the surface-state lifetimes. The most important difference is the observation that the surface resistivity (normalized to the number of layers) hardly depends on the film thickness, whereas the inverse surface-state lifetimes remarkably differ for distinct thicknesses. The reason for this behavior probably is the different nature of the investigated quantities: While the inverse lifetime depends on $\mathbf{k}$, and especially for thin films differs for the two surface states, where the splitting is large, the surface resistivity is integrated over all states.

Further investigations of surface-state lifetimes including spin-orbit coupling effects will be presented in chapter 8.

CHAPTER 8

Effects of spin-orbit coupling in noble metal thin films

In the last two chapters we have investigated spin-orbit coupling effects in copper and gold fcc bulk crystals, chapter 6, and surface-state lifetimes for fcc copper, silver and gold (111) films without spin-orbit coupling, chapter 7. Both effects are induced by impurity scattering. Now, we will combine these two aspects and finally investigate effects of spin-orbit coupling in noble metal films. In doing so, we will consider two different scenarios, entailing different mechanisms of spin relaxation; first, we will consider symmetric films, in which – analogously to bulk crystals – all **k**-points on the Fermi surface are two-fold degenerate. Then, the Elliott-Yafet mechanism as well as impurity spin-orbit coupling induce spin relaxation. Secondly, films without inversion symmetry will be considered. The lack of structural inversion symmetry lifts the spin degeneracy, leading to a splitting of bands, i.e. a splitting of rings on the Fermi surface. This type of splitting is a general phenomenon observed in the bulk of semiconductors, asymmetric semiconductor heterostructures, or metal surface states. Depending on details of the band structure, it is known as Rashba [101, 102] or Dresselhaus [103] splitting. In its presence, another mechanism of spin relaxation takes effect, the D'yakonov-Perel' mechanism [10]. This mechanism is rather characterized by spin dephasing than spin relaxation, since it is caused by precession around a local spin axis together with ordinary momentum scattering.

In the first part of this chapter we will give an introduction to the above-mentioned theoretical concepts. Then, we present results obtained for gold and copper films. We consider that the epitaxial growth direction of the films is along the z-axis, which is also taken as the spin quantization axis of the system. We start with the investigation of symmetric (111) and (001) films with different film thicknesses and calculate the corresponding spin-mixing parameter. Furthermore, spin-flip scattering processes due to scattering at self-adatoms are studied, and results for spin-conserving and spin-flip scattering lifetimes are presented. Afterwards, asymmetric copper and gold (111) and (001) films will be investigated; their

symmetry has been broken by covering them with one layer of Zn. For both surface orientations and different film thicknesses, spin-orbit fields are calculated and compared to each other.

The chapter ends with a summary of the most important results.

8.1 Spin-orbit coupling effects in systems without structural inversion symmetry

8.1.1 The Rashba effect

We consider systems without internal or external magnetic field. For such systems, disregarding the question whether space-inversion is given or not, the time-reversal transformation does not alter the physical properties of the system. Since time reversal reverts the direction of motion (i.e. $\mathbf{k}$ to $-\mathbf{k}$) as well as the spin (i.e. σ to $-\sigma$), the energy of a spin-up particle with momentum $\mathbf{k}$ has the same energy as a spin-down particle moving in the opposite direction (with wave vector $-\mathbf{k}$)

$$E_{\mathbf{k}}^{\uparrow} = E_{-\mathbf{k}}^{\downarrow} \,. \tag{8.1}$$

This property is also known as Kramers degeneracy [104]. For systems invariant under space inversion, additionally $E_{\mathbf{k}}^{\sigma} = E_{-\mathbf{k}}^{\sigma}$, $\sigma = \uparrow, \downarrow$ is valid and, therefore, all bands are twofold degenerate[1]. In contrast, in systems without structure inversion symmetry, where $V(\mathbf{r}) \neq V(-\mathbf{r})$, this degeneracy is lifted; the presence of a non-centrosymmetric potential implicates a potential gradient or electric field $\mathbf{E}(\mathbf{r})$. This becomes clear when considering the Taylor expansion of the potential $V(\mathbf{r})$

$$V(\mathbf{r}) = V(0) + e\mathbf{E}(0) \cdot \mathbf{r} + \dots \,. \tag{8.2}$$

Hence, in lowest order, the inversion asymmetry can be characterized by an electric field $\mathbf{E}(\mathbf{r})$. A moving electron with an effective mass $m^{\star}$ propagating with a velocity $\mathbf{v} = 1/m^{\star}\,\mathbf{k}$ will experience this field Lorentz-transformed in its local frame as a magnetic field

$$\mathbf{B} = \frac{1}{c}\,\mathbf{v} \times \mathbf{E} = \frac{1}{cm^{\star}}\,\mathbf{k} \times \mathbf{E} \,, \tag{8.3}$$

coupling to the electron spin. Multiplying this field with the spin (i.e. the Pauli-matrices) yields the expression

$$H_{\mathrm{R}} = \alpha_{\mathrm{R}}\boldsymbol{\sigma} \cdot (\mathbf{k} \times \mathbf{E}) \,, \tag{8.4}$$

which equals the spin-orbit Hamiltonian of eq. (4.10) and is called the Rashba or Bychkov-Rashba Hamiltonian [101, 102].

We will rewrite the Rashba Hamiltonian in terms of the so-called spin-orbit field $\boldsymbol{\Omega}(\mathbf{k})$ [8]

$$H_{\mathrm{R}} = \frac{\hbar}{2}\boldsymbol{\sigma} \cdot \boldsymbol{\Omega}(\mathbf{k}) \,. \tag{8.5}$$

---

[1]This is the case for the bulk crystals considered in chapter 6 and the symmetric surfaces studied in a later part of the current chapter.

The direction of $\mathbf{\Omega}(\mathbf{k})$ at each $\mathbf{k}$ defines the spin quantization axis, while its absolute value determines the strength of the splitting. Of course, the spin-orbit fields $\mathbf{\Omega}(\mathbf{k})$ are material-specific and depend on the spin-orbit coupling strength, the band gap, the proximity to the surface and other parameters. We will present spin-orbit fields for Cu and Au surfaces in section 8.3.

The effect is present in different structures. First, it appears in bulk semiconductors of the zinc-blende type [103, 105], where the two atoms in the unit cell are not equivalent and, therefore, inversion symmetry is not fulfilled. Then, the spin-orbit field at and close to the conduction-band minimum can be written as

$$\mathbf{\Omega}_{\mathrm{D}}(\mathbf{k}) = \frac{\alpha\hbar^2}{\sqrt{2m^\star E_{\mathrm{g}}}} \left[k_x \left(k_y^2 - k_z^2 \right) \mathbf{e}_x + k_y \left(k_z^2 - k_x^2 \right) \mathbf{e}_y + k_z \left(k_x^2 - k_y^2 \right) \mathbf{e}_z \right] , \qquad (8.6)$$

where E_{g} is the band gap of the semiconductor and α is a material-dependent parameter (e.g., for GaAs $\alpha = 0.07$). The corresponding Hamiltonian $H_{\mathrm{D}} = \hbar/2\, \boldsymbol{\sigma} \cdot \mathbf{\Omega}_{\mathrm{D}}(\mathbf{k})$ is known as Dresselhaus Hamiltonian and leads to a spin splitting proportional to k^3.

Secondly, the Rashba Hamiltonian allows to describe the splittings appearing in a two-dimensional electron gas. This is realized e.g. in asymmetric quantum well heterostructures [106, 107] as well as in the surface states of metallic and semi-metallic systems [108], e.g. Ag, Au [109] and Bi (111) surfaces or surface alloys. Choosing the z-axis in direction of growth of the heterostructure (or perpendicular to the surface, respectively) and adding up the kinetic energy, the full Hamiltonian takes the form

$$\begin{aligned} H_{\mathrm{R}} &= H_{\mathrm{kin}} + H_{\mathrm{R}} \\ &= \frac{\mathbf{p}_\parallel^2}{2m^\star} + \alpha_{\mathrm{R}} \left(\boldsymbol{\sigma} \times \mathbf{p}_\parallel \right)_{|z} \\ &= \frac{\mathbf{p}_\parallel^2}{2m^\star} + \alpha_{\mathrm{R}} \left(\sigma_x p_y - \sigma_y p_x \right) . \end{aligned} \qquad (8.7)$$

This form allows for an analytic solution. Assuming the $\mathbf{k}$-vector to be oriented in the plane of the two-dimensional electron gas and $\mathbf{k}_\parallel = k_\parallel \left(\cos\phi, \sin\phi, 0 \right)$, the eigenstates can be written as a product of plane waves and two-component spinors

$$\Psi_{\mathbf{k}_\parallel}^{\uparrow,\downarrow} = \frac{e^{i\mathbf{k}_\parallel \cdot \mathbf{r}_\parallel}}{2\pi} \cdot \frac{1}{\sqrt{2}} \begin{pmatrix} ie^{-i\phi/2} \\ \pm e^{i\phi/2} \end{pmatrix} . \qquad (8.8)$$

The corresponding eigenenergies are

$$\begin{aligned} E_{\mathbf{k}_\parallel}^{\uparrow,\downarrow} &= \frac{\mathbf{k}_\parallel^2}{2m^\star} + \alpha_{\mathrm{R}} \left(\sigma \times \mathbf{k}_\parallel \right)_{|z} \\ &= \frac{\mathbf{k}_\parallel^2}{2m^\star} \pm \alpha_{\mathrm{R}} |\mathbf{k}_\parallel| \\ &= \frac{1}{2m^\star} \left(k_\parallel \pm k_{\mathrm{SOC}} \right)^2 - \Delta_{\mathrm{SOC}} \end{aligned} \qquad (8.9)$$

with $k_{\mathrm{SOC}} = m^{\star}\alpha_{\mathrm{R}}$ and $\Delta_{\mathrm{SOC}} = m^{\star}\alpha_{\mathrm{R}}^2/2$. Apparently, for all $k_{\parallel}$ except the high-symmetry state $k_{\parallel} = 0$, the two states are split and have a difference in energy

$$\Delta E_{\mathbf{k}_{\parallel}}^{\uparrow,\downarrow} = 2\alpha_{\mathrm{R}} \left|\mathbf{k}_{\parallel}\right| \ . \tag{8.10}$$

In addition, due to the presence of structure inversion asymmetry and the spin-orbit inter-action, the origin of the parabola is lowered in energy by Δ_{SOC}. The orientation axis of the spin is given by the expectation values of the Pauli matrices $\boldsymbol{\sigma}$

$$2\mathbf{S}_{\mathbf{k}_{\parallel}}^{\uparrow,\downarrow} = \left\langle \Psi_{\mathbf{k}_{\parallel}}^{\uparrow,\downarrow} \left|\boldsymbol{\sigma}\right| \Psi_{\mathbf{k}_{\parallel}}^{\uparrow,\downarrow} \right\rangle = \pm \begin{pmatrix} \sin\phi \\ -\cos\phi \\ 0 \end{pmatrix} , \tag{8.11}$$

hence depends on the direction of $\mathbf{k}_{\parallel}$ only and not on its absolute value. Apart from that, the spins of the two electrons are – for all $\mathbf{k}_{\parallel}$ – oriented opposite to each other. The resulting spin-structure on the Fermi surface will be shown in figure 8.12 in section 8.3 at the example of the spin-split surface state of copper (111).

Before finishing this section and coming to the spin dephasing mechanism induced by the Rashba spin-splitting of bands, we will briefly comment on the order of magnitude of the observed splitting for different structures. Interestingly, the splitting found for metallic or semimetallic surface states can be much larger than for semiconductor heterostructures. First, this is the consequence of higher Rashba parameters, e.g. for a GaAs/InAs heterostruc-ture $\alpha_{\mathrm{R}} = 0.09\,\mathrm{eV\mathring{A}}$ [110] compared to $\alpha_{\mathrm{R}} = 0.33\,\mathrm{eV\mathring{A}}$ [109] for a Au (111) surface state. Secondly, one has to take into account that the splitting is proportional to k – for Au, k is determined by the Fermi surface (see section 8.3) and leads to a splitting of the order of $0.1\mathrm{eV}$, while in semiconductor heterostructures, the conduction band being much closer to the center of the Brillouin zone, it is much smaller. More information about the Rashba effect at metal surfaces can be found in [108]. A more detailed general overview is given in [74].

8.1.2 The D'yakonov-Perel' mechanism

In chapter 6 we have seen that in case of the Elliott-Yafet spin-flip mechanism present in systems with structure inversion symmetry, the increase of momentum scattering yields an enhancement of spin relaxation and therefore shorter spin-relaxation times. In contrast, in systems without structure inversion symmetry, the D'yakonov-Perel' mechanism [10] leads to the inverse effect. I.e., enhanced momentum scattering results in longer spin-relaxation times. In the following we will show that this is a consequence of the form of the Rashba spin splitting derived in the last section. We will follow arguments presented in [8, 111].

The spin-orbit field $\boldsymbol{\Omega}(\mathbf{k})$, which can be interpreted as an internal magnetic field, provokes a $\mathbf{k}$-dependent precession around the direction of $\boldsymbol{\Omega}(\mathbf{k})$ with frequency $|\boldsymbol{\Omega}(\mathbf{k})|$. In order to illustrate the above statements, we consider a system which can be described by the Rashba Hamiltonian eq. (8.5) and assume a wave packet ψ at time $t = 0$, characterized by a wave vector $\mathbf{k}$ with a spin $\mathbf{S}(0)$ oriented in an arbitrary direction. If the spin does not point in

the same direction as the spin-orbit field $\mathbf{\Omega}(\mathbf{k})$, it will be partly projected to the $\uparrow$ and the $\downarrow$ eigenfunction, i.e. $\psi(0) = a \, |\uparrow\rangle + b \, |\downarrow\rangle$). Then, after a time t the wavefunction has evolved to

$$\psi(t) = e^{i \frac{\hbar k^2}{2m^\star} t} \left[e^{i \frac{\Omega t}{2}} a \, |\uparrow\rangle + e^{-i \frac{\Omega t}{2}} b \, |\downarrow\rangle \right]. \tag{8.12}$$

The Rashba term in the Hamiltonian has caused a difference in phase of the two eigenstates $\psi_{\mathbf{k}}^{\uparrow}$ and $\psi_{\mathbf{k}}^{\downarrow}$ of the order of $\delta\phi = \Omega t$. As a consequence, the spin expectation value $\mathbf{S}(t) = 1/2 \, \langle \psi(t) | \boldsymbol{\sigma} | \psi(t) \rangle$ becomes time-dependent, and the spin of the electron precesses around the direction of the spin-orbit field $\mathbf{\Omega}(\mathbf{k})$ with frequency $\Omega = |\mathbf{\Omega}(\mathbf{k})|$. Of course, this happens only if the energy spread of the wave packet is larger than the spin-splitting $\hbar\Omega$.

Assuming that this condition is fulfilled, D'yakonov and Perel' considered a scattering event at time t_1 from state $\mathbf{k}$ to state $\mathbf{k}'$. The scattered electron is assumed not to change its spin expectation value $\mathbf{S}(t_1)$ during scattering and, arriving at $\mathbf{k}'$, it starts to precess around the local precession axis $\mathbf{\Omega}(\mathbf{k}')$, which in general differs from $\mathbf{\Omega}(\mathbf{k})$. After a certain time t, longer than the momentum-relaxation time[2] τ_{p}, the electron has experienced a few random scattering events followed by precession around different axes and its original spin orientation axis is lost. Hence, the interplay of momentum scattering and precession rather leads to spin dephasing than spin relaxation.

In the following, a relation between the momentum-relaxation time τ_{p} and the spin dephasing time T_2 will be established. The alternation of scattering and precession can be described as a spin precession around a fluctuating magnetic field, whose magnitude and direction change randomly after the average time step of τ_{p}. Hence, the spin phase follows a random walk and the total accumulated spin angle $\delta\phi$ after time t is both proportional to the number of random-walk steps $\sqrt{N} = \sqrt{t/\tau_{\mathrm{p}}}$ as well as to the change in phase at each step $\langle \Omega \rangle \tau_{\mathrm{p}}$

$$\delta\phi = \langle \Omega \rangle \, \tau_{\mathrm{p}} \sqrt{\frac{t}{\tau_{\mathrm{p}}}} = \langle \Omega \rangle \sqrt{t \tau_{\mathrm{p}}} \, . \tag{8.13}$$

Here, analogously to the definition of τ_{p}, the quantity $\langle \Omega \rangle$ is defined as an average of the local spin-orbit fields $\langle \mathbf{\Omega}(\mathbf{k}) \rangle$ over all possible wave vectors $\mathbf{k}$.

Defining the spin-relaxation time as the time where $\delta\phi \sim 1$, the result

$$T_2 = \frac{1}{\langle \Omega \rangle^2 \tau_{\mathrm{p}}} \tag{8.14}$$

is obtained. The important conclusion of the above estimate for the spin dephasing time T_2 is that it behaves inversely to the momentum-relaxation time τ_{p}; the higher the momentum scattering rate τ_{p}^{-1}, the longer the initial spin is retained. From a physical point of view, this corresponds to the concept of motional narrowing. If the momentum relaxation time is short, the electron spin does not have the time to precess in any particular direction, and the random changes in 'force' cancel each other.

---

[2] defined as the inverse of the average momentum scattering rate $P_{\mathbf{k}\mathbf{k}'}$, averaged over all $\mathbf{k}$ and $\mathbf{k}'$
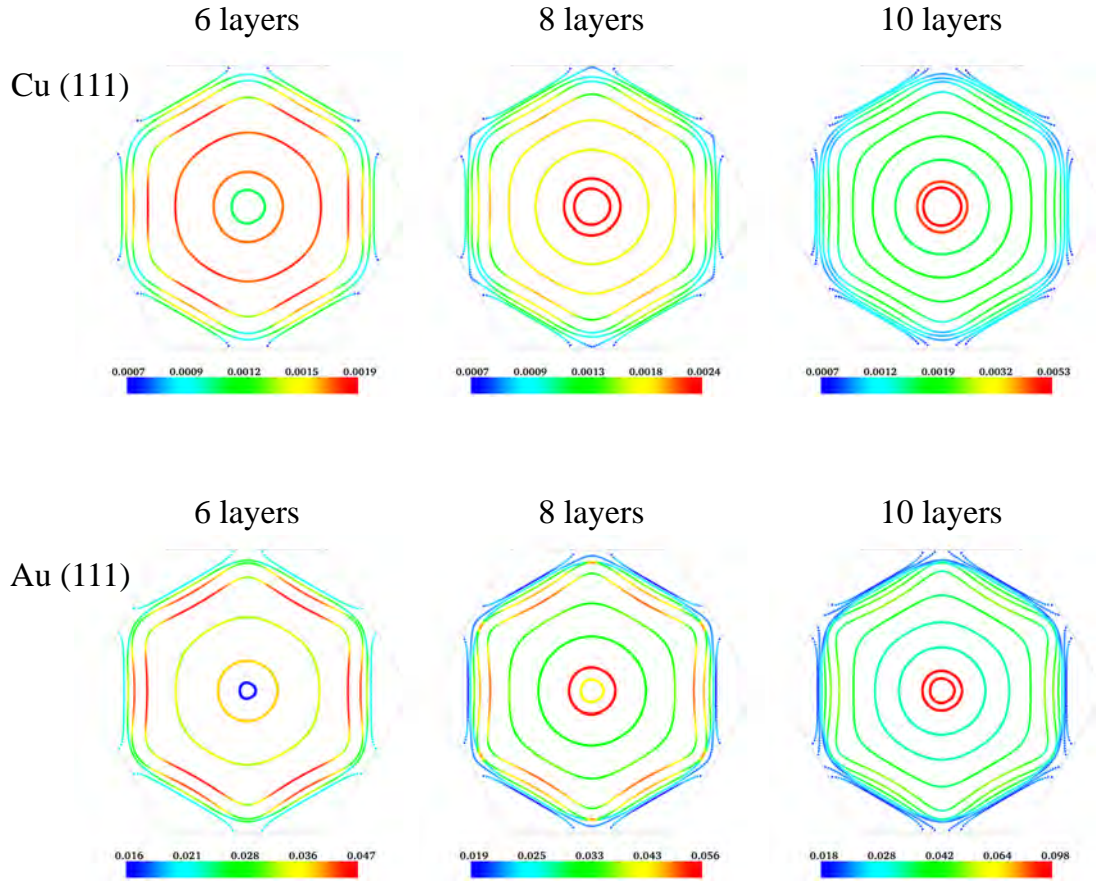
Figure 8.1.: Distribution of the spin-flip parameter $|b_\mathbf{k}|^2$ on the Fermi surfaces for copper (*top*) and gold (*bottom*) films, oriented in [111] direction for films with six (*left*), eight (*middle*) and ten (*right*) layers. Whereas for the six-layer films $|b_\mathbf{k}|^2$ is largest in some of the bulk states, for the films consisting of eight and ten layers the two surface states show the largest spin-mixing parameter. The maximal values of $|b_\mathbf{k}|^2$ increase with film thickness. This tendency is also found, when the average of $|b_\mathbf{k}|^2$ over the Fermi surface of the three films is compared. The averages are specified in table 8.1. Note that the distributions of $|b_\mathbf{k}|^2$ are presented on a logarithmic scale. While the qualitative behavior of the copper and the gold films is very similar, as expected higher spin-mixing parameter are found for the gold slabs.

8.2 Symmetric films

8.2.1 The Elliott-Yafet spin-mixing parameter $|b|^2$

We will start our presentation of spin-orbit coupling effects on surfaces of symmetric films and consider fcc copper and gold (111) and (001) films. The two orientations differ in one

important aspect: Whereas at (111) surfaces the formation of surface states takes place be-
cause of the band-gap in L-direction, at (001) surfaces no such surface states exist at E_F.
As we will see, this changes the physics.

Due to the inversion symmetry, all states on the Fermi surface are twofold degenerate; so we
expect the Elliott-Yafet mechanism (as explained in section 6.1.1) to induce spin relaxation.
In analogy to the situation in fcc bulk, see section 4.6, the degeneracy at each $\mathbf{k}$-point leads
to an arbitrary choice of the spin orientation axis, being different for each $\mathbf{k}$ on the Fermi
surface. Therefore, a common spin quantization axis has to be chosen, and a linear combi-
nation of the degenerate wavefunctions corresponding to this axis must be calculated. We
choose the z-axis, the direction perpendicular to the surface, as spin orientation axis. The
spin-orbit coupling provokes that the wavefunctions are a mixture of up and down states as
explained in section 6.1.1.

In order to estimate the strength of spin-orbit coupling on the Fermi surface, we have calcu-
lated the parameter $|a_\mathbf{k}|^2$ and $|b_\mathbf{k}|^2$ as defined in eq. (4.125), corresponding to the real-space
integrals of the two components $\psi_\mathbf{k}^{\uparrow\uparrow}(\mathbf{r})$ and $\psi_\mathbf{k}^{\uparrow\downarrow}(\mathbf{r})$. Furthermore, its averages $|a|^2$ and $|b|^2$
over the Fermi surfaces are determined.

The distribution of $|b_\mathbf{k}|^2$ on the Fermi surface for films oriented in [111] direction are pre-
sented in the upper panels of figure 8.1 for copper and in the lower panels of the same figure
for gold. The Fermi surfaces are similar to those of the films without spin-orbit coupling,
presented in chapter 7. The two innermost rings correspond to the two surface states; the
splitting between them is mostly caused by the coupling between the surface states belong-
ing to the two film surfaces and therefore strongly depends on the film thickness. However,
as we have included spin-orbit coupling in our calculations, the Rashba effect also leads to
a splitting which adds up to the splitting caused by the finite thickness. Evidently, for thin
films the latter one is much larger and totally covers the effect of the spin-orbit coupling.
However, for sufficiently thick films, the splitting induced by the hybridization of the two
surface states converges to zero and the Rashba splitting prevails. Since the calculation of
the Fermi surface for thick films is numerically very expensive, we have chosen another way
to determine the size of the Rashba splitting. It can be estimated by considering asymmetric
films, which are the subject of the next section.

Considering the distribution of the spin-mixing parameter $|b_\mathbf{k}|^2$ on the Fermi surface of the
(111) films (figure 8.1), a similarity for copper and gold can be observed: Whereas for the
films with six layers, the Elliott-Yafet parameter is largest for some bulk states in the outer
regions of the Fermi surfaces, for the films with eight and ten layers spin-mixing is highest
for the two surface states. Furthermore, an increase of the maximal obtained value of $|b_\mathbf{k}|^2$
with film thickness can be observed. This trend is also found when the average $|b|^2$ of $|b_\mathbf{k}|^2$
over the whole Fermi surface is considered. The averages of the spin-mixing parameter for
all films (copper and gold, different thicknesses, both orientations) are listed in table 8.1.
Comparing the values obtained for the [111] orientation to those obtained in Cu and Au
bulk given in table 4.2, large differences are observed. At the surface, the Elliott-Yafet pa-
rameter is remarkably larger than for the bulk materials. For gold, the ratio is about 1.5, and
for copper, the enhancement of $|b|^2$ is even much more pronounced, being approximately
7. Obviously, the effect of spin-orbit coupling is enhanced by the break of symmetry due
to the surface geometry and the formation of surface states. Considering the distribution

			$|a|^2$	$|b|^2$
Cu	(111)	6 layers	0.999	$1.41 \cdot 10^{-3}$
		8 layers	0.999	$1.49 \cdot 10^{-3}$
		10 layers	0.998	$1.69 \cdot 10^{-3}$
	(001)	6 layers	0.997	$2.94 \cdot 10^{-3}$
		8 layers	0.998	$2.03 \cdot 10^{-3}$
Au	(111)	6 layers	0.968	$3.23 \cdot 10^{-2}$
		8 layers	0.966	$3.41 \cdot 10^{-2}$
		10 layers	0.964	$3.59 \cdot 10^{-2}$
	(001)	6 layers	0.964	$3.51 \cdot 10^{-2}$
		8 layers	0.722	0.278

Table 8.1.: Elliott-Yafet parameters $|a|^2$ and $|b|^2$ averaged over the Fermi surfaces for copper and gold films oriented in [111] and [001] direction. While their distributions $|a_\mathbf{k}|^2$ and $|b_\mathbf{k}|^2$ on the Fermi surface strongly differ for the various thicknesses, the averages are very similar. In all cases, an increase with thickness can be observed. Furthermore, the spin-mixing parameters obtained for the [001] surfaces are much larger than those of the (111) surfaces. This is due to the anti-crossings, occurring at the boundaries of the Brillouin zone for the (001) geometry and leading to spin hot spots.

of $|b_\mathbf{k}|^2$ on the Fermi surfaces, this is (at least for the films with eight and ten layers) obvious, because the spin-mixing parameter are largest for the surface states. Although we have found an increase of $|b|^2$ with increasing film thickness, we do not necessarily expect a further increase for thicker films; there might be an oscillatory effect, converging to a value of $|b|^2$ lower than that calculated for the 10-layer films, since eventually the bulk value has to be reached in the limit of large thickness.

We will now turn to the (001) surfaces. In contrary to the (111) surfaces, at these surfaces there exist no surface states, see figure 8.2. Therefore, lower spin-mixing parameters might be expected. Interestingly, a different effect occurs, yielding locally very large spin-flip parameters, which are actually much larger than for the (111) surfaces: At the edge of the Brillouin-zone, anti-crossings of bands occur, leading to wavefunctions with a large contribution of both spins. These points are so-called spin hot spots, which have been predicted for all polyvalent metals in [14]. The effect is observed for copper as well as for gold (001) surfaces for both thicknesses, though the maximal values of $|b_\mathbf{k}|^2$, indicating the strength of the effect, strongly differ. This might be an artefact of the accuracy of the calculation – especially for copper, the $\mathbf{k}$-points on the Fermi surface with high $|b_\mathbf{k}|^2$ are very localized and the $\mathbf{k}$-points on the Fermi surface are calculated on a discrete mesh, which might not exactly coincide with those $\mathbf{k}$ for which $|b_\mathbf{k}|^2$ is maximized. Of course, these spin hot-spots
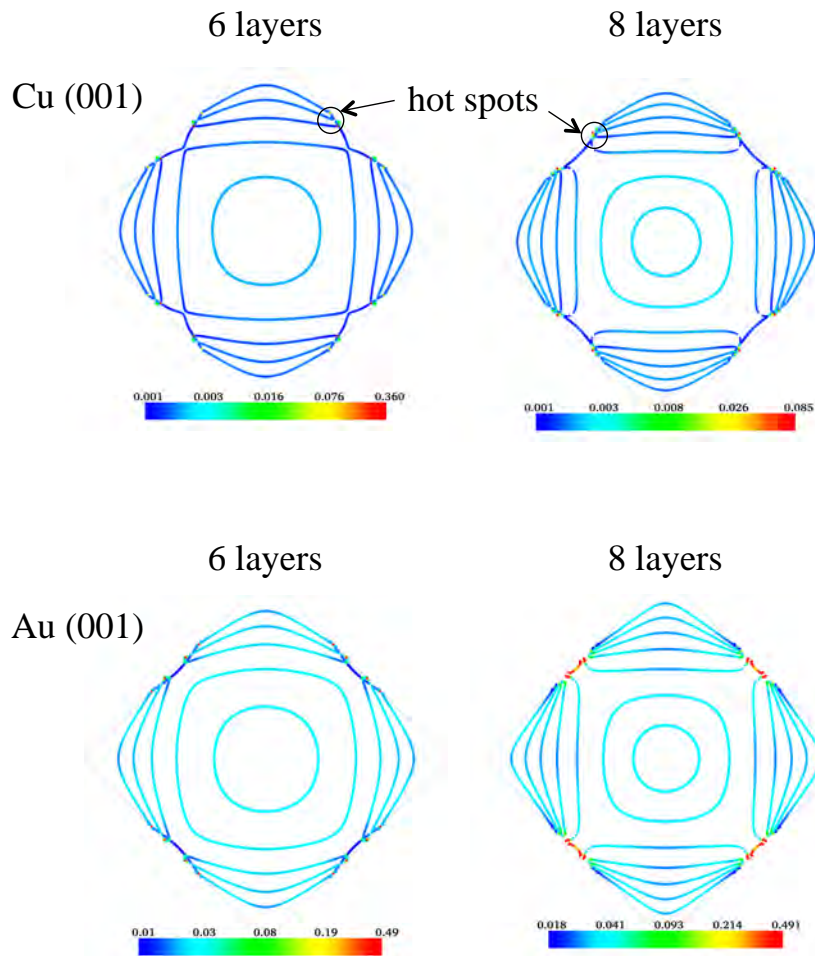
Figure 8.2.: Elliott-Yafet parameter $|b_{\mathbf{k}}|^2$ on the Fermi surfaces for copper (*top*) and gold (*bottom*) (001) films with six (*left*) and eight (*right*) layers. In both cases, $|b_{\mathbf{k}}|^2$ is small and almost constant for all states apart from a few 'hot spots' at the edge of the Brillouin zone, which are encircled and marked with an arrow for the copper films. In these regions, anti-crossings of bands lead to states with high contributions of spin-up and spin-down components and therefore large $b_{\mathbf{k}}$. The hot spots are most pronounced for the Au (001) film with 8 layers. Note that for the color code a logarithmic scale has been used. The averages of $|b_{\mathbf{k}}|^2$ over the whole Fermi surface are given in table 8.1.

enhance the Elliott-Yafet parameters $|b|^2$ averaged over the Fermi surface (see table 8.1); for copper, for the (001) films they are approximately twice as large as for the (111) films, while for gold, they reach values which are almost ten times larger.

After having discussed the Elliott-Yafet spin-mixing parameter, we will go on with the investigation of scattering at adatoms on these surfaces, i.e. spin-conserving and spin-flip life-

		τ^{bulk}	τ^{surf}	τ	T_1^{bulk}	T_1^{surf}	T_1
Cu	6 layers	0.822	$3.13 \cdot 10^{-2}$	0.104	394.2	15.8	58.3
	8 layers	0.709	$3.77 \cdot 10^{-2}$	0.145	381.0	6.4	36.8
	10 layers	0.660	$4.34 \cdot 10^{-2}$	0.169	462.6	2.8	20.0
Au	6 layers	0.579	$3.36 \cdot 10^{-2}$	0.108	8.2	1.36	2.98
	8 layers	0.525	$4.09 \cdot 10^{-2}$	0.144	10.0	0.38	1.91
	10 layers	0.541	$4.96 \cdot 10^{-2}$	0.183	11.6	0.16	1.2

Table 8.2.: Momentum-relaxation τ and spin-relaxation times T_1 in ps per one atomic per-
cent induced by scattering at adatoms on copper and gold (111) films. In addi-
tion to the averages over the whole Fermi surface, averages over the two surface
and the bulk states are given. Whereas the momentum-relaxation times increase
with increasing film thickness, for the spin-relaxation times T_1 a strong decrease
is observed. All values are obtained by averaging over the scattering rates, i.e. $\tau_{\mathbf{k}}^{-1}$
and $T_{1\mathbf{k}}^{-1}$ and not over the times $\tau_{\mathbf{k}}$ and $T_{1,\mathbf{k}}$ themselves.

times. This will be the topic of the next section.

8.2.2 Spin-flip and spin-conserving lifetimes due to scattering at adatoms

In chapter 7, we have investigated surface-state lifetimes due to scattering at impurities
and adatoms at noble metal (111) surfaces. There, the effect of spin-orbit coupling was
neglected. In this section, we take spin-orbit coupling into account and calculate spin-
conserving and spin-flip lifetimes. We restrict our calculations to copper and gold films,
oriented in [001] and [111] direction, considering scattering processes at copper adatoms
for copper films and gold adatoms for gold films. Because of the degeneracy of the wave-
functions at each $\mathbf{k}$-point, spin-conserving $T_{\mathbf{kk'}}^{\uparrow\uparrow}$, $T_{\mathbf{kk'}}^{\downarrow\downarrow}$ as well as spin-flip $T_{\mathbf{kk'}}^{\uparrow\downarrow}$, $T_{\mathbf{kk'}}^{\downarrow\uparrow}$ scatter-
ing matrix elements can be calculated for all $\mathbf{k}$, $\mathbf{k'}$ on the Fermi surface. Integration over
$\mathbf{k'}$ then yields the momentum-dependent spin-conserving lifetimes $\tau_{\mathbf{k}}^{\uparrow\uparrow}$, $\tau_{\mathbf{k}}^{\downarrow\downarrow}$ and the spin-
flip lifetimes $\tau_{\mathbf{k}}^{\uparrow\downarrow}$ and $\tau_{\mathbf{k}}^{\downarrow\uparrow}$, respectively. However, in analogy to the definitions in section
4.9, we present the inverse momentum-relaxation time $\tau_{\mathbf{k}}^{-1}$, the average of the inverse spin-
conserving relaxation times $\tau_{\mathbf{k}}^{\uparrow\uparrow}$ and $\tau_{\mathbf{k}}^{\downarrow\downarrow}$, and the inverse spin-relaxation time

$$T_{1,\mathbf{k}}^{-1} = \frac{1}{\tau_{\mathbf{k}}^{\uparrow\downarrow}} + \frac{1}{\tau_{\mathbf{k}}^{\downarrow\uparrow}} \ . \tag{8.15}$$

The distributions of $\tau_{\mathbf{k}}^{-1}$ and $T_{1,\mathbf{k}}^{-1}$ on the Fermi surfaces for (111) films (with 6 and 8 layers)
are shown in figures 8.3 and 8.4. Qualitatively, the distributions for 10 layers are very sim-
ilar to these, and are therefore omitted. Spin-conserving and spin-flip scattering rates are
highest for the surface states (note the logarithmic scale of the color code) close to the cen-

		$T_1^{\mathrm{bulk}}/\tau^{\mathrm{bulk}}$	$T_1^{\mathrm{surf}}/\tau^{\mathrm{surf}}$	T_1/τ
Cu	6 layers	425	505	558
	8 layers	537	169	259
	10 layers	2738	65	119
Au	6 layers	14.2	40.5	27.7
	8 layers	19.1	9.3	13.5
	10 layers	21.5	3.3	6.4

Table 8.3.: Ratio of the spin-relaxation T_1 and the momentum-relaxation times τ, specified for the average over the complete Fermi surface as well as over the bulk and the surface states.

ter of the Brillouin zone. However, a quantitative analysis reveals differences for the three film thicknesses both for copper and gold films; therefore, we have calculated the averages of the scattering rates $\tau_{\mathbf{k}}^{-1}$ and $T_{1,\mathbf{k}}^{-1}$ over the two surface states, the bulk states as well as over the total Fermi surface, yielding τ^{bulk}, τ^{surf}, τ, and T_1^{bulk}, T_1^{surf}, and T_1, respectively. The results are specified in table 8.2. Whereas the momentum-relaxation times averaged over the full Fermi surface increase with film thickness[3], the spin-relaxation times $T_{1,\mathbf{k}}$ strongly decrease. This trend is observed both for copper as well as gold surfaces. As expected, the spin relaxation times for gold are much shorter than for copper because of the stronger spin-orbit coupling. An analysis of the averages of $T_{1,\mathbf{k}}$ over the bulk and the surface states reveals that the strong decrease of the spin-relaxation time with increasing film thickness is mainly due to the distinct spin-relaxation times averaged over the surface states; the stronger interaction of the two surface states for the films with six layers leads to a reduction of spin-flip scattering. It would be worth to investigate this trend for thicker films. As already stated for the spin-mixing parameter, the trends found for T_1 and τ for the three film thicknesses do not necessarily continue for thicker films, because oscillatory effects might occur. The origin of such an oscillatory behavior might be due to the finite size and the formation of quantum-well states in the film. In order to analyze such a behavior, thicker films have to be investigated.

Considering the ratio T_1/τ, i.e. the number of scattering processes per one spin-flip event, given in table 8.3, the inverse behavior of τ and T_1 as a function of layer thickness results in a strong variation of ratios; the addition of two supplementary layers yields a reduction of T_1/τ by a factor of two. This behavior is observed both for the copper and the gold films, although the calculated values for gold are much smaller than those for copper. A direct comparison of T_1/τ with the values for impurities in copper and gold bulk is not possible, since – of course – the investigation of copper 'impurities' in copper, or gold in gold,

---

[3]Note that the inverse of the relaxation times, i.e. the scattering rates $\tau_{\mathbf{k}}^{-1}$ and $T_{1,\mathbf{k}}^{-1}$ are averaged over the Fermi surface and *not* the lifetimes themselves.
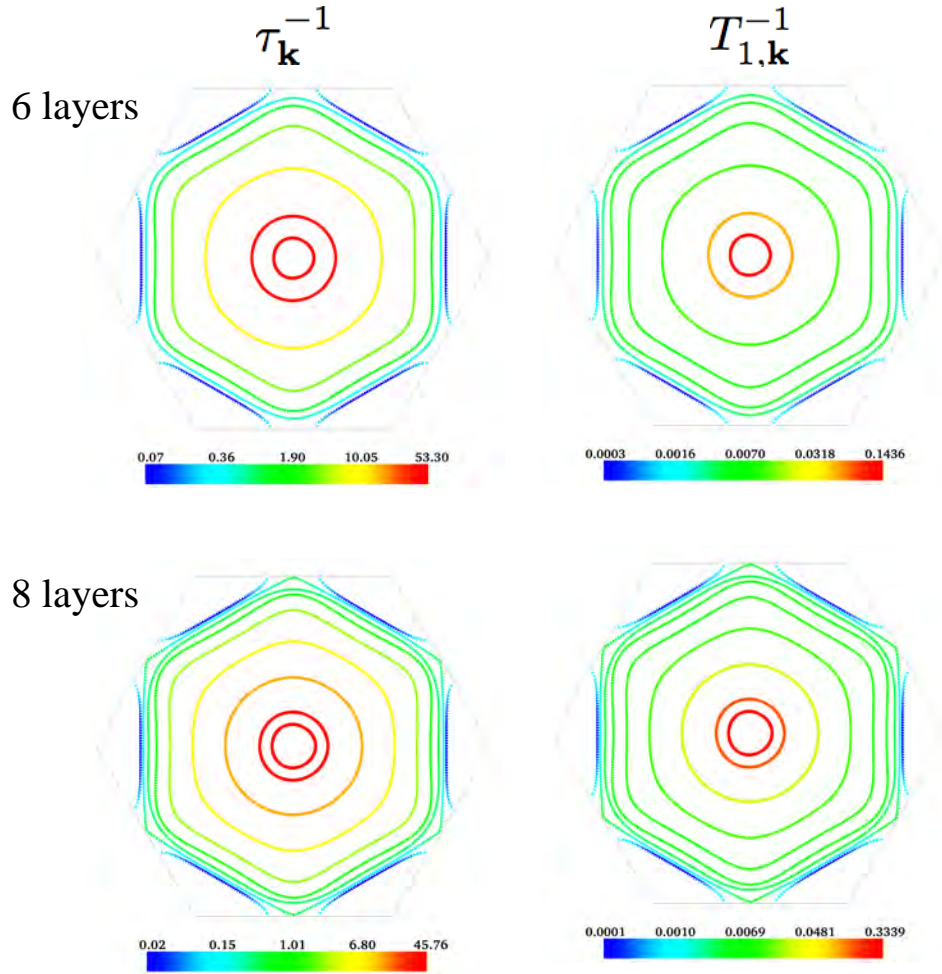
$$\tau_{\mathbf{k}}^{-1} \qquad\qquad\qquad T_{1,\mathbf{k}}^{-1}$$

6 layers

8 layers

| 0.07 | 0.36 | 1.90 | 10.05 | 53.30 |

| 0.0003 | 0.0016 | 0.0070 | 0.0318 | 0.1436 |

| 0.02 | 0.15 | 1.01 | 6.80 | 45.76 |

| 0.0001 | 0.0010 | 0.0069 | 0.0481 | 0.3339 |

Figure 8.3.: Distribution of the spin-conserving $\tau_{\mathbf{k}}^{-1}$ and spin-flip $T_{1,\mathbf{k}}^{-1}$ scattering rates in $[\mathrm{ps}^{-1}/at.\%]$ on the Fermi surfaces for (111) copper films with six (*top*) and eight (*bottom*) layers. The color code is given on a logarithmic scale. Scattering rates are highest for the surface states and decrease towards the outer boundary of the Brillouin zone.

respectively, does not lead to any impurity scattering. However, it is worthy to make a general comparison of the order of magnitude found for impurities in bulk, presented in figure 6.9. For copper bulk, ratios in the range of 55 (for Ni impurities) up to 10^4 for the light impurities have been found, while in a gold host a much smaller range, from about 3 to 30 scattering processes per one spin-flip event have been calculated. Hence, the ratios obtained for scattering at adatoms are relatively large, even for the thicker films, where lower ratios have been found. However, as found in chapter 7, scattering at adatoms is different from impurity scattering, and therefore other mechanisms are dominant; the perturbation
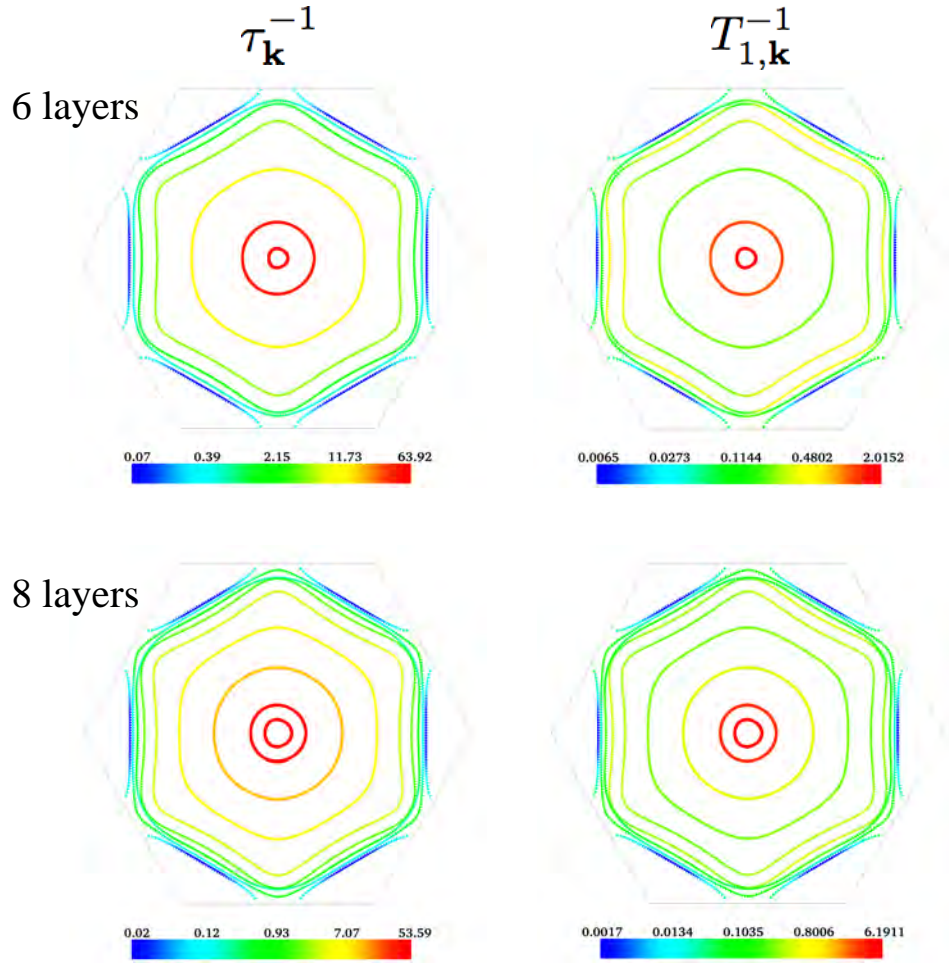
Figure 8.4.: Distribution of the spin-conserving $\tau_{\mathbf{k}}^{-1}$ and spin-flip $T_{1\mathbf{k}}^{-1}$ scattering rate in $[\text{ps}^{-1}/at.\%]$ on the Fermi surfaces for (111) gold films with six (*top*) and eight (*bottom*) layers. Similar as for the copper films, figure 8.3, for both film thicknesses, $\tau_{\mathbf{k}}$ and $T_{1\mathbf{k}}$ are shortest for the surface states and decrease towards the outer boundary of the Brillouin zone. Whereas the order of magnitude of the spin-conserving and spin-flip scattering rates are the same for both metals, the spin-flip scattering rates $T_{1\mathbf{k}}^{-1}$ are much higher for gold than for copper. A logarithmic color scale has been used.

caused by an adatom is much stronger than that of an impurity, where merely a host atom is replaced by the impurity. Note that the lowest ratios T_1/τ in bulk were obtained for resonant scattering, while a self-adatom (Cu or Au) does not produce resonant scattering. Before analyzing the scattering rates for the (001) films, we return to the distributions of $\tau_{\mathbf{k}}$ and $T_{1,\mathbf{k}}$ on the Fermi surface and consider the symmetry; without spin-orbit coupling, one
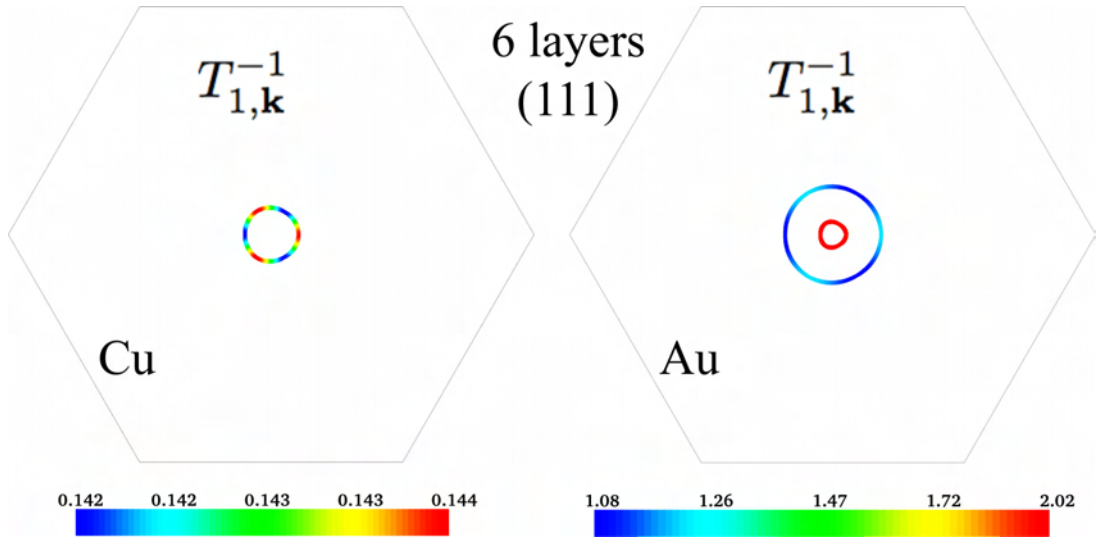
Figure 8.5.: Inverse spin-relaxation times $T_{1,\mathbf{k}}^{-1}$ in ps^{-1} per atomic percent for the innermost surface state of the copper film (*left*) and the two surface states of the gold film (*right*) with 6 layers, which have been already shown with lower resolution in figure 8.3 and figure 8.4, respectively. The higher resolution reveals the reduction of symmetry due to spin-orbit coupling. Whereas the irreducible part of the Brillouin zone for $\tau_{\mathbf{k}}$ amounts to $1/12$ of the full Brillouin zone, it is reduced to $1/6$ for $T_{1,\mathbf{k}}$.

irreducible part of the Fermi surface is $1/12$ of the full Brillouin zone. This is also what has been found when considering $\tau_{\mathbf{k}}$. Spin-orbit coupling reduces this symmetry by a factor of two. As it is a small effect, it is only very weakly visible for some of the bulk states of the gold films in figure 8.4. However, it is present in all states. We only demonstrate it for one of the surface states of a copper 6-layer film and the two surface states of the 6-layer gold films, presenting these states in a higher resolution in figure 8.5.

After having analyzed momentum- and spin-relaxation times for scattering at adatoms on the top of (111) surfaces, we will investigate the same quantities for (100) surfaces. As we have already discussed in the previous section, the absence of surface states strongly changes the physics of the two systems. Distributions of $\tau_{\mathbf{k}}^{-1}$ and $T_{1,\mathbf{k}}^{-1}$ on the Fermi surfaces are presented in figure 8.6 for copper and in figure 8.7 for gold films. For the (001) films, large differences in the distributions of $\tau_{\mathbf{k}}$ and $T_{1,\mathbf{k}}$ are observed[4]; while momentum-relaxation rates are largest for the states close to the center of the Brillouin zone, the $\mathbf{k}$-points on the Fermi surface with highest spin relaxation are found to be at the spin hot spots already detected by their high values of $|b_{\mathbf{k}}|^2$, situated close to the boundaries of the Brillouin zone. In

---

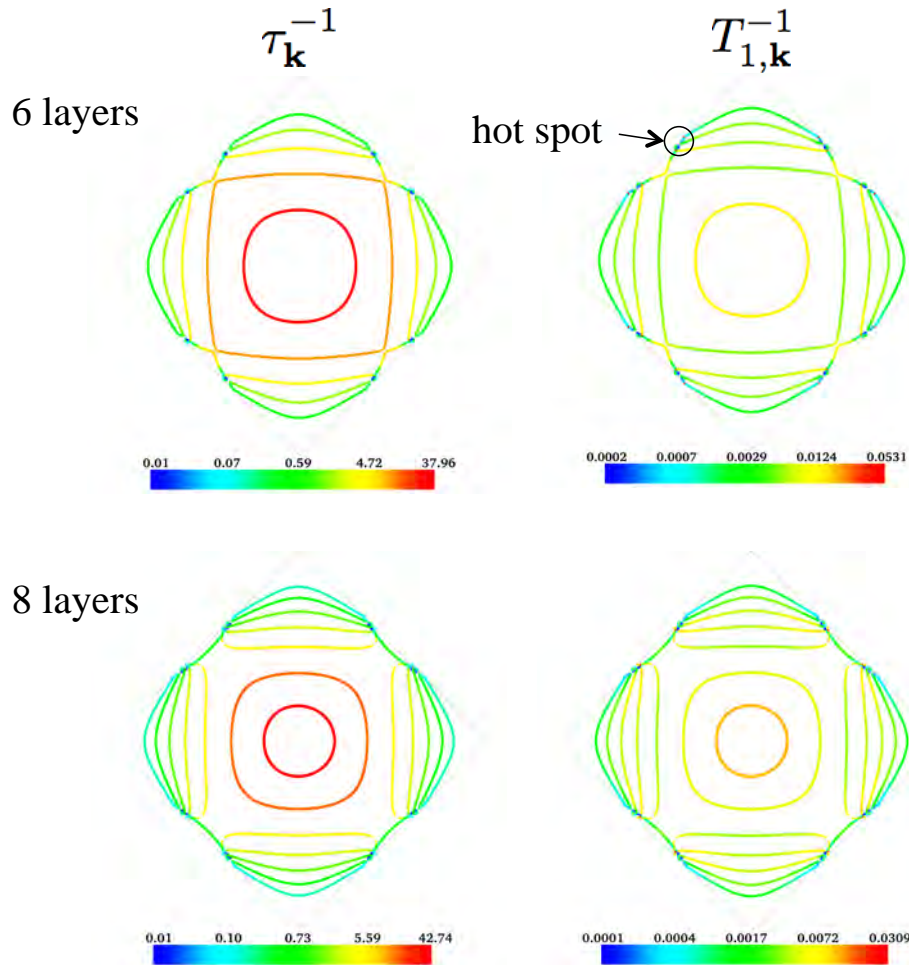[4]This difference is much more pronounced for the copper films as for the gold films.

Figure 8.6.: Distribution of the inverse spin-conserving $\tau_{\mathbf{k}}^{-1}$ and spin-flip lifetimes $T_{1,\mathbf{k}}^{-1}$ on the Fermi surfaces for copper (001) films with six (*top*) and eight (*bottom*) layers. Whereas the momentum scattering rates for spin-conserving scattering are largest for the states close to the center of the Brillouin zone, spin-flip scattering rates are largest for some points at the outer boundaries of the Brillouin zone. For the 6 layer-film, these points are encircled and marked with an arrow.

addition, for the 8 layer-films, relatively large spin-relaxation rates are found for the state closest to the center of the Brillouin zone, presumably because it is the one most extending into the vacuum, i.e., having the largest overlap with the adatoms.

The spin hot spots make the numerical treatment of the (001) films difficult, because locally spin-orbit coupling becomes very large. A high resolution and an exact tracing of the bands in these regions of the Fermi surface is necessary but not yet possible with the currently ex-

			τ	T_1	T_1/τ
Cu	(111)	6 layers	0.104	58.3	558
		8 layers	0.145	36.8	259
		10 layers	0.168	20.0	119
	(100)	6 layers	0.097	126.7	1306
		8 layers	0.185	281.3	1521
Au	(111)	6 layers	0.108	2.98	27.7
		8 layers	0.144	1.91	13.5
		10 layers	0.183	1.2	6.4
	(100)	6 layers	0.093	2.65	28.5
		8 layers	0.041	0.095	2.3

Table 8.4.: Spin-conserving scattering times τ and spin-relaxation times T_1 in ps per atomic percent of adatom concentration averaged over the Fermi surfaces for copper and gold (111) and (001) films. Whereas the momentum-relaxation times for copper and gold are of the same order of magnitude, strong differences are observed for T_1. Except for the (001) gold films, the momentum-relaxation times increase with increasing thickness. For the copper films, the spin-relaxation times for the [001] orientation are much longer than for [111].

isting code. Therefore, the distributions of the scattering rates $\tau_{\mathbf{k}}^{-1}$ and $T_{1,\mathbf{k}}^{-1}$ might be not very accurate, because they are already the result of the integration of $\left|T_{\mathbf{kk'}}^{\sigma\sigma'}\right|^2$ over the Fermi surface. Evidently, the same holds for the averages T_1 and τ.

Although not visible in the distributions of $\tau_{\mathbf{k}}^{-1}$ and $T_{1,\mathbf{k}}^{-1}$, the spin-orbit coupling leads to a reduction of symmetry for the spin relaxation time, just as in the case of the (111) films. Whereas the inverse momentum-relaxation time $\tau_{\mathbf{k}}^{-1}$ exhibits an eightfold symmetry on the Fermi surface, the spin-relaxation scattering rate $T_{1,\mathbf{k}}^{-1}$ merely obeys a fourfold symmetry.

Despite possible numerical inaccuracies for the (001) films, we will compare the averages of the spin-relaxation and momentum-relaxation times for the different orientations. The momentum-relaxation times for the (001) films are larger than for the (111) films. This behavior becomes reasonable when considering the contributions of $\tau_{\mathbf{k}}^{-1}$ for the (111) surface states, table 8.2, which dominate the whole effect.

Comparing the spin-relaxation times for the two surface orientations, differences between the copper and the gold films are observed. Whereas we find much longer spin relaxation times for the copper (001) films, T_1 of the gold films is in the same order of magnitude for the 6-layer film and much shorter for the 8-layer film. For copper, the increase of spin-relaxation times can be explained by the lack of surface states, for which high spin-relaxation rates have been found. In contrary, for the gold films this lack is compensated by the spin-
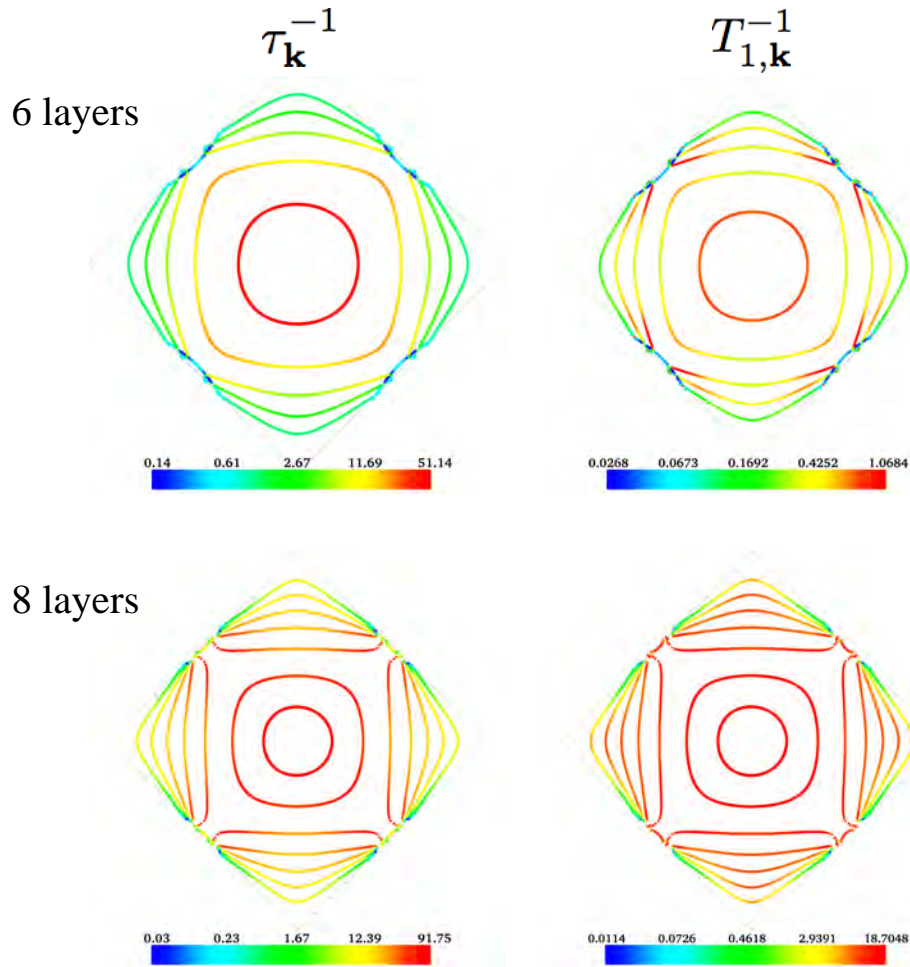
Figure 8.7.: Distribution of the spin-conserving and spin-flip scattering rates $\tau_{\mathbf{k}}^{-1}$ (*top*) and $T_{1,\mathbf{k}}^{-1}$ (*bottom*) on the Fermi surfaces due to scattering at adatoms on gold (001) films. Results for films with six (*top*) and eight (*bottom*) layers are presented. Whereas momentum-scattering rates are largest in the center of the Brillouin zone, $\mathbf{k}$-points with large spin-flip scattering rates are found for a small number of $\mathbf{k}$-points situated close to the boundary of the Brillouin zone and also in the center of the Brillouin zone. Concerning this aspect, the behavior of $T_{1,\mathbf{k}}^{-1}$ differs from that of the copper (001) films, for which high spin-flip scattering rates have been found exclusively at the boundary.

flip scattering induced by the strong spin hot spots and relatively spin-flip high scattering rates for the states close to the center of the Brillouin zone. An investigation of thicker films would be interesting.

8.3 Asymmetric films

In this section we will discuss effects of spin-orbit coupling for asymmetric films. In exper-
iment, ultrathin films are frequently deposited on a substrate, while their surface remains
free. In this situation, the wavefunction of the film are subject to asymmetric boundary
conditions which break the inversion symmetry. The details of the resulting band structure
depend of course on the exact nature of the substrate, but the general qualitative features do
not. Therefore we choose here one layer of Zn as as symmetry-breaking 'substrate' in order
to study these features.

We investigate copper and gold (111) and (001) films with 5, 7 and 9 layers to which one
layer of Zn has been attached on one side. The break of symmetry results in the lifting of the
degeneracy of all states, and hence a splitting of all rings on the Fermi surface. However,
the splitting is usually too small to easily resolve it visually; hence, as before, the number of
visible rings on the Fermi is the same as what one would expect in the degenerate case as
can be seen in the left columns of the figures 8.8, 8.9, 8.10 and 8.11. The color code visual-
izes the absolute value of the asymmetry-induced splitting $\Delta E(\mathbf{k})$ of the Fermi surface; its
values are given in mRyd and are calculated with the help of the Fermi velocity $v_{\mathbf{k}}$ via the
relation

$$\Delta E(\mathbf{k}) = \frac{\partial E_{\mathbf{k}}}{\partial \mathbf{k}} \cdot \Delta \mathbf{k}$$
$$= \hbar v_{\mathbf{k}} \Delta k \ . \tag{8.16}$$

Note that in figures 8.8 to 8.11 a logarithmic scale of the color-code has been used. The
splitting $\Delta E(\mathbf{k})$ corresponds to the absolute value of the spin-orbit fields $\Omega(\mathbf{k})$ presented
in the right columns of the four figures; the direction of $\Omega(\mathbf{k})$ is determined by the spin ex-
pectation value $\mathbf{S}(\mathbf{k})$. In particular, the spin expectation values of the two split states point
in opposite directions; considering the Rashba-Hamiltonian eq. (8.5), it becomes clear that
the spin-orbit field $\Omega(\mathbf{k})$ must point in the direction of the state with the higher energy – a
magnetic dipole $\mathbf{m} = -1/2 \langle \boldsymbol{\sigma} \rangle \cdot \mu_{\mathrm{B}}$ tends to orient parallel to a magnetic field to reduce its
energy.

On the right panels of figures 8.8 to 8.11, the direction of the spin-orbit fields $\Omega(\mathbf{k})$ is shown,
while a color-code is used to show its magnitude $|\Omega(\mathbf{k})|$. For legibility reasons, in the right
panel the $\mathbf{k}$-points are not chosen as dense, thus the color-codes are slightly different.

The figures 8.8 and 8.9 display the spin-orbit fields on the Fermi surfaces of the (111) and
(001) copper and gold films. In analogy to the symmetric films, the innermost state is a
surface state which decays exponentially in the film, but, in contrast to the symmetric sur-
faces, the asymmetry leads to the suppression of the second surface state originating from
the second surface of the film. The splitting of the surface state therefore corresponds to the
Rashba splitting purely induced by spin-orbit coupling. As expected from the theoretical
considerations in section 8.1.1, the z-component of the spin expectation values vanishes for
these two states and the spin is oriented perpendicular to the $\mathbf{k}$-vector on the Fermi surface.
This is shown in figure 8.12 at the example of the film with 7 layers of copper and one layer
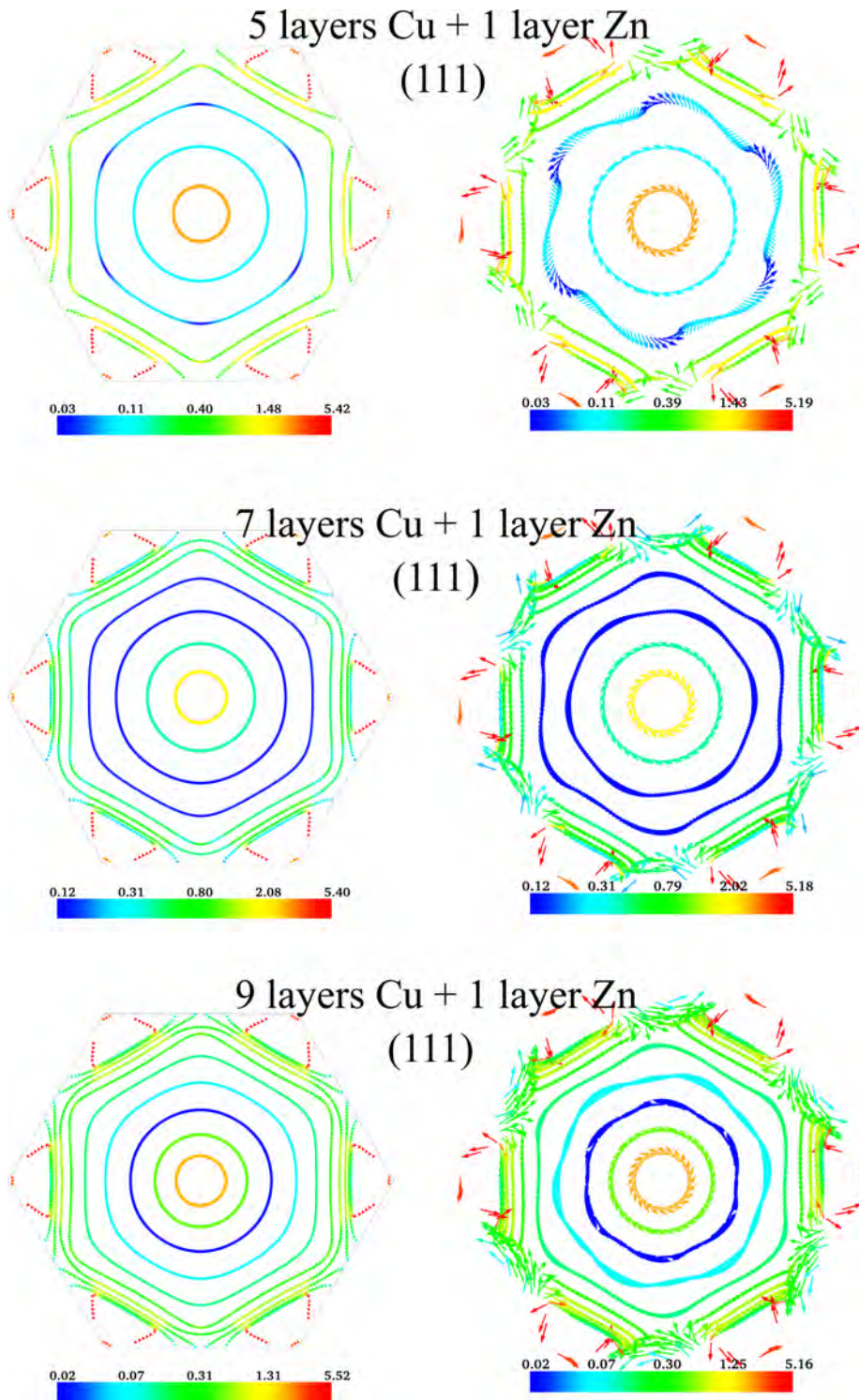of Zn; S_x and S_y are presented as a function of the angle in the k_x-k_y-plane, starting from

Figure 8.8.: Spin-orbit fields $\mathbf{\Omega}(\mathbf{k})$ in mRyd of Cu (111) films consisting of 5, 7 and 9 layers and an additional layer of Zn. In the left column, the splitting in energy of the split states on the Fermi surface is demonstrated, corresponding to $|\mathbf{\Omega}(\mathbf{k})|$. Note the logarithmic scale of the color code. Furthermore, the direction of $\mathbf{\Omega}(\mathbf{k})$ is visualized in the right column; the length of the arrows is chosen to be the same for all $\mathbf{k}$. The largest fields are found for some states close to the boundary of the Brillouin zone. Apart from that, the Rashba-splitting of the surface states leads to high (absolute) values of $\mathbf{\Omega}(\mathbf{k})$. Note that the absolute scale of the left and the right panels slightly differs; for a better visualization, the $\mathbf{k}$-point set was chosen less dense in the right panel.
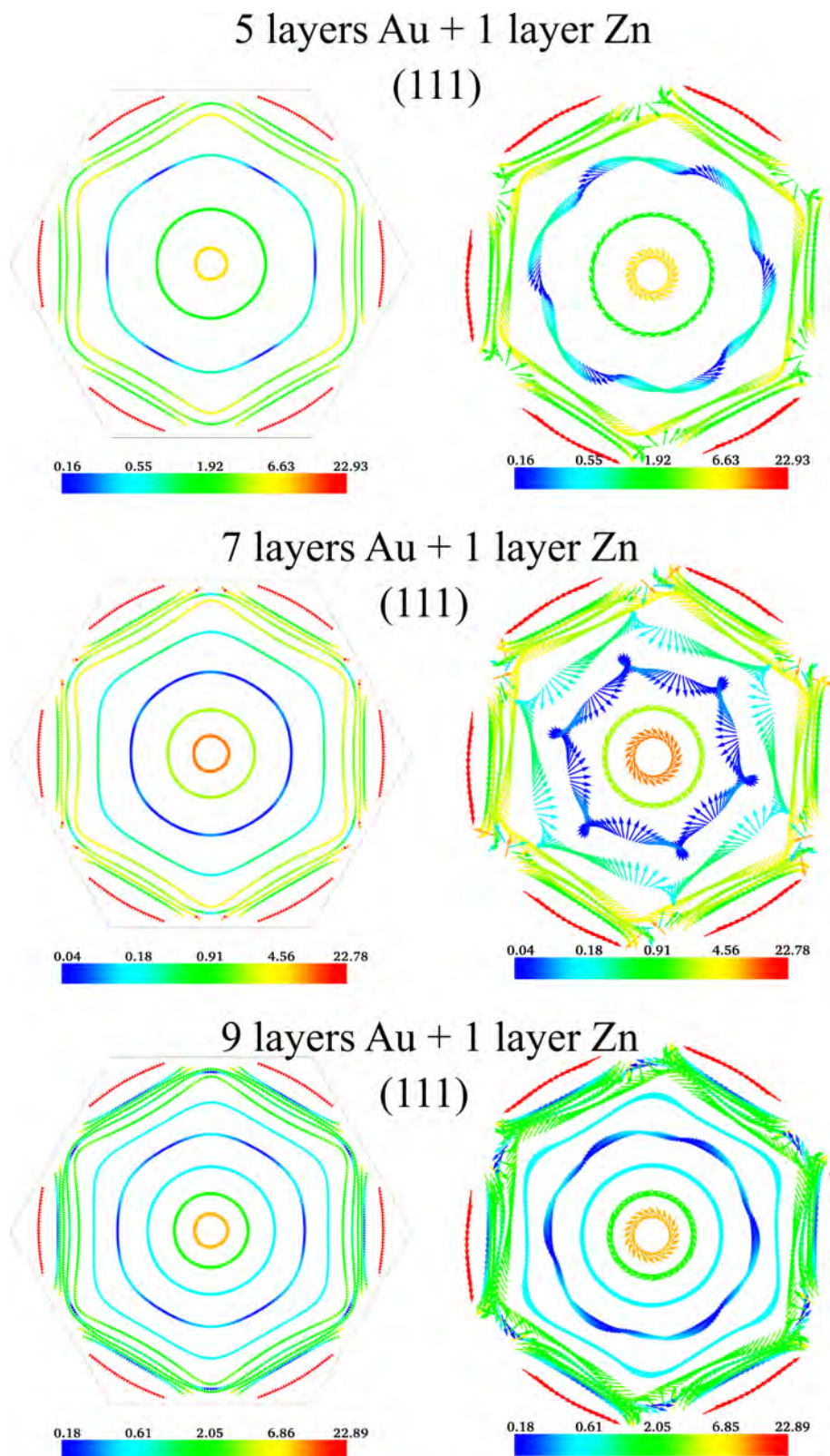
Figure 8.9.: The same figure as in figure 8.8 but for gold (111) films with an additional layer of Zn. Similar as for the copper films, strong fields are found for the surface states as well as for some states in outer parts of the Brillouin zone. The maximal calculated values of $|\mathbf{\Omega}(\mathbf{k})|$ are approximately four times larger than those obtained for copper.

		$\Delta E\,[\text{mRyd}]$	$\Delta E\,[\text{meV}]$
Cu	5 Cu + 1 Zn	2.41	32.79
	7 Cu + 1 Zn	2.23	30.34
	9 Cu + 1 Zn	2.15	29.25
Au	5 Au + 1 Zn	8.53	116.1
	7 Au + 1 Zn	9.99	135.9
	9 Au + 1 Zn	10.33	140.5

Table 8.5.: Splitting of the surface states for copper and gold (111) films. In order to break the inversion symmetry, one layer of Zn has been added on one side of the film. ΔE has been determined for the $\mathbf{k}$-points in the direction of k_y. However, the isotropic nature of the Fermi surface close to center of the Brillouin zone yields the splitting to be independent of the direction chosen for its determination.

the k_y-axis in clockwise direction. The picture is the same for the surface states of all copper and gold films.

The exact values of the Rashba-splittings are given in table 8.5, calculated at $\mathbf{k}_{\text{F}} = (0, k_y)$ for the $\mathbf{k}_{\text{F}}$ with smallest absolute value $|\mathbf{k}_{\text{F}}|$, i.e., the innermost ring[5]. The calculated Rashba-splitting of gold, table 8.5, agrees very well with experimental results obtained within angle-resolved photoemission spectroscopy; splittings between $110\,\text{meV}$ [109] and $150\,\text{meV}$ have been measured. For copper, the splitting is approximately four times smaller than for gold, and therefore probably at the edge of the resolution of photoemission spectroscopy; at 30 K, a bandwidth of about $30\,\text{meV}$ has been measured [86], which is expected to be due to phonon-scattering. Of course, the origin of the broadening cannot be identified exactly and might be a mixture of different effects.

We will continue the investigation of the spin-orbit fields presented in figure 8.8 and 8.9. Although we observe relatively strong fields for the surface state, the largest splittings $\Delta E = |\mathbf{\Omega}(\mathbf{k})|$ are found for some $\mathbf{k}$-points close to the outer boundaries of the Brillouin zone. The reason for this strong increase towards the boundary of the Fermi surface still has to be understood. Whereas the splitting of the surface state, i.e. the Rashba-splitting, is expected to remain almost constant with varying film thickness, the splitting of the bulk states is expected to decrease, since in the limit of very thick films the boundary condition should play a minor role and the inversion-symmetric bulk result should be recovered. However, it is difficult to deduce this from our data; the positions of the rings on the Fermi surface strongly change with varying film thickness, which makes a direct comparison difficult. An investigation of thicker films probably would be helpful for a better analysis.

Considering the direction of the spin-orbit fields, as expected we find them to be in the plane

---

[5]Because the surface band is practically isotropic in $\mathbf{k}$, the Rashba-splitting is almost constant on the whole ring.
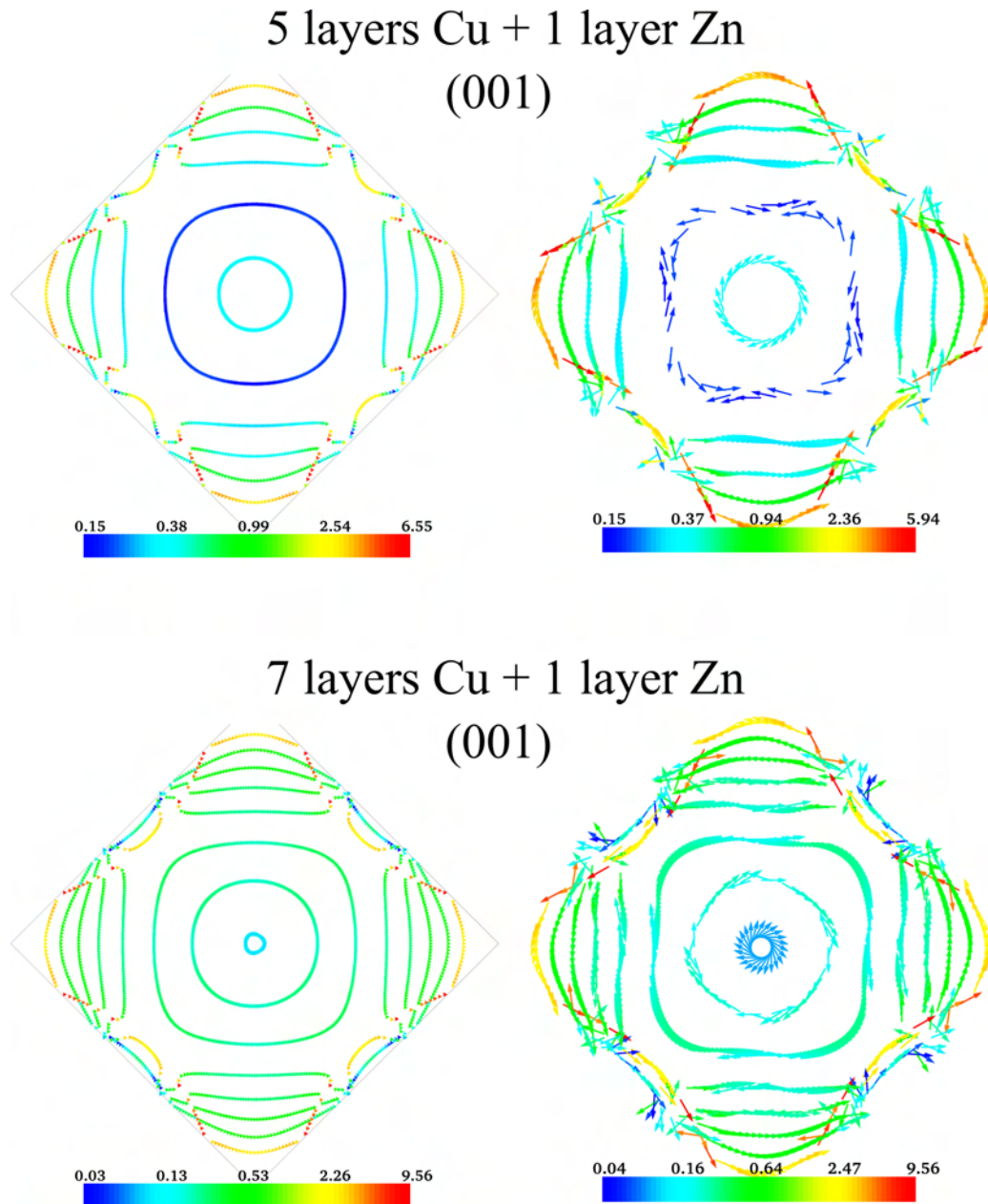
Figure 8.10.: The same figure as in figure 8.8 but for copper (001) films with 5 and 7 layers and an additional layer of Zn. Largest fields are observed for some states in the outer parts of the Brillouin zone, originating from the Zn layer.

of the Fermi surface for the surface states; however, departing from the center of the Fermi surface, the z-component gains importance, but there are no states which completely point out of plane. The z-component is always smaller than the parallel components. A comparison of the directions of $\mathbf{\Omega}(\mathbf{k})$ reveals a difference between the gold and the copper (111) films; while for the copper films all spin-orbit fields of neighboring rings point in a simi-
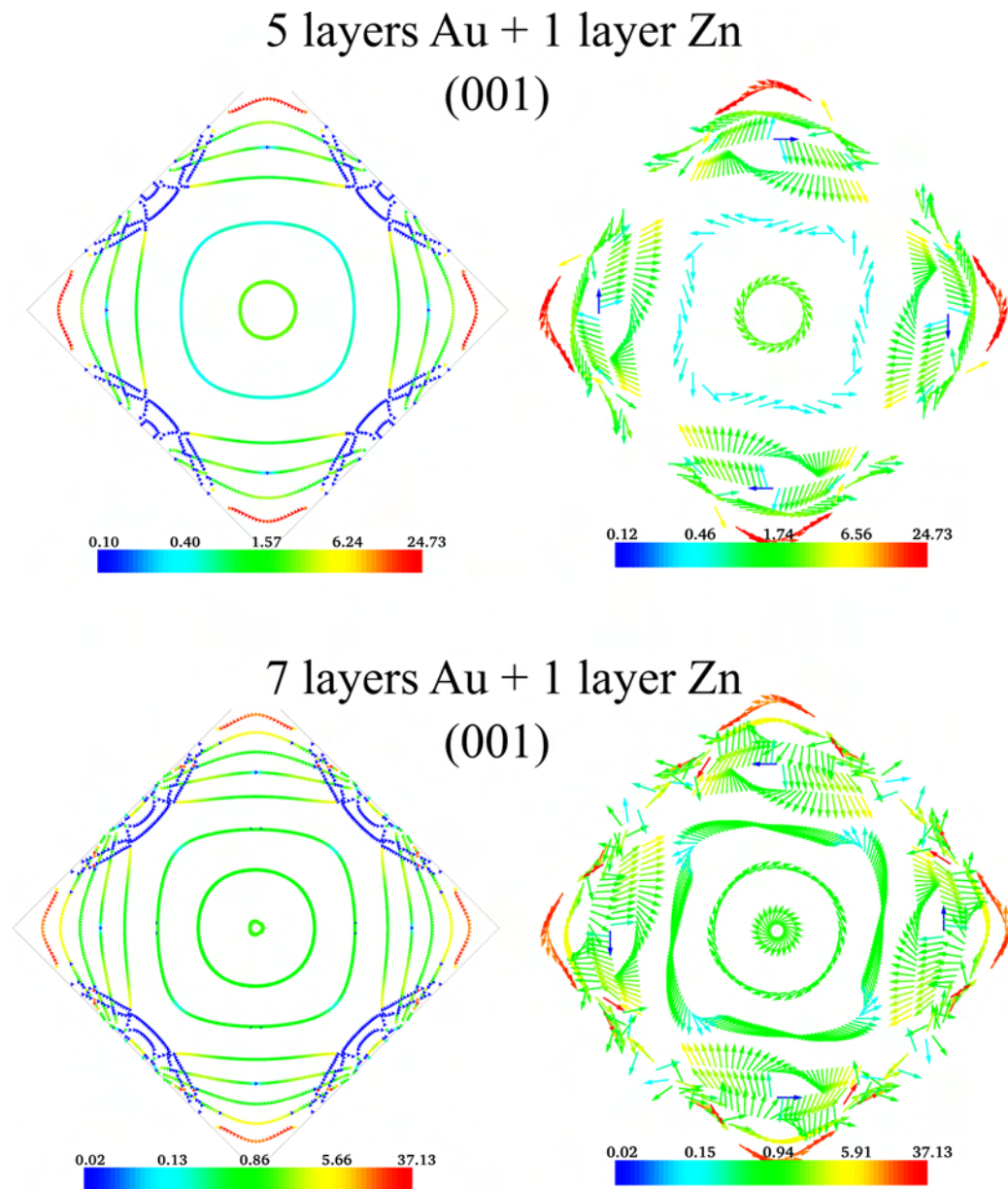
Figure 8.11.: The same figure as in figure 8.10 but for gold (001) films with 5 and 7 layers and an additional layer of Zn. The spin-orbit fields are slightly larger than those found for the gold films oriented in 111-direction. The states with a dark blue color in the left panels show a very large splitting, but are not included in the calculation of $\Omega(\mathbf{k})$. They do not contribute to the D'yakonov-Perel' mechanism of spin dephasing, because the necessary condition of the splitting to be smaller than the energy spread of the wave packet is not fulfilled. We have attributed to them the minimal obtained value of $|\Omega(\mathbf{k})|$ for visualization purposes. These states are not shown in the right panels.

lar direction, for gold this is not the case; there are rings among the bulk-like states whose spin-orbit fields point in the opposite direction compared to the neighboring ones.

For the copper film consisting of 9 layers, fluctuations of the direction on one of the rings are observed. These are probably of numerical origin, because the absolute values of $\Omega(\mathbf{k})$ at these $\mathbf{k}$-points are very small and therefore can be neglected.

So far, we have studied the spin-orbit fields at the Fermi surfaces of the (111) films. Now, we proceed with the (001) case. The results are presented in figure 8.10 for films with 5 and 7 layers of copper and one layer of Zn, and figure 8.11 for gold films also covered by one layer of Zn. One important difference compared to the spin-orbit fields of the (111) films is the lack of surface states, for which $|\Omega(\mathbf{k})|$ was relatively large. Both for copper and gold, $|\Omega(\mathbf{k})|$ is small for the states close to the center of the Brillouin zone, decreases when going to larger $|\mathbf{k}|$, but strongly increases again when approaching the outer boundaries of the Brillouin zone. Considering $|\Omega(\mathbf{k})|$ for the copper (001) films, maximal values are observed for states, which do not appear in the Fermi surfaces of the symmetric films and must therefore originate from the layer of Zn. A calculation of the layer-resolved density at some $\mathbf{k}$-points of these bands has confirmed this assumption, because these states have been found to be located at the Zn layer. In order to exclude that the large splitting is due to the spin-orbit coupling of the Zn layer, we have repeated our calculations neglecting the spin-orbit coupling of Zn and found similar results. These states are also present in the Fermi surfaces of the gold films, they are shown in the left panels of figure 8.11 in dark blue. They exhibit a much larger splitting than for the copper films of the order of $40\,\mathrm{mRyd}$, due to the stronger spin-orbit coupling for gold. The splittings are so large, that we do not show $|\Omega(\mathbf{k})|$ for these $\mathbf{k}$-points and just attributed to them the minimum value of $|\Omega(\mathbf{k})|$ for visualization purposes. Therefore, they are missing in the right panels. The neglect of these states in the calculation of $\Omega(\mathbf{k})$ is justified regarding that the D'yakonov-Perel' mechanism of spin dephasing only takes place, if the energy spread of the wave packet is larger than the splitting ΔE. This condition is not fulfilled for these $\mathbf{k}$-points.

Comparing the direction of the spin-orbit fields of the (001) surfaces to thoses of the (111) surfaces, a similarity can be detected; most states tend to point in the k_x-k_y-plane, although spin-orbit fields with a non-vanishing z-component can be found especially for the states in the regions close to the outer boundaries of the Brillouin zone.

8.4 Conclusion

In this chapter spin-orbit coupling effects on noble metal surfaces of finite films have been investigated. We presented calculations both for symmetric and antisymmetric films, oriented in [111] and [001] direction. Whereas for the symmetric films similar mechanisms of spin relaxation as in the investigated bulk materials occur, see chapter 6, in the case of systems without structure-inversion symmetry different mechanisms yield to spin-relaxation. Therefore, in the first part of this chapter we discussed the special form of the spin-orbit Hamiltonian for systems without structure-inversion symmetry and its consequences on the bandstructure. The interplay of spin-orbit coupling and the lack of inversion sym-
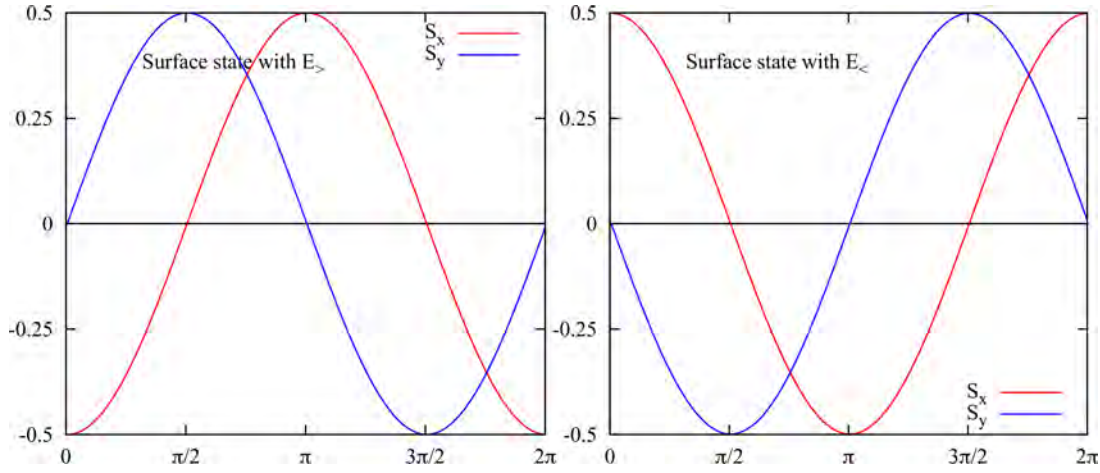
Figure 8.12.: Spin expectation values S_x and S_y of the Rashba-split surface states of a film consisting of 7 layers of Cu and one layer of Zn as function of the angle ϕ that describes the deviation from the k_y-axis in clockwise direction. Whereas in the left panel the spin expectation value of the innermost surface state which is higher in energy is shown, in the right panel S_x and S_y of the lower-lying Rashba-split surface state are presented. The expectation values of the two states are opposite to each other. As expected, the expectation value S_z vanishes for the surface states; this is not the case for the bulk states as can be seen from figure 8.8.

metry leads to the Rashba effect, i.e. the splitting of (surface) states. As a consequence, spin dephasing via the D'yakonov-Perel' mechanism occurs. In contrast to the Elliott-Yafet mechanism, present in systems which are invariant under inversion, the D'yakonov-Perel' mechanism predicts long spin-relaxation times when large momentum-scattering rates are obtained. Spin dephasing is caused by a precession of the spin around a local magnetic field, the spin-orbit field $\Omega(\mathbf{k})$, arising by the spin-orbit induced (energy)-splitting of states.

Before discussing our numerical results for the asymmetric films, we present calculations for symmetric films, for which, similar to the investigated bulk systems in chapter 6, all states $\mathbf{k}$ on the Fermi surface are two-fold degenerate. For copper and gold films oriented in [111] and [001] direction, the Elliott-Yafet parameter $|b_{\mathbf{k}}|^2$ as well as its averages over the Fermi surface $|b|^2$ have been calculated. We have found strong differences between the two surface orientations. Largest spin-mixing parameter have been found for the two surface states. In contrast, for the (001) surfaces, where surface states are lacking, we have calculated extraordinary high values of $|b_{\mathbf{k}}|^2$ for some states $\mathbf{k}$ of the Fermi surface, close to the outer boundary of the Brillouin zone. These $\mathbf{k}$-points, called spin hot spots, are due to band anti-crossings, and for the gold films values up to $|b_{\mathbf{k}}|^2 \approx 0.5$ have been found. The Elliott-Yafet parameters are strongly enhanced compared to the values obtained for the bulk materials. The enhancement is much larger for copper, where it amounts to a factor of about 7, than for gold, for which the ratio $|b_{\mathrm{SF}}|^2 / |b_{\mathrm{bulk}}|^2 \approx 1.5$ for the (111) surfaces. For the (001) surfaces, approximately two times larger values are obtained.

Furthermore, for the symmetric films we have considered scattering processes at self-adatoms,

i.e. Cu adatoms on top of copper films, and gold adatoms on gold. We have calculated both spin-conserving as well as spin-flip lifetimes. Whereas the momentum-relaxation times for the copper and gold films slightly increase with increasing film thickness, the spin-flip lifetimes T_1 exhibit a strong decay. Of course, the spin-flip lifetimes calculated for gold are much shorter than those on copper. The ratios T_1/τ, i.e. the number of spin-conserving scattering events per one spin-flip process, strongly decrease with increasing film thickness; obviously, for the thinner films, spin-flip scattering is disadvantaged by the large hybridization of the two surface states from the two sides of the film. However, the trend found for the calculated film thicknesses will not necessarily continue for thicker films.

The calculation of spin-conserving and spin-flip lifetimes for the (001) films has been occurred to be numerically difficult, since the precise integration over the Fermi surface requires a dense mesh of $\mathbf{k}$-points; the reason are anti-crossings of bands, yielding very localized spin hot spots.

For both surface orientations a reduction of symmetry by a factor of two is found for the spin-relaxation times T_1, while the full symmetry is kept for the distribution of $\tau_{\mathbf{k}}$. Hence, for the (111) surfaces, the 12-fold symmetry of the Brillouin zone for $\tau_{\mathbf{k}}$ is lowered to a 6-fold symmetry for $T_{1,\mathbf{k}}$, and for the (001) surfaces, a 4-fold symmetry for $T_{1,\mathbf{k}}$ instead of a 8-fold symmetry of $\tau_{\mathbf{k}}$ could be verified.

A comparison of the lifetimes averaged over the Fermi surfaces of the two orientations for copper reveals much longer spin-relaxation times for the surfaces oriented in [001] direction. The reason for that is the lack of surface states that results in high scattering. For the gold films, deviating results for the two thicknesses are obtained due to the appearance of spin hot spots.

In the second part of this chapter we have investigated effects of spin-orbit coupling occurring for copper and gold films, where an asymmetry is introduced by covering them with one layer of Zn. The break of symmetry results in a splitting of states, lifting the degeneracy of all $\mathbf{k}$-points on the Fermi surface. For the (111) surface state, the splitting corresponds to the Rashba-effect; the corresponding spin-orbit fields $\mathbf{\Omega_k}$ for the surface states are in-plane. In contrast, for the bulk-like states all three components of $\mathbf{\Omega_k}$ are not negligible, although the z-component (out of plane) is smaller than the in-plane components. The value of the Rashba-splitting calculated for the Au (111) surface states agrees very well with experimental data; the Rashba-splitting of copper is four times smaller and so far could not be resolved in photoemission spectroscopy.

High absolute values of spin-orbit fields $\mathbf{\Omega_k}$ are found for the (111) surface states and for some states at the outer boundaries of the Brillouin zone, both for the copper and the gold films. These states have their origin in the Zn layer.

In (001) films, the lack of surface states leads to small values of $\mathbf{\Omega_k}$ for the states close to the center of the Brillouin zone. Highest fields are found for states at the outer border of the Brillouin zone. For the gold (001) films, some of the states exhibit giant splittings. These states have not been taken into account in the calculation of spin-orbit fields, since the splittings are too large to account for the D'yakonov-Perel' mechanism of spin-dephasing. Furthermore, a calculation of a layer-resolved density of states has revealed that they are located at the Zn layer just as in the (111) films.

We expected the splitting of the bulk states to decrease with increasing layer thickness, even-

tually vanishing as the sample becomes bulk-like at large thickness. Whether this is the case could not be clearly deduced from our results, since relatively strong changes of the position of the states on the Fermi surface are observed. An investigation of thicker films would be interesting, remaining for future work.

<div style="text-align: right">CHAPTER **9**</div>

Conclusion

In this thesis, we pursued three main goals: First, we systematically investigated momentum- and spin-relaxation times due to impurity scattering in the noble metals copper and gold. Secondly, we studied extensively the lifetime reduction of surface-states induced by scattering at adatoms and impurities in the first and second surface layers of the (111) surfaces of copper, silver and gold. Finally, the third aim of this work was to combine the two previous aspects and investigate the effects of spin-orbit coupling on scattering at the noble-metal surfaces copper and gold.

In all our calculations we used the KKR-Green function method for electronic structure calculations, which is particularly suited for the numerical treatment of scattering processes because of its multiple scattering ansatz.

Spin relaxation in copper and gold bulk

The first step on our way to calculate momentum- and spin-relaxation times was the integration of spin-orbit coupling in the KKR-formalism and its implementation in the code. We calculated the spin expectation values and spin-mixing parameters on the Fermi surfaces and solved the problems occurring for degenerate states. We showed that the resulting spin-mixing parameter for copper and gold agree well with those given in the literature.

In order to obtain momentum- and spin-relaxation times, the Lippmann-Schwinger equation for impurity scattering including spin-orbit coupling was solved and the scattering matrix in momentum space was calculated.

The inversion symmetry of the fcc bulk metals copper and gold leads to a degeneracy of all **k**-points on the Fermi surface. Therefore, spin relaxation is induced by the Elliott-Yafet mechanism and impurity spin-orbit coupling. We have provided a systematic study of momentum- and spin-relaxation times induced by scattering at the $3d$, $4sp$, $4d$, $5sp$ and $5d$ impurities in copper and gold hosts. The influence of the spin-orbit coupling in the

host has been investigated, showing that the spin-orbit induced effects are large for a gold host and small for a copper host. In addition, this finding helped to explain why similar momentum-relaxation but deviating spin-relaxation rates for copper and gold hosts are found. The spin-relaxation times for the gold host are much shorter than those calculated for the copper host.

Furthermore, strong qualitative differences between the trends for momentum- and spin-relaxation times have been found. While momentum-relaxation rates are high for the d and the sp impurities, the trends for spin-relaxation rates exhibit only a maximum for the d impurities, and not for the sp scatterers. This behavior is much more pronounced for the copper host than for the gold host, since the spin-relaxation rates in gold are highly influenced by the spin-orbit coupling of the gold host. The different behavior of the spin-conserving and spin-flip scattering rates for the d and sp scatterers could be explained with the help of a simple model, relating the spin-relaxation rates to the Wigner delay times, accounting for the time the wavepacket requires for the scattering process. Larger delay times are found for the d scatterers, while short times for the s and p impurities have been obtained. Hence, we concluded that resonant scattering is very important for spin relaxation, as the electrons spend much more time at the d-resonance than at the sp impurities and therefore are exposed a much longer time to the impurity spin-orbit coupling.

When investigating the ratio of spin-relaxation and momentum-relaxation times, i.e. the number of momentum-scattering processes per one spin-flip we find large differences between the copper and the gold host. Whereas in the copper host ratios between 10^4 for light impurities and 3 for the chemically similar elements Ag and Au have been found, in gold we observe ratios within a much smaller range, reaching from 30 to 3. Thus, for gold the spin-orbit coupling effects of the host prevails – spin-relaxation is dominated by the Elliott-Yafet mechanism.

The investigation of correlated scattering by impurity dimers completes the study of spin-relaxation in bulk materials. We showed that correlated scattering effects are important only for the d impurities situated at nearest neighboring sites. For these, scattering times are enhanced up to a factor of 1.5 compared to scattering at independent impurities.

Lifetime reduction of surface states

The second goal of this thesis was to study the reduction of surface-state lifetimes induced by scattering at adatoms and impurities in and below the first surface layer of copper, silver and gold (111) films. Therefore, the spin-conserving scattering matrix in momentum-space was calculated for all states on the Fermi surface. Integration over the Fermi surface then yields the surface-state lifetimes and the momentum-relaxation times for the bulk states.

The analysis of the scattering rates at the $3d$ and the $4sp$ impurities in and on a copper film showed that scattering at adatoms qualitatively strongly differ from scattering at impurities in and below the surface. The perturbation caused by an adatom is much stronger than that which is caused by replacing a copper atom by another element. Furthermore, the extent of the adatom into the surrounding vacuum plays a big role.

In order to understand the trend observed for the scattering rates at adatoms, we have made

an orbital-momentum resolved calculation. We found that for the d scatterers a constructive interference of the s- and the d-channel takes place, whereas for the sp scatterers the s- and the p-channel interfere destructively. This ansatz could be confirmed by a calculation of the Friedel oscillations.

The dependence of the surface-state lifetime on the film thickness has also been examined. The surface-state lifetimes of the innermost surface state decrease with increasing number of layers, which is mostly due to an energy shift of the states at the two surfaces, as well as due to the reduction of the overlap of the surface states with the impurity for larger thicknesses, when the state can penetrate more into the bulk.

However, in the calculation of surface resistivities, which also have been extracted from the scattering matrix, this effect is hardly seen, because this quantity entails a further averaging over all states, surface- and bulk-like states.

To complete the picture, surface-state lifetimes induced by scattering at magnetic adatoms on the copper film have been studied. As expected, we observed a double-peak structure as the impurity atomic number is varied, which is due to the split d-resonance crossing the Fermi level.

Spin-orbit induced effects on copper and gold thin films

The third goal of this thesis was the investigation of spin-orbit induced effects occurring in copper and gold films with different surface orientations. We have considered symmetric thin films as well as thin films where the inversion symmetry was broken by replacing one layer of Cu/Au by one layer of Zn. The prevailing spin-relaxation mechanisms are completely different for these two kinds of systems; whereas in the symmetric systems all states are twofold degenerate (similar as in the bulk samples) and therefore spin relaxation via the Elliott-Yafet mechanism takes place, the break of symmetry for the asymmetric slabs lifts the degeneracy and leads to a splitting of all states on the Fermi surface; then, the D'yakonov-Perel' mechanism leads to spin dephasing.

For the symmetric films, we started with the discussion of the Elliott-Yafet parameter. For all film thicknesses and both surface orientations ((001) and (111)) we have calculated spin-flip parameter which are enhanced compared to the values that we have found for the bulk systems. Whereas for the (111) surfaces largest parameters have been found for the surface states, anticrossings of bands on the Fermi surfaces of the (001) films lead to spin hot spots close to the Brillouin zone edge and very large values of $|b|^2$. This effect is much larger for the gold than for the copper films.

Furthermore, the study of momentum- and spin-relaxation times due to scattering at adatoms on top of the (111) surfaces revealed a strong dependence on film thickness; whereas momentum-relaxation times increase with film thickness, spin-relaxation times show a strong decrease. This behavior has been found for copper and for the gold films. Considering scattering rates at adatoms on (001) surfaces, we found strong differences for copper and gold. For the copper films, the lack of the surface states for this surface orientation results in much longer spin-relaxation times. In contrast, the strong spin hot spots appearing on the Fermi surfaces of the gold films compensate the lack of surface states.

In asymmetric films, the splitting of states caused by the lack of inversion symmetry together with spin-orbit coupling lead to the formation of local effective magnetic fields, the so-called spin-orbit fields. Spin dephasing is obtained by precession of the electron spin around these local spin-orbit fields together with momentum scattering, resulting in a change of the precession axis after each scattering event. We have calculated the spin-orbit fields for copper and gold (001) and (111) films. We found a Rashba-splitting of the surface states which agrees with experiment and previous calculations. In addition, we found significant contributions from the bulk-like states for both orientations, especially in the vicinity of the Zn-like states.

APPENDIX A

Some details on the KKR-formalism

A.1 Derivation of the Dyson equation for an arbitrary reference system

In order to derive the Dyson equation for an arbitrary reference system, we start from the algebraic Dyson equation (2.47)

$$G_{LL'}^{nn'}(E) = g_{LL'}^{nn'}(E) + \sum_{n''L''L'''} g_{LL''}^{nn''}(E) t_{L''L'''}^{n''} G_{L'''L'}^{n''n'}(E) \tag{A.1}$$

where the $g_{LL''}^{nn''}(E)$ represent the free space structure constants. In matrix notation, the above equation can be rewritten as

$$\mathbf{G}(E) = \mathbf{g}(E) + \mathbf{g}(E)\mathbf{t}(E)\mathbf{G}(E). \tag{A.2}$$

Since this equation is valid for an arbitrary $V(\mathbf{r})$, i.e. $\mathbf{t}(E)$, the same holds for a reference system of potentials with $V^{\mathrm{ref}}(\mathbf{r})$ (to be given in detail below) placed at the lattice sites of the crystal

$$\mathbf{G}^{\mathrm{ref}}(E) = \mathbf{g}(E) + \mathbf{g}(E)\mathbf{t}^{\mathrm{ref}}(E)\mathbf{G}^{\mathrm{ref}}(E). \tag{A.3}$$

Equations (A.1) and (A.3) can be rewritten as

$$\mathbf{g}(E)^{-1} = \mathbf{G}(E)^{-1} - \mathbf{t}(E) \tag{A.4}$$

and

$$\mathbf{g}(E)^{-1} = (\mathbf{G}^{\mathrm{ref}}(E))^{-1} - \mathbf{t}^{\mathrm{ref}}(E), \tag{A.5}$$

respectively. Combination leads then to

$$(\mathbf{G}(E))^{-1} = (\mathbf{G}^{\mathrm{ref}}(E))^{-1} - (\mathbf{t}(E) - \mathbf{t}^{\mathrm{ref}}(E)), \tag{A.6}$$

and a simple transformation to the sought-after Dyson equation

$$\mathbf{G}(E) = \mathbf{G}^{\mathrm{ref}}(E) + \mathbf{G}^{\mathrm{ref}}(E)\Delta\mathbf{t}(E)\mathbf{G}(E), \tag{A.7}$$

with

$$\Delta\mathbf{t}(E) = \mathbf{t}(E) - \mathbf{t}^{\mathrm{ref}}(E). \tag{A.8}$$

A.2 Practical calculation of the band structure

To obtain the band structure $E(\mathbf{k})$, i.e. the solution of eq. (3.45) or (3.49), respectively, the problem is transformed to an eigenvalue problem. Therefore, in a first step eq. (3.49) is rewritten as

$$\sum_{\mu',L'L''} \left[\delta_{\mu\mu'} \left(\Delta t_{LL'}^{\mu'}(E) \right)^{-1} - G_{LL'}^{\mathrm{r},\mu\mu'}(\mathbf{k};E) \right] \Delta t_{L'L''}^{\mu'}(E) c_{\mathbf{k}L''}^{\mu'} = 0, \tag{A.9}$$

separating the scattering properties of a single atomic potential described by $\Delta t_{LL'}^{\mu}(E)$ from the structure described by the lattice site $\mathbf{R}^n$ and the structural Green function $G_{LL'}^{\mathrm{r},\mu\mu'}(\mathbf{k};E)$. Interpreting the vector $\Delta t_{LL''}^{\mu'}(E) c_{\mathbf{k}L'}^{\mu'}$ as an eigenvector of the system belonging to the eigenvalue

$$\lambda(\mathbf{k}, E_{\mathbf{k}}) = 0, \tag{A.10}$$

eq. (A.9) can be reformulated as

$$\left(\Delta t^{-1}(E) - G^{\mathrm{r}}(\mathbf{k};E) \right) \Delta t(E) c_{\mathbf{k}} = \lambda(\mathbf{k}, E_{\mathbf{k}}) \Delta t(E) c_{\mathbf{k}}. \tag{A.11}$$

The matrix $\left(\Delta t^{-1}(E) - G^{\mathrm{r}}(\mathbf{k};E) \right)$ is the so-called KKR-matrix, since it contains all information about the band structure $E(\mathbf{k})$ of the system.

 In order to calculate the band structure, it is sufficient to determine the eigenvalues $\lambda(\mathbf{k}, E_{\mathbf{k}})$ of the KKR-matrix and then search the pairs $(\mathbf{k}, E)$ for which one of the eigenvalues becomes zero.

A realization of this method for systems without spin-orbit coupling was realized by P. Zahn [70]. In his implementation, the non-hermitian KKR-matrix $\left[\Delta t^{-1}(E) - G^{\mathrm{r}}(\mathbf{k};E) \right]$ is transformed to a hermitian matrix in order to obtain real eigenvalues. Then, the reciprocal space vector $\mathbf{k}$ is kept constant while the energy is varied. For each energy point the eigenvalues $\lambda(\mathbf{k};E)$ are calculated and the number of negative (or positive) eigenvalues is counted - whenever one of the eigenvalues changes its sign, the number changes and a point of the band structure is obtained. For more information about the transformation of the KKR-matrix and other calculational details see [70].

However, the procedure becomes complicated for brute-force application whenever complicated structures such as band crossings occur. In this case, it might be that two eigenvalues change their sign, but the number of positive and negative eigenvalues stays the same (see figure A.1).

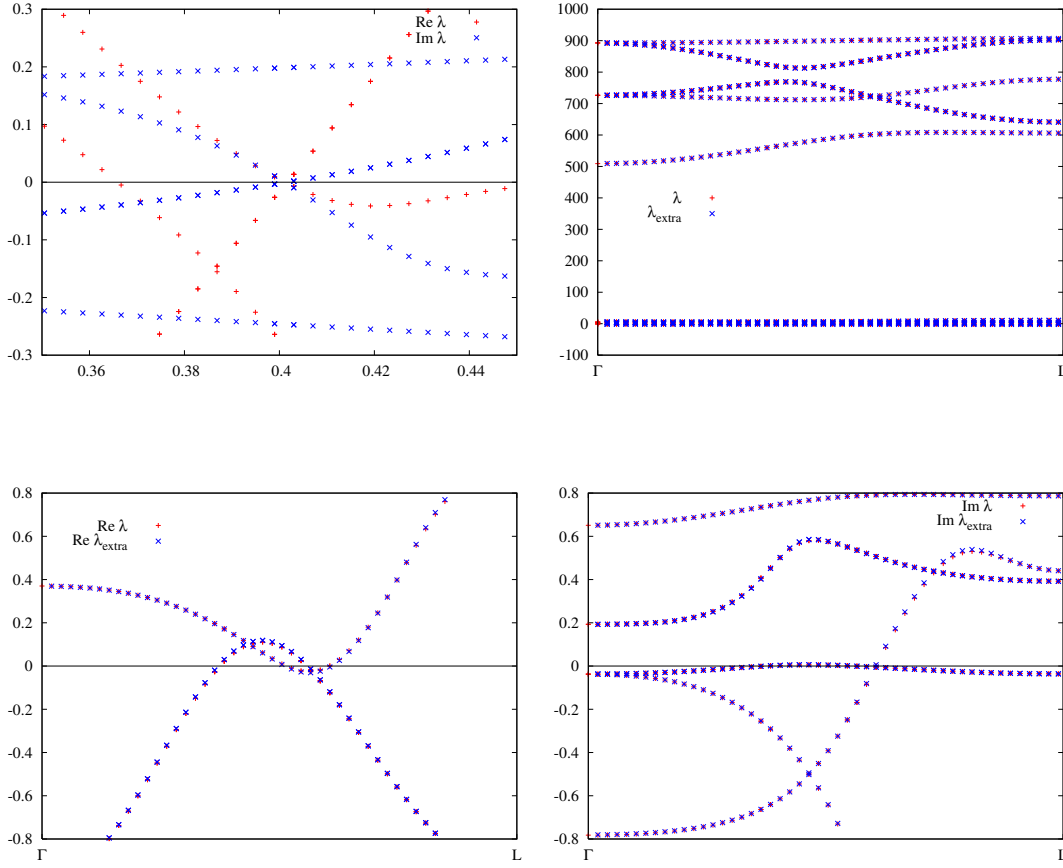Additionally, for systems including spin-orbit coupling and/or taking the non-spherical

Figure A.1.: Eigenvalues of the KKR-matrix of Au bulk, full potential calculation without spin-orbit coupling, as a function of reciprocal space vectors **k** in 111-direction. *Top left:* Real and imaginary part of the eigenvalues at E fixed to $E = -3.83eV$. The crossing of bands leads to the intersection with the x-axis of two eigenvalues in one interval $[k, k + \Delta k]$. Additionally, at $k \approx 0.365$, the real part of λ becomes zero while the imaginary part does not. *Top right:* Real and imaginary part of exact and extrapolated eigenvalues. *Bottom:* Real and imaginary part of exact and extrapolated eigenvalues restricted to small eigenvalues. The extrapolated eigenvalues agree very well for intervals, in which the run of the curve is almost linear, for more complex curves a small deviation can be seen.

contributions of the potential into account (full potential calculation) the transformation is which transforms the t-matrix to a hermitian matrix is not obvious. Hence, the eigenvalues are complex and both the real part and the imaginary part must be zero[1].

The above reasons make it necessary to modify the method for band structure calculation in order to overcome the above-mentioned problems. We developed a new, more gen-

---

[1] The real and the imaginary part of λ might have exclusive zeros as can be seen in figure A.1.

eral scheme to calculate the points $(\mathbf{k}, E)$ fulfilling the condition $\lambda(\mathbf{k}, E_{\mathbf{k}}) = 0$, which is sketched in the following:

We start by calculating the eigenvalues $\lambda(\mathbf{k}, E)$ for a given pair of $(\mathbf{k}, E)$, keep the energy E constant while varying the reciprocal space vector $\mathbf{k}$. To obtain the eigenvalues at the next k-point $(\mathbf{k} + \Delta \mathbf{k})$ there are two possibilities: Either the eigenvalues can be calculated directly by diagonalizing the KKR-matrix or first order perturbation theory can be used to extrapolate the eigenvalues at $(\mathbf{k} + \Delta \mathbf{k}, E)$ from the eigenvalues calculated at $(\mathbf{k}, E)$. Doing both, every eigenvalue at the new k-point $(\mathbf{k} + \Delta \mathbf{k}, E)$ calculated exactly can be traced back to the corresponding eigenvalue at $\mathbf{k}$ (by virtue of the extrapolation) and all crossings of the eigenvalues with the x-axis can be easily identified.

For the second method, i.e. the extrapolation from $\mathbf{k}$ to $\mathbf{k} + \Delta \mathbf{k}$ we expand $G^{\mathrm{r}}(\mathbf{k}; E)$ for small $\Delta \mathbf{k}$ around $\mathbf{k}$ writing

$$G^{\mathrm{r}}(\mathbf{k} + \Delta \mathbf{k}; E) \approx G^{\mathrm{r}}(\mathbf{k}; E) + \Delta \mathbf{k} \cdot \nabla_{\mathbf{k}} G^{\mathrm{r}}(\mathbf{k}; E). \tag{A.12}$$

In the following it must be distinguished whether one of the eigenvalues at $(\mathbf{k}, E)$ is degenerate or not. We will first discuss the procedure for the non-degenerate case, and then continue with degenerate eigenvalues. First order perturbation theory for non-hermitian matrices is used as developed in [112, 113]. The left and right eigenvectors of the KKR-matrix $(\Delta t^{-1}(E) - G^{\mathrm{r}}(\mathbf{k}; E))$ corresponding to $\lambda(\mathbf{k}, E) = 0$ are defined as

$$\left(\Delta t^{-1}(E) - G^{\mathrm{r}}(\mathbf{k}; E)\right) \left| \phi_{\lambda,\mathbf{k}} \right\rangle = 0 \tag{A.13}$$

or

$$\left\langle \tilde{\phi}_{\lambda,\mathbf{k}} \right| \left(\Delta t^{-1}(E) - G^{\mathrm{r}}(\mathbf{k}; E)\right) = 0, \tag{A.14}$$

respectively. The right eigenvector is related to the coefficients $c_{\mathbf{k}}$ following

$$\left| \phi_{\lambda,\mathbf{k}} \right\rangle = \Delta t(E) c_{\mathbf{k}}. \tag{A.15}$$

The projector $\mathrm{P}_{\lambda,\mathbf{k}}$ of the right and the left eigenvector is then calculated as

$$\mathrm{P}_{\lambda,\mathbf{k}} = \left| \phi_{\lambda,\mathbf{k}} \right\rangle \left\langle \tilde{\phi}_{\lambda,\mathbf{k}} \right|. \tag{A.16}$$

According to the perturbation theory for non-hermitian matrices developed in [112, 113], the extrapolated eigenvalues at $\mathbf{k} + \Delta \mathbf{k}$ for non-degenerate eigenvalues λ are given by

$$\lambda(\mathbf{k} + \Delta \mathbf{k}) \approx \lambda(\mathbf{k}) + |\Delta \mathbf{k}| \operatorname{Tr} \left[\mathrm{P}_{\lambda,\mathbf{k}} \frac{dG^{\mathrm{r}}(\mathbf{k}; E)}{dk} \right], \tag{A.17}$$

where the derivative $dG^{\mathrm{r}}(\mathbf{k}; E)/dk$ is calculated in the direction of $\Delta \mathbf{k}$.

If the eigenvalue λ is n-times degenerate, there are n linearly independent right and left eigenvectors

$$\left| \phi_{\lambda,\mathbf{k}}^{i} \right\rangle, \left\langle \tilde{\phi}_{\lambda,\mathbf{k}}^{i} \right| \quad , \quad i = 1, n. \tag{A.18}$$

In this case, a generalized matrix of the product of the ith right eigenvector and the jth left eigenvector can be defined

$$\mathrm{P}_{\lambda,\mathbf{k}}^{ij} = \left| \phi_{\lambda,\mathbf{k}}^{i} \right\rangle \left\langle \tilde{\phi}_{\lambda,\mathbf{k}}^{j} \right|. \tag{A.19}$$

Analogously to perturbation theory for non-degenerate eigenvalues for hermitian matrices (for example see [114]) and the above result for non-hermitian matrices, the first order correction of the eigenvalues $\lambda_{\mathbf{k}}$ are obtained by calculating the eigenvalues $\lambda_{\mathbf{k}}^{'i}$ of the quadratic n times n-matrix

$$\mathrm{Tr}\left[\mathrm{P}_{\lambda,\mathbf{k}}^{ij}\, \frac{dG^{\mathrm{r}}\left(\mathbf{k};E\right)}{dk} \right]\,, \quad i,j = 1,n\,. \tag{A.20}$$

Finally, we obtain for the eigenvalues at $\mathbf{k} + \Delta\mathbf{k}$

$$\lambda(\mathbf{k} + \Delta\mathbf{k}) \approx \lambda(\mathbf{k}) + |\Delta\mathbf{k}|\,\lambda_{\mathbf{k}}^{'i}\,, \quad i = 1,n\,. \tag{A.21}$$

Since the eigenvalues in general are complex (because of the non-hermiticity of the KKR-matrix), in a first step we look for the roots of the imaginary part and then check whether the real part is zero or not. If both the imaginary and the real part of the eigenvalue shows a zero-crossing, i.e. change their sign in the interval $[\mathbf{k}, \mathbf{k} + \Delta\mathbf{k}]$, a linear extrapolation allows to estimate the k-vector $\mathbf{k}_{\mathrm{cross}}$, for which the condition $\lambda = 0$ is fulfilled.
For the case of non-degenerate eigenvalues $\mathbf{k}_{\mathrm{cross}}$ is given by

$$\mathbf{k}_{\mathrm{cross}} \approx \mathbf{k} - \frac{\mathrm{Im}\lambda_{\mathbf{k}}}{\mathrm{Im}\left[\mathrm{Tr}\left[\mathrm{P}_{\lambda,\mathbf{k}}\frac{dG^{\mathrm{r}}(\mathbf{k};E)}{dk}\right]\right]} \cdot \frac{\Delta\mathbf{k}}{|\Delta\mathbf{k}|} \tag{A.22}$$

whereas for n-times degenerate eigenvalues the degeneracy might be lifted and maximally n different crossing points $\mathbf{k}_{\mathrm{cross}}$ can be obtained

$$\mathbf{k}_{\mathrm{cross}} \approx \mathbf{k} - \frac{\mathrm{Im}\lambda_{\mathbf{k}}}{\mathrm{Im}\lambda_{\mathbf{k}}^{'i}} \cdot \frac{\Delta\mathbf{k}}{|\Delta\mathbf{k}|} \quad i = 1,n. \tag{A.23}$$

In order to obtain a sufficient accuracy the cluster of reference atoms for the calculation of $G^{\mathrm{r}}\left(\mathbf{k};E\right)$ has to be chosen large. Otherwise the crossing of the real and the imaginary part with the x-axis differ considerably as is demonstrated in figure A.2 and table A.1. In table A.1, the real part of the eigenvalue at the zero point of the imaginary part as a function of the numbers of atoms in the cluster of the reference system for the example of gold at the Fermi energy in [100] direction is specified. We see that the accuracy strongly increases with the cluster size, while the value of the calculated $\mathbf{k}_{\mathrm{cross}}$ shows only a small deviation.

Finally, in figure A.2 we show an example of a band structure calculation for gold bulk without spin-orbit coupling as well as including spin-orbit coupling. While important changes can be seen in the band structure for energies below the Fermi level, the value of the Fermi wave vector $\mathbf{k}_{\mathrm{cross}} = \mathbf{k}_{\mathrm{F}}$ in the [100] direction stays almost the same.

A.2.1 The Fermi surface

The calculation scheme of the Fermi surface is very similar to the band structure calculation as explained in the last section; the energy is fixed to $E = E_F$ while the $\mathbf{k}$ vector is varied. Whenever one of the eigenvalues of the matrix $(\Delta\mathbf{t}^{-1}(E) - \mathbf{G}^{\mathrm{r}}(\mathbf{k};E))$ becomes zero, one point of the Fermi surface is obtained.
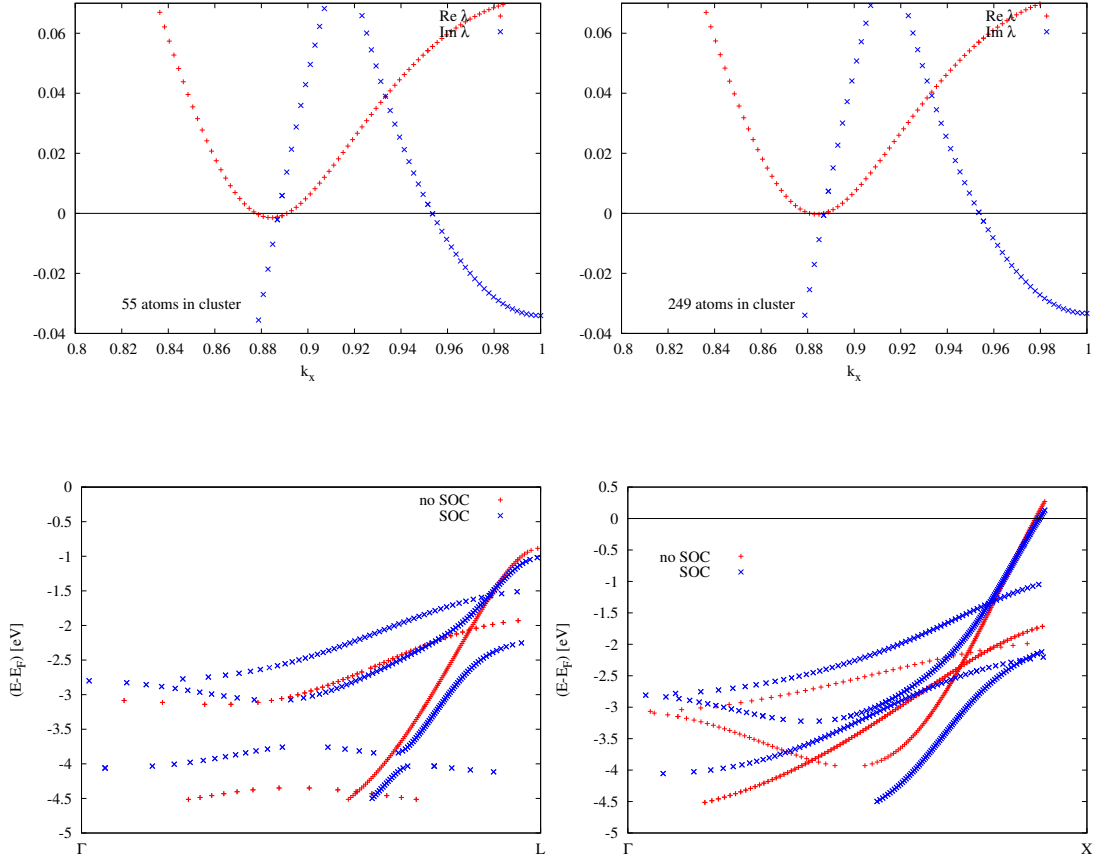
Figure A.2.: *Top:* Eigenvalues of the KKR-matrix of Au bulk without spin-orbit coupling, as a function of reciprocal space vectors **k** in [100] direction at the Fermi energy for different sizes of the cluster of the reference system. If the cluster size is chosen too small, (*left panel*, 55 atoms in the cluster) the real and the imaginary part of the eigenvalues do not cross the x-axis simultaneously. A large cluster size is necessary (*right panel*, 249 atoms) to obtain a good accuracy. *Bottom:* band structure for Au bulk without spin-orbit coupling as well as including spin-orbit coupling in [111] (*left panel*) and [100] (*right panel*) direction. Spin-orbit coupling lifts the degeneracy of some bands, and, in the [111] direction leads to an anticrossing of bands. However, at the Fermi level almost no difference can be detected.

Once the **k**-vectors $\mathbf{k}_\mathrm{F}$ obeying eq. (3.49) are found, the corresponding eigenvectors $|\phi_{\lambda=0,\mathbf{k}_\mathrm{F}}\rangle = \Delta t^\mu_{LL'}(E)c^{0,\mu}_{\mathbf{k}L'}$ can be determined, which allow to obtain the coefficients $c^{n,\mu}_{\mathbf{k}L}$. In order to identify the full wavefunctions $\psi_\mathbf{k}(\mathbf{r})$ at the Fermi surface, the regular solutions $R_L(\mathbf{r};E)$ of the Schrödinger equation have to be calculated by solving the Schrödinger equation as described in chapter 2, section 2.2 or 2.4, respectively.

number of atoms in reference cluster	Re $\lambda(\mathbf{k}_{\text{cross}}, E_{\text{F}})$	$\mathbf{k}_{\text{cross}}[2\pi/a]$
55	$1.1 \cdot 10^{-3}$	0.887397
79	$2.5 \cdot 10^{-4}$	0.887114
135	$7.3 \cdot 10^{-5}$	0.887036
249	$4.2 \cdot 10^{-7}$	0.887025

Table A.1.: Real part of the eigenvalue $\lambda(\mathbf{k}_{\text{cross}}, E_{\text{F}})$ at the zero point of the imaginary part of $\lambda(\mathbf{k}_{\text{cross}}, E_{\text{F}})$ as a function of the numbers of atoms in the cluster of the reference system for the example of fcc gold at the Fermi energy in [100] direction. The accuracy strongly increases with the cluster size, while the value of the calculated $\mathbf{k}_{\text{cross}}$ shows only a small deviation.

A.3 The radial Lippmann-Schwinger equation for non-spherical potential

The aim of this section is to derive the Lippmann-Schwinger equation for the non-spherical wavefunction-components $R_{L'L}^{\text{imp}}(r; E)$ of a system characterized by $V^{\text{imp}}(\mathbf{r})$, which in the following are to be understood as perturbation to a system characterized by $V(\mathbf{r})$ with corresponding components $R_{L'L}(r; E)$. The relations are not only valid for the impurity problem; they hold for two arbitrary systems with $\Delta V(\mathbf{r}) = V^{\text{imp}}(\mathbf{r}) - V(\mathbf{r})$. However, since we will apply them to the case of an impurity in a host, we address all variables of the perturbed system with 'imp'.

We start the derivation from the radial Lippmann-Schwinger equation valid for the radial wave functions $R_L^{\text{imp}}(\mathbf{r}; E)$, expressing it in terms of the radial wavefunction $R_L(\mathbf{r}; E)$ and the Green function $G(\mathbf{r}, \mathbf{r}'; E)$ of the host system and the difference in potential $\Delta V(\mathbf{r})$

$$R_L^{\text{imp}}(\mathbf{r}; E) = R_L(\mathbf{r}; E) + \int d^3r' \, G(\mathbf{r}, \mathbf{r}'; E)\Delta V(\mathbf{r}')R_L^{\text{imp}}(\mathbf{r}'; E) \,. \tag{A.24}$$

Using the expansions

$$R_L^{\text{imp}}(\mathbf{r}; E) = \sum_{L'} R_{L'L}^{\text{imp}}(r; E)Y_{L'}(\hat{r}), \tag{A.25}$$

$$R_L(\mathbf{r}; E) = \sum_{L'} R_{L'L}(r; E)Y_{L'}(\hat{r}), \tag{A.26}$$

$$G(\mathbf{r}, \mathbf{r}'; E) = \sum_{LL'} G_{LL'}(r, r'; E)Y_L(\hat{r})Y_{L'}(\hat{r}') \quad \text{and} \tag{A.27}$$

$$\Delta V(\mathbf{r}') = \sum_{L} \Delta V_L(r')Y_L(\hat{r}'), \tag{A.28}$$

the above equation results in

$$
\sum_{L'} R^{\text{imp}}_{L'L}(r;E)Y_{L'}(\hat{r}) = \sum_{L'} R_{L'L}(r;E)Y_{L'}(\hat{r})+
$$
$$
\int d^3r' \sum_{L'L''} Y_{L'}(\hat{r})G_{L'L''}(r,r';E)Y_{L''}(\hat{r}')
$$
$$
\sum_{L'''} \Delta V_{L'''}(r')Y_{L'''}(\hat{r}') \sum_{L''''} R^{\text{imp}}_{L''''L}(r';E)Y_{L''''}(\hat{r}'), \quad \text{(A.29)}
$$

which can be simplified to

$$
\sum_{L'} R^{\text{imp}}_{L'L}(r;E)Y_{L'}(\hat{r}) = \sum_{L'} R_{L'L}(r;E)Y_{L'}(\hat{r})+
$$
$$
\int r'^2 dr' \sum_{L'L''L''''} Y_{L'}(\hat{r})G_{L'L''}(r,r';E)\Delta V_{L''L''''}(r')R^{\text{imp}}_{L''''L}(r;E). \quad \text{(A.30)}
$$

The linear independence of the spherical harmonics finally leads to

$$
R^{\text{imp}}_{L'L}(r;E) = R_{L'L}(r;E) + \int r'^2 dr' \sum_{L''L'''} G_{L'L''}(r,r';E)\Delta V_{L''L'''}(r')R^{\text{imp}}_{L'''L}(r;E)
$$
$$
\text{(A.31)}
$$

q.e.d..

Before closing the section, we will shortly express the scattering matrix $\Delta t_{LL'}(E)$ in terms of the $R_{LL'}(r;E)$. The scattering matrix $\Delta t_{LL'}(E)$ is defined as

$$
\Delta t_{LL'}(E) = \int d^3r \, R_L(\mathbf{r})\Delta V(\mathbf{r})R^{\text{imp}}_{L'}(\mathbf{r}) \,, \quad \text{(A.32)}
$$

and thus

$$
\begin{aligned}
\Delta t_{LL'}(E) &= \int d^3r \sum_{L''} R_{L''L}(r)Y_{L''}(\hat{r}) \sum_{L'''} \Delta V_{L'''}(r)Y_{L'''}(\hat{r}) \sum_{L''''} R^{\text{imp}}_{L''''L'}(r)Y_{L''''}(\hat{r}) \\
&= \int r^2 dr \sum_{L''L''''} R_{L''L}(r)\Delta V_{L''L''''}(r)R^{\text{imp}}_{L''''L'}(r).
\end{aligned} \quad \text{(A.33)}
$$

A.4 The Δt^n_l-Matrix

In this section it has to be proven that

$$
\Delta t^n_l(E) = \int r^2 dr \, R^{\text{r},n}_l(r;E)\Delta V^n(r)R^n_l(r;E), \quad \text{(A.34)}
$$

by tracing this equation back to the definition of the atomic scattering matrices $t^n_l(E)$ and $t^{\text{r},n}_l(E)$, thus to the definition

$$
\Delta t^n_l(E) = t^n_l(E) - t^{\text{r},n}_l(E). \quad \text{(A.35)}
$$

We proceed following Zeller [64]. Using the definition $\Delta V^n(r) = V^n(r) - V^{\mathrm{r},n}(r)$ and the property $G_l^{\mathrm{r}}(r, r'; E) = G_l^{\mathrm{r}}(r', r; E)$, the radial Lippmann-Schwinger equations

$$
\begin{aligned}
R_l^{\mathrm{r},n}(r; E) &= j_l(r; E) + \int r'^2 dr'\, G_l^{\mathrm{r}}(r, r'; E) V^{\mathrm{r},n}(r') R_l^{\mathrm{r},n}(r'; E) \\
&= j_l(r; E) + \int r'^2 dr'\, R_l^{\mathrm{r},n}(r'; E) V^{\mathrm{r},n}(r') G_l^{\mathrm{r}}(r', r; E) \qquad \text{(A.36)}
\end{aligned}
$$

and

$$
R_l^n(r; E) = j_l(r; E) + \int r'^2 dr'\, G_l^{\mathrm{r}}(r, r'; E) V^n(r') R_l^n(r'; E), \qquad \text{(A.37)}
$$

eq. (A.34) can be rewritten as

$$
\begin{aligned}
\Delta t_l^n(E) =& \\
& \int r^2 dr \left[j_l(r; E) + \int r'^2 dr'\, R_l^{\mathrm{r},n}(r'; E) V^{\mathrm{r},n}(r') G_l^{\mathrm{r}}(r', r; E) \right] V^n(r) R_l^n(r; E) \\
& - \int r^2 dr\, R_l^{\mathrm{r},n}(r; E) V^{\mathrm{r},n}(r) \left[j_l(r; E) + \int r'^2 dr'\, G_l^{\mathrm{r}}(r, r'; E) V^n(r') R_l^n(r'; E) \right].
\end{aligned}
$$
$$\text{(A.38)}$$

From that follows

$$
\begin{aligned}
\Delta t_l^n(E) =& \int r^2 dr\, j_l(r; E) V^n(r) R_l^n(r; E) \\
& + \int r^2 dr \int r'^2 dr'\, R_l^{\mathrm{r},n}(r'; E) V^{\mathrm{r},n}(r') G_l^{\mathrm{r}}(r', r; E) V^n(r) R_l^n(r; E) \\
& - \int r^2 dr\, j_l(r; E) V^{\mathrm{r},n}(r) R_l^{\mathrm{r},n}(r; E) \\
& - \int r^2 dr \int r'^2 dr'\, R_l^{\mathrm{r},n}(r; E) V^{\mathrm{r},n}(r) G_l^{\mathrm{r}}(r, r'; E) V^n(r') R_l^n(r'; E).
\end{aligned}
$$
$$\text{(A.39)}$$

The second and the forth term cancel; the first and the third term are just the atomic scattering matrices $t_l^n(E)$ and $t_l^{\mathrm{r},n}(E)$,

$$
\begin{aligned}
\Delta t_l^n(E) &= \int r^2 dr\, j_l(r; E) V^n(r) R_l^n(r; E) - \int r^2 dr\, j_l(r; E) V^{\mathrm{r},n}(r) R_l^{\mathrm{r},n}(r; E) \\
&= t_l^n(E) - t_l^{\mathrm{r},n}(E), \qquad \text{(A.40)}
\end{aligned}
$$

q. e. d..

A.5 Impurity scattering

In this section, we derive the relation of the impurity-wavefunction coefficients $c_{\mathbf{k}L}^{\mathrm{imp},n}$ to the coefficients $c_{\mathbf{k}L}^n$ of the host crystal. As described in chapter 3, section 3.2, we start from the Lippmann-Schwinger-equation 3.51

$$
\begin{aligned}
\psi_{\mathbf{k}}^{\mathrm{imp}}(\mathbf{r} + \mathbf{R}^n; E) =& \\
& \psi_{\mathbf{k}}(\mathbf{r} + \mathbf{R}^n; E) + \sum_{n'} \int d^3 r'\, G(\mathbf{r} + \mathbf{R}^n, \mathbf{r}' + \mathbf{R}^{n'}; E) \Delta V^{n'}(\mathbf{r}') \psi_{\mathbf{k}}^{\mathrm{imp}}(\mathbf{r}' + \mathbf{R}^{n'}) \quad \text{(A.41)}
\end{aligned}
$$

and insert the expansions of the wavefunctions as well as the Green function in terms of spherical harmonics $Y_L(\hat{r})$.

A.5.1 Atomic sphere approximation

In the atomic sphere approximation, the expansion in orbital components is

$$\psi_{\mathbf{k}}^{\mathrm{imp}}(\mathbf{r} + \mathbf{R}^n; E) = \sum_L c_{\mathbf{k}L}^{\mathrm{imp},n} R_l^{\mathrm{imp},n}(r; E) Y_L(\hat{r}), \tag{A.42}$$

and

$$G(\mathbf{r} + \mathbf{R}^n, \mathbf{r}' + \mathbf{R}^{n'}; E) =$$
$$\sum_L G_l^{\mathrm{s},nn}(r, r'; E) Y_L(\hat{r}) Y_L(\hat{r}') \delta_{nn'} + \sum_{LL'} R_L^{\mathrm{n}}(\mathbf{r}; E) G_{LL'}^{nn'}(E) R_{L'}^{n'}(\mathbf{r}'; E), \tag{A.43}$$

where the first term is the solution of the homogeneous system (see e.g. section 2.3, eq. (2.44)) with

$$G_l^{\mathrm{s}}(r, r'; E) = \begin{cases} -i\sqrt{E} R_l(r; E) H_l(r'; E) & \text{for } r \leq r' \\ -i\sqrt{E} R_l(r'; E) H_l(r; E) & \text{for } r > r' \end{cases} . \tag{A.44}$$

The difference in potential is given by

$$\Delta V^n(\mathbf{r}) = \Delta V^n(r) = V^{\mathrm{imp},n}(r) - V^n(r) . \tag{A.45}$$

Inserting the three eqs. (A.42), (A.43) and (A.45) in the Lippmann-Schwinger equation eq. (A.41), the latter equation yields

$$\sum_L c_{\mathbf{k}L}^{\mathrm{imp},n} R_l^{\mathrm{imp},n}(r; E) Y_L(\hat{r}) = \sum_L c_{\mathbf{k}L}^n R_l^n(r; E) Y_L(\hat{r})$$
$$+ \sum_{n'} \int d^3r' \left[\sum_L G_l^{\mathrm{s},nn}(r, r'; E) Y_L(\hat{r}) Y_L(\hat{r}') \delta_{nn'} \Delta V^{n'}(r') \sum_{L'} c_{\mathbf{k}L'}^{\mathrm{imp},n'} R_{l'}^{\mathrm{imp},n'}(r'; E) Y_{L'}(\hat{r}') \right.$$
$$\left. + \sum_{LL'} R_l^n(r; E) Y_L(\hat{r}) G_{LL'}^{nn'}(E) R_{l'}^{n'}(r'; E) Y_{L'}(\hat{r}') \Delta V^{n'}(r') \sum_{L''} c_{\mathbf{k}L''}^{\mathrm{imp},n'} R_{l''}^{\mathrm{imp},n'}(r'; E) Y_{L''}(\hat{r}') \right]. \tag{A.46}$$

Integration over the angles $d\Omega'$ leads to

$$\sum_L c_{\mathbf{k}L}^{\mathrm{imp},n} R_l^{\mathrm{imp},n}(r; E) Y_L(\hat{r}) = \sum_L c_{\mathbf{k}L}^n R_l^n(r; E) Y_L(\hat{r})$$
$$+ \sum_{n'} \int r'^2 dr' \left[\sum_L G_l^{\mathrm{s},nn}(r, r'; E) Y_L(\hat{r}) \delta_{nn'} \Delta V^{n'}(r') c_{\mathbf{k}L}^{\mathrm{imp},n'} R_l^{\mathrm{imp},n'}(r'; E) \right.$$
$$\left. + \sum_{LL'} R_l^n(r; E) Y_L(\hat{r}) G_{LL'}^{nn'}(E) R_{l'}^{n'}(r'; E) \Delta V^{n'}(r') c_{\mathbf{k}L'}^{\mathrm{imp},n'} R_{l'}^{\mathrm{imp},n'}(r'; E) \right], \tag{A.47}$$

or

$$\sum_L c_{\mathbf{k}L}^{\text{imp},n} \left[R_l^{\text{imp},n}(r;E) - \int r'^2 dr' \, G_l^{\text{s},nn}(r,r';E) \Delta V^n(r') R_l^{\text{imp},n}(r';E) \right] Y_L(\hat{r})$$

$$= \sum_L c_{\mathbf{k}L}^n R_l^n(r;E) Y_L(\hat{r})$$

$$+ \sum_{n'} \sum_{LL'} R_l^n(r;E) Y_L(\hat{r}) G_{LL'}^{nn'}(E) c_{\mathbf{k}L'}^{\text{imp},n'}$$

$$\int r'^2 dr' R_{l'}^{n'}(r';E) \Delta V^{n'}(r') R_{l'}^{\text{imp},n'}(r';E) \,, \tag{A.48}$$

respectively.

For the next step, we need the Lippmann-Schwinger equation of the radial wavefunction, which we write in the form

$$R_l^n(r;E) = R_l^{\text{imp},n}(r;E) - \int r'^2 dr' \, G_l^{;nn}(r,r';E) \Delta V^n(r') R_l^{\text{imp},n}(r';E) \,. \tag{A.49}$$

The right-hand side of eq. (A.49) is just the term in brackets of eq. (A.48). Replacing this by $R_l^n(r;E)$, we obtain

$$\sum_L c_{\mathbf{k}L}^{\text{imp},n} R_l^n(r;E) Y_L(\hat{r}) = \sum_L c_{\mathbf{k}L}^n R_l^n(r;E) Y_L(\hat{r})$$

$$+ \sum_{n'} \sum_{LL'} R_l^n(r;E) Y_L(\hat{r}) G_{LL'}^{nn'}(E) c_{\mathbf{k}L'}^{\text{imp},n'} \int r'^2 dr' R_{l'}^{n'}(r';E) \Delta V^{n'}(r') R_{l'}^{\text{imp},n'}(r';E) \,. \tag{A.50}$$

Using the Δt-matrix, eqs. (A.34) and (A.35), the latter equation (A.50) further simplifies to

$$\sum_L c_{\mathbf{k}L}^{\text{imp},n} R_l^n(r;E) Y_L(\hat{r}) =$$

$$\sum_L c_{\mathbf{k}L}^n R_l^n(r;E) Y_L(\hat{r}) + \sum_{n'} \sum_{LL'} R_l^n(r;E) Y_L(\hat{r}) G_{LL'}^{nn'}(E) \Delta t_{l'}^{n'}(E) c_{\mathbf{k}L'}^{\text{imp},n'} \,. \tag{A.51}$$

The above equation is fulfilled, if each coefficient satisfies

$$c_{\mathbf{k}L}^{\text{imp},n} = c_{\mathbf{k}L}^n + \sum_{n'} \sum_{L'} G_{LL'}^{nn'}(E) \Delta t_{l'}^{n'}(E) c_{\mathbf{k}L'}^{\text{imp},n'} \,, \tag{A.52}$$

or

$$\sum_{n'} \sum_{L'} \left(\delta_{LL'} \delta_{nn'} - G_{LL'}^{nn'}(E) \Delta t_{l'}^{n'}(E) \right) c_{\mathbf{k}L'}^{\text{imp},n'} = c_{\mathbf{k}L}^n, \tag{A.53}$$

respectively. Therefore, we finally obtain the sought-after expression for the impurity coefficients

$$c_{\mathbf{k}L}^{\text{imp},n} = \left[\sum_{n',L'} \left(\delta_{LL'} \delta_{nn'} - G_{LL'}^{nn'}(E) \Delta t_{l'}^{n'}(E) \right) \right]^{-1} c_{\mathbf{k}L'}^{n'}. \tag{A.54}$$

A.5.2 Full potential

Dealing with the full potential entails a more cumbersome derivation of the relation between the perturbed and the unperturbed coefficients $c_{\mathbf{k}L}^{\mathrm{imp},n}$ and $c_{\mathbf{k}L}^{n}$, although the derivation leads to a very similar expression as obtained in the atomic sphere approximation. The enhanced complexity is due to the fact that scattering from one orbital with angular momentum L to another orbital characterized by L' is no longer forbidden; therefore, we end up with a non-spherical atomic scattering t-matrix $t_{LL'}$, corresponding to the expansion of the potential in L and L' ($V_{LL'}(r)$).

Hence, inserting the expression for the wavefunctions

$$\psi_{\mathbf{k}}(\mathbf{r} + \mathbf{R}^{n}) = \sum_{LL'} c_{\mathbf{k}L}^{n} R_{L'L}^{n}(r; E) Y_{L'}(\hat{r}), \tag{A.55}$$

the potential

$$\Delta V^{n'}(\mathbf{r}') = \sum_{L} \Delta V_{L}^{n'}(r') Y_{L}(\hat{r}) \tag{A.56}$$

and the Green function

$$
\begin{aligned}
G(\mathbf{r} + \mathbf{R}^{n}, \mathbf{r}' + \mathbf{R}^{n'}; E) \\
&= -i\sqrt{E} \sum_{L} R_{L}^{n}(\mathbf{r}_{<}; E) H_{L}^{n}(\mathbf{r}_{>}; E) + \sum_{n'} \sum_{LL'} R_{L}^{n}(\mathbf{r}; E) G_{LL'}^{nn'}(E) R_{L'}^{n'}(\mathbf{r}'; E) \\
&= -i\sqrt{E} \sum_{LL'L''} R_{L'L}^{n}(r_{<}; E) Y_{L'}(\hat{r}_{>}) H_{L''L}^{n}(r_{>}; E) Y_{L''}(\hat{r}_{>}) \\
&\quad + \sum_{n'} \sum_{LL'L''L'''} Y_{L''}(\hat{r}) R_{L''L}^{n}(r; E) G_{LL'}^{nn'}(E) R_{L'''L'}^{n'}(r'; E) Y_{L'''}(\hat{r}')
\end{aligned}
\tag{A.57}
$$

into the Lippmann-Schwinger equation

$$
\begin{aligned}
\psi_{\mathbf{k}}^{\mathrm{imp}}(\mathbf{r} + \mathbf{R}^{n}; E) = \psi_{\mathbf{k}}(\mathbf{r} + \mathbf{R}^{n}; E) \\
&+ \sum_{n'} \int d^{3}r'\, G(\mathbf{r} + \mathbf{R}^{n}, \mathbf{r}' + \mathbf{R}^{n'}; E) \Delta V^{n'}(\mathbf{r}') \psi_{\mathbf{k}}^{\mathrm{imp}}(\mathbf{r}' + \mathbf{R}^{n'})\,,
\end{aligned}
\tag{A.58}
$$

which provides the basis for the derivation results in

$$
\begin{aligned}
\sum_{LL'} c_{\mathbf{k}L}^{\mathrm{imp},n} R_{L'L}^{\mathrm{imp},n}(r; E) Y_{L'}(\hat{r}) &= \sum_{LL'} c_{\mathbf{k}L}^{n} R_{L'L}^{n}(r; E) Y_{L'}(\hat{r}) \\
&+ \int d^{3}r' \sum_{L'L''} Y_{L'}(\hat{r}) G_{L'L''}^{\mathrm{s},nn}(r, r'; E) Y_{L''}(\hat{r}') \sum_{L'''} \Delta V_{L'''}^{n}(r') Y_{L'''}(\hat{r}') \\
&\qquad\qquad \sum_{L''''L} c_{\mathbf{k}L}^{\mathrm{imp},n} R_{L''''L}^{\mathrm{imp},n}(r'; E) Y_{L''''}(\hat{r}') \\
&+ \sum_{n'} \int d^{3}r' \sum_{L'L'''} \sum_{L''L''''} R_{L'L''}^{n}(r; E) Y_{L'}(\hat{r}) G_{L''L'''}^{nn'}(E) R_{L'''L''''}^{n'}(r'; E) Y_{L'''}(\hat{r}') \\
&\qquad\qquad \sum_{L''''} \Delta V_{L''''}^{n'}(r') Y_{L''''}(\hat{r}') \sum_{LL''''''} c_{\mathbf{k}L}^{\mathrm{imp},n'} R_{L''''''L}^{\mathrm{imp},n'}(r'; E) Y_{L''''''}(\hat{r}').
\end{aligned}
\tag{A.59}
$$

In analogy to the previous section A.5.1, eq. (A.44), we have used the abbreviation

$$G^{s,nn'}_{L'L''}(r,r';E) = -i\sqrt{E}\sum_L R_{L'L}(r_<;E)H_{L''L}(r_>;E) \, . \tag{A.60}$$

As already mentioned in chapter 3, in a first step the integration over the solid angles $d\Omega'$ is performed; the integral over the three spherical harmonics $Y_{L''}(\hat{r}')$, $Y_{L'''}(\hat{r}')$ and $Y_{L''''}(\hat{r}')$ (or $Y_{L'''}(\hat{r}')$, $Y_{L''''}(\hat{r}')$ and $Y_{L'''''}(\hat{r}')$ for the second summand) yields the Gaunt coefficients $C_{L''L'''L''''}$ (or $C_{L'''L''''L'''''}$, respectively). Combining them with the potential $\Delta V^n_L(r)$ brings us to the definition of the potential $\Delta V^n_{LL'}(r)$

$$\sum_{L''} C_{LL'L''}\Delta V^n_{L''}(r') = \Delta V^n_{LL'}(r'). \tag{A.61}$$

With these simplifications, the Lippmann-Schwinger equation (A.59) results in

$$\begin{aligned}
\sum_{L'}Y_{L'}(\hat{r})\sum_L c^{\text{imp},n}_{\mathbf{k}L} R^{\text{imp},n}_{L'L}(r;E) &= \sum_{L'}Y_{L'}(\hat{r})\sum_L c^n_{\mathbf{k}L} R^n_{L'L}(r;E) \\
&+ \sum_{L'}Y_{L'}(\hat{r})\int r'^2 dr' \sum_{LL''L''''} G^{s,nn}_{L'L''}(r,r';E)\Delta V^n_{L''L'''}(r')c^{\text{imp},n}_{\mathbf{k}L} R^{\text{imp},n}_{L'''L}(r';E) \\
&+ \sum_{L'}Y_{L'}(\hat{r})\sum_{n'}\int r'^2 dr' \sum_{LL''L'''L''''} R^n_{L'L''}(r;E)G^{nn'}_{L''L'''}(E)R^{n'}_{L'''L''''}(r';E) \\
&\qquad \sum_{L'''''} \Delta V^{n'}_{L''''L'''''}(r')c^{\text{imp},n'}_{\mathbf{k}L} R^{\text{imp},n'}_{L'''''L}(r';E) \, .
\end{aligned} \tag{A.62}$$

Since the spherical harmonics are linearly independent, the sum over L' and the multiplication with $Y_{L'}(\hat{r})$ can be left out, and we obtain

$$\begin{aligned}
\sum_L c^{\text{imp},n}_{\mathbf{k}L} R^{\text{imp},n}_{L'L}(r;E) &= \sum_L c^n_{\mathbf{k}L} R^n_{L'L}(r;E) \\
&+ \int r'^2 dr' \sum_{LL''L''''} G^{s,nn}_{L'L''}(r,r';E)\Delta V^n_{L''L'''}(r')c^{\text{imp},n}_{\mathbf{k}L} R^{\text{imp},n}_{L'''L}(r';E) \\
&+ \sum_{n'}\int r'^2 dr' \sum_{LL''L'''L''''} R^n_{L'L''}(r;E)G^{nn'}_{L''L'''}(E)R^{n'}_{L'''L''''}(r';E) \\
&\qquad \sum_{L'''''} \Delta V^{n'}_{L''''L'''''}(r')c^{\text{imp},n'}_{\mathbf{k}L} R^{\text{imp},n'}_{L'''''L}(r';E) \, . \quad \tag{A.63}
\end{aligned}$$

Similar as in the previous section A.5.1, we rewrite the Lippmann-Schwinger equation for the radial wavefunctions $R^{\text{imp},n}_{L'L}(r;E)$, the regular solutions of the Schrödinger equation, (see Appendix A.3, eq. (A.31)) as

$$R^n_{L'L}(r;E) = R^{\text{imp},n}_{L'L}(r;E) - \int r'^2 dr' \sum_{L''L''''} G^{s,nn}_{L'L''}(r,r';E)\Delta V^n_{L''L'''}(r')R^{\text{imp},n}_{L'''L}(r';E) \, . \tag{A.64}$$

It can be used to subsume the term on the left-hand side of eq. (A.63) with the term on the right-hand side containing the single-site Green function, yielding

$$
\sum_L c_{\mathbf{k}L}^{\mathrm{imp},n} R_{L'L}^n(r;E) = \sum_L c_{\mathbf{k}L}^n R_{L'L}^n(r;E)
$$
$$
+ \sum_{n'} \int r'^2 dr' \sum_{LL''L'''L''''} R_{L'L''}^n(r;E) G_{L''L'''}^{nn'}(E) R_{L'''L''''}^{n'}(r';E)
$$
$$
\sum_{L'''''} \Delta V_{L'''L'''''}^{n'}(r') c_{\mathbf{k}L}^{\mathrm{imp},n'} R_{L'''''L}^{\mathrm{imp},n'}(r';E) . \quad \text{(A.65)}
$$

The last term on the right-hand side contains the atomic scattering matrix

$$
\Delta t_{L'''L}^n = \int r'^2 dr' \sum_{L'''L'''''} R_{L'''L'''}^n(r';E) \Delta V_{L''L'''''}^n(r') R_{L'''''L}^{\mathrm{imp},n}(r';E) \quad \text{(A.66)}
$$

and hence equation (A.65) becomes

$$
\sum_L c_{\mathbf{k}L}^{\mathrm{imp},n} R_{L'L}^n(r;E) = \sum_L c_{\mathbf{k}L}^n R_{L'L}^n(r;E)
$$
$$
+ \sum_{n'} \sum_L \sum_{L''L''''} R_{L'L''}^n(r;E) G_{L''L'''}^{nn'}(E) \Delta t_{L'''L}^{n'} c_{\mathbf{k}L}^{\mathrm{imp},n'} . \quad \text{(A.67)}
$$

The above equation is satisfied, if each summand of the sum over L fulfills

$$
c_{\mathbf{k}L}^{\mathrm{imp},n} = c_{\mathbf{k}L}^n + \sum_{n'} \sum_{L'L''} G_{LL'}^{nn'}(E) \Delta t_{L'L''}^{n'} c_{\mathbf{k}L''}^{\mathrm{imp},n'} . \quad \text{(A.68)}
$$

A.6 Calculation of the Green function $G_{LL'}^{\mathrm{imp},nn'}$ at E_F

Although the impurity Green function $G_{LL'}^{\mathrm{imp},nn'}$[2] is well behaved at real energy E_F, its calculation via the Dyson equation becomes problematic, as the host Green function has poles at real E_F. A way out of this problem is to exploit the fact, that the Green function is analytic for imaginary energies.

The Green function at the (real) Fermi energy can be expanded in a Taylor series according to

$$
G^{\mathrm{imp}}(E_\mathrm{F}) \approx G^{\mathrm{imp}}(E_\mathrm{F} + i\Gamma) + (-i\Gamma) G^{\mathrm{imp}'}(E_\mathrm{F} + i\Gamma) + \frac{1}{2}(-i\Gamma)^2 G^{\mathrm{imp}''}(E_\mathrm{F} + i\Gamma). \quad \text{(A.69)}
$$

For its evaluation we need the first and the second derivative of G at the complex energy $E_F + i\Gamma$. A numerical approximation of the first derivation is given by

$$
G^{\mathrm{imp}'}(E_\mathrm{F} + i\Gamma) \approx \frac{G^{\mathrm{imp}}(E_\mathrm{F} + i\Gamma + z) - G^{\mathrm{imp}}(E_\mathrm{F} + i\Gamma - z)}{2z}, \quad \text{(A.70)}
$$

---

[2]The Green function either of the unperturbed or the perturbed system is needed to calculate the impurity coefficients $c_{\mathbf{k}L}^{\mathrm{imp}}$ as well as the scattering matrix $T_{\mathbf{k}\mathbf{k}'}$ and consequently the lifetime $\tau_{\mathbf{k}}$.

and of the second derivative by

$$G^{\text{imp}''}(E_F + i\Gamma) \approx \frac{G^{\text{imp}}(E_{\text{F}} + i\Gamma + z) - 2G^{\text{imp}}(E_{\text{F}} + i\Gamma) + G(E_{\text{F}} + i\Gamma - z)}{z^2}. \quad \text{(A.71)}$$

At this point, the analycity of the Green function is required, because under this condition it does not matter whether z is a real or a complex number. Choosing z to be real, the two derivatives (and the Green function itself, too) can be calculated just with the Green function at the three energies $E_{\text{F}} + i\Gamma$, $E_{\text{F}} + i\Gamma + z$ and $E_{\text{F}} + i\Gamma - z$ (lying on a line parallel to the real energy axis).

Evaluation of L · S in terms of real spherical harmonics

In order to calculate the action of the three orbital-momentum operators L_+, L_- and L_z on real spherical harmonics $Y_L(\hat{r})$, the results of eqs. (4.33), (4.35) and (4.36), namely the action of the above operators on the basis set of complex spherical harmonics $\mathcal{Y}_L(\hat{r})$, as well as the transformations from one basis set to the other (eqs. (4.38) and (4.39)) are required. In matrix notation, these transformations become

$$|Y_{lm}\rangle \;=\; \sum_{m'} U_{mm'} |\mathcal{Y}_{lm'}\rangle \qquad \text{or} \tag{B.1}$$

$$|\mathcal{Y}_{lm}\rangle \;=\; \sum_{m'} U^{\dagger}_{mm'} |Y_{lm'}\rangle \;, \tag{B.2}$$

respectively, where the matrices U and $U^{\dagger}$ are given by

$$U = \begin{pmatrix}
\frac{i}{\sqrt{2}} & 0 & \cdots & 0 & \cdots & 0 & -\frac{(-1)^l i}{\sqrt{2}} \\
0 & \frac{i}{\sqrt{2}} & \cdots & 0 & \cdots & -\frac{(-1)^{l-1} i}{\sqrt{2}} & 0 \\
\vdots & \vdots & \ddots & \vdots & \iddots & \vdots & \vdots \\
0 & 0 & \cdots & 1 & \cdots & 0 & 0 \\
\vdots & \vdots & \iddots & \vdots & \ddots & \vdots & \vdots \\
0 & \frac{1}{\sqrt{2}} & \cdots & 0 & \cdots & \frac{(-1)^{l-1}}{\sqrt{2}} & 0 \\
\frac{1}{\sqrt{2}} & 0 & \cdots & 0 & \cdots & 0 & \frac{(-1)^l}{\sqrt{2}}
\end{pmatrix} \tag{B.3}$$

and

$$
U^{\dagger} =
\begin{pmatrix}
\frac{1}{\sqrt{2}i} & 0 & \cdots & 0 & \cdots & 0 & \frac{1}{\sqrt{2}} \\
0 & \frac{1}{\sqrt{2}i} & \cdots & 0 & \cdots & \frac{1}{\sqrt{2}} & 0 \\
\vdots & \vdots & \ddots & \vdots & \iddots & \vdots & \vdots \\
0 & 0 & \cdots & 1 & \cdots & 0 & 0 \\
\vdots & \vdots & \iddots & \vdots & \ddots & \vdots & \vdots \\
0 & \frac{(-1)^{l-1}i}{\sqrt{2}} & \cdots & 0 & \cdots & \frac{(-1)^{l-1}}{\sqrt{2}} & 0 \\
\frac{(-1)^{l}i}{\sqrt{2}} & 0 & \cdots & 0 & \cdots & 0 & \frac{(-1)^{l}}{\sqrt{2}}
\end{pmatrix}.
\tag{B.4}
$$

These transformation matrices can be used to transform a matrix $\hat{M}$ from the basis set of complex spherical harmonics $(M_{mm'}^{\mathrm{C}})$ to that of real spherical harmonics $(M_{mm'}^{\mathrm{R}})$ following

$$
\begin{aligned}
M_{mm'}^{\mathrm{R}} = \langle Y_{lm} | \hat{M} | Y_{lm'} \rangle &= \sum_{m_1, m_2} \langle Y_{lm} | \mathcal{Y}_{lm_1} \rangle \langle \mathcal{Y}_{lm_1} | \hat{M} | \mathcal{Y}_{lm_2} \rangle \langle \mathcal{Y}_{lm_2} | Y_{lm'} \rangle \\
&= \sum_{m_1, m_2} U_{m_1 m}^{\dagger} M_{m_1 m_2}^{\mathrm{C}} U_{m' m_2} \\
&= \sum_{m_1, m_2} \left(U^{\dagger} \right)_{m_1 m} M_{m_1 m_2}^{\mathrm{C}} \left(U^{T} \right)_{m_2 m'}.
\end{aligned}
\tag{B.5}
$$

We can now apply the three angular momentum operators L_z, L_+ and L_- on the real spherical harmonics. Starting with L_z, we obtain

$$
\begin{aligned}
L_z Y_{l,-m} &= \frac{i}{\sqrt{2}} \left[L_z \mathcal{Y}_{l,-m} - (-1)^m L_z \mathcal{Y}_{lm} \right] \\
&= \frac{i}{\sqrt{2}} \left[-m \mathcal{Y}_{l,-m} - m(-1)^m \mathcal{Y}_{lm} \right] \\
&= -mi \frac{1}{\sqrt{2}} \left[\mathcal{Y}_{l,-m} + (-1)^m \mathcal{Y}_{lm} \right] \\
&= -mi \, Y_{l,m}
\end{aligned}
\tag{B.6}
$$

and

$$
\begin{aligned}
L_z Y_{l,m} &= \frac{1}{\sqrt{2}} \left[L_z \mathcal{Y}_{l,-m} + (-1)^m L_z \mathcal{Y}_{lm} \right] \\
&= \frac{1}{\sqrt{2}} \left[-m \mathcal{Y}_{l,-m} + m(-1)^m \mathcal{Y}_{lm} \right] \\
&= -\frac{m}{i} \frac{i}{\sqrt{2}} \left[\mathcal{Y}_{l,-m} - (-1)^m \mathcal{Y}_{lm} \right] \\
&= mi \, Y_{l,-m}.
\end{aligned}
\tag{B.7}
$$

Therefore, the matrix $\langle Y_{lm} | L_z | Y_{l'm'} \rangle$ becomes

$$
\langle Y_{lm} | L_z | Y_{l'm'} \rangle = -im \, \delta_{ll'} \delta_{m,-m'},
\tag{B.8}
$$

or, in matrix notation

$$\langle Y_{lm}|L_z|Y_{lm'}\rangle = \begin{pmatrix} 0 & & & \cdots & & 0 & il \\ & & & & & i(l-1) & 0 \\ & & \ddots & & \iddots & & \\ \vdots & & & 0 & & & \vdots \\ & & \iddots & & \ddots & & \\ 0 & -i(l-1) & & & & & \\ -il & 0 & & \cdots & & & 0 \end{pmatrix}. \tag{B.9}$$

Application of the raising operator for $m \geq 2$ leads to

$$\begin{aligned} L_+Y_{l,-m} &= \frac{i}{\sqrt{2}} \left[L_+\mathcal{Y}_{l,-m} - (-1)^m L_+\mathcal{Y}_{lm} \right] \\ &= \frac{i}{\sqrt{2}} \left[\sqrt{l(l+1)+m(-m+1)}\mathcal{Y}_{l,-m+1} - (-1)^m\sqrt{l(l+1)-m(m+1)}\mathcal{Y}_{l,m+1} \right] \\ &= \frac{i}{\sqrt{2}} \left[\sqrt{l(l+1)+m(-m+1)}\left(\frac{1}{\sqrt{2}i}Y_{l,-m+1} + \frac{1}{\sqrt{2}}Y_{l,m-1} \right) \right. \\ &\quad \left. -(-1)^m\sqrt{l(l+1)-m(m+1)}\left(\frac{(-1)^{m+1}}{\sqrt{2}}Y_{l,m+1} + \frac{(-1)^{-(m+1)}i}{\sqrt{2}}Y_{l,-(m+1)} \right) \right] \\ &= \sqrt{l(l+1)+m(-m+1)}\left[\frac{1}{2}Y_{l,-m+1} + \frac{i}{2}Y_{l,m-1} \right] + \\ &\quad \sqrt{l(l+1)-m(m+1)}\left[\frac{i}{2}Y_{l,m+1} - \frac{1}{2}Y_{l,-(m+1)} \right]. \tag{B.10} \end{aligned}$$

For $m = -1$, we obtain

$$\begin{aligned} L_+Y_{l,-1} &= \frac{i}{\sqrt{2}} \left[L_+\mathcal{Y}_{l,1} + L_+\mathcal{Y}_{l,-1} \right] \\ &= \frac{i}{\sqrt{2}} \sqrt{l(l+1)}Y_{l,0} + \sqrt{l(l+1)-2}\left[\frac{i}{2}Y_{l,2} - \frac{1}{2}Y_{l,-2} \right], \tag{B.11} \end{aligned}$$

for $m = 0$

$$\begin{aligned} L_+Y_{l,0} &= L_+\mathcal{Y}_{l,0} \\ &= \sqrt{l(l+1)}\mathcal{Y}_{l,1} \\ &= \sqrt{l(l+1)}\left[\frac{-1}{\sqrt{2}}\left(Y_{l,1} + iY_{l,-1} \right) \right], \tag{B.12} \end{aligned}$$

for $m = 1$

$$\begin{aligned} L_+Y_{l,1} &= \frac{1}{\sqrt{2}} \left[L_+\mathcal{Y}_{l,-1} - L_+\mathcal{Y}_{l,1} \right] \\ &= \frac{\sqrt{l(l+1)}Y_{l,0}}{\sqrt{2}} + \sqrt{l(l+1)-2}\left[-\frac{1}{2}Y_{l,2} - \frac{i}{2}Y_{l,-2} \right] \tag{B.13} \end{aligned}$$

and, finally, for $m \geq 2$

$$
\begin{aligned}
L_+ Y_{l,m} &= \frac{1}{\sqrt{2}} \left[L_+ \mathcal{Y}_{l,-m} + (-1)^m L_+ \mathcal{Y}_{lm} \right] \\
&= \frac{1}{\sqrt{2}} \left[\sqrt{l(l+1) + m(-m+1)} \mathcal{Y}_{l,-m+1} + (-1)^m \sqrt{l(l+1) - m(m+1)} \mathcal{Y}_{l,m+1} \right] \\
&= \frac{1}{\sqrt{2}} \left[\sqrt{l(l+1) + m(-m+1)} \left(\frac{1}{\sqrt{2}i} Y_{l,-m+1} + \frac{1}{\sqrt{2}} Y_{l,m-1} \right) \right. \\
&\qquad \left. + (-1)^m \sqrt{l(l+1) - m(m+1)} \left(\frac{(-1)^{m+1}}{\sqrt{2}} Y_{l,m+1} + \frac{(-1)^{-(m+1)} i}{\sqrt{2}} Y_{l,-(m+1)} \right) \right] \\
&= \sqrt{l(l+1) + m(-m+1)} \left[\frac{1}{2i} Y_{l,-m+1} + \frac{1}{2} Y_{l,m-1} \right] + \\
&\qquad \sqrt{l(l+1) - m(m+1)} \left[-\frac{1}{2} Y_{l,m+1} - \frac{i}{2} Y_{l,-(m+1)} \right]. \tag{B.14}
\end{aligned}
$$

Thus, the matrix takes the form

$$
\left\langle Y_{lm} | L_+ | Y_{lm'} \right\rangle =
$$

$$
\begin{pmatrix}
0 & -\frac{\sqrt{2l}}{2} & 0 & & \cdots & & & 0 & -\frac{i\sqrt{2l}}{2} & 0 \\
\frac{\sqrt{2l}}{2} & 0 & -\frac{\sqrt{4l-2}}{2} & & & & & -\frac{i\sqrt{4l-2}}{2} & 0 & -\frac{i\sqrt{2l}}{2} \\
0 & \ddots & \ddots & \ddots & & & & \iddots & \iddots & \iddots & 0 \\
& & & 0 & -\frac{i\sqrt{l(l+1)}}{\sqrt{2}} & 0 & & & & \\
\vdots & & & \frac{i\sqrt{l(l+1)}}{\sqrt{2}} & 0 & \frac{\sqrt{l(l+1)}}{\sqrt{2}} & & & & \vdots \\
& & & 0 & -\frac{\sqrt{l(l+1)}}{\sqrt{2}} & 0 & & & & \\
0 & \iddots & \iddots & \iddots & & & & \ddots & \ddots & \ddots & 0 \\
\frac{i\sqrt{2l}}{2} & 0 & \frac{i\sqrt{4l-2}}{2} & & & & & -\frac{\sqrt{4l-2}}{2} & 0 & \frac{\sqrt{2l}}{2} \\
0 & \frac{i\sqrt{2l}}{2} & 0 & & \cdots & & & 0 & -\frac{\sqrt{2l}}{2} & 0
\end{pmatrix}.
$$

$$\tag{B.15}$$

For the lowering operator we obtain analogously, setting $m \geq 2$,

$$
\begin{aligned}
L_- Y_{l,-m} &= \frac{i}{\sqrt{2}} \left[L_- \mathcal{Y}_{l,-m} - (-1)^m L_- \mathcal{Y}_{lm} \right] \\
&= \frac{i}{\sqrt{2}} \left[\sqrt{l(l+1) + m(-m-1)}\mathcal{Y}_{l,-m-1} - (-1)^m \sqrt{l(l+1) - m(m-1)}\mathcal{Y}_{l,m-1} \right] \\
&= \frac{i}{\sqrt{2}} \left[\sqrt{l(l+1) + m(-m-1)} \left(\frac{1}{\sqrt{2}i} Y_{l,-m-1} + \frac{1}{\sqrt{2}} Y_{l,m+1} \right) \right. \\
&\qquad \left. -(-1)^m \sqrt{l(l+1) - m(m-1)} \left(\frac{(-1)^{m-1}}{\sqrt{2}} Y_{l,m-1} + \frac{(-1)^{-(m-1)}i}{\sqrt{2}} Y_{l,-m+1} \right) \right] \\
&= \sqrt{l(l+1) - m(m+1)} \left[\frac{1}{2} Y_{l,-m-1} + \frac{i}{2} y_{l,m+1} \right] + \\
&\qquad \sqrt{l(l+1) - m(m-1)} \left[\frac{i}{2} Y_{l,m-1} - \frac{1}{2} Y_{l,-m+1} \right], \quad (\text{B.16})
\end{aligned}
$$

$$
\begin{aligned}
L_- Y_{l,-1} &= \frac{i}{\sqrt{2}} \left[L_- \mathcal{Y}_{l,1} - L_- \mathcal{Y}_{l,-1} \right] \\
&= \frac{i}{\sqrt{2}} \sqrt{l(l+1)} Y_{l,0} + \sqrt{l(l+1) - 2} \left[\frac{i}{2} Y_{l,2} + \frac{1}{2} Y_{l,-2} \right], \quad (\text{B.17})
\end{aligned}
$$

$$
\begin{aligned}
L_- Y_{l,0} &= L_- \mathcal{Y}_{l,0} \\
&= \sqrt{l(l+1)}\mathcal{Y}_{l,-1} \\
&= \sqrt{l(l+1)} \left[\frac{1}{\sqrt{2}} (Y_{l,1} - i Y_{l,-1}) \right] \quad (\text{B.18})
\end{aligned}
$$

$$
\begin{aligned}
L_- Y_{l,+1} &= \frac{1}{\sqrt{2}} \left[L_- \mathcal{Y}_{l,-1} - L_- \mathcal{Y}_{l,1} \right] \\
&= \frac{-1}{\sqrt{2}} \sqrt{l(l+1)} Y_{l,0} + \sqrt{l(l+1) - 2} \left[\frac{1}{2} Y_{l,2} - \frac{i}{2} Y_{l,-2} \right], \quad (\text{B.19})
\end{aligned}
$$

and

$$
\begin{aligned}
L_- Y_{l,m} &= \frac{1}{\sqrt{2}} \left[L_- \mathcal{Y}_{l,-m} + (-1)^m L_- \mathcal{Y}_{lm} \right] \\
&= \frac{1}{\sqrt{2}} \left[\sqrt{l(l+1) + m(-m-1)}\mathcal{Y}_{l,-m-1} + (-1)^m \sqrt{l(l+1) - m(m-1)}\mathcal{Y}_{l,m-1} \right] \\
&= \frac{1}{\sqrt{2}} \left[\sqrt{l(l+1) + m(-m-1)} \left(\frac{1}{\sqrt{2}i} Y_{l,-m-1} + \frac{1}{\sqrt{2}} Y_{l,m+1} \right) \right. \\
&\qquad \left. +(-1)^m \sqrt{l(l+1) - m(m-1)} \left(\frac{(-1)^{m-1}}{\sqrt{2}} Y_{l,m-1} + \frac{(-1)^{-(-m+1)}i}{\sqrt{2}} Y_{l,-m+1} \right) \right] \\
&= \sqrt{l(l+1) - m(m+1)} \left[\frac{1}{2i} Y_{l,-(m+1)} + \frac{1}{2} Y_{l,m+1} \right] + \\
&\qquad \sqrt{l(l+1) - m(m-1)} \left[-\frac{1}{2} Y_{l,m-1} - \frac{i}{2} Y_{l,-m+1} \right]. \quad (\text{B.20})
\end{aligned}
$$

Similar to the raising operator, the matrix of the lowering operator $\langle Y_{lm}|L_-|Y_{l'm'}\rangle$ in terms of real spherical harmonics finally becomes

$$\langle Y_{lm}|L_-|Y_{lm'}\rangle =$$

$$\begin{pmatrix} 0 & \frac{\sqrt{2l}}{2} & 0 & & \cdots & & 0 & -\frac{i\sqrt{2l}}{2} & 0 \\ -\frac{\sqrt{2l}}{2} & 0 & \frac{\sqrt{4l-2}}{2} & & & & -\frac{i\sqrt{4l-2}}{2} & 0 & -\frac{i\sqrt{2l}}{2} \\ 0 & \ddots & \ddots & \ddots & & & \iddots & \iddots & \iddots & 0 \\ & & & 0 & -\frac{i\sqrt{l(l+1)}}{\sqrt{2}} & 0 & & \\ \vdots & & & \frac{i\sqrt{l(l+1)}}{\sqrt{2}} & 0 & -\frac{\sqrt{l(l+1)}}{\sqrt{2}} & & & \vdots \\ & & & 0 & \frac{\sqrt{l(l+1)}}{\sqrt{2}} & 0 & & \\ 0 & \iddots & \iddots & \iddots & & & \ddots & \ddots & \ddots & 0 \\ \frac{i\sqrt{2l}}{2} & 0 & \frac{i\sqrt{4l-2}}{2} & & & & \frac{\sqrt{4l-2}}{2} & 0 & -\frac{\sqrt{2l}}{2} \\ 0 & \frac{i\sqrt{2l}}{2} & 0 & & \cdots & & 0 & \frac{\sqrt{2l}}{2} & 0 \end{pmatrix}.$$

$$(B.21)$$

However, it would not be necessary to evaluate the matrix $\langle Y_{lm}|L_-|Y_{lm'}\rangle$ as we did, since the raising and the lowering operator are adjunct to each other, i.e.

$$L_+^\dagger = L_- \quad \text{and} \tag{B.22}$$
$$L_-^\dagger = L_+ . \tag{B.23}$$

Hence, as can be verified easily considering eq. (B.15) and eq. (B.21), the equality

$$\langle Y_{lm}|L_-|Y_{lm'}\rangle = \langle Y_{lm'}|L_+|Y_{lm}\rangle^\star \tag{B.24}$$

holds.

Tight-binding formalism for spin-flip scattering due to spin-orbit coupling

The results for the momentum and spin-relaxation times caused by scattering at impurities as presented in chapter 6 led to quite unexpected results, as they do not fulfill the previously expected symmetry properties. We assumed previously that $\tau_{\mathbf{k}}^{\sigma\sigma'}$ equals $\tau_{-\mathbf{k}}^{-\sigma-\sigma'}$ for reasons of time-inversion symmetry. As shown in chapter 6, section 6.2 at the example of a Nickel impurity in copper bulk (see table 6.1) this is not the case if non-spherical contributions of the potential are taken into account or if more than one impurity is considered. Therefore, a simple tight-binding model for spin-flip scattering due to spin-orbit coupling was developed in order to examine the symmetry properties of $\tau_{\mathbf{k}}^{\sigma\sigma'}$ and to test whether the results calculated with the KKR program are correct.

In the first section, the basic ideas of the formalism will be presented, while in the second section some results obtained within this model are discussed.

C.1 Basic ideas

C.1.1 The spin-orbit Hamiltonian in the tight-binding formalism and its eigenstates

In real space, the basis functions $|\sigma L \mathbf{R}\rangle$ are characterized by the spin index σ, the lattice site $\mathbf{R}$ and the angular momentum L. In order to keep the formalism as simple as possible we restrict our consideration to s and p orbitals, thus choose $L \in (s, p_x, p_y, p_z)$.

The total Hamiltonian is composed of an atomic part H_{at} and the hopping part H_{hop},

$$H = H_{\mathrm{at}} + H_{\mathrm{hop}}. \tag{C.1}$$

In real space, the atomic part of the Hamiltonian at each lattice point $\mathbf{R}$ is

$$
\begin{aligned}
H_{\mathrm{at}}(\mathbf{R}) = {} & \sum_{L\sigma} |\sigma L \mathbf{R}\rangle \langle \sigma L \mathbf{R}| \, \epsilon_L \\
& + \frac{1}{2} \sum_{LL'\sigma\sigma'} \left(\xi_{LL'\sigma\sigma'} |\sigma L \mathbf{R}\rangle \langle \sigma' L' \mathbf{R}| + \xi_{LL'\sigma\sigma'} |\sigma' L' \mathbf{R}\rangle \langle \sigma L \mathbf{R}| \right),
\end{aligned}
\tag{C.2}
$$

where $\xi_{LL'\sigma\sigma'} := \xi \, (\mathbf{L} \cdot \mathbf{S})_{LL'\sigma\sigma'}$ is the on-site matrix element of the spin-orbit Hamiltonian and the parameter ξ determines the magnitude of the spin-orbit coupling.

For simplicity, we confine ourselves to simple cubic crystal structures and nearest neighbor hopping

$$
H_{\mathrm{hop}} = \delta_{\sigma\sigma'} \sum_{\mathbf{R}L} \sum_{\mathbf{R}'L'} t_{LL'} \, |\sigma L \mathbf{R}\rangle \langle \sigma' L' \mathbf{R}'| \, ,
\tag{C.3}
$$

thus the sum over $\mathbf{R}'$ comprises the nearest neighbors only. $t_{LL'}$ is the hopping matrix element which quantifies the hopping from the orbital L at lattice site $\mathbf{R}$ to L' at the neighboring site $\mathbf{R}'$.

A change of representation to $\mathbf{k}$-space makes it useful to define Bloch functions

$$
|\sigma L \mathbf{k}\rangle = \frac{1}{\sqrt{N}} \sum_{\mathbf{R}} e^{i\mathbf{k}\cdot\mathbf{R}} |\sigma L \mathbf{R}\rangle \, ,
\tag{C.4}
$$

where N is the number of atoms in the crystal and the Bloch functions are orthonormal

$$
\langle \sigma L \mathbf{k} | \sigma' L' \mathbf{k}'\rangle = \delta_{LL'}\delta_{\sigma\sigma'}\delta_{\mathbf{k}\mathbf{k}'}.
\tag{C.5}
$$

It is easy to show that the Hamiltonian is diagonal in $\mathbf{k}$

$$
H_{LL'}^{\sigma\sigma'\mathbf{k}\mathbf{k}'} = \langle \sigma L \mathbf{k} | H | \sigma' L' \mathbf{k}'\rangle = H_{LL'}^{\sigma\sigma'}(\mathbf{k})\delta_{\mathbf{k}\mathbf{k}'}
\tag{C.6}
$$

with the definition

$$
H_{LL'}^{\sigma\sigma'}(\mathbf{k}) := \langle \sigma L \mathbf{k} | H | \sigma' L' \mathbf{k}\rangle = H_{\mathrm{at},LL'}^{\sigma\sigma'} + \delta_{\sigma\sigma'} \sum_{\mathbf{R}'\in\mathrm{NN}} e^{i\mathbf{k}\cdot\mathbf{R}'} t_{L_0 \, L'_{\mathbf{R}'}} \, .
\tag{C.7}
$$

The eigenfunctions are expanded as

$$
\begin{aligned}
\psi_{\mathbf{k}} \quad = {} & \sum_{L\sigma} c_{L\sigma}(\mathbf{k}) \langle \sigma L \mathbf{k}) \rangle \\
= {} & \frac{1}{\sqrt{N}} \sum_{L\sigma} c_{L\sigma}(\mathbf{k}) \sum_{\mathbf{R}} e^{i\mathbf{k}\cdot\mathbf{R}} |\sigma L \mathbf{R}\rangle \\
= {} & \sum_{\mathbf{R}} e^{i\mathbf{k}\cdot\mathbf{R}} \frac{1}{\sqrt{N}} \sum_{L\sigma} c_{L\sigma}(\mathbf{k}) |\sigma L \mathbf{R}\rangle \, .
\end{aligned}
\tag{C.8}
$$

They can be found by solving the eigenvalue problem

$$
H(\mathbf{k})\psi_{\mathbf{k}} = \epsilon_{\mathbf{k}}\psi_{\mathbf{k}} \, .
\tag{C.9}
$$

The above equation can be transformed to an equation for the coefficients $c_{L\sigma}(\mathbf{k})$

$$\sum_{L'\sigma'} H_{LL'}^{\sigma\sigma'}(\mathbf{k})c_{L'\sigma'}(\mathbf{k}) = \epsilon_{\mathbf{k}}c_{L\sigma}(\mathbf{k}) . \tag{C.10}$$

In reciprocal space, the Green function $G(\mathbf{k}; z)$ of the system can then be found either via inversion or via the spectral representation

$$\begin{aligned} G(\mathbf{k}; z) &= (z - H(\mathbf{k}))^{-1} \\ &= \sum_n \frac{|\psi_{n\mathbf{k}}\rangle \langle \psi_{n\mathbf{k}}|}{z - \epsilon_{\mathbf{k}}} \quad \text{with} \quad z \in \mathbb{C} . \end{aligned} \tag{C.11}$$

Fourier transformation of $G(\mathbf{k}; z)$ to real space leads to

$$G(\mathbf{R}, \mathbf{R}'; z) = \frac{1}{V_{\text{BZ}}} \int d^3k \, G(\mathbf{k}; z)e^{i\mathbf{k}\cdot(\mathbf{R}-\mathbf{R}')} \tag{C.12}$$

and

$$G_{LL'}^{\sigma\sigma'}(\mathbf{R}, \mathbf{R}'; z) = \frac{1}{V_{\text{BZ}}} \int d^3k \, \langle \sigma'L'\mathbf{R}' | G(\mathbf{k}; z) |\sigma L\mathbf{R} \rangle . \tag{C.13}$$

The Green function is required for the calculation of the scattering matrix T as will be shown in the next section. Furthermore, the Green function will be useful for calculating the density of states

$$\rho(\mathbf{R}; z) = -\frac{1}{\pi}\text{Im Tr } G(\mathbf{R}, \mathbf{R}; z) \tag{C.14}$$

where the trace denotes a summation over the diagonal elements of the matrix $G_{LL'}^{\sigma\sigma'}(\mathbf{R}, \mathbf{R}; z)$.

C.1.2 Impurity scattering

In order to construct an impurity Hamiltonian and at the same time keep things as simple as possible, we assume that only the on-site Hamiltonian changes, but the hopping stays the same

$$\Delta H = H^{\text{imp}} - H = H_{\text{at}}^{\text{imp}} - H_{\text{at}}. \tag{C.15}$$

For example, ΔH might be caused by a difference in the spin-orbit coupling parameter ξ or a different on-site element ϵ_L, $L \in (s, p_x, p_y, p_z)$.
The Green function G^{imp} of the system including the impurity can be found via the Dyson equation

$$\begin{aligned} G^{\text{imp}} &= G + G \, \Delta H \, G^{\text{imp}} \\ &= [1 - G \, \Delta H]^{-1} \cdot G . \end{aligned} \tag{C.16}$$

It is sufficient to include the matrix elements of G at the impurity site only, if solely these elements of G^{imp} are to be found. This scheme can be easily generalized to more than one impurity, just the matrices ΔH and G^{imp} become larger.

ϵ_s	ϵ_p	ξ_{LS}	t_{ss}	$t_{sp\sigma}$	$t_{pp\sigma}$	$t_{pp\pi}$
0.0	3.0	0.5	−1.5	0.5	−2.0	0.5

Table C.1.: Parameters for the TB-problem.

The Green function G^{imp} is needed for calculating the scattering matrix T; the relation between the two quantities can be found from the Lippmann-Schwinger equation for a scattered state $\psi_{n\mathbf{k}}^{\mathrm{scat}}$ (which is not an eigenstate of H) in the presence of an impurity

$$
\begin{aligned}
\psi_{n\mathbf{k}}^{\mathrm{imp}} &= \psi_{n\mathbf{k}} + \psi_{n\mathbf{k}}^{\mathrm{scat}} \\
&= \psi_{n\mathbf{k}} + G\,\Delta H\,\psi_{n\mathbf{k}}^{\mathrm{imp}} \\
&= \psi_{n\mathbf{k}} + G\,\Delta H(1 + G^{\mathrm{imp}}\Delta H)\,\psi_{n\mathbf{k}} \\
&\equiv \psi_{n\mathbf{k}} + G\,T\,\psi_{n\mathbf{k}}\,,
\end{aligned}
\tag{C.17}
$$

hence

$$
T = \Delta H + \Delta H\,G^{\mathrm{imp}}\,\Delta H\,.
\tag{C.18}
$$

Finally, the transition amplitude $T_{\mathbf{k}\mathbf{k}'}^{\sigma\sigma'}$ yields

$$
\begin{aligned}
T_{\mathbf{k}\mathbf{k}'}^{\sigma\sigma'} &= \left\langle \psi_{n\mathbf{k}}^{\sigma} \middle| T \middle| \psi_{n'\mathbf{k}'}^{\sigma'} \right\rangle \\
&= \sum_{\mathbf{R}L\sigma}\sum_{\mathbf{R}'L'\sigma'} c_{\mathbf{R}L\sigma}^{\star}(\mathbf{k})T_{LL'}^{\sigma\sigma'}c_{\mathbf{R}'L'\sigma'}(\mathbf{k}')\,.
\end{aligned}
\tag{C.19}
$$

The spin- and momentum relaxation times $\tau_{\mathbf{k}}^{\sigma\sigma'}$, $\sigma,\sigma' \in (\uparrow,\downarrow)$ are then found by integrating $T_{\mathbf{k}\mathbf{k}'}^{\sigma\sigma'}$ over the Fermi surface

$$
\begin{aligned}
\tau_{\mathbf{k}}^{\sigma\sigma'} &= \int d^3k'\,|T_{\mathbf{k}\mathbf{k}'}^{\sigma\sigma'}|^2 \\
&= \int \frac{dS_{\mathbf{k}'}}{v_{\mathbf{k}'}}\,|T_{\mathbf{k}\mathbf{k}'}^{\sigma\sigma'}|^2\,.
\end{aligned}
\tag{C.20}
$$

C.2 Test results

For test purposes, we choose the TB-parameters as specified in table C.1, which lead to a bandstructure shown in figure C.1. The hopping t-matrix $t_{LL'}$ is derived from these within the Slater-Koster-scheme [115].

The red curve reflects the situation of a spin-orbit coupling parameter of $\xi = 0.5$, while the black dots show the bandstructure of the system without spin-orbit coupling.

For the following calculations, spin-orbit coupling is chosen to be non-zero in the impurity only, and the spin-orbit parameter ξ in the impurity Hamiltonian is set to $\xi = 0.5$. The
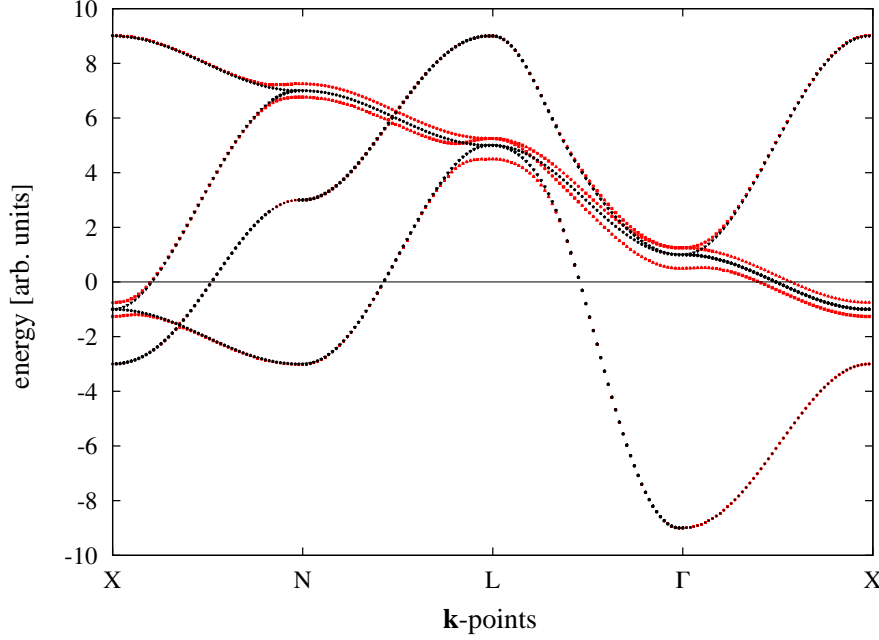
Figure C.1.: Bandstructure of the TB-system. The black dots represent the bandstructure of the system without spin-orbit coupling, while the red points reflect the situation of a spin-orbit coupling parameter of $\xi = 0.5$.

momentum- and spin-relaxation times or the scattering matrix $T_{\mathbf{kk}}^{\sigma\sigma'}$, respectively, are calculated at $E = -6.0$. At this energy, the $\mathbf{k}$-points at the Fermi surface are not degenerate and the Fermi surface is almost spherical.

Single impurity

The simplest case is a single impurity at the origin

$$\mathbf{R}_1 = \begin{pmatrix} 0 \\ 0 \\ 0 \end{pmatrix}. \tag{C.21}$$

Then, the momentum- and spin-relaxation times behave as

$$\tau_{\mathbf{k}}^{\sigma\sigma'} = \tau_{-\mathbf{k}}^{\sigma\sigma'} \quad \text{and} \tag{C.22}$$

$$\tau_{\mathbf{k}}^{\sigma\sigma'} = \tau_{-\mathbf{k}}^{\sigma'\sigma} \quad \text{thus} \tag{C.23}$$

$$\tau_{\mathbf{k}}^{\sigma\sigma'} = \tau_{\mathbf{k}}^{\sigma'\sigma}. \tag{C.24}$$

The first equation must be valid because the system is invariant under space inversion symmetry. The second equality is expected because of time-reversal symmetry, which flips the spin (thus changes σ to $-\sigma$) and reverts the momentum $\mathbf{k}$ to $-\mathbf{k}$, while the third equivalence follows from the two upper ones.

Two impurities

Also in the case of two impurities situated at

$$\mathbf{R}_1 = \begin{pmatrix} 0 \\ 0 \\ 0 \end{pmatrix} \quad \text{and} \quad \mathbf{R}_2 = \begin{pmatrix} 1 \\ 0 \\ 0 \end{pmatrix}, \tag{C.25}$$

the system is invariant under space inversion[1], which manifests in

$$\tau_{\mathbf{k}}^{\sigma\sigma'} = \tau_{-\mathbf{k}}^{\sigma\sigma'}. \tag{C.26}$$

In contrast, our calculations show that the second equality (C.23) is *not* valid any more, hence

$$\tau_{\mathbf{k}}^{\sigma\sigma'} \neq \tau_{-\mathbf{k}}^{\sigma'\sigma}. \tag{C.27}$$

The relative difference which is almost independent of the choice of the absolute value of the spin-orbit coupling parameter ξ is

$$\left| \tau_{\mathbf{k}}^{\uparrow\uparrow} - \tau_{-\mathbf{k}}^{\downarrow\downarrow} \right| \approx 0.1\% \tag{C.28}$$

$$\left| \tau_{\mathbf{k}}^{\uparrow\downarrow} - \tau_{-\mathbf{k}}^{\downarrow\uparrow} \right| \approx 1\%, \tag{C.29}$$

where we have chosen a representative $\mathbf{k}$-point $\mathbf{k} = (0, 1.34, 0.77)$ on the Fermi surface for which this large deviation is found. However, the averages over the Fermi surface fulfill

$$\tau^{\uparrow\uparrow} = \tau^{\downarrow\downarrow} \quad \text{and} \tag{C.30}$$

$$\tau^{\uparrow\downarrow} = \tau^{\downarrow\uparrow} \tag{C.31}$$

up to the numerical accuracy of about 10^{-9}.

Three impurities

When placing three impurities at the positions

$$\mathbf{R}_1 = \begin{pmatrix} 0 \\ 0 \\ 0 \end{pmatrix}, \quad \mathbf{R}_2 = \begin{pmatrix} 1 \\ 0 \\ 0 \end{pmatrix} \quad \text{and} \quad \mathbf{R}_3 = \begin{pmatrix} 0 \\ 1 \\ 0 \end{pmatrix}. \tag{C.32}$$

---

[1]This is valid for arbitrary positions of the impurities when an appropriate center is chosen.

	$\mathbf{k}_1$	$\mathbf{k}_2$
$\tau_{\mathbf{k}}^{\uparrow\uparrow}$	0.106798	0.112749
$\tau_{-\mathbf{k}}^{\downarrow\downarrow}$	0.106888	0.1126949
$\tau_{\mathbf{k}}^{\downarrow\downarrow}$	0.106811	0.1126480
$\tau_{-\mathbf{k}}^{\uparrow\uparrow}$	0.106827	0.1126653
$\tau_{\mathbf{k}}^{\uparrow\downarrow}$	$8.509927 \cdot 10^{-5}$	$7.88453 \cdot 10^{-5}$
$\tau_{-\mathbf{k}}^{\downarrow\uparrow}$	$8.496228 \cdot 10^{-5}$	$7.82864 \cdot 10^{-5}$
$\tau_{\mathbf{k}}^{\downarrow\uparrow}$	$8.453999 \cdot 10^{-5}$	$7.882741 \cdot 10^{-5}$
$\tau_{-\mathbf{k}}^{\uparrow\downarrow}$	$8.498709 \cdot 10^{-5}$	$7.912631 \cdot 10^{-5}$

Table C.2.: Lifetimes at $\mathbf{k}_1 = (0, 1.29, 0.83)$ and $\mathbf{k}_2 = (1.19, 0.43, 0.85)$, two representative $\mathbf{k}$-points on the Fermi surface with large deviations for three impurities.

the system is not invariant under space inversion any more and we find

$$\tau_{\mathbf{k}}^{\sigma\sigma'} \neq \tau_{-\mathbf{k}}^{\sigma\sigma'} \tag{C.33}$$

and

$$\tau_{\mathbf{k}}^{\uparrow\uparrow} \neq \tau_{\mathbf{k}}^{\downarrow\downarrow} . \tag{C.34}$$

Analogously to the case of two impurities we also find

$$\tau_{\mathbf{k}}^{\sigma\sigma'} \neq \tau_{-\mathbf{k}}^{\sigma'\sigma} . \tag{C.35}$$

In table C.2 the values of $\tau_{\mathbf{k}}^{\sigma\sigma'}$ are given at two $\mathbf{k}$-points. The average over the Fermi surface is – as for two impurities – gives

$$\tau^{\uparrow\uparrow} \;=\; \tau^{\downarrow\downarrow} \qquad\qquad \text{and} \tag{C.36}$$

$$\tau^{\uparrow\downarrow} \;=\; \tau^{\downarrow\uparrow} \tag{C.37}$$

up to a numerical accuracy of about 10^{-9}.

A refinement of the mesh chosen for the $\mathbf{k}$-integration over the Fermi surface did not change these results significantly.

C.3 Conclusion

The momentum- and spin-relaxation times calculated for the cases of two and three impurities demonstrate that the expected equivalence of $\tau_{\mathbf{k}}^{\sigma\sigma'}$ and $\tau_{-\mathbf{k}}^{-\sigma-\sigma'}$ on the Fermi surface due to time-reversal symmetry is not fulfilled. Thus, within this simple tight-binding model, the same behavior of $\tau_{\mathbf{k}}^{\sigma\sigma'}$ as within the KKR formalism is found. The reasons of this symmetry breaking are still to be understood. However, the results obtained in this simple model allows us to trust in the results of the much more complicated KKR formalism.

Bibliography

[1] N. F. Mott, Proceedings of the Royal Society of London. Series A - Mathematical and Physical Sciences **156**, 368 (1936)

[2] N. F. Mott, Proceedings of the Royal Society of London. Series A - Mathematical and Physical Sciences **153**, 699 (1936)

[3] M. N. Baibich, J. M. Broto, A. Fert, F. N. Van Dau, F. Petroff, P. Etienne, G. Creuzet, A. Friederich, and J. Chazelas, Phys. Rev. Lett. **61**, 2472 (1988)

[4] G. Binasch, P. Grünberg, F. Saurenbach, and W. Zinn, Phys. Rev. B **39**, 4828 (1989)

[5] M. Johnson and R. H. Silsbee, Phys. Rev. Lett. **55**, 1790 (1985)

[6] M. Johnson and R. H. Silsbee, Journal of Applied Physics **63**, 3934 (1988)

[7] J. Fabian and S. D. Sarma, Journal of Vacuum Science and Technology B **17**, 1708 (1999)

[8] I. Zutic, J. Fabian, and S. Das Sarma, Rev. Mod. Phys. **76**, 323 (2004)

[9] R. J. Elliott, Phys. Rev. **96**, 266 (1954)

[10] M. I. D'yakonov and V. I. Perel, Fiz. Tverd. Tela **13**, 3581 (1971)

[11] V. P. Zhukov, E. V. Chulkov, and P. M. Echenique, physica status solidi (a) **205**, 1296 (2008)

[12] N. Papanikolaou, N. Stefanou, P. H. Dederichs, S. Geier, and G. Bergmann, Phys. Rev. Lett. **69**, 2110 (1992)

[13] D. V. Fedorov, P. Zahn, M. Gradhand, and I. Mertig, Phys. Rev. B **77**, 092406 (2008)

[14] J. Fabian and S. Das Sarma, Phys. Rev. Lett. **81**, 5624 (1998)

[15] P. Monod and F. Beuneu, Phys. Rev. B **19**, 911 (1979)

[16] T. W. Griswold, A. F. Kip, and C. Kittel, Phys. Rev. **88**, 951 (1952)

[17] G. Feher and A. F. Kip, Phys. Rev. **98**, 337 (1955)

[18] M. Johnson, Journal of Applied Physics **75**, 6714 (1994)

[19] M. Johnson, Applied Physics Letters **65**, 1460 (1994)

[20] T. Seki, Y. Hasegawa, S. Mitani, S. Takahashi, H. Imamura, S. Maekawa, J. Nitta, and K. Takanashi, Nat. Mater. **7**, 125 (2008)

[21] O. Mosendz, V. Vlaminck, J. E. Pearson, F. Y. Fradin, G. E. W. Bauer, S. D. Bader, and A. Hoffmann, Phys. Rev. B **82**, 214403 (2010)

[22] J. Kröger, M. Becker, H. Jensen, T. von Hofe, N. Néel, L. Limot, R. Berndt, S. Crampin, E. Pehlke, C. Corriol, V. Silkin, D. Sánchez-Portal, A. Arnau, E. Chulkov, and P. Echenique, Progress in Surface Science **82**, 293 (2007)

[23] P. M. Echenique, R. Berndt, E. V. Chulkov, T. Fauster, A. Goldmann, and U. Höfer, Surface Science Reports **52**, 219 (2004)

[24] R. Matzdorf, Chemical Physics **251**, 151 (2000)

[25] T. Fauster and W. Steinmann, in *Electromagnetic Waves: Recent Developments in Research*, Vol. 2, edited by P. Halevi (North-Holland, Amsterdam, 1995) Chap. 8, p. 347

[26] K. Giesen, F. Hage, F. J. Himpsel, H. J. Riess, and W. Steinmann, Phys. Rev. Lett. **55**, 300 (1985)

[27] F. Reinert, G. Nicolay, S. Schmidt, D. Ehm, and S. Hüfner, Phys. Rev. B **63**, 115415 (2001)

[28] P. Hohenberg and W. Kohn, Phys. Rev. **136**, B864 (1964)

[29] W. Kohn and L. J. Sham, Phys. Rev. **140**, A1133 (1965)

[30] J. Korringa, Physica **13**, 392 (1947)

[31] W. Kohn and N. Rostoker, Phys. Rev. **94**, 1111 (1954)

[32] T. Kimura, Y. Otani, T. Sato, S. Takahashi, and S. Maekawa, Phys. Rev. Lett. **98**, 156601 (2007)

[33] L. H. Thomas, Mathematical Proceedings of the Cambridge Philosophical Society **23**, 542 (1927)

[34] E. Fermi, Atti Accad. Naz. Lincei, Cl. Sci. Fis., Mat. Nat. **6**, 602 (1927)

[35] M. Levy, Proceedings of the National Academy of Sciences of the United States of America **76**, 6062 (1979)

[36] N. D. Mermin, Phys. Rev. **137**, A1441 (1965)

[37] R. Zeller, in *Computational Condensed Matter Physics*, Schriften des Forschungszentrums Jülich, Vol. 32, edited by S. Blügel, G. Gompper, E. Koch, H. Müller-Krumbhaar, R. Spatschek, and R. Winkler (Forschungszentrum Jülich GmbH, 2006)

[38] P. H. Dederichs and R. Zeller, Phys. Rev. B **28**, 5462 (1983)

[39] D. M. Ceperley and B. J. Alder, Phys. Rev. Lett. **45**, 566 (1980)

[40] S. Vosko, L. Wilk, and M. Nusair, Canadian Journal of Physics **58**, 1200 (1980)

[41] J. P. Perdew and A. Zunger, Phys. Rev. B **23**, 5048 (1981)

[42] J. P. Perdew, J. A. Chevary, S. H. Vosko, K. A. Jackson, M. R. Pederson, D. J. Singh, and C. Fiolhais, Phys. Rev. B **46**, 6671 (1992)

[43] J. P. Perdew, K. Burke, and M. Ernzerhof, Phys. Rev. Lett. **77**, 3865 (1996)

[44] T. H. Dupree, Annals of Physics **15**, 63 (1961)

[45] J. L. Beeby, Proceedings of the Royal Society of London. Series A. Mathematical and Physical Sciences **302**, 113 (1967)

[46] N. Papanikolaou, R. Zeller, and P. H. Dederichs, Journal of Physics: Condensed Matter **14**, 2799 (2002)

[47] R. Zeller and P. H. Dederichs, Phys. Rev. Lett. **42**, 1713 (1979)

[48] K. Wildberger, R. Zeller, and P. H. Dederichs, Phys. Rev. B **55**, 10074 (1997)

[49] R. Zeller, P. H. Dederichs, B. Újfalussy, L. Szunyogh, and P. Weinberger, Phys. Rev. B **52**, 8807 (1995)

[50] M. Asato, A. Settels, T. Hoshino, T. Asada, S. Blügel, R. Zeller, and P. H. Dederichs, Phys. Rev. B **60**, 5202 (1999)

[51] I. Galanakis, G. Bihlmayer, V. Bellini, N. Papanikolaou, R. Zeller, S. Blügel, and P. H. Dederichs, EPL (Europhysics Letters) **58**, 751 (2002)

[52] M. Freyss, N. Papanikolaou, V. Bellini, R. Zeller, and P. H. Dederichs, Phys. Rev. B **66**, 014445 (2002)

[53] B. Nonas, K. Wildberger, R. Zeller, P. H. Dederichs, and B. L. Gyorffy, Phys. Rev. B **57**, 84 (1998)

[54] P. Mavropoulos, O. Wunnicke, and P. H. Dederichs, Phys. Rev. B **66**, 024416 (2002)

[55] N. Papanikolaou, J. Opitz, P. Zahn, and I. Mertig, Phys. Rev. B **66**, 165441 (2002)

[56] A. Vernes, H. Ebert, and J. Banhart, Phys. Rev. B **68**, 134404 (2003)

[57] V. Popescu, H. Ebert, B. Nonas, and P. H. Dederichs, Phys. Rev. B **64**, 184407 (2001)

[58] P. Mavropoulos and N. Papanikolaou, in *Computational Nanoscience: Do It Yourself!*, NIC series, Vol. 31, edited by J. Grotendorst, S. Blügel, and D. Marx (John von Neumann Institute for Computing, Jülich, 2006) pp. 131--158, `http://www.fz-juelich.de/nic-series/volume31`

[59] P. Ziesche and G. Lehmann, *Ergebnisse in der Elektronentheorie der Metalle* (Akademie Verlag Berlin, 1983)

[60] R. Newton, *Scattering Theory of Particles and Waves* (Springer, 1982)

[61] E. Economou, *Green's functions in Quantum Physics* (Springer Series in Solid-State Sciences 7, Springer Verlag Berlin, 1979)

[62] G. Arfken, *Mathematical Methods for Physicists* (Academic Press International Edition, 1970)

[63] R. Zeller, Journal of Physics C: Solid State Physics **20**, 2347 (1987)

[64] R. Zeller, Journal of Physics: Condensed Matter **20**, 035220 (2008)

[65] B. Drittler, M. Weinert, R. Zeller, and P. Dederichs, Solid State Communications **79**, 31 (1991)

[66] R. Zeller, Journal of Physics: Condensed Matter **16**, 6453 (2004)

[67] N. Stefanou, H. Akai, and R. Zeller, Computer Physics Communications **60**, 231 (1990)

[68] N. Stefanou and R. Zeller, Journal of Physics: Condensed Matter **3**, 7599 (1991)

[69] I. Mertig, E. Mrosan, and P. Ziesche, *Multiple Scattering Theory of Point Defects in Metals: Electronic Properties*, Teubner-Texte zur Physik, Vol. 11 (G. Teubner Verlagsgesellschaft Leipzig, 1987)

[70] P. Zahn, *Screened Korringa-Kohn-Rostocker-Methode für Vielfachschichten*, Ph.D. thesis, Technische Universität Dresden (1998)

[71] P. J. Braspenning, *Self-consistent muffin-tin impurity potentials, local electron densities of states and cluster-model de Haas-van-Alphen relaxation times*, Ph.D. thesis, Vrije universiteit te Amsterdam (1982)

[72] A. Bohm, *Quantum mechanics: Foundations and Applications* (Springer, 1993)

[73] R. Podloucky, R. Zeller, and P. H. Dederichs, Phys. Rev. B **22**, 5777 (1980)

[74] G. Bihlmayer, in *Spintronics - From GMR to Quantum Information*, Schriften des Forschungszentrums Jülich, Vol. 10, edited by S. Blügel, D. Bürgler, M. Morgenstern, C. M. Schneider, and R. Waser (Forschungszentrum Jülich GmbH, 2009) Chap. B 6, p. A 1

[75] E. M. Rose, *Relativistische Elektronentheorie*, Vol. 2 (Hochschultaschenbücher-

Verlag, 1971)

[76] J. Blatt and V. Weisskopf, *Theoretical Nuclear Physics* (Wiley, 1952)

[77] B. Drittler, *KKR-Greensche Funktionsmethode für das volle Zellpotential*, Ph.D. thesis, Institut für Festkörperforschung, Forschungszentrum Jülich (1991)

[78] E. Anderson, Z. Bai, C. Bischof, S. Blackford, J. Demmel, J. Dongarra, J. Du Croz, A. Greenbaum, S. Hammarling, A. McKenney, and D. Sorensen, *LAPACK Users' Guide*, 3rd ed. (Society for Industrial and Applied Mathematics, Philadelphia, PA, 1999) http://www.netlib.org/lapack/

[79] M. Gradhand, M. Czerner, D. V. Fedorov, P. Zahn, B. Y. Yavorsky, L. Szunyogh, and I. Mertig, Phys. Rev. B **80**, 224413 (2009)

[80] M. Gradhand, D. V. Fedorov, P. Zahn, and I. Mertig, Phys. Rev. B **81**, 020403 (2010)

[81] R. Zeller and H. Ebert, *The SPR-TB-KKR package*, http://olymp.cup.uni-muenchen.de/ak/ebert/SPR-TB-KKR

[82] Y. Yafet, in *Solid State Physics*, Vol. 14, edited by F. Seitz and D. Turnbull (Academic Press International Edition, 1963) p. 2

[83] D. V. Fedorov, P. Zahn, M. Gradhand, and I. Mertig, Phys. Rev. B **79**, 059901 (2009)

[84] L. S. Rodberg and R. M. Thaler, *Introduction to the Quantum Theory of Scattering* (Elsevier Science and Technology, 1967)

[85] Monod, P. and Schultz, S., J. Phys. France **43**, 393 (1982)

[86] B. A. McDougall, T. Balasubramanian, and E. Jensen, Phys. Rev. B **51**, 13891 (1995)

[87] R. Matzdorf, R. Paniago, G. Meister, and A. Goldmann, Solid State Communications **96**, 799 (1995)

[88] R. Paniago, R. Matzdorf, G. Meister, and A. Goldmann, Surface Science **336**, 113 (1995)

[89] J. Kröger, L. Limot, H. Jensen, R. Berndt, S. Crampin, and E. Pehlke, Progress in Surface Science **80**, 26 (2005)

[90] L. Limot, E. Pehlke, J. Kröger, and R. Berndt, Phys. Rev. Lett. **94**, 036805 (2005)

[91] M. Hirschmann and T. Fauster, Applied Physics A: Materials Science and Processing **88**, 547 (2007)

[92] I. Mertig, E. Mrosan, R. Zeller, P. H. Dederichs, and P. Ziesche, phys. stat. sol. (b) **117**, 335 (1983)

[93] W. Shockley, Phys. Rev. **56**, 317 (1939)

[94] J. O. Linde, Annalen der Physik **402**, 52 (1931)

[95] J. O. Linde, Annalen der Physik **406**, 353 (1932)

[96] *Periodic table of elements*, http://www.mateck.com/Pse/pse.htm

[97] A. C. Hewson, *The Kondo problem to heavy fermions* (Cambridge Univ. Press, 2003)

[98] P. T. Coleridge, N. A. W. Holzwarth, and M. J. G. Lee, Phys. Rev. B **10**, 1213 (1974)

[99] M. D. Daybell and W. A. Steyert, Phys. Rev. Lett. **20**, 195 (1968)

[100] M. D. Daybell and W. A. Steyert, Phys. Rev. Lett. **18**, 398 (1967)

[101] Y. A. Bychkov and E. I. Rashba, Journal of Physics C: Solid State Physics **17**, 6039 (1984)

[102] Y. A. Bychkov and E. I. Rashba, Sov. Phys. JETP Letter **39**, 78 (1984)

[103] G. Dresselhaus, Phys. Rev. **100**, 580 (1955)

[104] H. A. Kramers, Proc. Amsterdam Acad. Sci. **33**, 959 (1930)

[105] M. I. D'yakonov and V. I. Perel, Sov. Phys. JETP Letter **33**, 1053 (1971)

[106] E. I. Rashba, Sov. Phys. Solid State **2**, 1224 (1960)

[107] T. Schäpers, J. Knobbe, and V. A. Guzenko, Phys. Rev. B **69**, 235323 (2004)

[108] G. Bihlmayer, Y. Koroteev, P. Echenique, E. Chulkov, and S. Blügel, Surface Science **600**, 3888 (2006)

[109] S. LaShell, B. A. McDougall, and E. Jensen, Phys. Rev. Lett. **77**, 3419 (1996)

[110] J. Luo, H. Munekata, F. F. Fang, and P. J. Stiles, Phys. Rev. B **38**, 10142 (1988)

[111] J. Fabian, A. Matos-Abiaque, C. Ertler, P. Stano, and I. Zutic, acta physica slovaca **57**, 565 (2007)

[112] T. Bergmann, *Paritätsverletzende Polarisationsrotationen von Deuterium in elektrischen Feldern*, Ph.D. thesis, Ruprecht-Karls-Universität Heidelberg (2003)

[113] G. W. Botz, D. Bruss, and O. Nachtmann, Annals of Physics **240**, 107 (1995)

[114] C. Cohen-Tannoudji, B. Diu, and F.Laloe, *Quantum mechanics*, Vol. 2 (Wiley, 2006)

[115] W. A. Harrison, *Elementary electronic structure* (World Scientific Singapore, 1999)

Acknowledgment

There is a long list of people, who supported me during this thesis. I am very thankful to all of them.

First of all I want to thank my supervisor Prof. Dr. Stefan Blügel for giving me the opportunity to write this thesis in the friendly atmosphere of the institute 'Quantum theory of materials'. I gratefully acknowledge the interesting discussions, giving me new ideas and inspirations for further work.

Next I want to thank Prof. Dr. Riccardo Mazzarello for his kind acceptance to provide the second opinion of my thesis.

Special thanks go to Dr. Phivos Mavropoulos who was the best supervisor I could imagine. I am sincerely grateful for the innumerable discussions concerning my work, your clear and competent physical explanations and your patience in answering my questions. Apart from that I thank you for motivating me when I needed it, never loosing the belief in the accomplishment of this work.

I thank also Dr. Rudolf Zeller for his helpful comments about KKR and the thorough proof-reading of my thesis. Your detailed knowledge of the method had been very helpful.

Many thanks go to Prof. Dr. Peter H. Dederichs for his sincere interest in my work.

I want to thank Dr. Gustav Bihlmayer for his helpful illuminations concerning spin-orbit induced effects on surfaces. Your experience in this field of physics helped me to check the consistency of important parts of my program.

Furthermore, much thanks goes to Dr. Samir Lounis for introducing me into the impurity KKR code.